OPERANDO RAMAN SPECTROSCOPY STUDY OF ELECTRODE SURFACES

A Dissertation
Presented to
The Academic Faculty

by

Jun Hyuk Kim

In Partial Fulfillment
of the Requirements for the Degree
Doctor of Philosophy in the
School of Chemical & Biomolecular Engineering

Georgia Institute of Technology
December 2018

OPERANDO RAMAN SPECTROSCOPY STUDY OF ELECTRODE SURFACES

Approved by:

Dr. Meilin Liu, Advisor
School of Materials Science and Engineering
Georgia Institute of Technology

Dr. Dennis Hess
School of Chemical and Biomolecular Engineering
Georgia Institute of Technology

Dr. Thomas Fuller, Co-advisor
School of Chemical and Biomolecular Engineering
Georgia Institute of Technology

Dr. John Zhang
School of Chemistry and Biochemistry
Georgia Institute of Technology

Dr. Carson Meredith
School of Chemical and Biomolecular Engineering
Georgia Institute of Technology

Date Approved: [Dec. 14th, 2018]

Joy will decay, though a heart will remember.

ACKNOWLEDGEMENTS

Foremost, my deepest gratitude goes to my advisor, Dr. Meilin Liu, a true scientist who ceaselessly pursues to understand the mechanisms of energy conversion and storage. I am privileged to be served as a Raman spectroscopy operator in his lab to unravel mechanisms toward oxidation/reduction and activation/contamination of various energy materials. He gave me freedom in choosing the research topics and directions, while he provided critical advice to amend/build solid conclusions in my study. Not only for his academic guidance, but I also benefitted to have connection with many professional computation experts who were senior of our lab to have complete validation of mechanistic study observed by Raman spectroscopy. These valuable networks cannot be attainable without Dr. Liu's introduction, which I appreciate much.

Dr. Thomas Fuller is a great mentor for me. While it can be easily missed to satisfy graduate requirements, he guided me to be on right track so that I can safely acquire my Ph.D degree. I appreciate much about his true caring toward student and I also enjoyed many of the thought-provoking discussions with him. I would also like to give thanks to the rest of my Ph.D thesis committees, Dr. Carson Meredith, Dr. Dennis Hess, and Dr. John Zhang for their guidance and suggestions.

Dr. Dongchang Chen was a great Raman spectroscopy teacher for me. He spared his valuable time to train me as a Raman expert. He is a true master of vibrational spectroscopy, and he is an exceptional role-model for me to benchmark. His insightful suggestions helped me to set priorities and find efficient routes to accomplish my Ph.D study.

Dr. Seonyoung Yoo, who is a master of material fabrication, helped me tremendously in both experimentally and mentally. In electrode materials design, she gave me valuable know-how to prepare ceramics in right way and give useful tips on ceramic processing as well. Not only for material design, but she also has significant knowledge & expertise in solid oxide fuel cell cathode materials, and shared many valuable information with me. Her earnestness toward research has inspired me to establish a correct mindset toward my degree. She was also a good lunch-mate with me and we discussed a lot of things about research as well as daily-life in lab. Had it not been for her, I could not bear stresses I get from work. Therefore, I deeply appreciate the fact that she was a great mentor for me.

I am also in debt to Dr. Yongman Choi and Dr. Jenghan Wang who contributed to this work. They are both great professionals, providing valuable computational studies to support my mechanistic studies. In particular, Dr. Yongman Choi helped develop molecular insight in cathode Oxygen Reduction Reaction studies, and Dr. Jenghan Wang conducted modeling toward sulfur-poisoning studies in anode. Their outstanding capability toward computational modeling was a valuable resource for me, and I cannot thank enough for their efforts.

My sincere appreciation is due to our excellent SOFC team – Dr. Yu Chen, Kai, Ben deGlee, Weilin, Ryan Murphy, Nick Kane, Lei Zhang, Yuchen Liu – as well. The team greatly dedicated in our lab to complete/surpass milestones in many SOFC projects (DOE-SECA, Arpa-E, Phillips66, Millenitek etc.) and every member served as an expert in their part, thus we could be an efficient and powerful group at the same time. Especially, Nick Kane provided valuable model cells which enable my *operando* Raman

spectroscopy study on Oxygen Reduction Reactions on LSCF. I also thank other group members rather than SOFC team as well.

My special thanks goes to Ki Hwan Jang, one of my best friend in high school, come to Georgia Tech in 2017 spring as visiting scholar. This is the time when my *in situ* Raman spectroscopy experiment starts to work out, and my honor goes to Ki Hwan, since his existence in Atlanta gave me refreshment to escape from negative thoughts and pursue my research. Without my friend's encouragement at this time, I could have not successfully pass through hard times. Similarly, Sungbin Richard Sorn visited Atlanta twice, and I could have positive reinforcement from his visit. I cannot thank enough for my dearest friends. I also thank many friends who kindly welcomed me when I had vacation in Korea. Many friends in Georgia Tech, including Korean student associate of CHBE and MSE made enjoyable life while studying abroad. I hope I can maintain my valuable network obtained in Georgia Tech.

I was lucky to be in Gerogia Tech as it has world-class athletic facility; Campus Recreation Center. I would be very mournful about the fact that I can no longer exercise there every morning. I thank the excellent facility that I could train myself to remain in strong physique as old Roman phrase, "A sound mind in a sound body."

I could not finish my acknowledgement without recognizing my families. My families have given me constant support so that I can stay brave and keep up with my Ph.D. degree. Frequent calls and messages with full of encouragements made me feel that I stay tuned with them, even though the fact that I am on the other side of the earth. And finally, my dog, Harriet, you are my delight. Thanks for your emotional support when I

am off work. Walking with you has been a great time for me to straighten out my thoughts.

And I also thank myself, who has never given up my way and continued to pursuit Ph.D. degree while going through hardship and adversity. I am very proud of my bravery that I decided to pursue doctorate abroad in such a young age. It has been wonderful time to study abroad with lots of traveling which I enjoyed much.

TABLE OF CONTENTS

LIST OF TABLES

LIST OF FIGURES

LIST OF SYMBOLS AND ABBREVIATIONS

BCO	$BaCoO_{3-x}$
BZCYYb	$BaZr_{0.1}Ce_{0.7}Y_{0.1}Yb_{0.1}O_{3-\delta}$
BZY	$BaZr_{1-x}Y_xO_{3-\delta}$
CCM	Cathode contact material
DFT	Density functional theory
EDX	Energy dispersion X-ray spectroscopy
EIS	Electrochemical impedance spectroscopy
GDC	Gadolinium doped ceria
IR	Infrared spectroscopy
LPG	Liquefied petroleum gas
LSM	$La_{1-x}Sr_xMnO_{3-\delta}$
LSCF	$La_{1-x}Sr_xCo_{1-y}Fe_yO_{3-\delta}$
LSPR	Localized surface plasmon resonance
MCFC	Molten-carbonate fuel cell
MIEC	Mixed ionic & electronic conductor
OCV	Open circuit voltage
ORR	Oxygen reduction reaction
PBCC	$PrBa_{0.8}Ca_{0.2}Co_2O_{5+d}$
PCFC	Protonic ceramic fuel cell
PEMFC	Proton exchange membrane fuel cells
R_p	Polarization Resistance
SCO	$SrCoO_{3-x}$

SDC	Samarium doped ceria
SEM	Scanning electron microscopy
SERS	Surface enhanced Raman spectroscopy
SHINERS	Shell-isolated nanoparticle enhanced Raman spectroscopy SHINERS
SOEC	Solid oxide electrolysis cell
SOFC	Solid oxide fuel cell
SSC	$Sm_{1-x}Sr_xCoO_{3-\delta}$
S/C	Steam to carbon ratio
TEM	Transmission electron microscopy
TEOS	Tetraethyl orthosilicate
TPB	Triple phase boundary (of electrolyte, electrode, and gas phase)
XRD	X-ray diffraction
YSZ	Yttrium stabilized zirconia

SUMMARY

Solid oxide fuel cells (SOFCs) are promising energy technology providing high efficiency with low emission. For SOFCs, a little modification on electrode surface can either dramatically enhance or hinder electrode processes. However, the inability to probe surface species/phases under operating conditions, lack of information on the local properties of hot spots on heterogeneous surfaces, and inadequate understanding of electro-catalytic mechanisms remain as critical challenges to understanding corrosion/promoting dynamics of electrode surfaces. To tackle these problems, I used *in situ/operando* Raman spectroscopy coupled with electrochemical impedance spectroscopy as a strong tool to monitor electrode surfaces.

For example, while sulfur poisoning is widely observed in SOFC electrodes, the fundamental information about corrosion/tolerance dynamics was obscure for a long period of time because sulfur molecule exists in extreme low concentrations. Unique characterization tools presented in this thesis are used to overcome these aforementioned issues, providing superior sensitivity, and successfully connecting electrode polarization arising from surface intermediates. Therefore, corrosion/tolerance dynamics regarding sulfur, which was an unsolved enigma for a long period time, is successfully explained with *operando* Raman spectroscopic platform.

Likewise, investigations into complex mechanisms associated with SOFC electrode materials are provided in this thesis, by applying unique set-up of *in situ/operando* Raman spectroscopy. One of the strong benefits of an *operando* Raman spectroscopy platform is that it can be readily transferred to study various materials under

controlled and desired atmospheres at different temperatures. Therefore, during my Ph.D., I could elucidate a formidable amount of surface science about SOFC electrodes.

While Raman spectroscopy is integral to the studies, the technical approach is not limited to Raman analysis. To understand how things work, various electrochemical techniques, morphology characterization, and molecular modeling is included in this work. I hope fundamental information gained from my study can give valuable insights and therefore can guide future electrode designs.

CHAPTER 1. INTRODUCTION

The solid oxide fuel cell (SOFC) is a next generation energy conversion system which operates at high temperature, from 500^{o}C to 1000^{o}C; thus, it demonstrates the highest energy conversion efficiency (>50%) among all fuel-cell types (Molten-carbonate fuel cell (MCFC), Proton exchange membrane fuel cell (PEMFC) etc.). Therefore, if commercialization of SOFCs is successfully conducted, CO_2 emission during electrochemical conversion of fossil fuels would be significantly reduced. Also, the high operating temperature of SOFC does not require expensive platinum catalyst to accelerate oxygen reduction reaction. High temperature operation also enables partial internal reforming of carbonaceous fuels such as natural gas, propane, liquefied petroleum gas (LPG) etc. into Hydrogen (H_2); and SOFCs are not vulnerable to carbon monoxide (CO), which has destructive impact on PEMFC catalysts. However, vulnerability toward sulfur poisoning has been widely observed in SOFCs, therefore, investigation into sulfur corrosion/mitigation dynamics should be performed to fully achieve fuel flexibility of SOFCs. Application into combined heat and power system or heat engine energy recovery devices are highly promising for SOFCs, because it can further increase overall fuel efficiency (80% ~ 90%).

Because of aforementioned merits, the SOFC is considered as essential device in future energy conversion/storage market, and technology advancements and development of SOFCs are proceeding worldwide. For example, in the USA, Department of Energy (DOE) is targeting scale-up of SOFC systems, and leading the Solid-state Energy Conversion Alliance (SECA) program. The goal of the program is to develop electrodes

that exhibit high-electrocatalytic activity and are contaminant-tolerance at the same time. Our group led by my Professor. Meilin Liu has been dedicated to this project. Bloom Energy company successfully assembled a 100 kW SOFC system, and they launched commercialized products, "Bloom Box". These have been installed in the facilities of Google, E-bay and Apple, to name a few. Bloom Energy mainly targets stationary markets, focusing on building security. Japan is leading the development of SOFCs for residential distribution. In a push toward commercialization of SOFCs, researchers in Japan gained experience and identified some remaining technical challenges from extensive field-tests. A total of 233 SOFC systems were deployed in Japan from 2007 to 2010; and the longest time of operation recorded was 25,843 hours (~3 years) with electrochemical efficiency over 45%. Japan conducted further field-tests in 2012, and they achieved 700 kW combined heat and power system with 90% efficiency. In Korea, KIST recently identified protonic ceramic fuel cell (PCFC) as promising technology because of the reduced operating temperature to 400~600^{o}C, which can further lower operation cost while maintaining useful merits of SOFCs. As described above, many developed countries are leading various SOFC technology research & development programs to resolve energy depletion and to mitigate environmental pollution and global warming.

1.1 Challenges of the Solid Oxide Fuel Cells

While small SOFC systems appear poised for commercialization in distributed generation, broad market penetration will require continuous innovation of materials and

fabrication processes to prolong system lifetimes and reduce cost. One technical opportunity is to enhance the durability of the electrodes, which still contribute the most to performance degradation and efficiency loss in the existing SOFCs. One of the major causes of electrode degradation is contaminant poisoning. The electrodes of SOFC, both cathode and anode, can go through fast degradation upon exposure to contaminants (Figure 1).

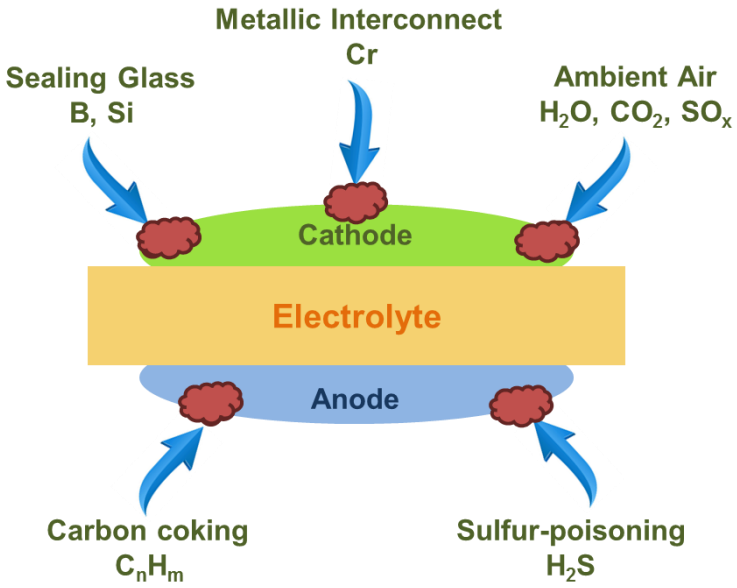

Figure 1. Schematic diagram showing the source of contaminants for SOFC cathode and anode

In the cathode, contaminants includes chromium (Cr) from typical Cr-containing interconnect materials, boron (B) and silicon (Si) from sealing glasses, and SO_x, CO_2, H_2O found in the ambient air stream. For the anode, the types of contaminants are largely divided in two: carbon coking from hydrocarbon reforming, and sulfur poisoning from odorant and/or from natural source, which can be found while operating with readily

available fuels, city gas, natural gas and liquefied petroleum (LP) gas for example. In reality, it is impractical to fully prevent the exposure of electrode materials to these various contaminants. It is thus crucial to obtain a fundamental understanding of the contaminant-poisoning process of SOFC electrodes and to implement an effective approach to minimize the degradation effect associated with contaminant poisoning. However, to date, the search for novel material for SOFCs is still largely dependent on experience and intuition, rather than a systematic scientific approach. This heuristic method is used because the degradation mechanism of the electrode and the regeneration mechanism from contaminants are still unclear. One important step forward is to systematically study the degradation mechanism of the state-of-the-art SOFC electrode materials using powerful characterization tools, especially the ***in situ*** and ***operando Raman spectroscopy***, to probe and map surface species and incipient phases under realistic operating conditions.

1.2 Research Objectives

To truly understand the mechanism, *in situ/ operando* measurements to follow the surface reactions are needed. Raman spectroscopy, one of the vibrational spectroscopy, is the ideal technique to confront the challenge. The advantages of Raman spectroscopy are evident. First, while many *ex situ* characterizations have potential risk of improper sample transfer and introducing artifacts, *in situ/ operando* Raman scattering is capable of providing immediate finger-printing of vibrational bonds in solid-gas interaction. Second, Raman spectroscopy can perform *operando* characterization for a

wide range of temperature and pressure since it does not require vacuum. Although *operando* Raman study may have insufficient sensitivity to monitor low concentrations of surface species, Surface Enhanced Raman Spectroscopy (SERS) can dramatically improve the detection limits to surface species, especially reaction intermediates, which are hard to detect with ordinary Raman. Further, the most exclusive benefit of *operando* characterization is the possibility for direct correlation with different measurements performed in the same time period. For instance, intermediate species identified by Raman spectroscopy could be directly linked to data collected during simultaneous electrochemical measurement, such as impedance spectroscopy. Coupling Raman results with electrochemical results can validate the electrode degradation mechanism in most effective way and the combination of different techniques can synthesize a powerful predictive model.

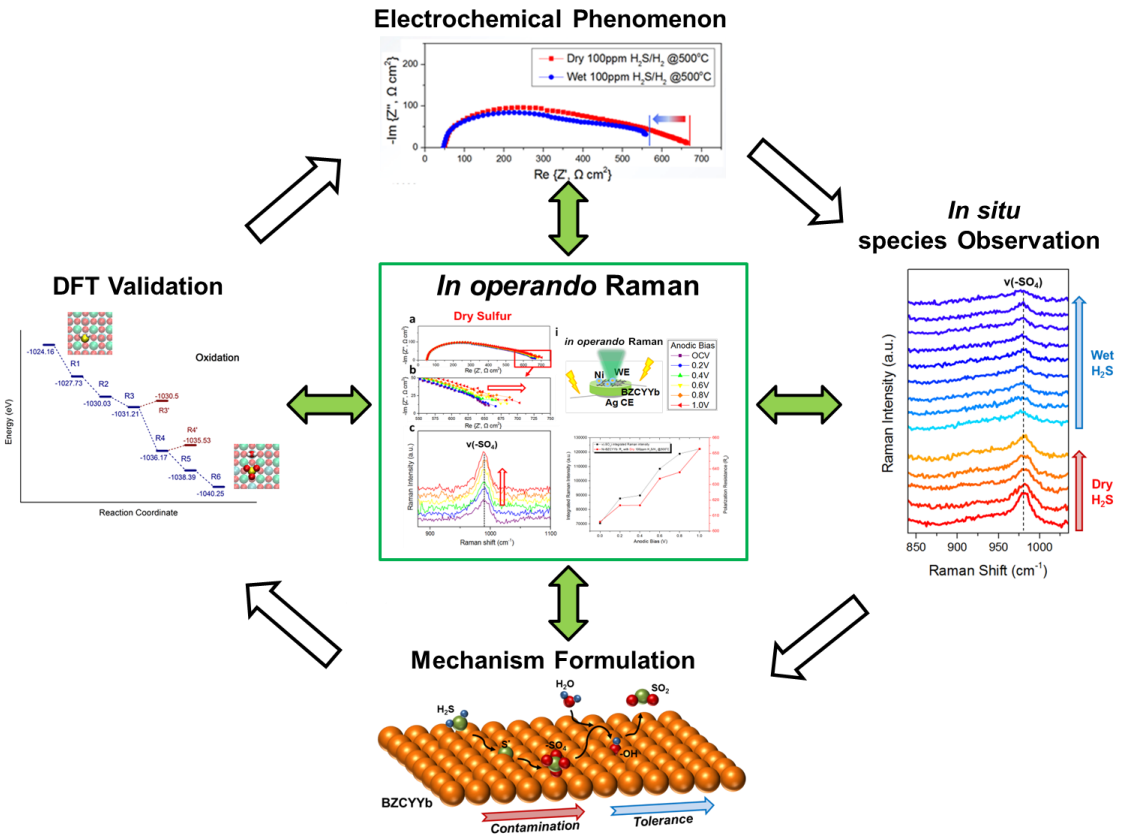

Figure 2. Schematic of technical approaches to unravel surface catalytic reactions using advanced *Operando* Raman spectroscopy as major technique.

For example, the detailed information of water-mediated sulfur tolerance mechanism of Ni-$BaZr_{0.1}Ce_{0.7}Y_{0.1}Yb_{0.1}O_{3-d}$ (BZCYYb) in realistic operating condition empowered by surface-sensitive, *operando* surface enhanced Raman spectroscopy (SERS) analysis coupled with impedance spectroscopy are shown in Figure 2. In contrast to the conventional view that introduced sulfur(S^*) will be mainly removed through oxygen anion delivery from ionic conductor phase,[1] the -SO_4 surface functional group was found to be a primary intermediate species on the proton conducting oxide. As

reflected in SERS spectral features, the presence of water and distinctive water uptake characteristics of proton conducting oxides is proposed as the means to facilitate SO_2 reforming from adsorbed $–SO_4$. This hypothesis synthesized from surface science guided by Raman spectroscopy is successfully linked to molecular dynamics as well, indicating that the technique is solid and powerful. The unique approach of *operando* SERS with model electrodes offers an effective tool for investigating complex mechanisms.

Unique characterization methodology can be readily transferred to the other studies of SOFC electrode materials. For instance, cermet model electrode can be replaced readily by different metal (e.g., Pt, Cu) or different oxygen ion conductors (e.g., YSZ, GDC). By controlling the inlet fuel gas, not only sulfur-poisoning but also carbon coking or steam reforming on model anode could be easily studied. Moreover, the unique experimental set-up and methodologies are not limited to studies of the anode. The approach can also be applied for cathode contamination studies as well as used to unravel the degradation mechanism by the H_2O, CO_2, volatile Cr, SO_2, and borates.

Comprehensive studies to observe the electrode surface, the structure of the interface, and the participating reactants are an essential step to develop novel materials for SOFCs. Understanding of electrode surface reaction is even more meaningful, because up to date study to design SOFC electrode is still mostly based on trial and error. Without a detailed, mechanistic understanding of the surface catalytic reaction, dynamics of performance of SOFCs cannot be understood. So, the new insights gained by this *operando* Raman spectroscopy will directly benefit the SOFC community by unraveling the cause of performance degradation in SOFCs when exposed to various contaminants

and can give guidance to develop a novel electrode structures to have excellent durability against contaminant contained fuels.

1.3 Structure of the Thesis

The Thesis focuses on studying surface catalytic reactions on SOFC electrodes utilizing advanced characterization methods, including *in situ / Operando* Raman, SERS, EIS performed under realistic operating condition to gain insight into the surface species, intermediates and mechanisms that critically related to the performance of electrodes.

Chapter 2 provides the background of the thesis. Basic knowledge about SOFC working principles are described. Fundamentals of Raman spectroscopy, surface enhanced Raman scattering are also presented in this chapter as well. Basics about electrochemical impedance spectroscopy are described and technical approach to combine two different techniques to build *operando* platform is described in this section.

Chapter 3 presents the study of steam-reforming and sulfur-poisoning on Ni-YSZ anodes. Long-term fuel cell performance based on Ni-YSZ is conducted with steam-methane reforming (Steam to carbon ratio (S/C) = 2). Additionally, ppm levels of sulfur are introduced with methane to see the impact of sulfur on steam-reforming catalytic activity of Ni-YSZ. To understand the sulfur-poisoning mechanism, a model electrode with well-defined triple phase boundary is designed and *in situ / Operando* SERS study is followed to elucidate the possible mechanisms.

In Chapter 4, water-mediated sulfur tolerance mechanism of BZCYYb is investigated. Time-resolved Raman analysis shows $–SO_4$ development on surface of BZCYYb upon exposure to 100 ppm H_2S/H_2 and H_2O introduction quickly reduces the intensity of $–SO_4$. A mechanism is hypothesized and validated with designed *operando* SERS coupled with EIS. Moreover, the proposed mechanism is further supported by DFT calculations.

In Chapter 5, enhanced ORR pathway on PBCC driven by surface proton is studied. To elucidate electrochemical performance of PBCC, EIS is utilized. A wet-annealed surface of PBCC is carefully studied with various morphology characterization tools, such as SEM, TEM, and EDX. *In situ / operando* Raman spectroscopy is used to identify oxygen intermediates upon exposure to humid air. Water uptake capability of PBCC is assessed with TGA and Raman profilometry. Also, complementary DFT calculations are used to assign Raman bands and to suggest possible proton-concerting ORR pathways.

In Chapter 6, *operando* Raman spectroscopy is utilized to monitor surface structure and intermediates upon ORR on LSCF model electrode. Dense model electrode fabrication is enabled by RF sputtering. By infiltration of catalysts, the relationship between polarization resistance and oxygen intermediates is suggested.

Chapter 7 summarizes the scientific results along with mechanisms unraveled with Raman surface characterization. In addition, limitation and challenges of these characterization methods are discussed with potential solutions.

In Chapter 8, recommendations are made for development of future works.

CHAPTER 2. BACKGROUND AND TECHNICAL APPROACH

2.1 General Background knowledge of SOFC

Fuel cells usually classified by their electrolyte materials, and solid oxide fuel cell (SOFC) uses a solid oxide electrolytes which has ionic conductivities. Generally, these electrolytes allow transport of oxygen anion (O^{2-}). The conventional materials for SOFC electrolytes are Yttria-Stablized-Zirconia (YSZ), Gadolinium-doped-Ceria (GDC) and Samarium-doped-Ceria (SDC). More recently, protonic ceramic fuel cells (PCFC) which allows transport of both proton and oxygen anion is developed. Barium Zriconates – Cerates derivatives ($BaZr_{1-x}Ce_xO_{3-d}$) are widely used as proton conducting electrolyte materials. Utilization of protonic ceramics shows promising prospects in lower temperature ($400^oC \sim 600^oC$) rather than SOFC ($500^oC \sim 1000^oC$).

Rather than electrolytes, there are two key components in individual cell; cathode and anode. These electrodes usually display porous morphology to enable facile gas transport. The schematic for SOFC single cell with 3 key components can be found in Figure 3[1]. In the cathode, oxygen reduction reaction (ORR) occurs and reaction sequences are followed[2];

$O_{2(g)} + e^- = O_2^-$ (Gaseous oxygen adsorption, superoxide formation)

$O_2^- + e^- = O_2^{2-}$ (peroxide formation)

$O_2^{2-} + 2e^- = 2O^{2-}$ (oxygen-dissociation)

$2O^{2-} + 2V_o`` = 2O_o^x$ (Oxygen fill in the vacancy)

Overall, $\frac{1}{2}O_{2(g)} + V_o`` + 2e^- = O_o^x$

The oxygen anion (O_o^x or O^{2-}) then diffused through gas-tight electrolytes, and in the anode, fuel is electrochemically oxidized with oxygen anion transferred from cathode. As mentioned earlier, SOFC has merit in fuel flexibility, therefore fuels including from H_2 to carbonaceous fuels, such as CH_4 and multi-chain carbon molecules, even octane[3] can be oxidized to generate electricity. In high operating temperature of SOFC, carbonaceous fuel can go through internal reforming into H_2 fuels with help of steam (steam-reforming)[4]. For simplicity, if we assume fuel is pure H_2, the fuel oxidation reaction happen in anode can be described as followed.

$$\mathbf{H_2 + O^{2-} = H_2O + 2e^-}$$

Because cathode consumes electrons while anode generates electrons, external circuit of connecting two different electrodes will break equilibrium and lead to flow of electrons. The cathodes material for SOFC is mostly based on perovskite-structured oxides (ABO_3), and prevailing cathodes for commercial use are $La_{1-x}Sr_xMnO_{3-d}$ (LSM) or $La_{1-x}Sr_xCo_yFe_{1-y}O_{3-d}$ (LSCF). The anode is usually composed as ceramic-metal composite (cermet) and the state-of-the-art anode is based on Ni-YSZ.

The aforementioned reactions; either reduction or oxidation, are known to preferentially happen in triple phase boundary (TPB). Triple phase boundary refers to a region where three different phases are in contact, where the three phases are electrolyte (ionic conductor), electrode (electronic conductor) and gaseous fuels. The electrochemical reactions that produce electricity occur in the presence of these three phases, thus TPB can be thought as reaction-hotspot/active area of the cell. Therefore, increasing TPB area can lead to a total cell performance increase. To extend TPB area,

one effective strategy is to using composite electrodes that has ionic conductor well dispersed with electronic conductor (such as $Sr_{0.5}Sm_{0.5}CoO_{3-d}$-GDC composite cathode or Ni-YSZ anode). More recently, technique of infiltration or exsolution is employed to establish nano-structured electrode with denser TPB area and it successfully led to substantial increase in performance of SOFC[5,6].

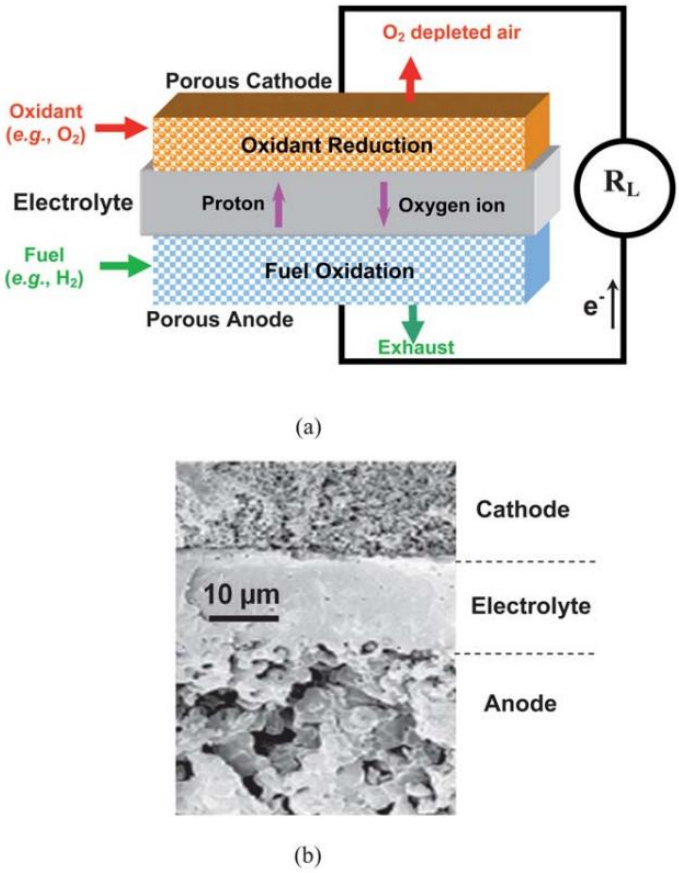

Figure 3. (a) A schematic for an SOFC single cell and (b) a cross-sectional view (SEM micrograph) of a single cell with a thin (~12 μm) electrolyte. (Reprinted with permission from *Energy Environ. Sci.*, 2011, **4**, 4380-4409. © Royal Society of Chemistry)

The electrolytes should be a gas impermeable layer to separate direct fuel-oxygen contact, and gas partial pressure difference between cathode and anode will generate a Nernst potential. If we assume that fuel is pure H_2 as we mention above, Nernst equation would look like:

$$\mathbf{E} = \boldsymbol{E^o} + \frac{\boldsymbol{RT}}{\boldsymbol{2F}} \boldsymbol{ln} \frac{\boldsymbol{P_{H2}} \boldsymbol{P_{O2}^{\frac{1}{2}}}}{\boldsymbol{P_{H2O}}}$$

Where E refers to equilibrium cell potential, E^o refers to standard cell potential, R is the universal gas constant, T means temperature in kelvin, F refers to Faraday constant and P for partial pressure of each gas. At zero current flow, E is referred as open circuit voltage (OCV). Theoretical OCV value of YSZ electrolytes is ~1.1V at 850^{o}C[7]. However, experimental OCV obtained in real case is smaller than equilibrium potential E[8], and this is responsible from irreversible potential loss:

$$\mathbf{V = E - (\eta_{ohmic} + \eta_{electrode} + \eta_{nernst\ loss})}$$

Where η_{ohmic} refers to a loss from ohmic resistance which mainly stems from electrolyte and $\eta_{electrode}$ refers to polarization loss from cathode and anode. $\eta_{electrode}$ can be further divided in activation polarization and concentration polarization. $\eta_{nernst\ loss}$ does not originate from electrochemical character of cell, and it rather comes from structure of stack, flow rate of fuels and fuel utilization rate. Generally, major loss comes from ohmic loss and polarization loss. SOFC operates at very high temperature, and the reason mainly springs from character of solid oxides which shows sufficient electric conductivities when it is at high temperatures. As temperature increases, overall

electrochemical reaction rates can be accelerated and ohmic & polarization resistance from each component reduces in order of magnitude (Figure 4(A))[9]. Therefore, fuel cell efficiency generally increases in higher temperature. However, high temperature operation readily leads to micro-structure coarsening, and makes issues about chemical compatibilities which eventually menace overall long-term stability of the fuel cell. Also, the choice of sealant and interconnect material are limited at elevated temperatures therefore it leads to overall operation cost raise. Thus, effort to cooling down the operation temperature of SOFC while maintaining exceptional performance is ongoing[10,11]. Typical current-voltage curve of SOFC can be found in Figure 4(B). Due to high temperature, SOFC has fast kinetics therefore has no activation loss in low current density region. However, concentration polarization represented in above equation takes place in high current density therefore power density curve shows increasing trend and make a peak power density, then return to decreasing trend as current density gets higher[12].

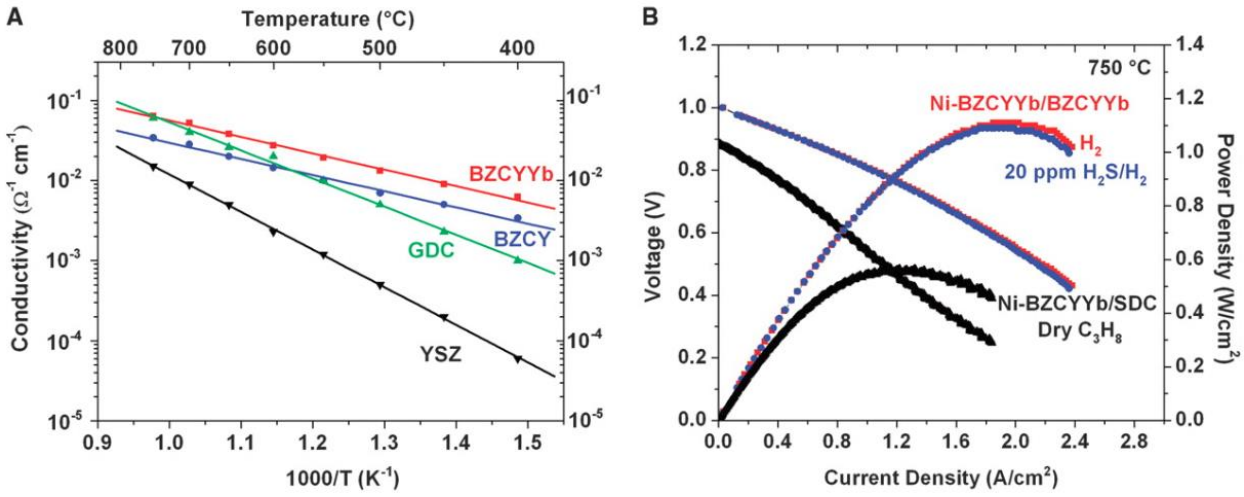

Figure 4. (A) ionic conductivities of BZCYYb, BZCY, GDC, and YSZ as measured at 400° to 750℃ in wet oxygen (with ~3 vol % H_2O). (B) Typical current-voltage characteristics and the corresponding power densities measured at 750℃ for a cell with a configuration of Ni-BZCYYb | BZCYYb | BZCY-LSCF when ambient air was used as oxidant and hydrogen as fuel (with or without 20 ppm H_2S contamination), and for another cell with a configuration of Ni-BZCYYb | SDC | LSCF when dry propane was used as fuel. (Reprinted with permission from *Science* 02 Oct 2009 Vol. 326, Issue 5949, pp. 126-129. © American Association for the Advancement of Science)

Author's note : To assess better knowledge about solid oxide materials, I highly recommend to take MSE 6010 "Functional Materials" course taught by Prof. Meilin Liu. For the electrochemistry, I strongly recommend to take CHBE 6130 "Electrochemical Engineering" course taught by prof. Tom Fuller.

2.1.1 Contaminants for SOFCs

As mentioned earlier in chapter 1, there are many volatile species that can potentially threat long-term stability of the SOFC life-time. Upon exposure to these contaminants, electrode usually demonstrates an increasing behaviour of polarization resistance. To remind, cathode can suffer from contaminants including Chromium (Cr), Boron (b) from cell/stack components, and SO_x, CO_2, H_2O in ambient air stream. Among these, one prominent cathode degradation process is Cr-poisoning when a typical Cr-containing alloy is used as interconnect. To have high power output, it is necessary to stack cells on one another[11]. To achieve fuel cell stacks, interconnect is added between individual cells to separate air/fuel streams. Therefore the material requirements for the interconnects are : high electronic conductivity; chemical and thermal stability in desired temperature, thermal expansion comparability, and impervious to gas flow. One widely used interconnect material is Crofer22APU, an iron-chromium alloy which satisfies high-temperature stability, good electrical conductivity and low thermal expansion mismatch. However, in an oxidizing atmosphere at high temperature, volatile Cr species such as CrO_3, and $Cr(OH)_2O_2$ are generated over the Cr oxide scale intrinsic to these alloys[13]. However, it is still unclear how these volatile species interact on electrode surface to degrade cathode performance. Therefore, techniques to monitor surface species responsible for degradation mode, and at the same time, tracking electrochemical polarization of electrode should be performed to formulate rigorous mechanism. If systematic study reveals comprehensive understanding, more effective strategy to mitigate poisoning can be designed.

Currently, deposition of protective layer on cathode is widely employed to mitigate Cr-poisoning. Use of multi-functional cathode contact material (CCM) can be

an option to alleviate Cr diffusion from Crofer22APU to cathode. CCM refers to a material that is used to paste the cathode with interconnect alloy. The reason of using CCM is cathode alone may not provide satisfactory bonding with interconnect alloy. By employing appropriate CCM, adequate bonding can be secured and role of both cathode and interconnect alloy can be fully promoted. Although it is unpublished work, I spent my time on developing CCM that has beneficial effect toward Cr-poisoning in my early Ph.D. year. By providing $(La_{0.6}Sr_{0.4})(Co_{0.5}Cu_{0.5})O_{3-d}$ layer as CCM between SSC-GDC composite cathode and interconnect alloy, we could have significantly lower Cr-deposition on cathode material (Figure 5, Figure 6)

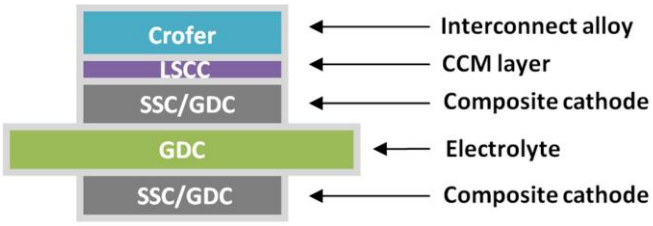

Figure 5. Cell configuration of SSC-GDC cell with LSCC CCM layer with interconnect alloy

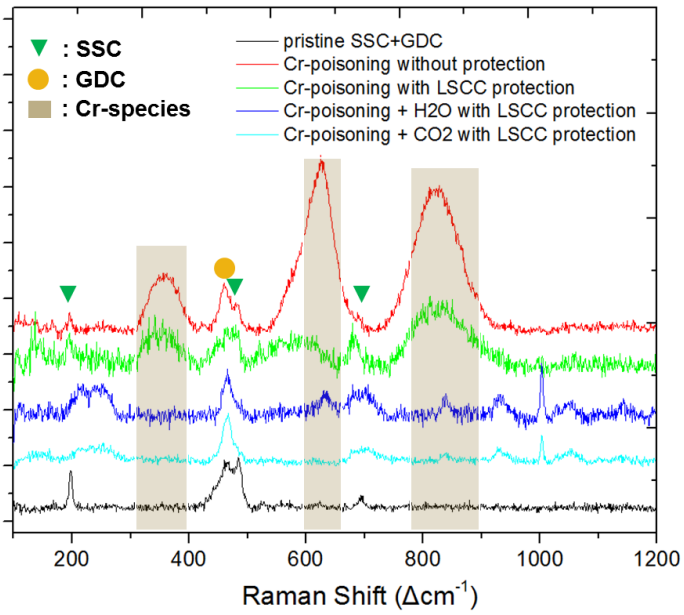

Figure 6. Ex situ Raman spectra to reveal Cr-deposition on cathode after long-term stability testing

Also, coating the electrode with nano-sized catalyst by solution infiltration also proven to have beneficial effect toward Cr-poisoning[14]. Chen et al., provided a hybrid catalyst coating of $PrNi_{0.5}Mn_{0.5}$ and PrO_x on LSCF electrodes, and it showed least Cr-species deposition rather than bare LSCF.

Likewise, sulfur poisoning is severe problem in the anode. In anode, Ni is the most widely used metal for its exceptional catalytic activity toward H_2 oxidation, high electronic conductivities, good agreement with YSZ electrolyte's thermal expansion coefficient and its low cost rather than expensive novel metal catalysts[1]. However, the critical problem of Ni-based anode is sulfur poisoning, which leads to increase in polarization increase even in ppb concentration of sulfur presence (Figure 7)[15,16]. To avoid issues with sulfur poisoning, SOFC system usually adds desulfurization unit

(Figure 8)[1]. However, installment of desulfurization unit results in more complex system with higher cost thus decreases overall system efficiency. Also, even with desulfurization unit, it is possible that ppb level of sulfur still remains in the fuel. Therefore development of sulfur-tolerant anode should be achieved to have simple and cost-effective fuel cell system.

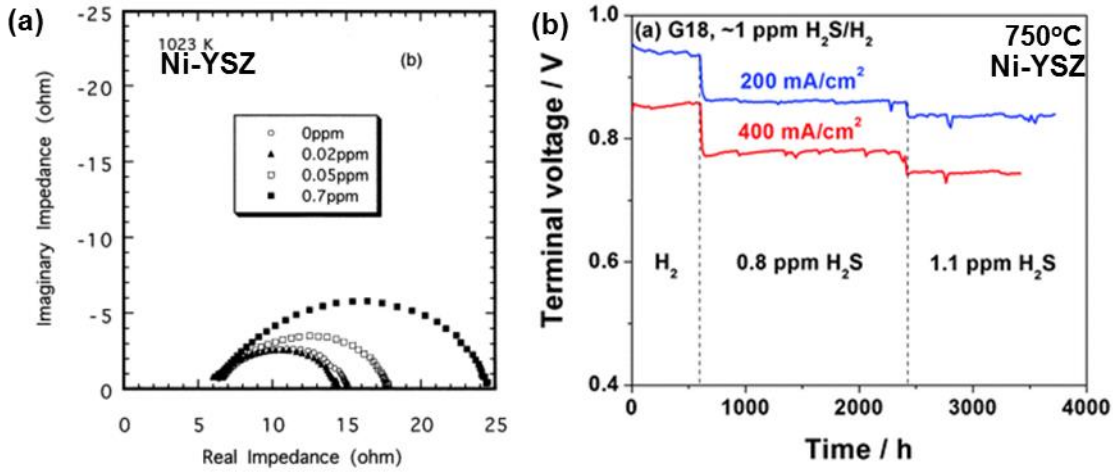

Figure 7. (a) Impedance spectra describing polarization increase of Ni-YSZ anode in ppb level sulfur exposure. (Reprinted with permission form *Solid State Ionics* volume 132, Issues 3-4, 2 July 2000, Pages 261-269. Copyright © 2000 Elsevier Science B.V. All rights reserved.) (b) Voltage tracking of Ni-YSZ electrode upon sulfur exposure under constant current density draw. (Reprinted with permission form *Energy Environ. Sci.*, 2010, **3**, 1804-1809 © Royal Society of Chemistry)

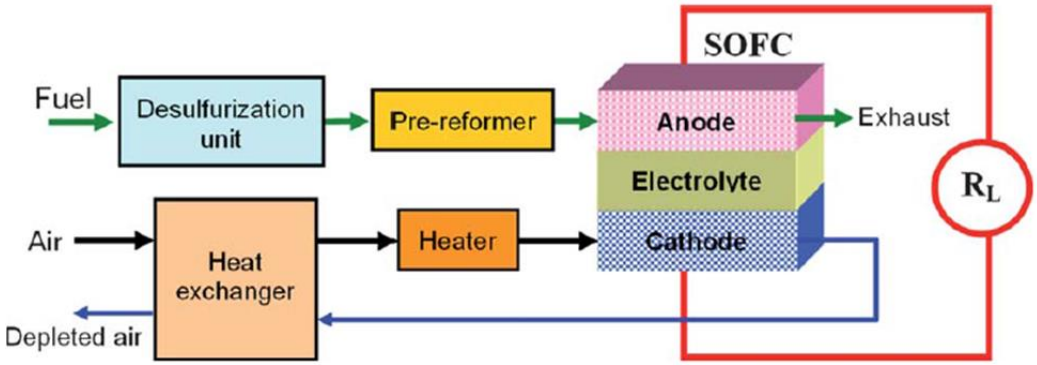

Figure 8. A simplified schematic for an SOFC system including desulfurization unit (Reprinted with permission from *Energy Environ. Sci.*, 2011, **4**, 4380-4409. © Royal Society of Chemistry)

Sulfur adsoprtion on nickel surface is widely accepted as the key step responsible for sulfur deactivation. However, challenges have been existed in identifying and quantifying the sulfur species deposition on Ni surface and detailed mechanism is still unveiled. Previously, by using *in situ* Raman spectroscopy, Cheng et al., identified bulk sulfide formation on the Ni-YSZ surface at ~440^{o}C in a fuel with pH_2S/pH_2 of 100ppm[17]. However, this study had too low temperature compared to actual SOFC operating condition, and according to thermodynamic calculation carried by K.Lee et al.,[18] formation of bulk sulfide is not preferable on operating condition as high as ~750^{o}C. Based on their Gibbs energy calculation, adsorption of atom sulfur would be most stable state in SOFC operating condition. However, Direct *in situ* identification of sulfur atom at elevated temperature with ppm-level H_2S has never been successful[17]. Furthermore, even there are a lot of materials claimed to have sulfur tolerance such as BZCYYb[9] however, few materials were investigated for their catalytic mechanism.

Therefore, I cannot emphasize enough for development of *operando* platform, which will enable tracking electrode surface in both electrochemically and molecularly. The effort to understand degradation mode of electrode will eventually lead to building a robust electrode system for practical application. One effective technique to follow electrode polarization is **electrochemical impedance spectroscopy (EIS)**. The basics about EIS are explained in later of this section 2.3. To monitor surface chemistry, one of the vibrational spectroscopy, **Raman scattering** can deliver immediate molecular information. Fundamentals about Raman scattering is also briefly introduced in next section 2.2.

2.2 Fundamentals of Raman Scattering

Raman spectroscopy relies on inelastic scattering. Scattering refers to a phenomenon that light deviates from its straight trajectory. Generally, Raman scattering uses one wavelength laser which is different from its counterpart, Infrared spectroscopy (IR). Raman effect was first discovered by Indian scientist, C. V. Raman, who won 1930 Nobel prize in physics for this discovery. Raman spectroscopy measures change in molecule polarizability. As described below (Figure 9), illuminating laser on sample can excite molecules which were originally in ground state. The excitation puts molecules into a virtual energy state, and after a short period of time, photon will be emitted. If the emitted photon shifts to different energy, wavelength will analogously change and it is called Raman scattering. If final energy state is higher than original state, it is called stokes shift, and if final state is lower, then it is called anti-stokes shift. Fraction of

Raman scattering is much smaller ($1/10^8$) to elastic scattered radiation, Rayleigh scattering (laser radiation). Therefore, notch filter is employed to remove Rayleigh scattering in Raman spectrometer.

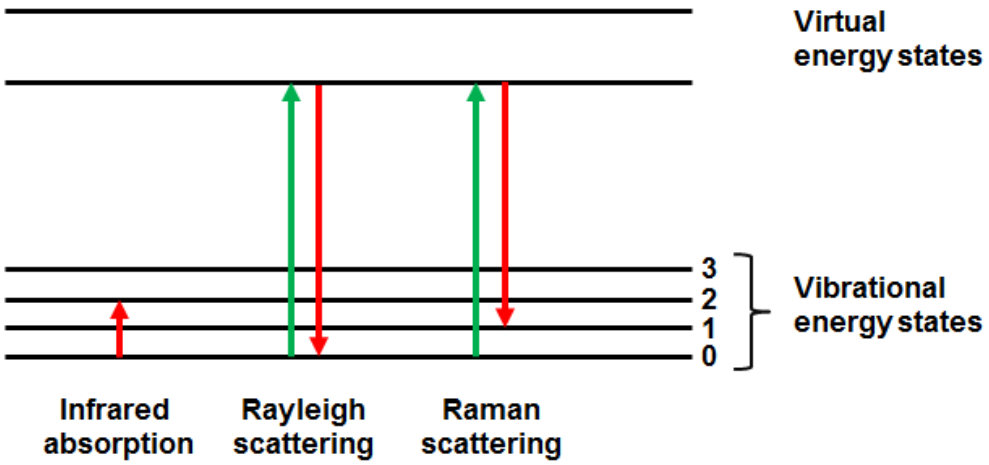

Figure 9. Energy-level diagram showing the states involved Raman spectra

2.2.1 Symmetry of molecules

Photon energy given from laser source will excite illuminated molecules, and how molecules vibrate is decided by its symmetry. Different vibrational mode has different energy states therefore identification of vibrational mode of a molecule is possible by an inelastic scattering process. Therefore, understanding of symmetry of molecule is important. Molecular symmetry operation refers to an action that moves chemical compound into a new orientation that is equivalent to its original one. The types of symmetry operations are; identity, rotation, inversion, improper rotation, mirror plane

Let's take an example with a carbonate ($-CO_3$) group. Carbonate has prominent peak in Raman spectroscopy (~1060cm^{-1}), and observation of $-CO_3$ is an important sign of cathode contamination with CO_2. It is known that Strontium (Sr) element doped in perovskite B site tend to escape from its original crystal and forms SrO on surface. Soon, SrO reacts with volatile species in air such as CO_2, and forms $–CO_3$ on surface. Formation of $SrCO_3$ can act as ORR blocking area and hampers electrocatalytic activity of electrode[19].

By considering which symmetry is allowed in a molecule, identification of point group can be obtained. To perform, using point group flow chart is an easiest way. To follow, Carbonate molecule is not linear, and has rotation axes centred in carbon atom. Rotation operation can be completed when $360^o/3 = 120^o$ is rotated (C_3). No rotations that is over C_n with n>2 is allowed rather than C_3. Carbonate then possess mirror plane perpendicular to rotation axes. Therefore, Carbonate belongs to D_{3h} point group.

By confirming point group, we can assess if molecule is Raman active and/or IR active by irreducible representation. Irreducible representation is IR active if it transforms as x, y, z, and Raman active if it transform as combination such as $x^{2,}$ y^2, z^2, xy, xz, yz.

Author's Note : To assess better knowledge about symmetry of molecules, I highly recommend to take CHEM 6172 "Physical Method – Inorganic Chemistry" course taught by Prof. John Zhang.

2.2.2 Fluorescence and choice of laser source

Sometimes, strong power of laser illuminating the sample can excite molecules to another electronic state and gives off fluorescence to come down in ground state. Unfortunately, fluorescence possesses strong intensity with broad hump which exhibits overall baseline rise up in Raman intensity, therefore Raman shift which we desired to recognize can be covered/hid by fluorescence. While the basic essence principal of fluorescence and Raman scattering is same, the major difference is that fluorescence is anchored to one specific frequency, whereas Raman shift shows constant separation from excitation frequency as shown in next equation.

$$\Delta w(\mathrm{cm}^{-1}) = \left(\frac{1}{\lambda_0(\mathrm{nm})} - \frac{1}{\lambda_1(\mathrm{nm})}\right) \times \frac{(10^7\mathrm{nm})}{(\mathrm{cm})}.$$

Therefore, we can get around with fluorescence by using different wavelength laser (Figure 10). In Dr. Liu's group, two laser sources are installed; 633 nm (Red laser), 532 nm (Green laser). Choice of laser wavelength should be considered carefully by right purposes, since laser power output is different. Energy of lase source can be described as followed

$$E = \frac{hc}{\lambda}.$$

Where, *h* refers to Planck constant, λ for laser wavelength and c for speed of light. Usually, red laser is more suitable for organic materials, since its power is not destructive. However, red laser can sometimes encounter problem with fluorescence and its low

power lead to poor Raman signal. On the other hand, green laser is more suitable for inorganic analysis. Green laser demonstrates much higher Raman intensity rather than red laser. However, its high laser power output can potentially burn-out organics, and illuminated nanoparticles possibly oxidized under Green laser.

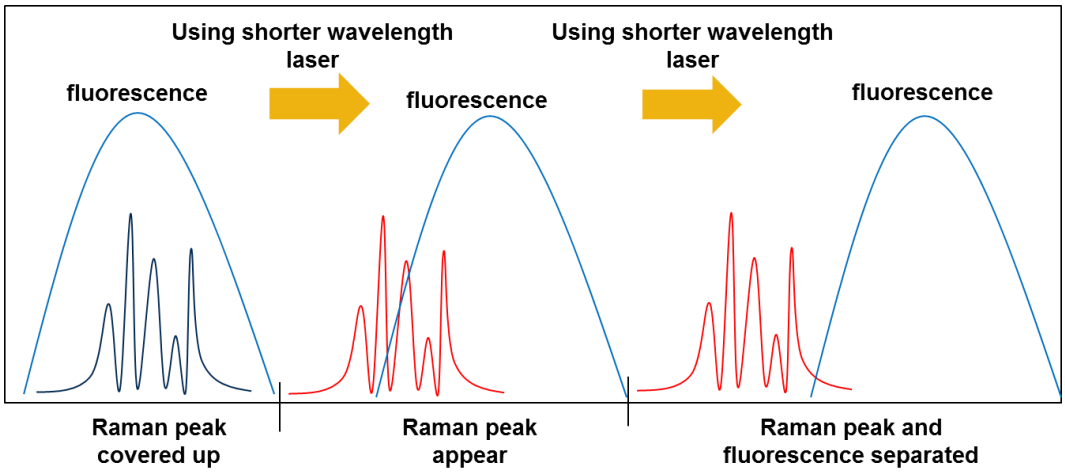

Figure 10. A tactic to evade fluorescence effect.

2.2.3 Geometry of Raman Spectrometer

After the choice of right laser source, the laser will then enter the Raman spectrometer system. Change of Raman beam between two wavelengths is specifically described in Ben deGlee's dissertation, and manual should be provided around Raman spectrometer as well.

First, beam entering the Raman box will first go through beam expander. Then these laser beam hits several mirrors to get in microscope linked to the Raman box (Figure 11). Laser can be converged with the lens on microscope and confocality can be controlled by setting the height of sample stage (Figure 12). The resolution of Raman laser is 2μm, however, a slight defocus can be beneficial to have larger scanning area (~5 μm).

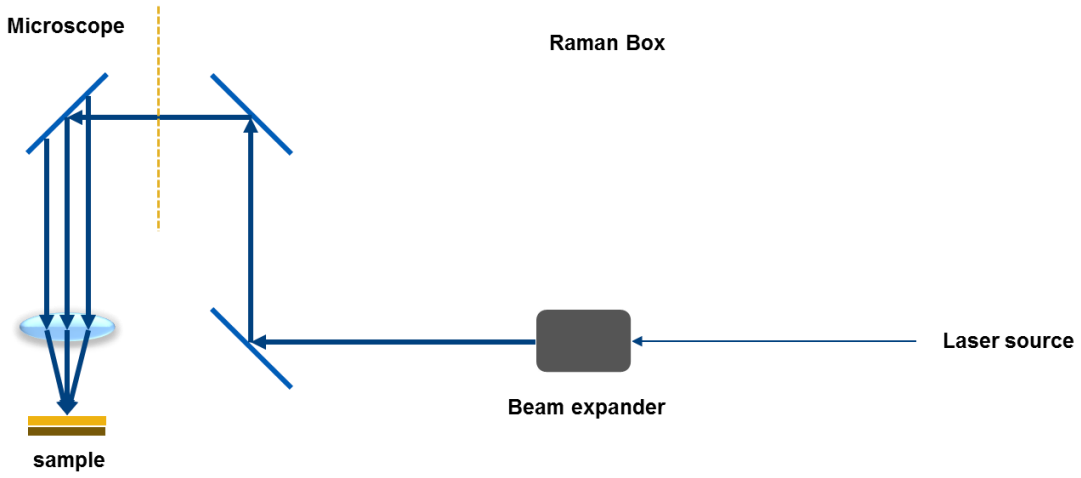

Figure 11. Geometry of Raman spectrometer. Laser entered to illuminate sample surface.

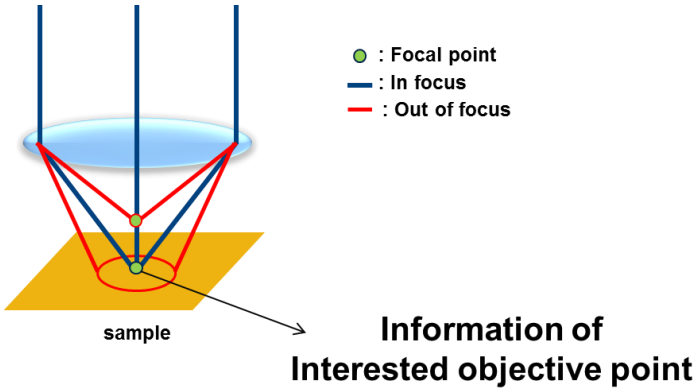

Figure 12. Confocality

After laser hits the interested objective point, scattered light will be reflected through mirror and then goes back into Raman box for further processing (Figure 13). Since ratio of Raman scattered light is much smaller than Rayleigh scattered light, notch filter is provided to cut Rayleigh scattering and only deliver Raman scattered light to the slit. By adjusting the slit distance, amount of beam passing can be controlled (Figure 14). If slit distance is wide, we will have overall high Raman intensity however its signal to noise ratio can be low. If slit width is narrow, low intensity but high signal to noise ratio can be achieved. There is a trade-off between two, thus slit width should be well controlled to have quality data. After Raman beam go through slit, and gets to grating system which will disperse beam line into a spectrum. Finally, these information will hit CCD camera and after computation, Raman signal will be finally presented in Computer program, Wire 2.0.

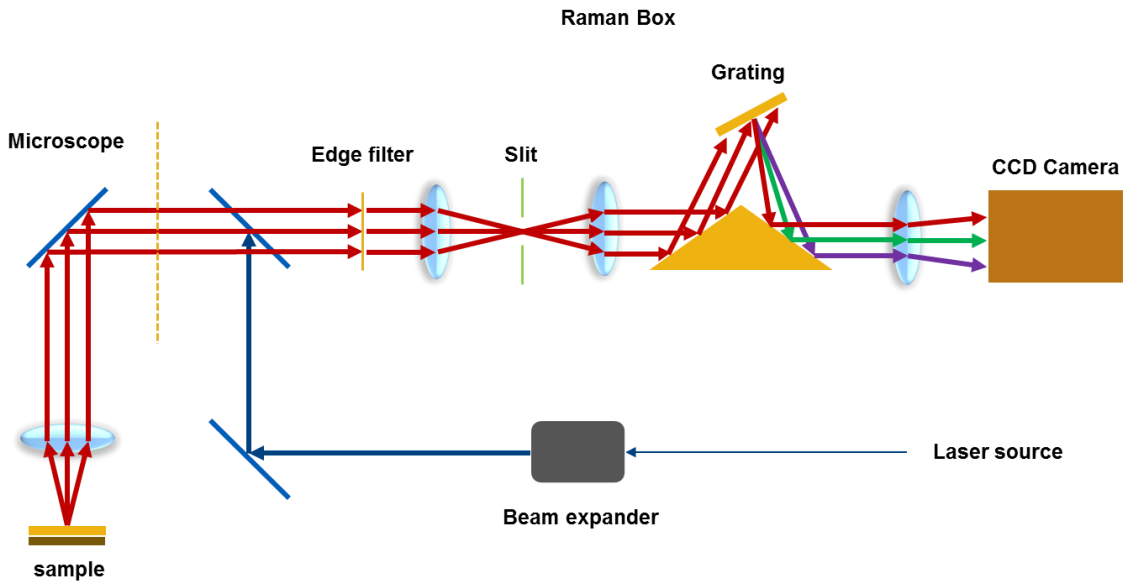

Figure 13. Geometry of Raman, Explaining further processing after beam hits the sample.

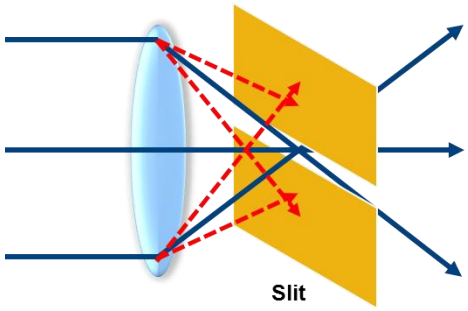

Figure 14. Role of slit to separate well-scattered light.

2.2.4 Surface Enhanced Raman Scattering (SERS)

While Raman spectroscopic analysis is a great candidate technique to scan surface science, there are several challenges to address before application in SOFC electrode

studies. First, as mentioned in earlier section, the probability of Raman scattering is much lower compared to elastic scattering (Rayleigh) and/or IR absorption. Although many adsorbed species are known to have Raman active vibrational modes, the reaction intermediates on surface of SOFC electrode are present in trace amount and therefore has limited sensitivity with normal Raman spectroscopy. Second, many perovskite materials used as SOFC electrodes such as LSM or LSCF shows centrosymmetric symmetry, and therefore their intrinsic Raman polarizability is very low and limits the application of Raman spectroscopic study. Third, high temperature *in situ/ operando* Raman spectroscopy poses a particular challenge of low signal-to-noise ratios attribute to variation of all Raman modes increases at elevated temperature. Therefore, Raman bands are broadened and weakened in high temperature.

For aforementioned reasons, amplification of Raman signal is very essential by all means. One of the successful approaches was using Surface Enhanced Raman Scattering (SERS). By using small nanoparticles of Ag, yield of Raman scattering around the nanoparticles can be greatly enhanced. The basic principal of SERS is based on Localized Surface Plasmon (LSP) effect, which refers to electron cloud oscillation of metal particles by excitation laser. These LSP will greatly affect nearby analyte molecules thus the polarizability of molecule is multiplied.

Although SERS technique shows promising prospects to apply on SOFC electrode studies, applying Ag nanoparticles to an *in situ* study introduces two new complications. Firstly, silver itself is catalytically active, so silver nanoparticles would bias the performance measurements and confound the reaction mechanism study at the TPB. Secondly, silver nanoparticles are not stable at elevated temperatures and, due to

Ostwald ripening, tend to coarsen into larger particles that have weaker LSP effects, which results in very small, or even no, enhancement of the Raman scattering. Therefore, an inert shell is needed to restrain the catalytic activity of Ag and to prevent nanoparticle coarsening.

One of the main successful strategies to make *in situ* high temperature SERS possible is to use a thin silica shell on the Ag nanoparticle in core-shell geometry. Recently, the van Duyne group found that nanoscale Ag particles with a thin layer of Al_2O_3 retained their shape and LSP after annealing at high temperatures[20,21]. Also, the "shell-isolated nanoparticle enhanced Raman spectroscopy" (SHINERS) technique was developed by Tian et al[22]. By utilizing Ag and Au nanoparticles with Al_2O_3 or SiO_2 coating a few nanometers thick, the Raman signals of the underlying materials were enhanced without interfering with the original surface properties.

Xiaxi Li, one of the senior members in prof. Liu group successfully applied SERS techniques to SOFC electrode studies[23]. In his dissertation, detailed information about fabrication of thermally robust $Ag@SiO_2$ shell is well explained. The application of SERS into SOFC electrodes are also well described in his recent review paper, "In situ and Surface-Enhanced Raman Spectroscopy study of electrode materials in Solid Oxide Fuel Cells"[24]. In this study, I followed Xiaxi's previous work to fabricate $Ag@SiO_2$ NPs and applied these particles to my later Raman spectroscopy analysis.

To provide enhanced Raman sensitivity at elevated temperatures, Ag nanoparticles with a SiO_2 shell (abbr. $Ag@SiO_2$) were fabricated. To form the Ag seeds, 0.25g of $AgNO_3$ is reduced with 3 mL of anhydrous ethylene glycol (EG, 99.8%) and

polyvinyl pyrrolidone (PVP, M_w = ~55,000 g mol^{-1}) was mixed to promote homogeneous size distribution of nanoparticles. The resulting solution was kept at 120 ℃ for 1 h under vigorous stirring. Afterward, 20 mL of ethanol was added to form homogeneous Ag colloidal suspension. The resulting particle size was 86 nm with standard deviation of 12 nm. The average sizes of the Ag cores and their standard deviations were obtained from the SEM images in Figure 15.

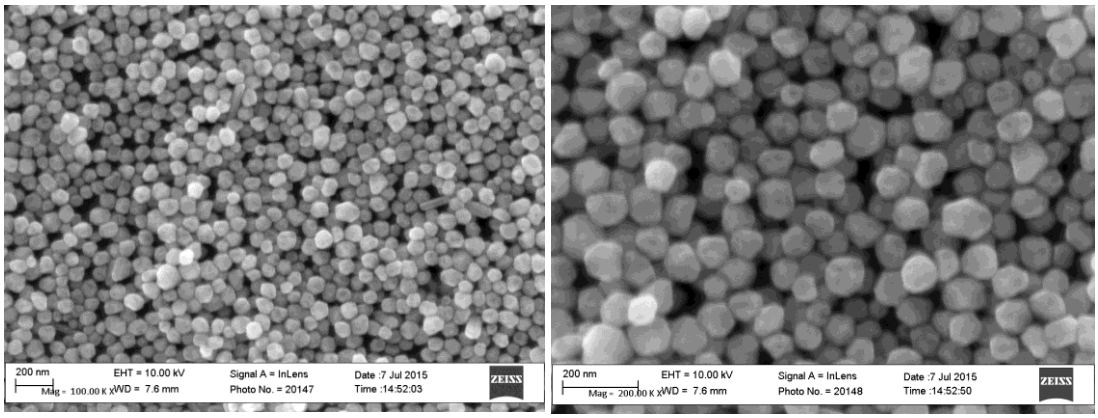

Figure 15. High resolution SEM images of the Ag nanoparticle cores.

Prior to the application of SiO_2 coating, 1 mL of concentrated NH_4OH was added into the Ag suspension to create a suitable basicity for SiO_2 growth. The thicknesses of the SiO_2 coating were controlled by the volume of tetraethyl orthosilicate (TEOS) solution added to the solution of Ag nanocrystals after the seeding process. Shown in the Table 1 are the processing parameters to develop the various thickness of SiO_2 coating on Ag nanocrystals after letting the set for 1 hour. Ag@SiO_2 core@shell nanoparticles were extracted from the colloidal solution by repeated centrifugation at 6000 rpm with ethanol and D.I. water. After each centrifuge step, the supernatant liquid was decanted to remove

excess organic precursors. SEM images shown in Figure 16 shows samples of each processing parameter.

Table 1. Processing parameters for $Ag@SiO_2$.

Sample name	TEOS/Ag Solution	Thickness (± St. Dev.)
No TEOS Ag	No / 3 mL	No shell
x1 $Ag@SiO_2$	0.05 mL/ 3 mL	20 ± 5.3 nm
x2 $Ag@SiO_2$	0.1 mL / 3 mL	22 ± 3.6 nm
x3 $Ag@SiO_2$	0.2 mL / 3 mL	35 ± 6.6 nm
x4 $Ag@SiO_2$	0.5 mL / 3 mL	47 ± 5.5 nm

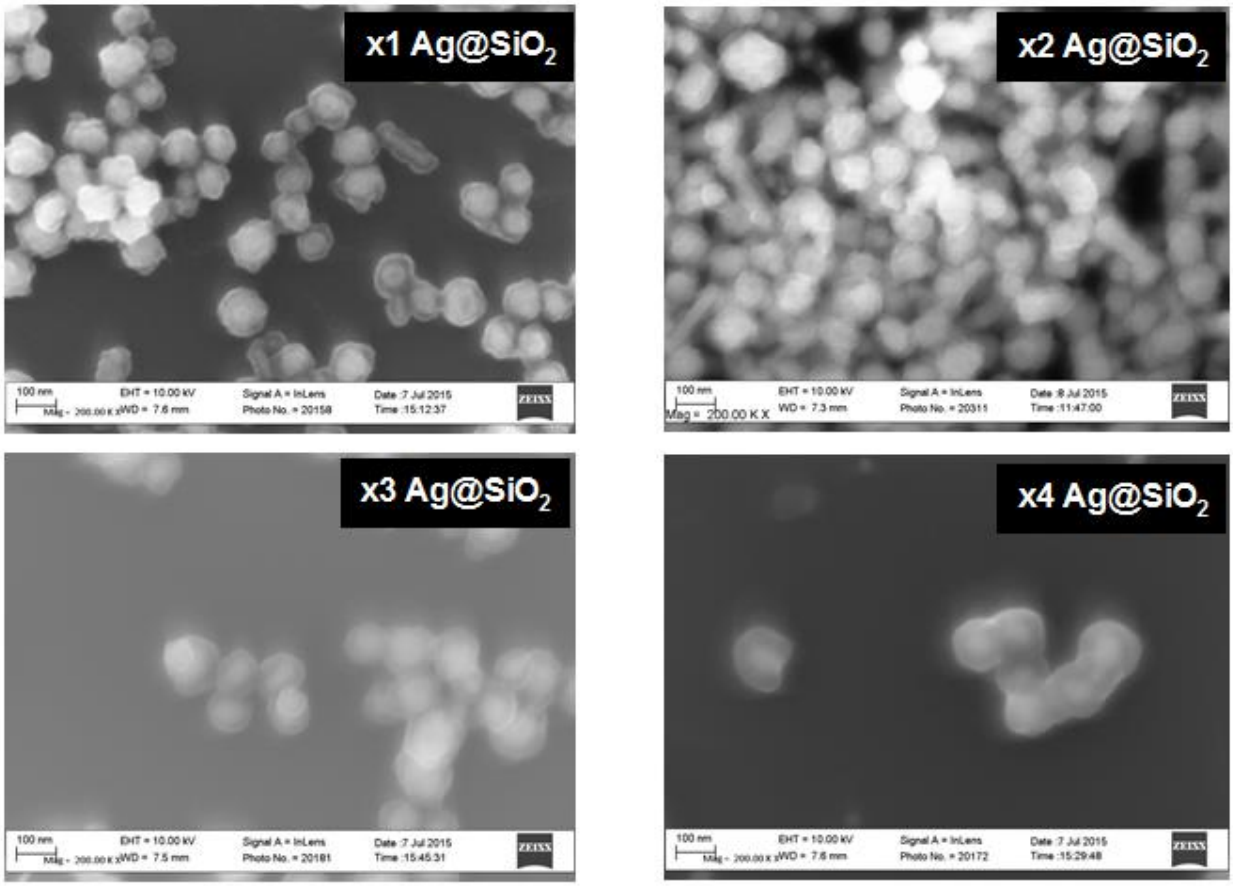

Figure 16. High resolution SEM images of $Ag@SiO_2$. By varying the volume of TEOS added, the shell thickness could be controlled.

Thickness of the shell is important to prevent particle sintering at elevated temperatures during *in situ* SERS. While an adequate thickness is necessary, an excessive thickness eventually blocks the LSP resonance field that enhances the Raman signal of the probed substrate. The relation of the Raman intensity with the nanoparticle properties is known by the following equation:[25]

$$I = \left(1 + \frac{r}{a}\right)^{-10}$$

where, I represents the intensity of the Raman mode after the enhancement by $Ag@SiO_2$ nanoparticles, r represents the thickness of the shell, while a denotes the size of the silver nanoparticles.

To ensure effectiveness of SERS Nanoparticles, I analyzed Rhodamine with SERS. Rhodamine is a dye molecule with very high fluorescence (Figure 17). Therefore with normal Raman analysis, no significant peak can be revealed (Figure 18). However, after applying SERS nanoprobes, Raman intensity can be enhanced in order of magnitude and peak of Rhodamine can be revealed (Figure 19). Application of SERS was done by mixing NPs with Rhodamine solution. As predicted, bare silver nanoparticles had most significant enhancement since its SERS enhancement is not disturbed by SiO_2 Shell.

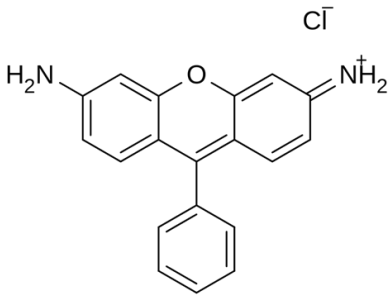

Figure 17. Picture description of fluorescent Rhodamine and its molecular structure.

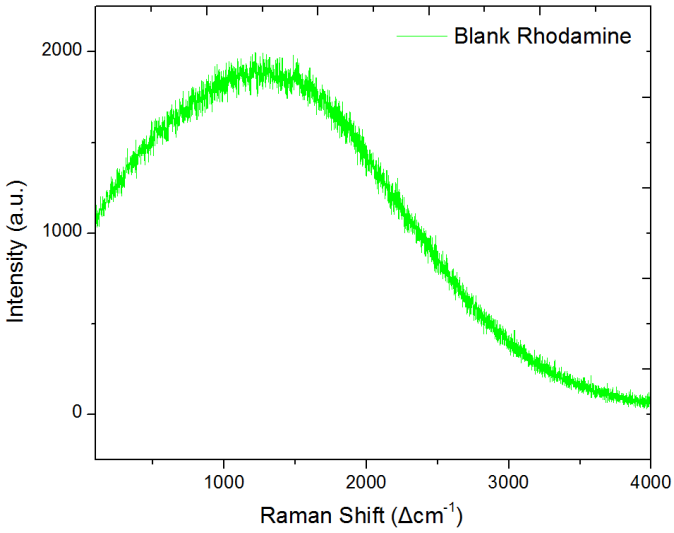

Figure 18. Blank Rhodamine analysis with normal Raman without SERS

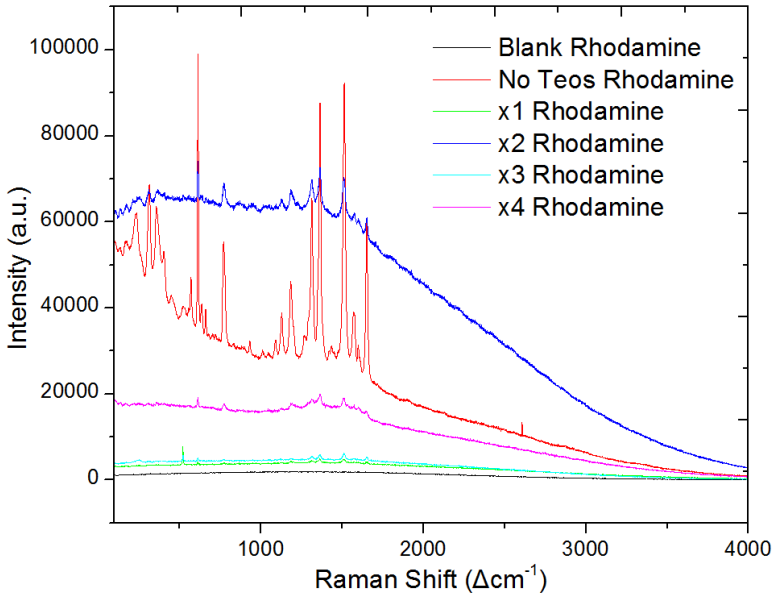

Figure 19. SERS analysis with Rhodamine

2.3 Electrochemical Impedance Spectroscopy (EIS)

As mentioned above, correlating surface science with electrochemical performance of the cell can be extremely important, and Electrochemical Impedance Spectroscopy (EIS) is one of the best options available to measure surface polarization of electrodes. Concept of impedance spectroscopy is based on elementary concept of electrical resistance known as Ohm's law.

$$R = \frac{V}{I}$$

Where R refers to resistance, V is voltage, and I denotes current. Usually, impedance (Z) is measured by applying AC potential to cell. Addition of an externally defined potential can affect dynamics of chemical reactions happening on electrode surfaces and response of the system as a function of the perturbation can reveal internal dynamics. The perturbation made in AC voltage can be represented as follow:

$V(t) = V_o \sin(\omega t) = V_o e^{i\omega t}$ (By euler's rule $e^{i\varphi} = cos\varphi + isin\varphi$)

Then current response to voltage perturbation can be represented as followed:

$I(t) = I_o \sin(\omega t - \varphi) = I_o e^{i(\omega t - \varphi)}$

Therefore, the resulting impedance (Z) will look like:

$$Z = \frac{V(t)}{I(t)} = \frac{V_o}{I_o} e^{i\varphi} = \frac{V_o}{I_o} (cos\varphi + isin\varphi)$$

Data presentation of impedance can be described with circuits. If we think a simple representative model for a solid oxide fuel cell electrode, it will have electrolyte resistance (R_Ω, ohmic resistance), polarization and charge transfer resistance from electrode (R_p), interface capacitance (C_d)[26] (Figure 20).

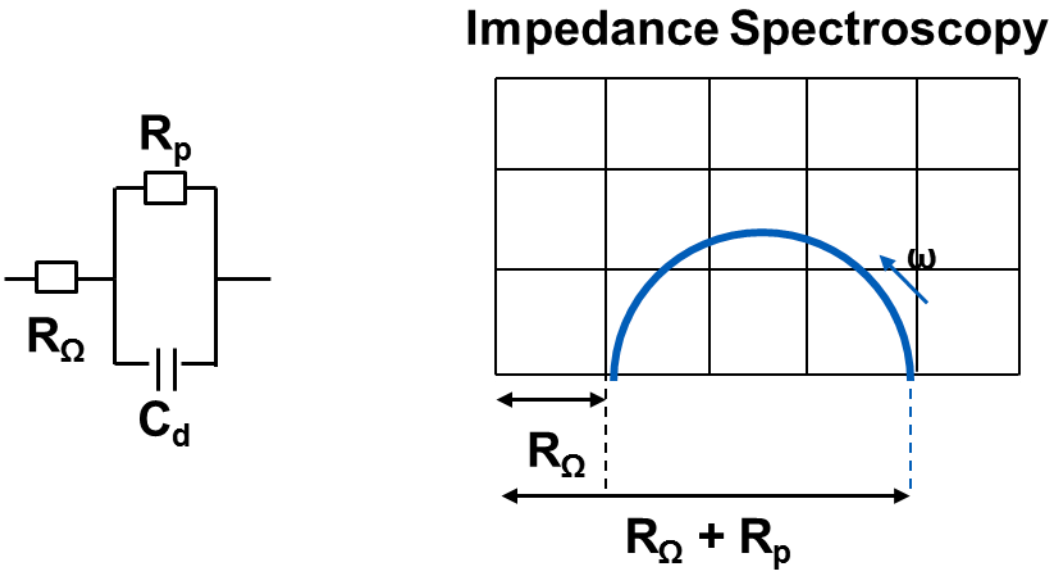

Figure 20. Typical electric circuit happening on electrochemical system, and resulting Nyquist Plot

The impedance for above circuit would be:

$$Z = R_\Omega + \frac{1}{\frac{1}{R_p} + i\omega C_d}$$

To interpret the Nyquist plot, the first x- intercept with high frequency will be ohmic resistance of the cell, and lower frequency x-intercept will be sum of polarization resistance of electrode and ohmic resistance. Note that as frequency, $\omega \rightarrow \infty$, impedance

becomes R_Ω, and as $\omega \rightarrow 0$, Z becomes $R_\Omega + R_p$. Therefore, by measuring the size of arc, we can have polarization resistance of electrode surfaces at desired kinetic conditions.

2.4 Technical approach - *operando* Raman spectroscopy platform coupled with EIS

To perform *operando* Raman spectroscopy study, the cell with interested electrode was faced upside to illuminate Raman laser and connected as working electrode. Raman scattering of working electrode was done simultaneously with impedance spectroscopy measurement (Figure 22, Figure 23). The other side electrode is connected as counter electrode. Usually, counter electrode was composed of porous Ag electrode. These electrodes are then connected with silver wire to EIS frequency analyzer. With the heating element inside of the chamber, the temperature of the platform can be elevated, while cooling water makes temperature stable. Also by flowing inlet gas with mass flow controller, the chamber can have controlled atmosphere. By using this platform, I tried to track the key spectroscopic evolution features of electrode of SOFC, focusing on new band, band shift, profile change and intensity change (Figure 24). These spectroscopic changes are later correlated with size of impedance arc, polarization resistance of the electrode. The major space groups and Raman modes of common SOFC electrode materials and adsorption species is well presented by Xiaxi et al., [24](Table 2).

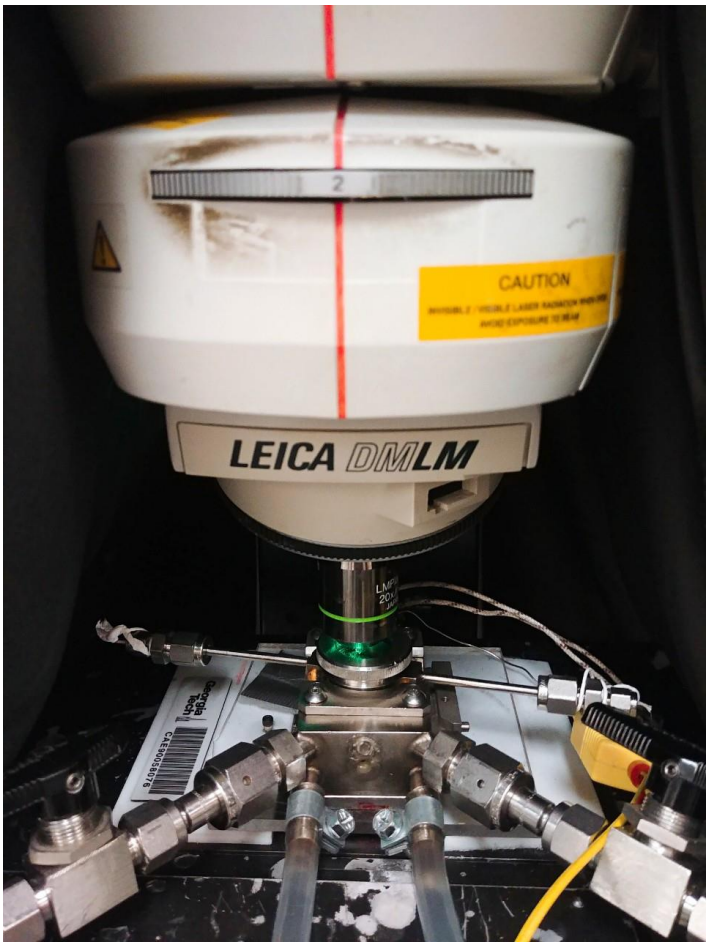

Figure 21. Harrick Chamber for *operando* Raman spectroscopy with electrical connection

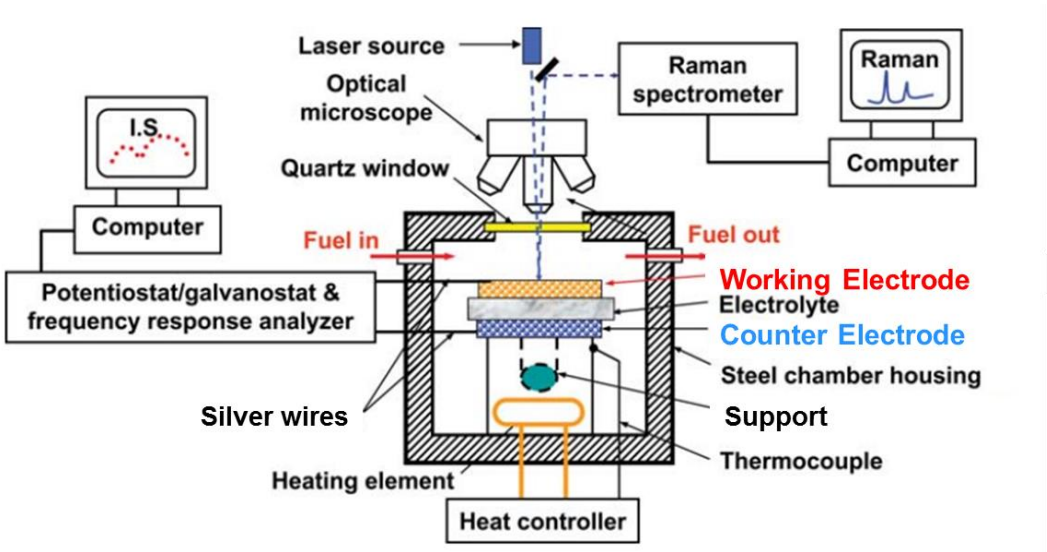

Figure 22. Schematic for the *operando* Raman spectroscopy system that is coupled with electrochemical measurement equipment (Reprinted with permission from *Energy Environ. Sci.*, 2011, **4**, 4380-4409. © Royal Society of Chemistry)

Figure 23. Raman spectrometer (Left) and EIS cart (Right)

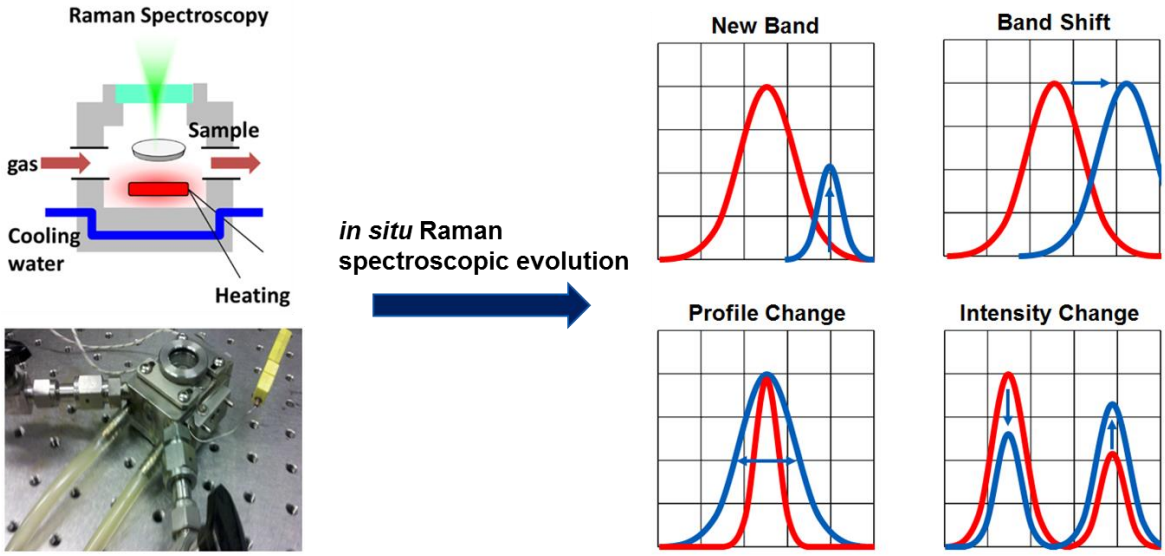

Figure 24. Raman spectroscopic evolution description of new band, band shift, profile change and intensity change.

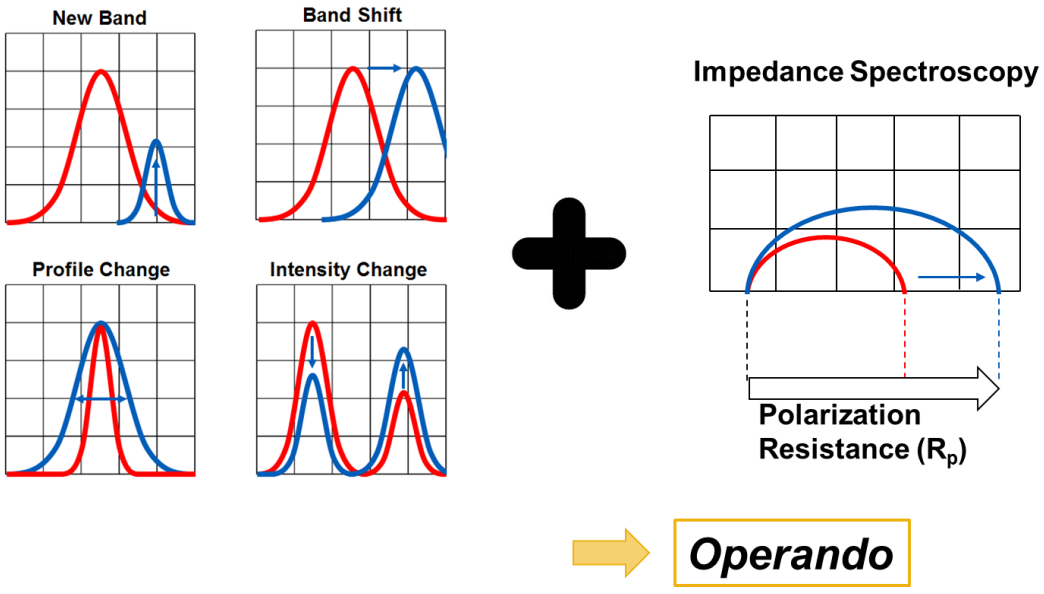

Figure 25. Direct correlation between simultaneous vibrational and electrochemical measurements which opens up an o*perando* study.

Table 2. Space groups and Raman modes of common SOFC electrode materials and adsorption species[24].

Phase/species	Group	Raman modes	Main peak(s)[a]
YSZ	O_h^6	F_{2g}	620
SDC	O_h^6	F_{2g}	460
LSM (La/Sr: 0.85/0.15)	D_{2h}^{16}	$7A_g+5B_{1g}+7B_{2g}+5B_{3g}$	535
LSM (La/Sr: 0.8/0.2)	D_{3d}^6	A_g+4E_g	697. 520
LSCF	D_{3d}^6	A_g+4E_g	646. 525
BZCYYb	D_{2h}^{16}	$7Ag+5B_{1g}+B_{2g}+5B_{3g}$	335
BZY	O_h^2	None	720[b]
BZYb	O_h^2	None	725[b]
C (Graphite)	D_{6h}^5	E_{2g}	1585
H_2O	C_2	$2A^1+B^2$	3716.3368. 1594
O_2	D_2	A_g	1598
SO_4^{2-}	T_d	A_1+E+2F_{2g}	980
CO_3^{2-}	D_{3h}	$A_{1g}+2E$	1059
C_3Hs	C_{2v}	xA_1+yB_2	1528
C_2H_4	D_{2h}	$3A_g+B_{1g}+2B_{3g}$	1425
COH	C_s	$2A_1+A_{2g}$	2483[c]
BaO_2	D_{4h}^{17}	$A_{1g}+Eg$	240. 800[c]

CHAPTER 3. DIRECT RAMAN OBSERVATION OF SULFUR SPECIES AND ITS IMPACT ON STEAM REFORMING CATALYTIC ACTIVITY OF NI-YSZ

3.1 Introduction

Solid oxide fuel cells (SOFCs) have drawn wide attraction because of their excellent efficiency, remarkable fuel flexibility, and the use of non-precious materials[27]. However, a long-term stack degradation is one of key obstacles for the commercialization of SOFCs. In particular, the deactivation at SOFC anodes significantly leads to the stack degradation by the direct use of natural gas as a fuel.[4,28-30] Natural gas (NG) is composed primarily of methane with small fractions of ethane, propane, C4+ gaseous hydrocarbons, carbon dioxide and nitrogen. NG contains several parts per million (ppm) level of total sulfur from naturally occurring sulfur-containing compounds or hydrogen sulfide (H_2S) odorants. SOFC degradations arise primarily from anode coarsening, coking and sulfur poisoning by using natural gas as fuel.[1] Similar to the steam reforming of methane (SMR) process producing synthesis gas, NG-fueled SOFCs also add H_2O at the anode to avoid coke formation.[4,31] To date, a range of operating strategies and anode materials have been proposed for NG-fueled SOFCs.[4,32-34] The most widely used SOFC anode is a nickel-yttria-stabilized zirconia (Ni-YSZ) cermet,[35] and its nickel metals are susceptible to coking[31,36,37] and sulfur poisoning.[38-41] While these degradation issues have been extensively studied, little information is available in the literature for the combined effect of coking and sulfur poisoning in SOFCs[42] because of the high complexity of the electrocatalytic systems. Moreover, numerous studies indicate sulfur poisoning has a

profound impact on the reforming activity of nickel-based catalysts.[31,39,43-46] Therefore, a systematic understanding of sulfur poisoning and coking at Ni-based anodes is imperative to rationally design novel SOFC anode materials exhibiting superior resistance to sulfur poisoning and coking under SOFC conditions. In addition, it may affect the determination of cost-effective fuel treatment approaches and the estimation of fuel cell's lifetime.

From a mechanistic point of view, sulfur adsoprtion on nickel surfaces is widely accepted as the key step responsible for sulfur deactivation.[1,47] However, it has been a grand challenge to identify and quantify sulfur species deposited on nickel surfaces, including the eludiation of its detailed mechanism. For example, sulfur-poisoning mechanisms may have been misinterpreted by using *ex situ* experimental results, proposing the formation of bulk nickel sulfide (Ni_3S_2) under SOFC conditions.[1,48,49] It was reported that the formation of bulk sulfides may not be formed at > 500 ^oC with 100 ppm H_2S in H_2, according to *ab initio* thermodynamic calculations.[50] Their sophisticated Gibbs energy calculations propose that the adsorption of atomic sulfur species (S*) on a Ni surface (*i.e.*, $H_2S \rightarrow H_2 + S^*$) is the final step rather than a bulk nickel sulfide formation (*i.e.*, $3Ni + 2H_2S \rightarrow Ni_3S_2 + 2H_2$) under a SOFC operating temperature at ~500 ^oC. Our previous study using *in situ* Raman spectroscopy excellently identified the bulk sulfide formation on Ni-YSZ at ~430^oC with 100 ppm H_2S in H_2, while no sulfide formation at > 500 ^oC was detected.[17] Although DFT calculations clearly validated the phase diagram,[50] to the best of our knowledge, a direct *in situ* temperature-depenent identification of sulfur species with ppm-level H_2S has not been reported[1,17] in the literature due to the difficulty of accurate detection of low-concentarion sulfur specise uisng conventional surface characterization approaches. In particular, *in situ* Raman spectroscopy has a sensitivity

problem owing to broadening of the vibration bands at high temperatures. To overcome this technical barrier of the *in situ* high-temperature Raman characterization approach, surface enhanced Raman spectroscopy (SERS)[23,51] can be effectively utilized. For example, by using core-shell-structured Ag@SiO_2 SERS nanoparticles, Raman signals can be significantly enhanced without interfering with the original surface properties.[19,24,52] In this study, to accurately identify surface sulfur-constaining species (*i.e.*, S_x and SH) formed at the Ni-YSZ anode, we applied *in situ* Raman spectrsocpy[51,52] along with a long-term electrochemical performance measurement under practical SOFC conditions., aiming at rationally design of SOFC operating conditions.

3.2 Electrochemical measurement of the mixtures of H_2S and CH_4 (S/C=2)

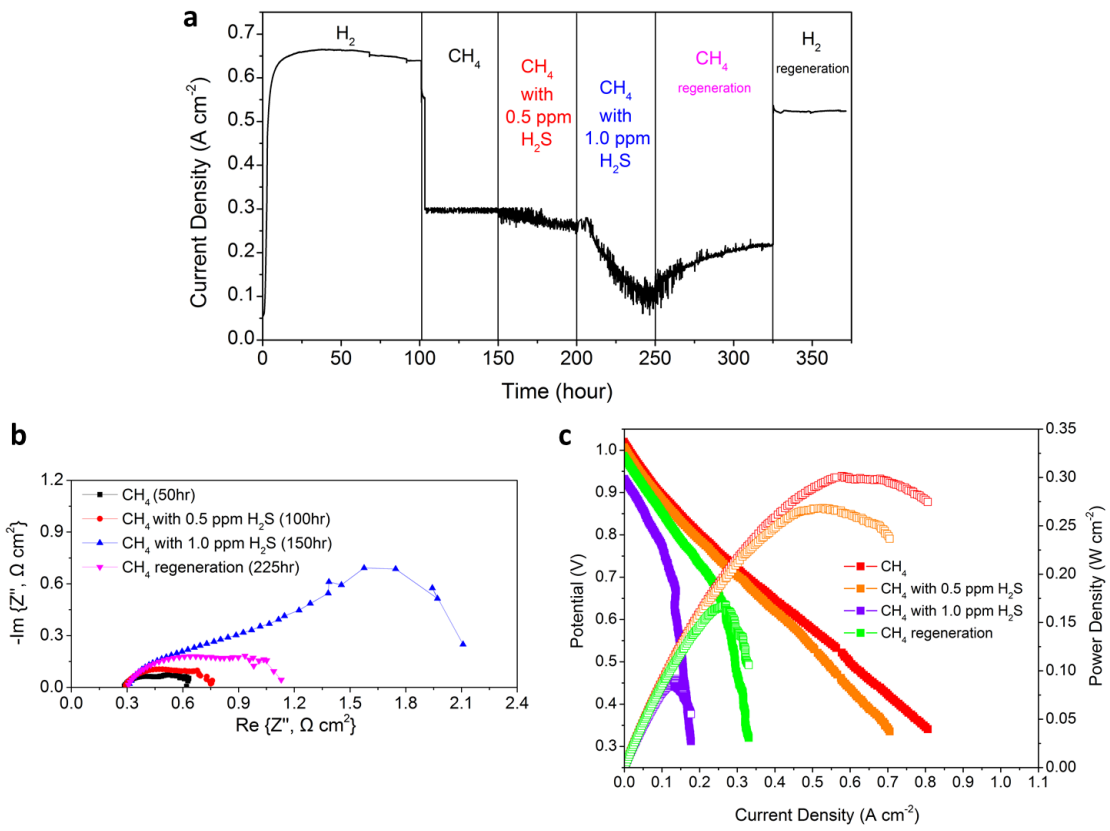

Figure 26. (a) Cell current density versus time at constant voltage of 0.7 V for Ni-YSZ with various sulfur concentrations at 700 ^{o}C. (b) Comparison of electrochemical impedance spectra at 0.7 V in CH_4 and the mixtures of 0.5 ppm H_2S and 1.0 ppm H_2S with CH_4. (c) Voltage and power density versus current density of a Ni-YSZ anode supported cell with different gases of CH_4, the mixtures of 0.5 ppm H_2S and 1.0 ppm H_2S with CH_4 and CH_4 regeneration after sulfur poisoning.

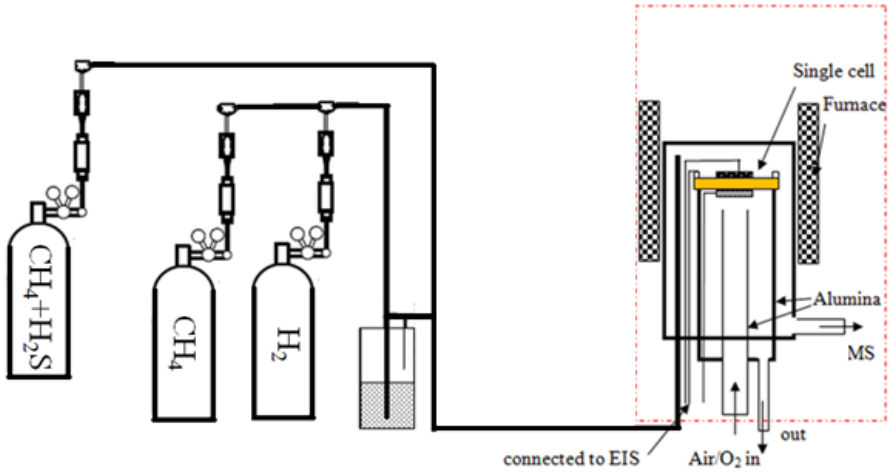

Figure 27. Schematic set-up for evaluation of Electrochemical measurement

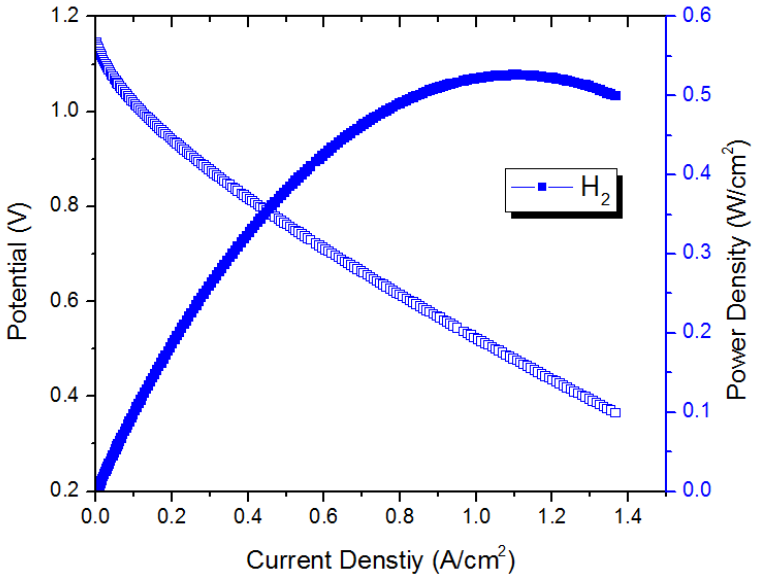

Figure 28. Voltage and power density versus current density of a Ni-YSZ anode supported cell with H_2.

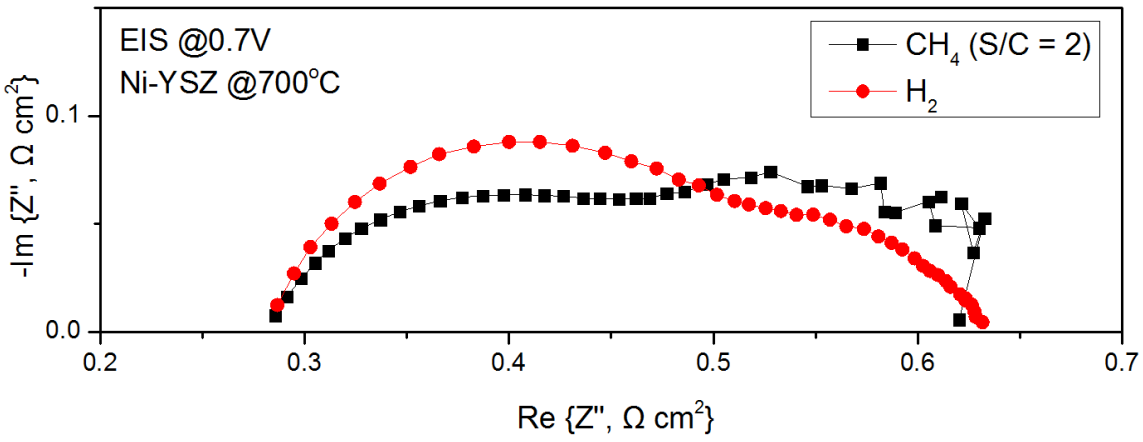

Figure 29. Comparison of electrochemical impedance spectra at 0.7 V in CH_4 (S/C = 2) operation and H_2.

A long-term stability study using a Ni-YSZ anode supported cell with the mixtures of 0.5 ppm and 1.0 ppm H_2S and CH_4 at 700 ^oC was performed to examine Ni-YSZ's electrocatalytic activities under a steam reforming condition (steam-to-carbon ratio, S/C = 2). Hereafter all of gases used in this study is in the same steam reforiming condition by mixing with water. A schematic for the electrochemical measurement is shown in Figure 27. After the stabilization for 100 hours in H_2, the open circuit voltage (OCV) reached 1.14 V, leading to a maximum power density of 0.52 W cm^{-2} (see Figure 28). The long-term stability result at 0.7 V is shown in Figure 26 (~15% fuel utilization for H_2 at 30 sccm). After 50 hours in CH_4 operation, a stable performance of ~0.3 A cm^{-2} with the fuel utilization of ~3.48 % at 30 sccm reaches. The stable current density after switching H_2 to CH_4 (~0.52 A cm^{-2} versus ~0.30 A cm^{-2}, respectively) may result from a lower H_2 yield from SMR since both of H_2 and CH_4 exhibit a similar polarization resistances at 0.7 V (Figure 29). It was reported that if coking occurs, the polarization posed on the interface should be arisen under CH_4 operation.[53] However, after the 0.5

ppm H_2S addition, its current density slowly decreases, indicating the deactivation of the stable steam reforming activity by sulfur poisoning. The degradation of the Ni-YSZ anode becomes more pronounced by the exposure to a higher concentration of 1.0 ppm H_2S, dropping to ~0.1 A cm^{-2}. To explore the reversibility of the degradation from sulfur poisoning, the mixture gas was switched back to CH_4. Although the regeneration process was continued until the performance reached a plateau, it could not be fully recovered due to an irreversible damage to the anode surface (*i.e.*, ~0.3 A cm^{-2} versus ~0.21 A cm^{-2}). Furthermore, even the regeneration process using H_2 could not make the anode cell fully recovered from sulfur poisoning (~0.64 A cm^{-2} versus ~0.52 A cm^{-2}). Similarly, the sulfur poisoning effect was examined at a higher temperature of 750 ^oC with the H_2S concentrations of 1.0, 2.0, and 2.5 ppm, and the detailed electrochemical performances are summarized in Figure 30. At the higher temperature, sulfur poisoning on Ni-YSZ can be alleviated[1] since the cell reached a stable current density of ~0.6 A cm^{-2} in a mixture of 1.0 ppm H_2S and CH_4. To determine the effect of H_2S on the polarization resistance (R_p) during the long-term stability examination at 0.7 V and at 700 ^oC, the electrochemical impedance spectroscopy (EIS) approach was applied. As shown in Figure 26, as the H_2S concentration increases, the R_p increases.[54] The higher R_p, due to a concentration-limited polarization, in the mixture of H_2S and CH_4 can be interpreted for a lower concentration of H_2 owing to a lower steam reforming electrocatalytic activity.[55,56] The concentration loss in high current density regime can be also identified in the curves of potential versus current density as illustrated in Figure 26. Therefore, it can be hypothesized that the accumulation of sulfur species on the anode makes a detrimental effect on the steam reforming capability of Ni-YSZ, resulting in a lower concentration of

H_2. However, *ex situ* EDS observations cannot assign the existence of sulfur on the surface of Ni (Figure 31). Therefore, to gain more insight into the sulfur poisoning mechanism under steam reforming, *in situ* monitoring of surface species upon exposure to the mixture of H_2S and CH_4 under SOFC conditions may be imperative. Accordingly, we conducted *in situ* SERS analyses using two different model electrodes, such as clean and sulfur-poisoned Ni-YSZ anodes as follows

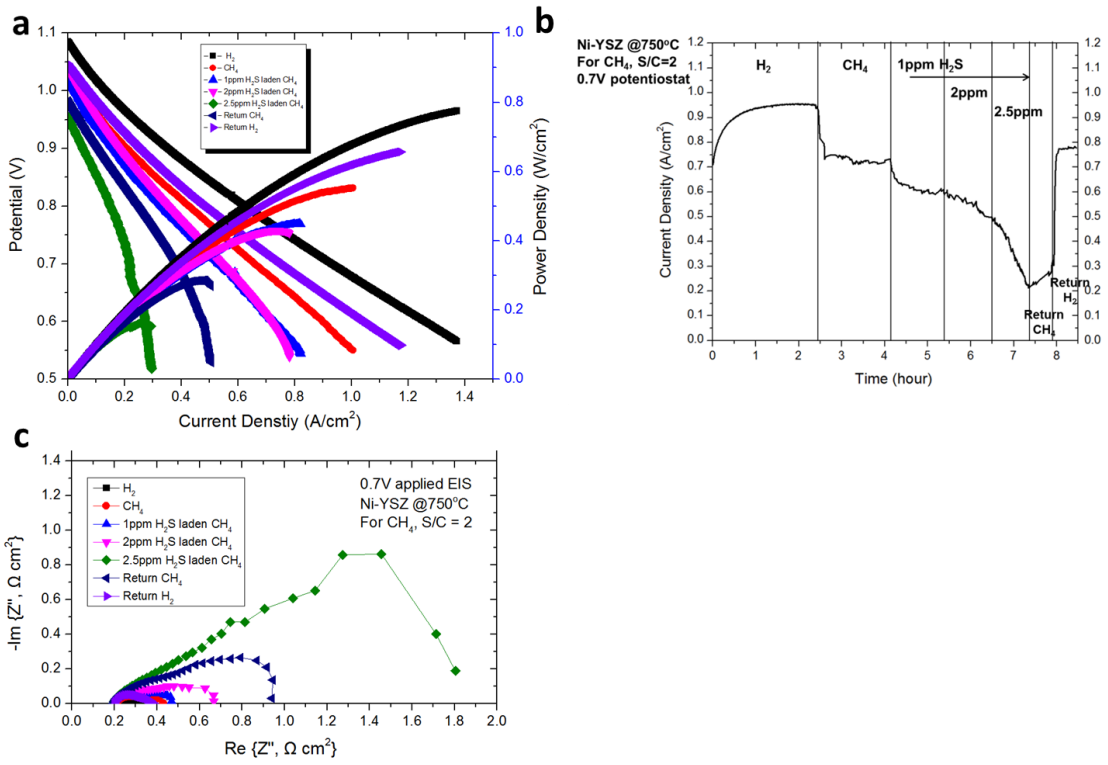

Figure 30. **(a)** Voltage and power density versus current density of a SOFC operated in different sulfur concentration at 750°C **(b)** Cell current density versus time at constant voltage (0.7V) for Ni-YSZ anode supported cell with varying the fuel gas composition at 750°C. The cell was first reduced with H_2 for several hours, and then operated in steam

methane, followed by sulfur laden methane. **(c)** Electrochemical impedance spectra of the Ni-YSZ anode operated in CH_4 with different sulfur concentration from 1ppm to 2.5ppm when operated at 0.7V.

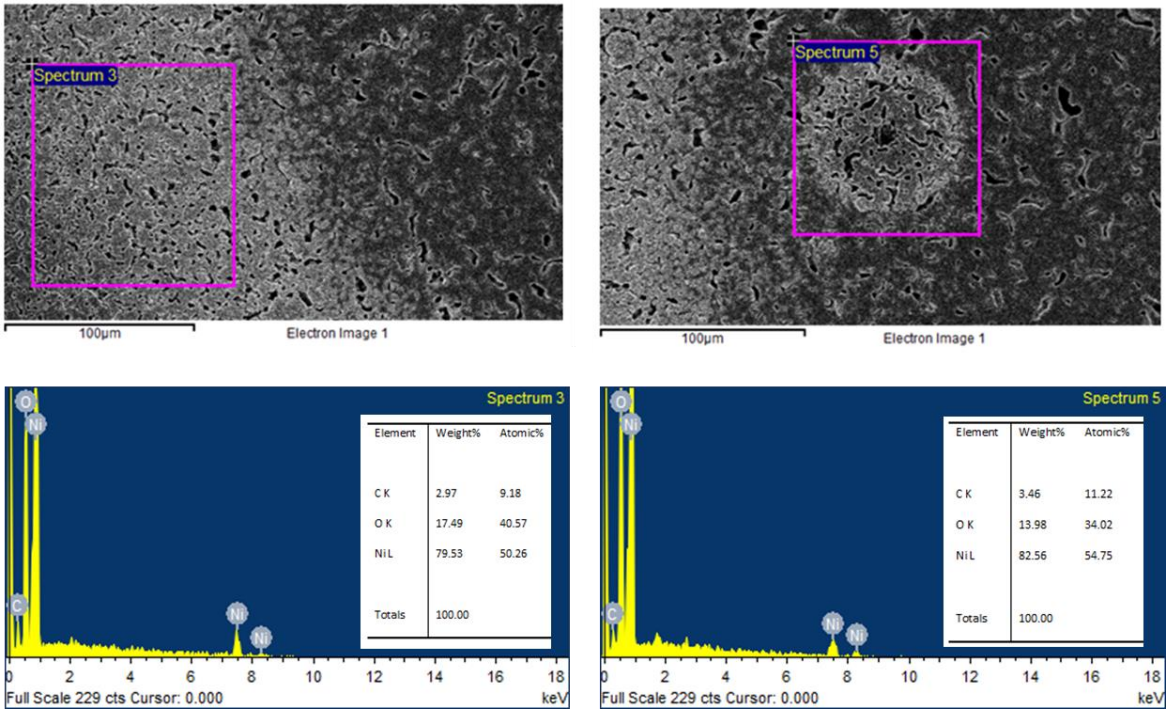

Figure 31. SEM and EDS taken from anodes after sulfur laden methane operation at 750^{o}C with 0.7V applied.

3.3 *In situ* Raman analysis for a Ni-YSZ model electrode before sulfur poisoning

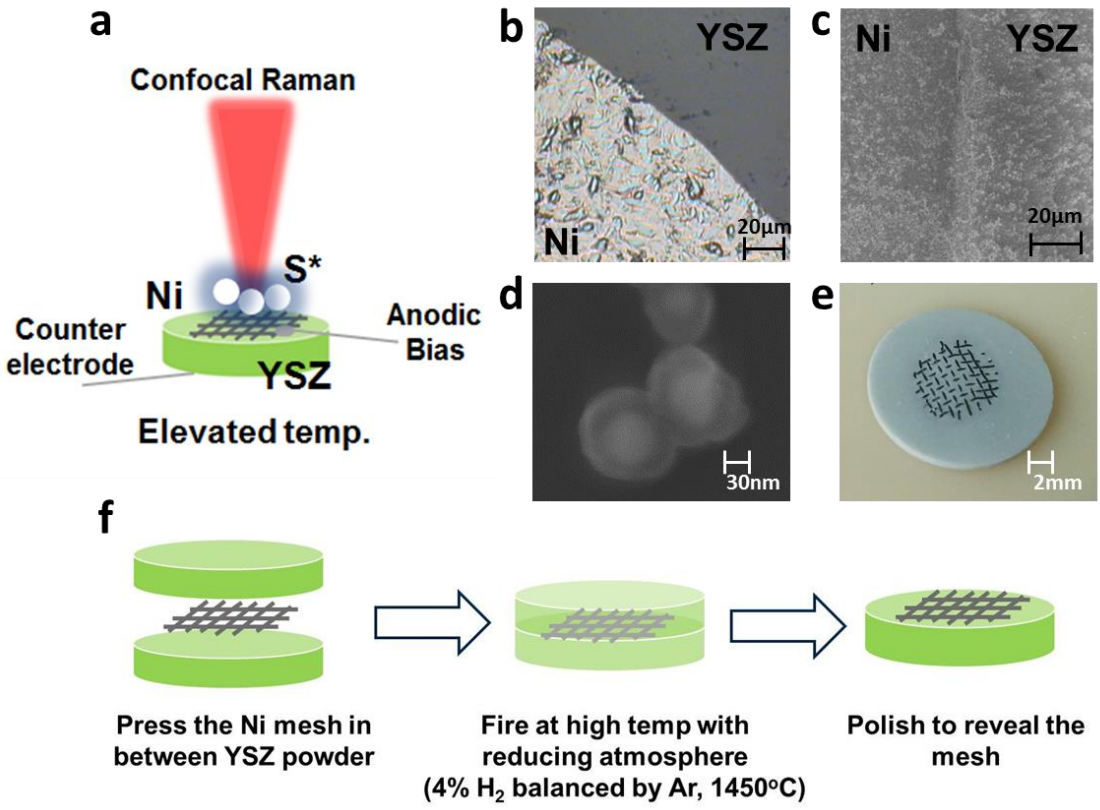

Figure 32. **(a)** A Schematic of the testing cell for *in situ/operando* SERS composed of patterned Ni electrode embedded in YSZ pellet **(b)** Optical microscope image of model electrode **(c)** SEM image of model electrode after deposition of SERS Nano probes **(d)** SEM image of $Ag@SiO_2$ nanoparticles for SERS analysis **(e)** Camera image of model electrode **(f)** Schematic for fabrication of patterned electrode through embedded mesh method

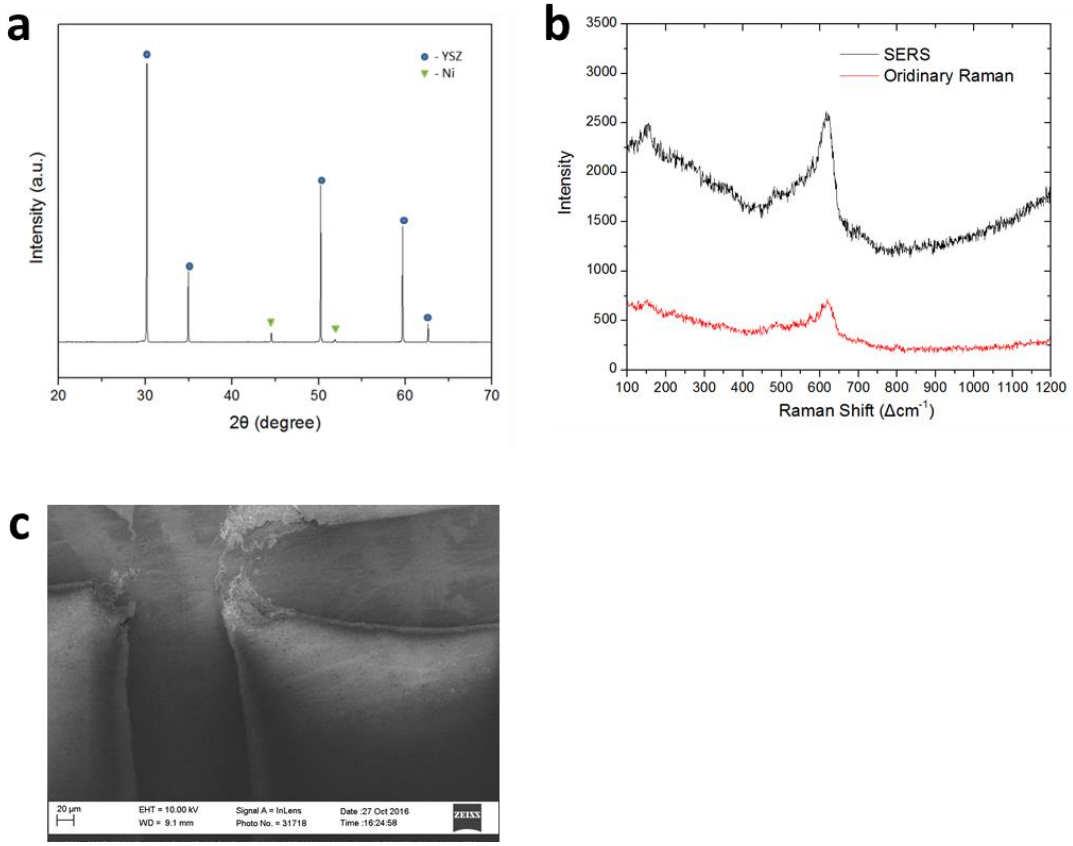

Figure 33. **Structural characterization of model electrode** (a) XRD of Ni-YSZ model electrode used for *in situ*/*operando* Raman measurement. (b) Comparison of Ni-YSZ substrate Raman intensity using SERS versus Ordinary Raman spectroscopy (c) SEM image of model electrode

Before introducing H_2S to Ni-YSZ, we performed *in situ* Raman spectroscopic measurements to unravel the seam reforming mechanism using CH_4 (see Figure 32, Figure 33).[23,51,57] As mentioned, to enhance the detection sensitivity of surface species, Ag@SiO_2 SERS NPs are used for the *in situ* SERS analysis of SOFC electrode materials under operating conditions.

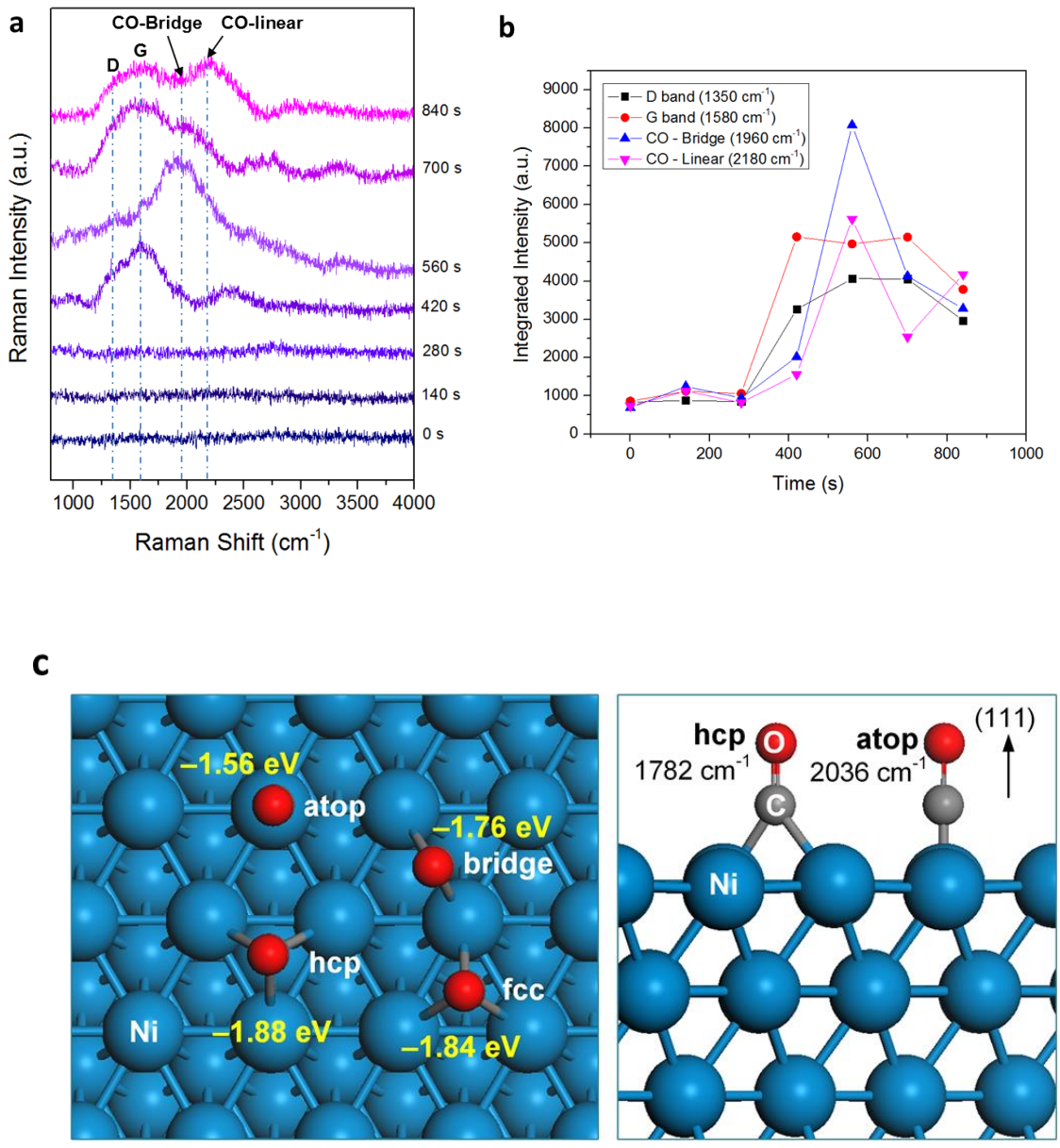

Figure 34. (a) Time-resolved *in situ* SERS analysis of a clean Ni-YSZ electrode upon exposure to CH_4 at 500 ^{o}C. (b) Integrated intensities of key spectral features as a function of time. Schematic diagram of reaction hypothesis of steam methane refoming on Ni-YSZ. (c) Top and side views of adsorbed CO species on Ni(111). The values in eV are the adsorption energies calculated using DFT calculations at PAW-PBE.

Table 3. Summary of calculated adsorption energies of CO on p(2×2) Ni(111) and their vibrational frequencies.

Adsorption site	Adsorption energy (eV)	ν(C≡O) stretching
hcp	–1.88	1782
fcc	–1.84	1786
bridge	–1.76	1853
atop	–1.56	2036

Table 4. Comparison of the vibrational frequencies of CO using Raman spectroscopy in different conditions.

Reference on Ni(111)[1]				This study[2]		
configuration	0.5 torr	1.0 torr	30 torr	expt.	calc.	assignment
linear	1770	1804	1940	1960	1782	hcp
bridge	2060	2086	2100	2180	2036	atop

After the *in situ* Raman flow cell reached 500 ^{o}C, CH_4 was introduced to the cell to monitor the steam reforming mechanism. Shown in Figure 34 are time-resolved SERS spectra. We carried out the SERS measurements at 500 ^{o}C because SiO_2 shelled SERS NPs do not show the localized surface plasmon (LSP) effect above 600 ^{o}C,[23] and as discussed, the bulk sulfide (Ni_xS_y) formation may not occur beyond 430 ^{o}C.[17] While no significant band initially appears before 280 s, Raman measurements at 420 s show a significant increase in the D band (1,350 cm^{-1}) and the G band (1,580 cm^{-1}), indicating carbon deposition on the Ni-YSZ electrode.[51] After 560 s and 700 s, the Raman spectra develop another band at 1,960 cm^{-1}. The peak is attributed to a carbon monoxide vibrational mode, [58] clearly demonstrating steam reforming. After 840 s, one more CO vibrational mode is identified at 2,180 cm^{-1}.[58] To verify their configurations, such as bridge or linear one,[58] we carried out density functional theory (DFT) calculations, as summarized in Figure 34c and Table 4, the adsorption energies on four active sites, such as "atop", "bridge", "fcc", and "hcp" (–1.56, –1.76, –1.84, and –1.88 eV, respectively), are correlated with their vibrational frequencies of the CO stretching (2,036, 1,853, 1,786, and 1,782 cm^{-1}, respectively). The trend of the adsorption energies are in good agreement with a previous study.[59] In particular, a careful comparison between pressure-dependent Raman peaks[58] and our DFT results (Table 5) indicate that the Raman peaks at 1,960 cm^{-1} and 2,180cm^{-1} can be assigned to the bridge and atop configurations on nickel metals, respectively. For a more detailed examination, each peak was integrated at a bandwidth of 20 cm^{-1} as shown in Figure 34. The D and G bands appear first, followed by the two CO vibrational modes at 560 s. This clearly suggests that adsorbed carbon species on Ni reacts with H_2O to form CO. Since CO is a major product of SMR ($CH_4 + H_2O \rightarrow CO +$

$3H_2$),[60] the *in situ* Raman analysis and DFT calculations demonstrate that CH_4 is first catalyzed on Ni-YSZ to produce surface carbon species (at 420 s in Figure 34), followed by the formation of CO (at 560 s in Figure 34), surface diffusion from a bridged active site to a "atop" site, and desorption.

Through time-resolved *in situ* Raman spectroscopy with CH_4, it confirms the Ni-YSZ cermet is electrocatalytically active to produce syngas via the steam reforming reaction, while it probes the existence of two different CO configurations on the SOFC anode surfaces using the *in situ* Raman spectroscopy.[58,61,62]

3.4 *Operando* Raman analysis for a Ni-YSZ electrode after sulfur poisoning

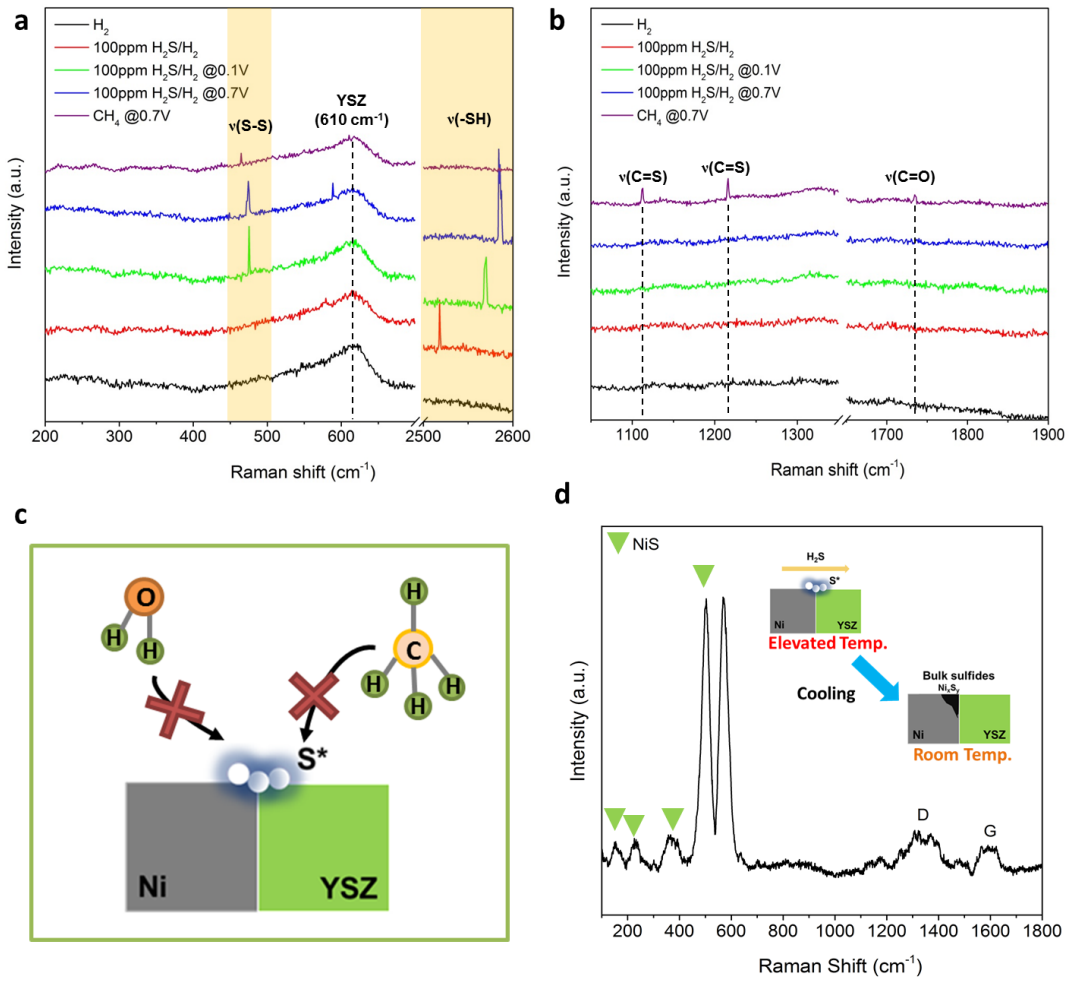

Figure 35. *In situ* SERS analysis of a Ni-YSZ electrode upon exposure to 100 ppm H_2S in H_2, followed by CH_4 at 500°C. (a) Raman spectra for the ν(S-S) and ν(S-H) bands, (b) Raman spectra for the ν(C=S) and ν(C=O) bands, (c) a schematic of a reaction mechanism of the formation of surface sulfur species on Ni-YSZ. (d) *Ex situ* Raman spectrum of the Ni-YSZ electrode after exposure to 100 ppm H_2S in H_2 and CH_4. The inset shows a schematic of the bulk nickel sulfide formation after cooling down from 500°C to room temperature.

It is known that surface modification by a trace amount of catalysts can significantly enhance the rate of electrode reaction, whereas minor amount of inactive phase can also quickly degrade electrode performance. In the case of sulfur poisoning, the amount of sulfur is only in ppm level but its presence may dramatically affect the overall activity of the fuel cell. Therefore, probing the surface species is critical to understanding the degradation mechanism. To boost the sensitivity to sulfur species, Ag@SiO_2 SERS NPs are employed on the electrode interface and a higher concentration of H_2S (100ppm) is used to better detect sulfur intermediates on our model electrode. To confirm if sulfur coverage on Ni-YSZ interface can impede steam-reforming catalytic activity toward CH_4, the designed model electrode is first sulfur-poisoned with 100ppm H_2S in H_2 to deposit sulfur species on the TPB (Figure 35**(c)**). After the sulfur species is deposited, pure CH_4 (S:C=2:1) is flown to monitor the CO band evolution for evidence of steam reforming as described in Figure 34.

After introducing 100ppm H_2S/H_2 on Ni-YSZ interface, the ν(S-H) was seen at 2520 cm^{-1}, indicating dissociative H_2S adsorption (Figure 35**(a)**)[63]. Note that position of ν(S-H) band can be altered by hydrogen bonding (e.g., S-H•••O, S-H•••S)[64-66]. Although, it was a different anode material, formation of S-H bond is also suggested by *ex situ* TOF-SIMS study after 0.5% H_2S annealing on $La_{0.4}Sr_{0.6}TiO_{3+\delta}$.[67] After applying 0.1V anodic bias on the model electrode, the ν(S-S) Raman band appeared at 470cm^{-1}.[68] Presumably, the anodic bias oxidizes the S-H bond to form S-S bonds. Both ν(S-S) and ν(S-H) intensities significantly increase at a stronger anodic bias of 0.7V. When the oxygen conducting ceramic phase in the anode (YSZ) pumps oxygen by the anodic bias, the electrochemical oxidation of S^* to SO_2 can occur[1]. Appearance of $\nu_{scissoring}(S_2O_4^{2-})$

was found at 0.7V to support this hypothesis[69]. Due to a concentration gradient, S^* on the metal surface (Ni) will migrate to the TPB region as adsorbed S* and is removed as SO_2 at the Ni-YSZ interface[1]. Therefore, when a stronger anodic bias is applied to the model electrode, the ν(S-S) and ν(S-H) band will increase as shown in the *operando* Raman result.

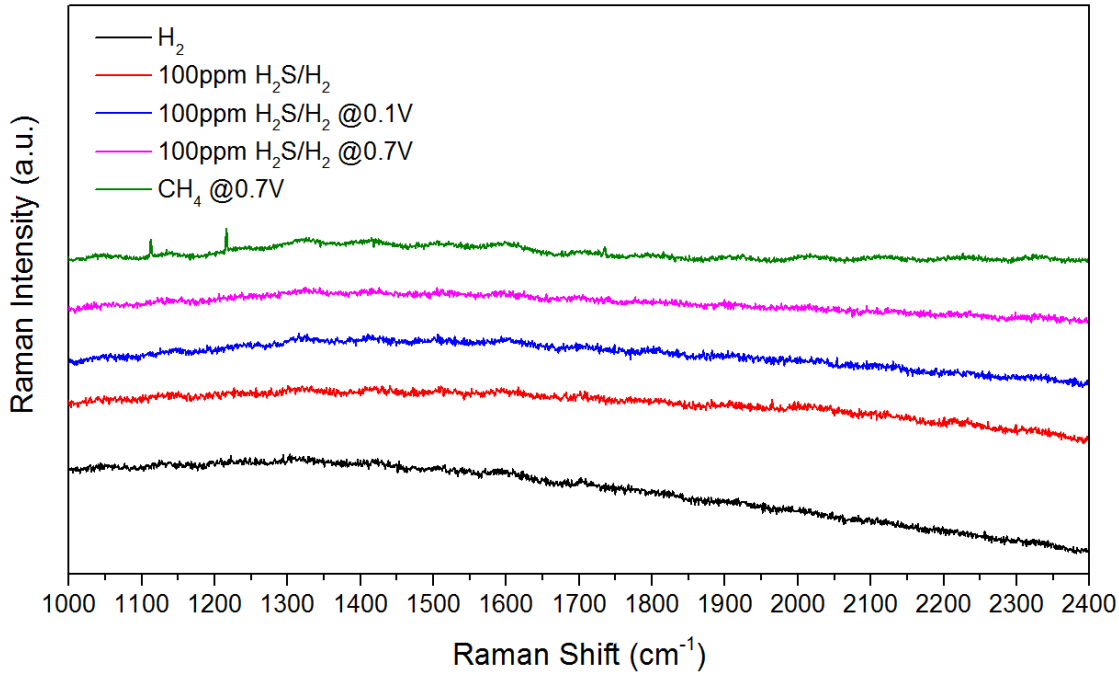

Figure 36. *Operando* SERS analysis of Ni-YSZ model electrode upon exposure to 100ppm H_2S in H_2 followed by steam-reforming of CH_4 at 500°C. Raman shift from 1000 to 2400cm^{-1} is shown while no visible D, G, CO band is found.

While the anodic bias is maintained at 0.7 V, the gas is switched to pure CH_4 to investigate if the sulfur-poisoned Ni-YSZ model cell still has the capability for steam reforming. Even with pure CH_4 (S:C=2:1) introduction, the evolution of D band, G band or CO band did not occur (Figure 36**)** indicating that the surface of Ni was passivated by

the sulfur[47]. The passivation of the Ni blocks the catalytic active site for CH_4 adsorption and the steam reforming reaction is prevented (Figure 36**(c)**). The Raman spectra shows the ν(C=S) instead[70,71] suggesting that adsorbed sulfur species would be removed as CS_2 which agrees with others mass spectroscopy data.[60] Also, the ν(S-H) bands completely disappeared and the ν(S-S) band weakened and shifted slightly when pure CH_4 was introduced. This is consistent with previous adsorption energy (E_{ads}) DFT calculations which showed SH*(E_{ads} : 3.72eV) has smaller adsorption energy than C*(E_{ads} : 7.27eV) on the Ni (100) surface. ($E_{ads\ of}$ S*: 5.96eV)[1,72,73]. This indicates some of adsorbed sulfur on the TPB can be replaced with adsorbed carbon as pure CH_4 is introduced. However, the TPB does not fully recover as we have already shown (Figure 26 **(c)**).

After *operando* Raman analysis, all gases were stopped and the cell was slowly cooled (~5^{o}C/min) to room temperature, and *ex situ* Raman spectroscopy was measured. At room temperature, bulk nickel-sulfide (Ni_xS_y) formation on Ni was confirmed with Raman analysis (Figure 36(d)). Because presence of bulk sulfide (Ni_xS_y) is not found with *in situ* Raman analysis at 500^{o}C, the formation of bulk sulfide can only have occurred while sample was cooled. This is consistent with ab-initio phase diagram study which showed that bulk sulfide formation(Ni_xS_y) is only preferable at low temperatures (for 100ppm H_2S/H_2, <430^{o}C)[18]. Therefore, the strong adsorption and accumulation of elemental sulfur on the TPB which reduces the steam reforming capability of Ni-YSZ is the main cause of performance degradation of SOFCs in the presence of H_2S above 500^{o}C[47].

3.5 Conclusion

In this study, *in situ* temperature-dependent Raman spectroscopy was successfully applied to identify the surface species on Ni-YSZ under practical SOFC conditions using the mixture of H_2S and CH_4. While the Ni-YSZ anode cell was stable in CH_4, the anode electrode was noticeably affected by the co-feeding of ppm levels of H_2S and CH_4, leading to an unrecoverable degradation of the surface. With a designed model electrode, *in situ* SERS analyses at 500^{o}C detected the two types of configurations of CO when Ni-YSZ was exposed to CH_4, clearly confirming the steam reforming reaction ($CH_4 + H_2O \rightarrow CO + 2H_2$) on the anode. In addition, the accumulation of ν(S-S) and ν(-SH) was found detected by using the *in situ* Raman approach. Also, our *in situ* characterization demonstrated that the Ni-YSZ's electrocatalytic activity is hampered by sulfur poisoning because the CO bands disappeared. Furthermore, we confirmed that the degradation phase is surface sulfur species not the bulk nickel sulfides under SOFC conditions, which is in excellent agreement with *ab initio* thermodynamic calculations. This information can rationally propose SOFC operation conditions, such as the necessary of NG-fueled SOFC's accurate purging before cooling down, which avoids the nickel sulfide formation.

3.6 Experimental

3.6.1 Electrochemical performance measurement

To assess the electrochemical performance in contaminant containing fuel standard procedures for single cell measurements as shown in Figure 27 was used. The fabrication method of Ni-YSZ anode supported button cells used in this study is described elsewhere.[3] Anode-supported single cells were prepared by the tape casting method, and the electrolyte is prepared by drop-casting. Electrochemical measurement is performed on Princeton Parstat and Arbin electrochemical workstations. The IV curves were measured from 1.2V to 0.3V with scan rate of 0.03V/s. Electrochemical impedance spectroscopy (EIS) is performed in the frequency range of 100 kHz - 1 mHz. Chronoamperometry is performed at a DC polarization of 0.7V. Prior to all electrochemical measurement, the Ni-YSZ anode is electrochemically activated via H_2 stabilization to ensure reproducible measurements. Ceramabond 552 (Aramco products) is used for sealing the cell to the alumina tube. For the current collector, Ag paste is applied on cathode while Ni paste is applied on anode. To simulate the practical fuels, ppm level sulfur laden methane is used. To ensure, H_2S did not dissolve in the bubbler, sulfur laden methane is mixed with steam-carrying methane after bubbler.

3.6.2 Fabrication of model electrode for Raman analysis

Patterned electrode was fabricated by embedded-mesh method (Figure 32). To fabricate model electrode with well-defined nickel-electrolyte interface, YSZ powder is pressed into pellet (300 Mpa for 30 sec) with nickel mesh (<1cm piece) embedded in the center. The pellets with a sandwich-like structure were then sintered in 4% H_2 /bal Ar at 1450^{o}C for 5 hours to densify the electrolyte and secure contact with Ni mesh. The sintered

sample was grinded and polished with diamond suspensions on one side to remove the excess electrolyte and reveal the Ni mesh. Schematic of fabrication is described in Figure 32**(f)** and the resulting samples are characterized as illustrated in Figure 32 **(b), (c), (d), (e)** and Figure 33.

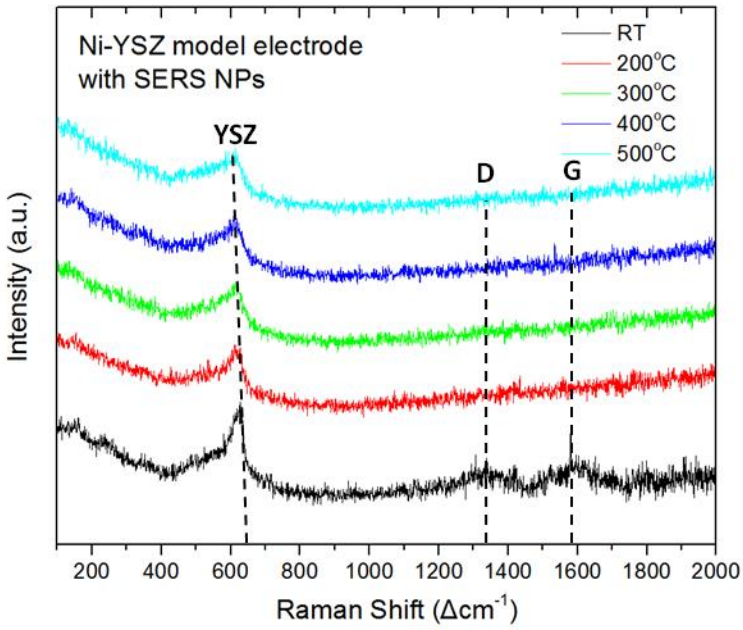

Figure 37. *In situ* SERS measurements of Ni-YSZ model electrode was performed to track the composition change with the temperature in a reducing atmosphere (1:1 = H_2 : Ar). No major composition change is observed while slight thermal shift of the YSZ band was found (610cm^{-1}).

CHAPTER 4. INVESTIGATION INTO WATER-MEDIATED SULFUR TOLERANT MECHANISM OF PROTON CONDUCTING OXIDE VIA OPERANDO SURFACE ENHANCED RAMAN SPECTROSCOPY

4.1 Introduction

Sulfur contaminants in the anode cermet (Ceramic-Metal) degrade the longevity of Solid Oxide Fuel Cell (SOFC) stacks, and intolerance to fuel impurities is considered as one of the key barriers for SOFC market penetration[1,17,47,55,74]. Sulfur contaminants are found in readily available fuels, such as natural gas and liquefied petroleum (LP)[1,47], therefore to fully achieve the fuel flexibility for SOFCs, the development of a contamination tolerant anode is vital. While kinetic activity of Nickel (Ni), the most widely used metal in SOFC anode, is known to be inadequate for many practical fuels due likely to the formation of elemental sulfur (S^*) blocking reactive sites at the triple phase boundary (TPB) [1,17,75,76], Ni still has prospects to be the state-of-the-art anode for its exceptional performance toward H_2 oxidation catalytic activity, high electronic conductivity, and its cost-efficiency. To take aforementioned advantages of Ni, the SOFC community took extensive efforts to study various alternative materials as potential ceramic counterparts to preserve Ni, plus enhancing sulfur tolerance of anode.

Over the past years, important strides have been made in demonstrating attractive sulfur tolerance utilizing proton conducting oxides (i.e., Barium cerates – zirconates derivatives, $Ba(Zr_{1-x}Ce_x)O_{3-d}$) combined with Ni[9,77,78]. While sulfur poisoning on Ni is

rigorously studied with *ab initio* atomistic calculation and *in situ* high temperature Raman spectroscopy[17,18,50,63], surface information of ceramic, essential counterparts of Ni, is yet an important missing piece of puzzle. Unraveling sulfur mitigation mechanism on proton conducting oxide would be unambiguously influential, since many pioneering works of top-notch SOFCs are driven by protonic ceramic based anodes[27,77,79-81]. However, to date, no clear understanding has been reported, while many speculated sulfur mitigation mechanism would ascribed to distinctive water adsorption capability of proton conducting oxide[1,9,77]. The challenge mainly stems from extreme low concentration of sulfur molecules (ppm level), and inability to capture surface chemistry during the electrochemical reaction processes.

One successful strategy to detect surface intermediates is employing Surface Enhanced Raman Spectroscopy (SERS) probes[20,23,51]. By utilizing electro-kinetically inert and thermally robust nano-probes (NPs), Li et al., successfully identified $-CO_3$ surface functional group during anti-coking mechanism of proton conducting oxides ($BaZr_{0.9}Y_{0.1}O_{3-d}$ (BZY) and BZCYYb) and important role of water regarding carbon elimination has been addressed[52]. While these studies have produced valuable insights, electrochemical polarization arising from surface species is yet elusive. Better understanding of surface dynamics would be achievable when surface science is correlated with concurrent *operando* measurement such as electrochemical impedance spectroscopy[82].

In this work, we probe the surface of Ni-BZCYYb model electrodes upon exposure to ppm level of sulfur (H_2S) at elevated temperature and we deliver three valuable information concerning sulfur mitigation mechanism of proton conducting

oxide. First, while surface science of sulfur exposure was obscure for a long period of time, SERS NPs significantly enhanced detection limit of Raman spectroscopy. Thus, we directly observed $–SO_4$ surface functional group as a major species on the surface of BZCYYb. Contemporaneous measurement of impedance spectroscopy allows us to build quantitative relationship between vibrational and electrochemical features. Second, by introducing water vapor pressure, dissolution of $–SO_4$ can be confirmed in time-resolved SERS and we propose critical role of water in anti-sulfur mechanism of proton conducting oxide. Our observation challenges current paradigm of protonic ceramic anode design, that water adsorption may possess higher priority over oxygen ion flux to remove adsorbed sulfur($S^* + 2O^{2-} \rightarrow SO_2 + 4e^-$)[1,47]. Third, to further expand our understanding to molecular dynamics, Density Functional Theory (DFT) calculation is carried to explore elementary reaction sequences.

4.2 Construction of O*perando* Surface Enhanced Raman Spectroscopy Platform

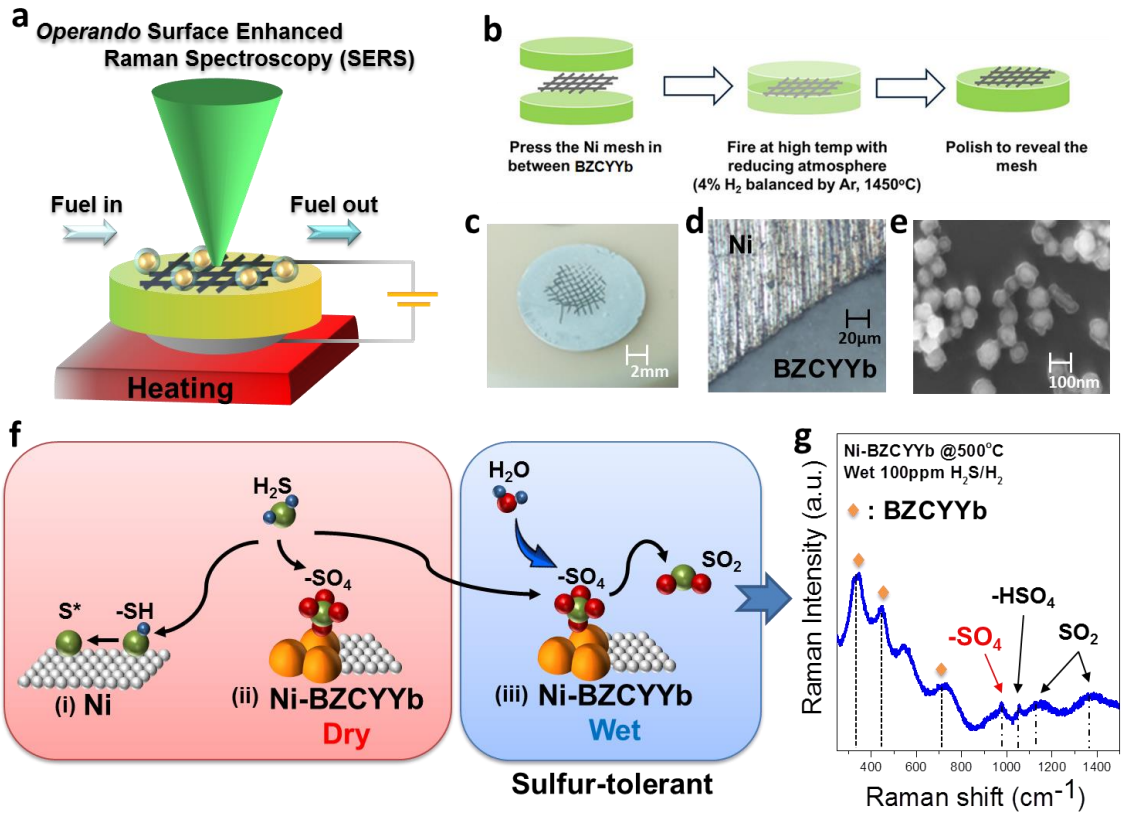

Figure 38. **(a)** A Schematic of the *operando* SERS platform with Ni-BZCYYb model electrode. **(b)** Schematic for fabrication of patterned-Ni electrode in BZCYYb powder through embedded mesh method. **(c)** Resulting camera image of model electrode. **(d)** Optical microscope image of model electrode showing Ni-BZCYYb interface **(e)** SEM image of SERS NPs ($Ag@SiO_2$) **(f)** Schematics for sulfur transitions and resistance mechanisms on **(i)** Ni, **(ii)** Dry Ni-BZCYYb, and **(iii)** Wet Ni-BZCYYb with resulting SERS spectrum described in **(g)** measured at 500°C with 3v% water mixed 100ppm H_2S/H_2 fuel.

From a practical point of view, it is essential to incorporate pores into the anode to facilitate mass transport of fuels. In addition, the electronically conductive phase should be well dispersed with the ionic conductor to maximize active TPB density. However, it is challenging to gain fundamental understanding of intrinsic properties of an electrode with conventional porosity since it is difficult to separate electrode performance from microstructure, morphology and surface chemistry. Therefore, to gain critical understanding of the intrinsic properties of Ni-BZCYYb anodes, we have devised a model cell through embedded mesh method (Figure 38 **(b),** see supplementary methods for fabrication details and additional characterizations are shown in Figure 42)[51,57]. While typical configuration of cermet may give complexity on identifying reactions happening on each material (Ceramic, Metal), model electrodes with well-established TPBs can give direct surface information happening on each material by simply changing the laser focus of Raman Spectrometer (Figure 38**(f), (g)**). The open structure of the patterned anode allows *operando* probing by Raman spectroscopy in parallel to the electrochemical testing.

Although sulfur contaminant can be found in various forms such as H_2S, thiols, CS_2 and COS, it mostly converts to H_2S under reducing atmospheres of anode[1,77]. Therefore, fuel of 100ppm H_2S/H_2 is chosen as source of sulfur contaminant. Since, only ppm level of sulfur is in the atmosphere, we can expect the key reaction intermediates that are present on surface of electrode will be in trace amount. Therefore, even though surface adsorbate has Raman active vibrational mode, ordinary Raman spectroscopy may yield insufficient information[24]. Furthermore, high temperature *in situ/ operando* Raman spectroscopy poses a particular challenge of low signal-to-noise ratios attribute to

variation of all Raman modes increases at elevated temperature. Although SERS technique with sputtered Nano islands of Ag shows promising prospects to apply in *ex situ* characterizations [24], applying Ag nanoparticles to an *in situ* study introduces two new complications. First, silver itself is catalytically active, so silver nanoparticles would bias the performance measurements and confound the reaction mechanism study. Second, silver nanoparticles are not stable at elevated temperatures and tend to coarsen into larger particles that have weaker LSPR effects, which results in very small, or even no, enhancement of the Raman scattering. Therefore, an inert shell is needed to restrain the catalytic activity of Ag and to prevent nanoparticle coarsening.

To overcome aforementioned issues, we employed electro-kinetically inert and thermally-robust Ag@SiO_2 (Core : silver, Shell : Silica) nanoparticles as SERS NPs on model cell (Figure 38**(e),** Figure 42) which showed promising localized surface plasmon resonance (LSPR) in high temperature equal to or below 500^oC[23,51]. Fabricated BZCYYb has pure perovskite phase supported by XRD, and i*n situ* SERS measurements of Ni-BZCYYb model electrode was performed to track the composition change with the temperature in reducing atmosphere (1:1 = H_2 : Ar) (Figure 42). In the temperature dependent Raman spectra, no major composition change is observed while slight thermal shift of the BZCYYb band is found (doublet ~ 350cm^{-1} (v_1, v_2), ~ 430cm^{-1} (v_3))[9,83]. In total, successful assembly of *operando* SERS platform is performed (Figure 38**(a)**), and investigation into surface chemistry of Ni-BZCYYb in realistic operating conditions containing sulfur contained atmospheres is followed.

4.3 Inspecting Water-assisted Anti-sulfur Nature of Proton Conducting Oxide

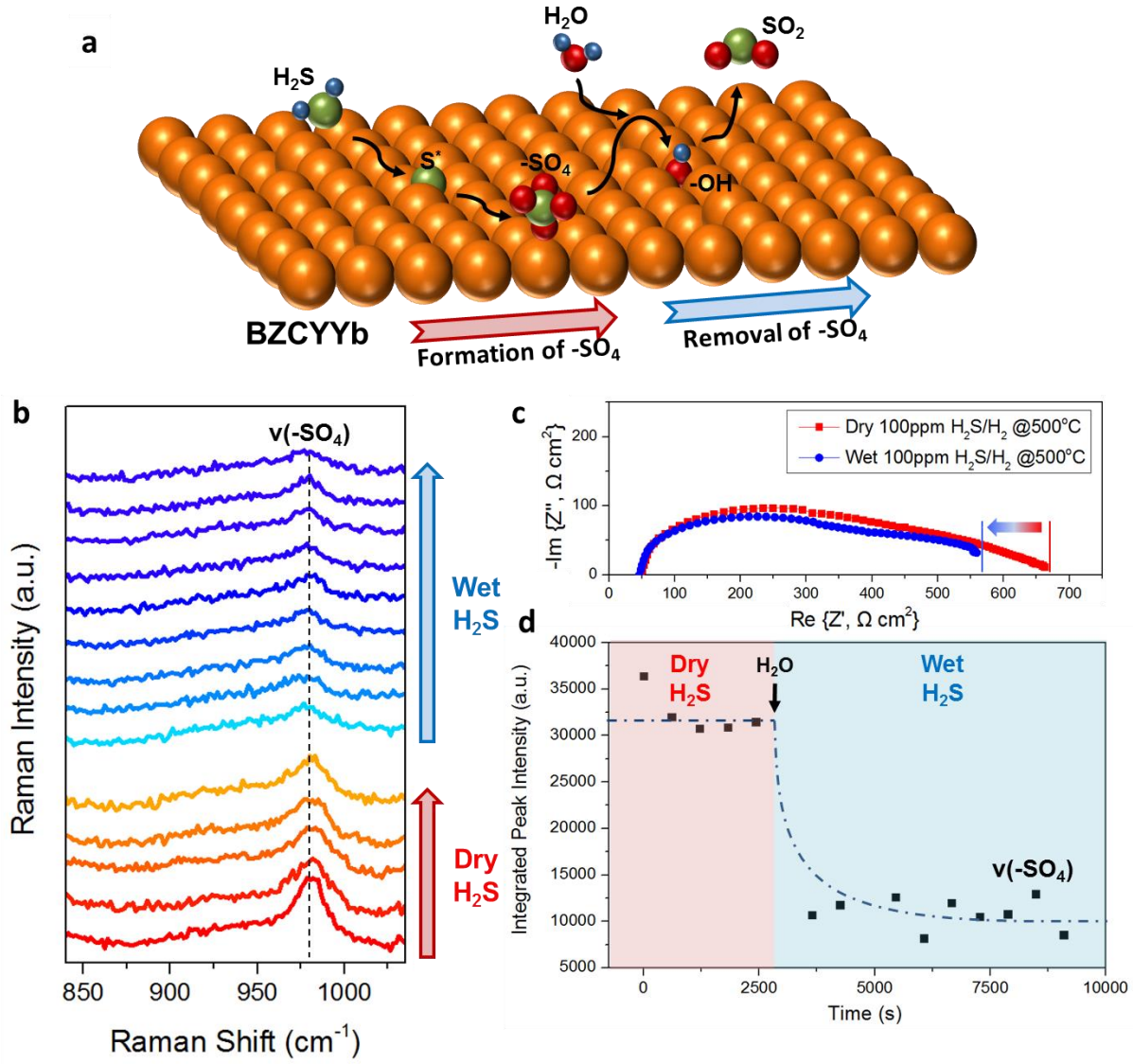

Figure 39. **(a)** Schematics for $–SO_4$ formation and water-mediated $–SO_4$ removal on proton conducting, BZCYYb. **(b)** *In situ* SERS analysis of Ni-BZCYYb model electrode upon exposure from dry to wet 100ppm H_2S/H_2 at 500°C. Laser was focused on BZCYYb. **(c)** Electrochemical impedance spectroscopy of Ni-BZCYYb model electrode upon exposure to dry and to wet 100ppm H_2S/H_2 at 500°C. **(d)** Integrated peak intensities

of key spectral features for (b) as function of time. v(-SO_4) shows fast decrease after introduction of 3v% water. A dotted line is added to guide the eye of the reader.

The principal evidence for active role of BZCYYb in sulfur mitigation mechanism is described by Time-resolved *operando* Raman spectroscopy accompanied by water vapor pressure change (Figure 39). Spectra are collected at a rate of 77s/spectrum, and the laser was focused on the BZCYYb surface adjacent to Ni (within 20μm) to ensure good electron transport. As displayed in Figure 39**(b)**, when dry 100 ppm H_2S/H_2 was introduced to the model electrode at 500^oC, band of sulfate (v(-SO_4), 980cm^{-1})[66,84-86] appeared quickly, an indication of sulfur oxidation on BZCYYb surface. According to Bartholomew et al., the toxicity of the sulfur species depends on how many electron pairs are available to interact with metal, therefore toxicity decreases as follows : H_2S > SO_2 > -SO_4[87]. Therefore, it suggests that formation of –SO_4 on BZCYYb can be advantageous to protect Ni. However without water introduction, -SO_4 persist to exist implying BZCYYb alone lacks ability to perform sulfur removal. Afterwards, to examine the effect of water on a –SO_4 developed BZCYYb model electrode, the gas is then switched to wet environment (3v% H_2O + 100ppm H_2S/H_2). After the introduction of water, v(-SO_4) at 980cm^{-1} was quickly eliminated as reflected in the integrated peak intensity of v(-SO_4) over time (Figure 39**(c)**). Additionally, the presence of water in the system developed v(SO_2) which is assigned to 520cm^{-1}, 1147cm^{-1} and 1334cm^{-1}(Figure 38**(g),** Figure 43**,** Figure 44)[88]. SO_2 production from H_2S reforming has been witnessed beforehand with mass spectroscopy[60,67,77], and our Raman results signify that H_2O facilitates –SO_4 removal on BZCYYb. Above hypothesis is strongly supported by Time-

resolved Raman observation of H_2O adsorption band ($3580cm^{-1}$) and formation of –OH($\sim3300cm^{-1}$) groups on BZCYYb[89] and it is now unambiguous that water plays a vital role in sulfur resistance mechanism as Yang et al., formerly suggested[1,9]**(**Figure 48**)**. Moreover, Duan et al., illustrated remarkable sulfur-resistance of $BaZr_{0.8}Y_{0.2}O_{3-d}$ (BZY20) and remarked the role of dissociative water adsorption on proton conducting oxide for its anti-sulfur nature[77,90]. These Raman results lead to a conclusion that H_2O is an effective reactant to remove $–SO_4$ which is developed on proton conducting oxide surface under H_2S exposure.

Although, Raman spectroscopy is not inherently a quantitative analysis technique, the amount of $–SO_4$ developed on surface was estimated by using pure $BaSO_4$ as a calibration sample using identical Raman scanning conditions. To perform, pure $BaSO_4$ pellet with same diameter as Ni-BZCYYb model electrode was prepared with equivalent amount of SERS NPs deposition, and the Raman spectrum was measured at 500^oC (Figure 45). By assuming pure $BaSO_4$ has utter surface coverage (100%) with $–SO_4$, by integration with bandwidth of $20cm^{-1}$, it was concluded that BZCYYb in dry 100ppm H_2S/H_2 has ~0.6% of $–SO_4$ surface coverage. By introducing H_2O, $-SO_4$ coverage on BZCYYb was reduced to ~0.2%, which indicates H_2O removes 2/3 of $–SO_4$ from the BZCYYb surface as SO_2.

This result is comparable with EIS measurement that is conducted in dry and wet 100ppm H_2S/H_2 (Figure 39**(c)**). Dry 100ppm H_2S/H_2 has higher polarization resistance (R_p) value ($-SO_4$ formation) and R_p recovers when water is introduced to the system ($-SO_4$ removal). So, it engenders a hypothesis that $–SO_4$ is the major surface functional group that contributes most to increase of polarization of the electrode under sulfur

contained atmosphere. This result is consistent with R_p measurement performed by Yang et al., that BZCYYb anodes show no R_p increase with wet sulfur (20ppm H_2S/H_2)[9].

Other than BZCYYb alone, Ni is also analyzed in both dry and wet 100ppm H_2S/H_2 atmosphere at 500^oC and the resulting *in situ* SERS evolution is shown in Figure 46**,** Figure 47**,** Figure 48. Since we observe –SH on Ni, which was envisioned in DFT studies[1,63], it is very plausible that H_2S preferentially cracked on Ni first and due to concentration gradient moved to BZCYYb to form $–SO_4$ functional group. The R_p of the electrode seems to be largely dependent on TPB area (where ceramic phase (BZCYYb) near to Ni (within 20 μm)), rather than metal phase alone (Ni) of the cell. This suggests that major polarization arises from interface between Ni and BZCYYb. While it is known that sulfur coverage of Ni is mainly blamed for malicious poisoning effect, to gain better sulfur tolerance for SOFC anodes, ceramic phase should act as sulfur removal catalyst. Therefore, ideal ceramic catalyst should have capability to attract sulfur adsorption in order to protect Ni, and in the same time, should possess catalytic activity to remove sulfur to exhaust. In this aspect, $Ba(Ce_{1-}Zr_x)\ O_3$-based ceramic shows better tendency to react with H_2S rather than Ni, which is shown by *ab initio* thermodynamic studies[50,91]. Moreover, it seems protonic ceramics' sulfur mitigation ability gets fully promoted when water adsorption takes place. This might explain why model electrode's R_p under exposure of H_2S was mainly controlled by TPB of the cell. Also, according to Chueh et al., it should be noted that the active sites of cermet model anodes may not only be confined to the metal, but can be very active with ceramic-gas 2 phase boundaries (2PB) as well[92]. Overall, $-SO_4$ development on proton conducting oxide and subsequent water-mediated $–SO_4$ removal is described.

4.4 Quantitative Analysis of Raman Spectra to Electrochemical Polarization

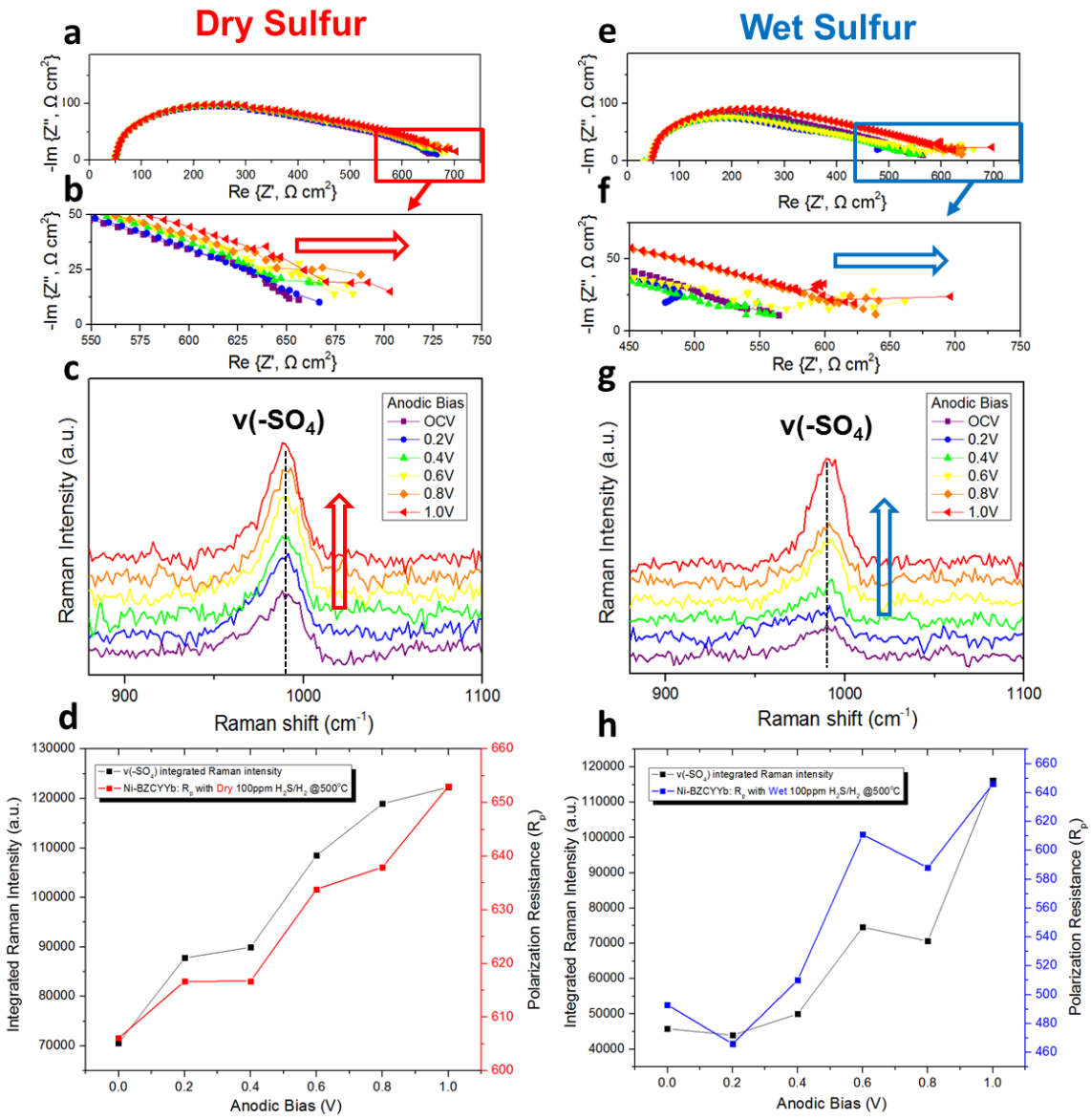

Figure 40. **(a),(e)** Electrochemical impedance spectroscopy of Ni-BZCYYb model electrode under (a) dry and (e) wet (3v% water) 100ppm H_2S/H_2 at 500°C. The anodic bias is applied from OCV to 1.0V. **(b),(f)** shows magnified inset image focusing on low frequency EIS for easy comparison respectively. **(c), (g)** *operando* Raman Spectroscopic

evolution of Ni-BZCYYb model electrode under (c) dry and (g) wet 100ppm H_2S/H_2 at 500^oC with anodic bias. Raman acquisitions are performed simultaneously with impedance spectroscopy at an interval of 0.2V. **(d), (h)** Quantitative correlation between key features, v(-SO_4) of *operando* Raman spectra and polarization resistance of the model electrode under (d) dry and (h) wet 100ppm H_2S/H_2 @500^oC

To further verify our hypothesis that –SO_4 is the major functional group that drives polarization of electrode, we designed additional *operando* Raman spectroscopy studies along with anodic bias. Coupling Raman results with electrochemical results can validate the electrode degradation mechanism in most effective way and combination of different techniques should be able to synthesize a powerful predictive model. By previous discussions, we can largely dissect sulfur transitions on BZCYYb in two reactions; **(1)** Sulfate formation, and **(2)** Sulfate removal (Figure 39**(a)**)

The reaction mechanism for formation of –SO_4 (Reaction **(1)**) could be hypothesized as followed;

$$\mathbf{H_2S_{(g)} + 6O^{2-} \rightarrow 2OH^- + SO_4^{2-} + 8e^-} \qquad \mathbf{(1)}$$

Since the hypothesized reaction generates electrons, applied anodic bias will draw electrons from anode to external circuit, and is expected to facilitate –SO_4 formation on the anode. If –SO_4 functional group impose dominant impacts polarization of surface, accumulation of –SO_4 on anode will eventually lead to an increase in R_p of model electrode as well.

While applying anodic bias from OCV to 1.0V, the v(-SO_4) exhibits obvious change. (Dry 100 ppm H_2S/H_2, Figure 40**(a),(b),(c)**) Not surprisingly, when higher anodic bias is applied to the cell, intensity of v(-SO_4) is greatly increased, pointing out anodic bias drives forward reaction of **(1)**. Concurrent measurement of EIS shows an increase in R_p accordingly. Therefore, the evolution of Raman band group of –SO_4 is undoubtedly an indication of the surface reaction induced by sulfur-poisoning.

Water-mediated sulfur tolerance mechanism (Reaction **(2)**) under wet atmosphere can be represented as followed;

$$\mathbf{SO_4^{2-} + 2H_2O_{(g)} + 2e^- \rightarrow 4(OH^-) + SO_{2(g)}} \qquad \mathbf{(2)}$$

Since suggested reaction needs electrons, applied anodic bias will prevent sulfur removal of the cell, resulting in less tolerance in wet atmosphere at high over-potential. To validate, model cell is exposed to wet sulfur and we performed an *operando* Raman applying anodic bias to the model electrode from OCV to 1.0V. When water is introduced to the system, intensity of v(-SO_4) and R_p of model electrode was quickly reduced (OCV) as we already discussed in earlier section (Figure 39). However, as anodic bias applied to the cell, v(-SO_4) and R_p increases suggesting that at high over-potential, the bias effect can overwhelm the chemical effect of H_2O to reform –SO_4. (Figure 40**(e),(f),(g)**)

The values of vibrational properties as a function of electrochemical operation can be considered as a semi-quantitative indication of surface functional group evolution induced by sulfur adsorption on electrode surface. To perform correlations with electrochemical properties, v(-SO_4) on BZCYYb was integrated with band width of 20cm^{-1}. Figure 40 **(d), (h)** shows quantitative correlation between polarization resistance

and integrated peak intensity of v(-SO_4). Whether it is in dry or wet atmosphere, it is clear that polarization resistance of the cell is determined by the integrated intensity of v(-SO_4) on the surface. Wet sulfur atmosphere showed much less polarization resistance and v(-SO_4) intensity in moderate anodic bias (OCV ~ 0.4V) proposing that water-mediating sulfur mitigation mechanism is operative as we already witnessed in long-term electrochemical performance studies[9,77]. Overall, *operando* Raman results with bias confirm the direction of electrons in suggested reactions (1), (2) and connect vibrational features to electrochemical traits which is authorized by concurrent impedance spectroscopy measurements.

4.5 Assessment of Molecular Dynamics via Density Functional Theory

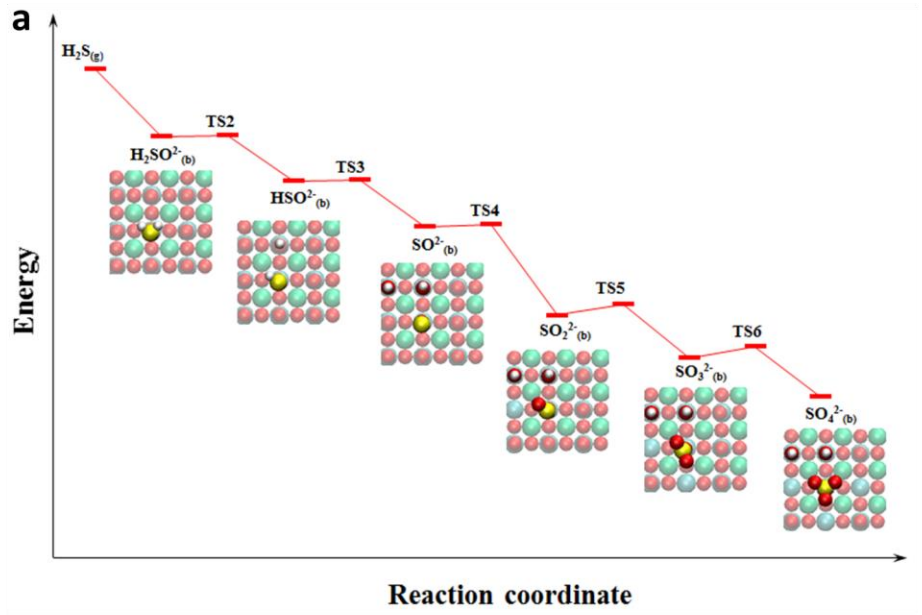
a
Energy
Reaction coordinate
$H_2S_{(g)}$
TS2
$H_2SO^{2-}_{(b)}$
TS3
$HSO^{2-}_{(b)}$
TS4
$SO^{2-}_{(b)}$
TS5
$SO_2^{2-}_{(b)}$
TS6
$SO_3^{2-}_{(b)}$
$SO_4^{2-}_{(b)}$

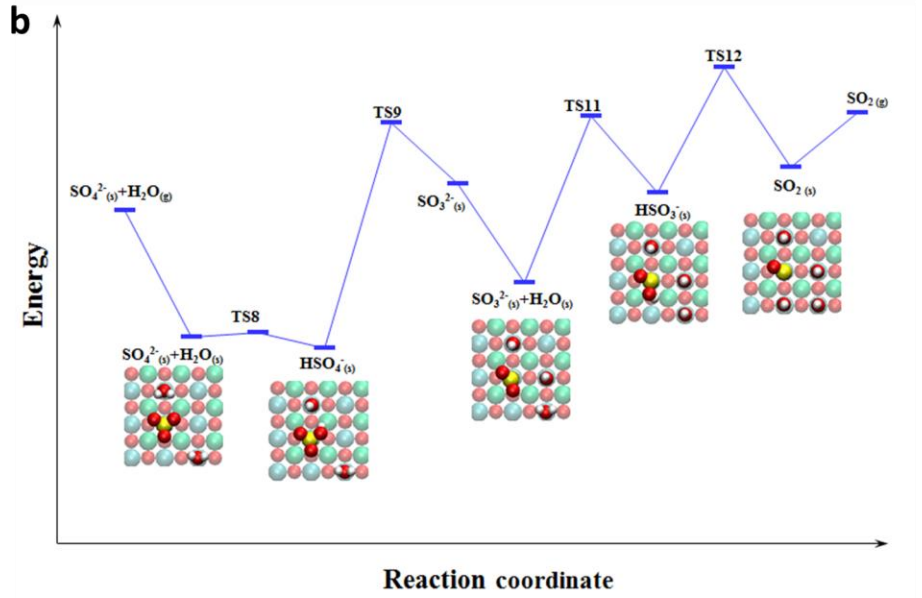
b
Energy
Reaction coordinate
$SO_4^{2-}{}_{(s)}+H_2O_{(g)}$
TS8
$SO_4^{2-}{}_{(s)}+H_2O_{(s)}$
$HSO_4^-{}_{(s)}$
TS9
$SO_3^{2-}{}_{(s)}$
$SO_3^{2-}{}_{(s)}+H_2O_{(s)}$
TS11
$HSO_3^-{}_{(s)}$
TS12
$SO_{2\,(s)}$
$SO_{2\,(g)}$

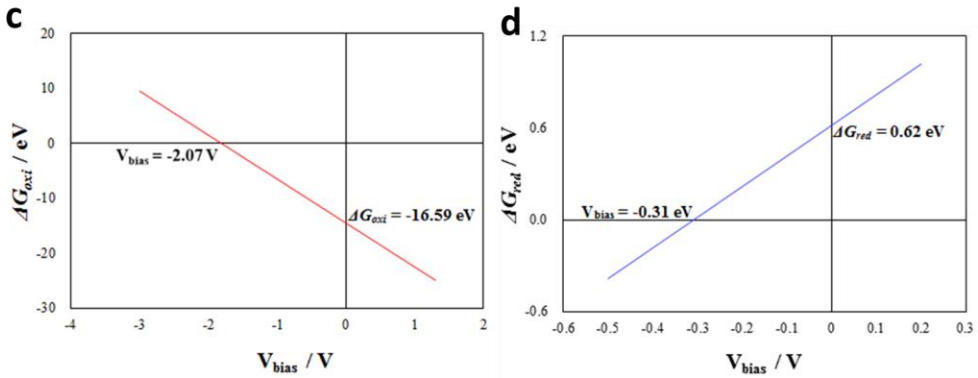
c
ΔG_{oxi} / eV
V_{bias} = -2.07 V
ΔG_{oxi} = -16.59 eV
V_{bias} / V
d
ΔG_{red} / eV
ΔG_{red} = 0.62 eV
V_{bias} = -0.31 eV
V_{bias} / V

Figure 41. PES and the related structures of intermediate states in each step for (a) sulfate formation : $H_2S_{(g)} + 6O^{2-}_{(b)} \rightarrow SO_4^{2-}{}_{(b)} + 2OH^-_{(b)} + 8e^-$ and (b) Water-mediated sulfate removal process: $SO_4^{2-}{}_{(b)} + 2H_2O_{(g)} + 2e^- \rightarrow SO_{2(g)} + 4OH^-_{(b)}$. The cyan, green, red, yellow and white spheres are represented as Zr, Ba, O, S and H atoms, respectively. The TS's indicate the transition states in the related step of R's. The computed Gibbs free energies in (c) sulfate formation, ΔG_{oxi}, and (d) water-mediated sulfate removal process, ΔG_{red}, processes as functions of the anodic bias potential, V_{bias}.

Table 5. **(a)** The computed ΔE and *Ea* for the elementary steps of **R1** to **R6** in the sulfate formation process from the $H_2S_{(g)}$ to the $SO_4^{2-}{}_{(b)}$ on the $BaZrO_3$. The corresponded PES is plotted in Figure 41(a). **(b)** The computed ΔE and *Ea* for the elementary steps of **R7** to **R13** in the water-mediated sulfate removal from the $SO_4^{2-}{}_{(b)}$ to the $SO_{2(g)}$ removal on the $BaZrO_3$. The corresponded PES is plotted in Figure 41(b).

(a)

Steps	ΔE (eV)	*Ea* (eV)
R1: $H_2S_{(g)} + O^{2-} \rightarrow H_2SO^{2-}_{(b)}$	-3.57	
R2: $H_2SO^{2-}_{(b)} + O^{2-}_{(b)} \rightarrow HSO^{2-}_{(b)} + HO^-_{(b)} + e^-$	-2.31	0.05
R3: $HSO^{2-}_{(b)} + O^{2-}_{(b)} \rightarrow SO^{2-}_{(b)} + HO^-_{(b)} + e^-$	-2.42	0.02
R4: $SO^{2-}_{(b)} + O^{2-}_{(b)} \rightarrow SO_2^{2-}{}_{(b)} + 2e^-$	-4.64	0.13

R5: $SO_2^{2-}{}_{(b)} + O^{2-}{}_{(b)} \rightarrow SO_3^{2-}{}_{(b)} + 2e^-$	-2.23	0.56
R6: $SO_3^{2-}{}_{(b)} + O^{2-}{}_{(b)} \rightarrow SO_4^{2-}{}_{(b)} + 2e^-$	-2.04	0.58

(b)

Steps	*ΔE* (eV)	*Ea* (eV)
R7: $SO_4^{2-}{}_{(b)} + H_2O_{(g)} \rightarrow SO_4^{2-}{}_{(b)} + H_2O_{(b)}$	-1.02	
R8: $SO_4^{2-}{}_{(b)} + H_2O_{(b)} \rightarrow HSO_4^-{}_{(b)} + OH^-{}_{(b)}$	-0.09	0.03
R9: $HSO_4^-{}_{(b)} + 2e^- \rightarrow SO_3^{2-}{}_{(b)} + OH^-{}_{(b)}$	1.32	1.81
R10: $SO_3^{2-}{}_{(b)} + H_2O_{(g)} \rightarrow SO_3^{2-}{}_{(b)} + H_2O_{(b)}$	-0.79	
R11: $SO_3^{2-}{}_{(b)} + H_2O_{(b)} \rightarrow HSO_3^-{}_{(b)} + OH^-{}_{(b)}$	0.72	1.33
R12: $HSO_3^-{}_{(b)} \rightarrow SO_{2(b)} + OH^-{}_{(b)}$	0.20	1.01
R13: $SO_{2(b)} \rightarrow SO_{2(g)}$	0.44	

Since surface science is guided by *Operando* Raman spectroscopic analysis, we further looked into elaborate molecular dynamics of reaction **(1)** and **(2)** by thorough DFT calculations. To simulate BZCYYb, the DFT model cell is simplified as undoped $BaZrO_3$ in the beginning, however, energetics of Y and Yb doped $BaZrO_3$ is also

considered as well (Figure 44**,** Figure 45). The reaction **(1)** corresponds to the 8-electron oxidation process, starting from $H_2S_{(g)}$ to subsequent formation of $SO_4^{2-}{}_{(b)}$ along with $OH^-{}_{(b)}$ on the $BaZrO_3$ (the subscripts (g) and (b) indicate the species in the gas phase and bulk, respectively). The reaction **(1)** can be decomposed to the elementary steps of **R1** to **R6,** as listed in Table 5**(a)** and shown in the corresponded potential energy surface (PES) in Figure 41**(a)** (The complete reaction processes are detailed in the animation in the Supporting Information, Figure 54). As stated in the reaction coordinates and Table 5**(a)**, each elementary sequences of reaction **(1)** displays high exothermicities with negligible activation energy barriers (*Ea*), proves that overall oxidation process readily occurs (overall ΔE_{oxi} = -17.21 eV) as we already identified with Raman spectroscopy. It is also worth noting that the Y and Yb doped $BaZrO_3$ describes similar energetics (Y doped ΔE_{oxi} : -17.46, Yb doped ΔE_{oxi} : -16.85 eV) indicating $–SO_4$ functional group formation is energetically favorable on proton conducting oxides (Figure 52).

The $SO_4^{2-}{}_{(b)}$ removal reaction **(2),** in the formation for $SO_{2(g)}$ along with dissociative $OH^-{}_{(b)}$ formation with help of water, is 2-electron reduction processes and the oxidation state of sulfur changes from +6 (SO_4^{2-}) to +4 (SO_2). The particular reaction sequence is decomposed into the elementary steps of **R7** to **R13**, as listed in Table 5**(b)** and shown in the corresponded PES in Figure 41**(c)** (The complete reaction processes are detailed in the animation in the Supporting Information, Figure 55). The reaction starts with the $H_2O_{(g)}$ adsorption, which has barrierless behavior on proton conducting oxide (**R7**). Then H_2O dissociation happens with negligible barrier to donate proton to $–SO_4$, forming $HSO_4^-{}_{(b)}$ + $OH^-{}_{(b)}$ (**R8)**. The formation of intermediate $-HSO_4$ is in good coincidence with Raman results (Figure 38**(g),** Figure 43**,** Figure 48),and calculated result

is comparable with DFT calculation from Bandura et al., that they found water dissociation can occur without a barrier on $BaZrO_3$[90]. Thus, presence of H_2O vapor should be the limiting steps to determine sulfate-removal reaction rate. $HSO_4^-{}_{(b)}$, the protonated $SO_4^{2-}{}_{(b)}$, can have better cleave the strong S-O bond ($\Delta E/Ea$ = 1.32/1.81 eV) compared to those in the S-O bond cleavage in unprotonated $SO_4^{2-}{}_{(b)}$ ($\Delta E/Ea$ = 2.23/2.79 eV) which can be found in reversed step of **R5**. The second water adsorption (**R10**) can provide additional proton source to protonate intermediate $SO_3^{2-}{}_{(b)}$ species (**R11**) to form $SO_{2(b)}$ (**R12**)**.** Finally, $SO_{2(b)}$ can desorb from the surface (**R13**) with a moderate desorption energy (ΔE = 0.44 eV) to complete the sulfur removal process. The overall reduction process shows very low endothermicity (overall ΔE_{red} = 0.78 eV), which implies that removal of $–SO_4$ can practically achieved when thermodynamic properties are adjusted as seen in Raman analysis. Please note that Yb doping further change the spontaneity of the-SO_4 removal, as overall ΔE_{red} cut down to 0.64 eV, indicating beneficial sulfur tolerant effect can be expected from Yb dopant (Figure 53). Overall, our DFT results demonstrate that surface adsorbed sulfur can be removed through formation of sulfate, however subsequent removal of $–SO_4$ requires –OH / H_2O.

To further examine the bias-dependent $–SO_4$ accumulation behaviors, we further applied the thermodynamic corrections from anodic bias voltage to examine the Gibbs free energy and the corresponding spontaneity. The Gibbs free energy of sulfate formation reaction **(1)** (ΔG_{oxi}) can be expressed as:

$$\Delta G_{oxi} = \Delta E_{oxi} + RT\ln(p_o/p_{H_2S}) - 8V_{bias} \qquad (3)$$

Where R is the ideal gas constant, T is the operation temperature at 500^{o}C (773 K), p_0 is the standard pressure of 1 bar, p_{H_2S} is the H_2S pressure of 100 ppm (10^{-4} bar), $-8V_{bias}$ corresponds to the 8-electron oxidation process, and V_{bias} is the applied anodic bias voltage varied from 0 to ~1 V. Analogously, the Gibbs free energy of sulfate removal reaction **(2)** (ΔG_{red}) can be expressed as:

$$\Delta G_{red} = \Delta E_{red} + RT\ln(p_{SO_2}/p_{H_2O}^{2}) + 2V_{bias} \qquad (4)$$

Where p_{SO_2} and p_{H_2O} correspond to the pressures of the product (70 ppm, 0.7×10^{-4} bar) and reactant (0.03 bar), respectively; and $+2V_{bias}$ corresponds to the 2-electron reduction process. The computed ΔG_{oxi} and ΔG_{red} as functions of V_{bias} are plotted in Figure 41**(c)** and Figure 41**(d)**, respectively.

Figure 41**(c)** shows that ΔG_{oxi} decreases steeply as V_{bias} increases, attributable to the $-8V_{bias}$ term in ΔG_{oxi}. The result indicates that the 8-electron oxidation reaction favors $SO_4^{2-}{}_{(b)}$ formation at higher V_{bias}, explaining the experimental observation that $v(SO_4^{2-})$ peak has larger intensity as higher anodic bias is applied on the cell. Figure 41**(d)** shows that ΔG_{red} increases slightly as V_{bias} increases, corresponding to the $+2V_{bias}$ term in the two-electron reduction process. The plot suggests that the spontaneity of water removal of $SO_4^{2-}{}_{(b)}$ diminishes at higher V_{bias}, rationalizing the experimental observation that intensity of $v(SO_4^{2-})$ drops at lower anodic bias in the present of water. The Gibbs free energy analysis satisfactorily explains the bias-driven $-SO_4$ accumulation described operando Raman spectroscopy (Figure 40), signifies our mechanism formulation of water-mediated sulfur mitigation reaction is solid and rigorous. Comprehensive studies to observe the electrode surface, the structure of the interface, and the participating reactants

are an essential step to develop sulfur-tolerant anode for SOFCs. Without a detailed, mechanistic understanding of the surface catalytic reaction, dynamics of performance degradation cannot be understood, while it is vital information to develop novel electrode.

4.6 Conclusions

In summary, by carrying out surface-sensitive *operando* SERS on Ni-BZCYYb model electrode during dry and wet sulfur exposure, we determined the surface science of proton conducting oxide under conditions relevant to SOFCs and protonic ceramic fuel cells. We found that $–SO_4$ is key surface functional group on BZCYYb and water-mediated sulfur mitigation is scrutinized. Our direct *operando* observation and atomistic calculation confirm the crucial role of water in anti-sulfur capability of proton conducting oxide. The current strategy to remove elemental sulfur(S^*) with sole expectation on oxygen anion flux might be insufficient to achieve sulfur tolerant anode. Rather, water-assisted sulfate reformation should be considered to have robust anode operation with sulfur contaminants. The new insights in this study will directly benefit the community by unraveling the cause of performance degradation in SOFCs when exposed to sulfur and can give guidance to develop a novel electrode structures to have excellent durability against sulfur contained fuels.

4.7 Methods

4.7.1 Fabrication of model electrode

Patterned electrodes are fabricated by an embedded-mesh method. To fabricate model electrodes with a well-defined nickel-electrolyte interface, BZCYYb powder was pressed into a pellet (300 MPa for 30 sec) with nickel mesh (<1cm piece) embedded. The pellets with a sandwich structure are then sintered in 4% H_2 /bal Ar at 1450^{o}C for 5 hours to densify the electrolyte and to ensure good contact with Ni mesh. One side of the sintered sample was ground and polished with diamond suspensions to remove the excess electrolyte enclosure and to reveal the interface between Ni and the electrolyte. Schematic of fabrication is described in Figure 38 **(f)** and the resulting samples are characterized as illustrated in Figure 38 and Figure 42.

4.7.2 Operando Raman Spectroscopy

Raman spectra were obtained using a Renishaw RM 1000 spectromicroscopy system (~2 μm spot size). An air-cooled Ar laser (CVI Melles Griot) emitted at 514 nm was used for excitation of Raman signal in this study with a total power of 10 mW. A Harrick environmental chamber was used for *in situ* Raman tests.[76] An *in situ* time-resolved study was conducted by placing the laser spot on the same location, with the laser slightly out of focus to cover a larger area of about 5 μm in diameter. To perform *operando* Raman spectroscopy study, Ni-BZCYYb side was connected as working electrode (WE), the other side is brush-painted with Ag paste to perform as counter electrode (CE). As a control, a Ag-Ag symmetric cell with BZCYYb electrolyte with same thickness was also tested. (Figure 49**,** Figure 50).

Gasses (4% H_2/bal Ar, H_2, Ar, 100ppm H_2S/H_2, UHP grade, Airgas) were metered with mass flow controllers and introduced into the chamber. To introduce 3v% water into the gas, a room temperature bubbler was used. To ensure H_2S does not dissolve in water, 100ppm H_2S/H_2 gas is mixed after Ar flowed through bubbler.

4.7.3 Electrochemical impedance spectra measurements

Impedance spectra were acquired using a Solartron SI 1255 HF frequency response analyzer interfaced with an EG&G PAR potentiostat model 273A with an AC amplitude of 10 mV in the frequency range from 100 kHz to 0.01 Hz.

4.7.4 Computational details

The density functional theory (DFT) calculations were performed using Vienna *Ab initio* Simulation Package (VASP).[93-95] The computational method employed the generalized gradient approximation[96] with Perdew-Wang 1991 formulation[97] for the exchange-correlation function, GGA-PW91, with the projector-augmented wave method (PAW)[98,99] that the cost-effective pseudopotential was utilized for core electron-ion interaction. The cutoff kinetic energy of the plane-wave basis for the valance electrons was set at 600 eV. The Brillouin-Zone (BZ) integration was examined in the reciprocal space and sampled by the Monkhorst-Pack scheme[100] at 0.05 × 2 (1/Å) interval.

$BaZrO_3$ surface was constructed by nine (3 × 3) metal layers containing a total of 135 atoms, in which the bottom two layers were fixed at the optimized crystal lattice and the top seven layers were free to relax, to simulate the BZCYYb electrolyte; Dopants of Y and Yb, which played an important role to create oxygen vacancy and showed small energetic difference. The energetic and gradient convergences of 1×10^{-4} and 1×10^{-2} eV, respectively, were applied for the structural optimization and reaction energy (ΔE) calculation for each step. The Gibbs free energy (ΔG) for the overall process were further examined by including the thermodynamic corrections of bias voltage (V_{bias}) and gas species pressures on the computed ΔE. The transition states were located by Nudged Elastic Band (NEB) method at the same convergence criterions for the reaction barrier (Ea) calculation.

4.8 Supplementary Information

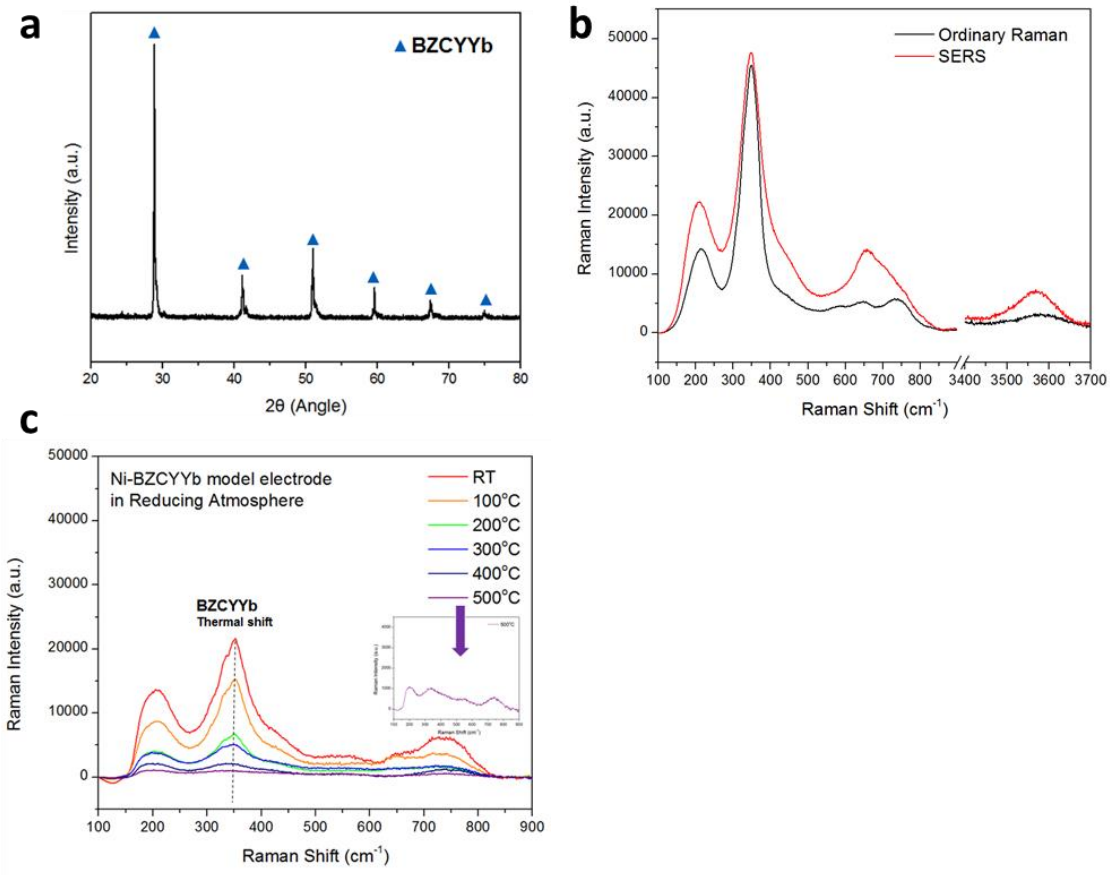

Figure 42. **(a)** XRD data of BZCYYb powder **(b)** Comparison of BZCYYb Raman intensity using SERS versus ordinary Raman spectroscopy **(c)** *In situ* SERS measurement of Ni-BZCYYb model electrode at different temperatures

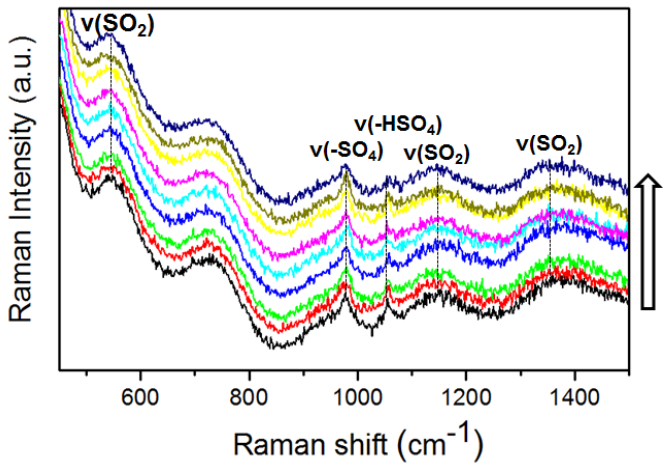

Figure 43. *In situ* SERS analysis of Ni-BZCYYb model electrode upon exposure to wet 100ppm H_2S/H_2 at 500°C. Laser was focused on BZCYYb

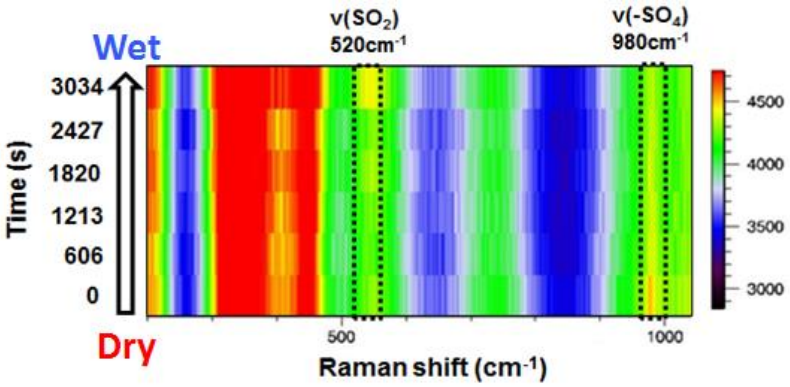

Figure 44. *In situ* Raman spectroscopic evolution of a BZCYYb model electrode acquired in 3v% H_2O introduction which was originally contaminated with dry 100ppm H_2S/H_2 at 500°C. Intensity of v($-SO_4$) fast decreasing upon water introduction and v(SO_2) develops at ~3034s as an indication of sulfur oxidation by water.

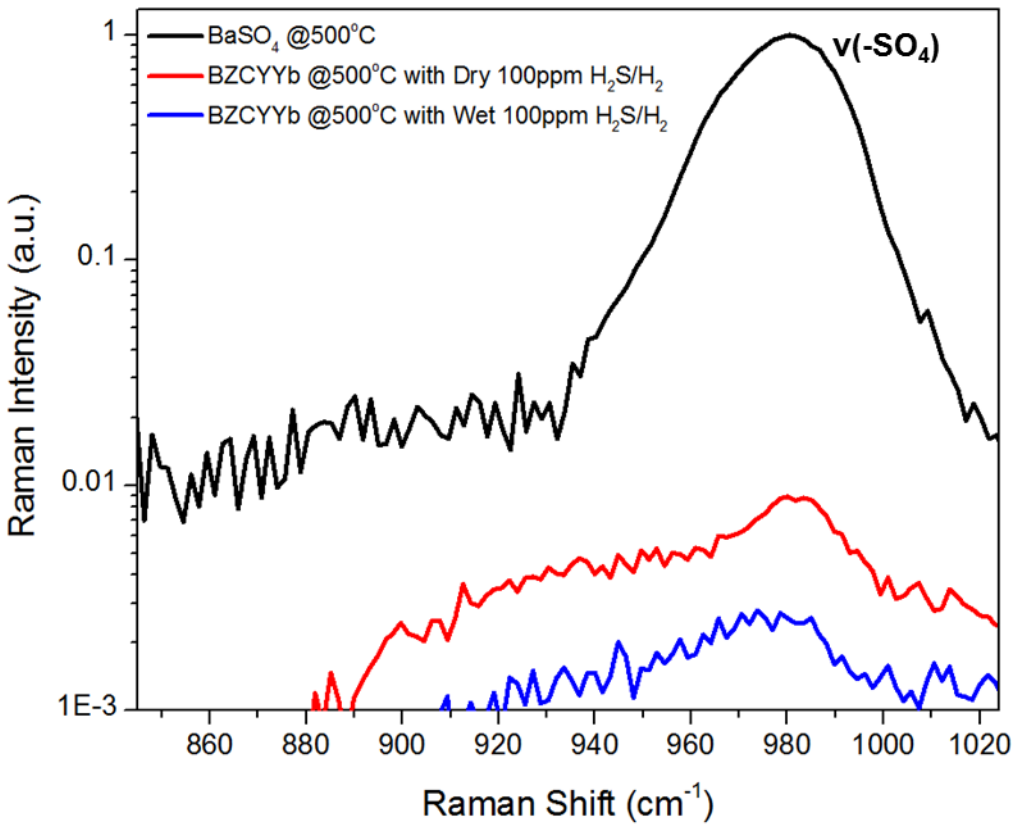

Figure 45. Comparison of v(-SO_4) intensity in pure $BaSO_4$, BZCYYb in Dry H_2S, BZCYYb in wet H_2S.

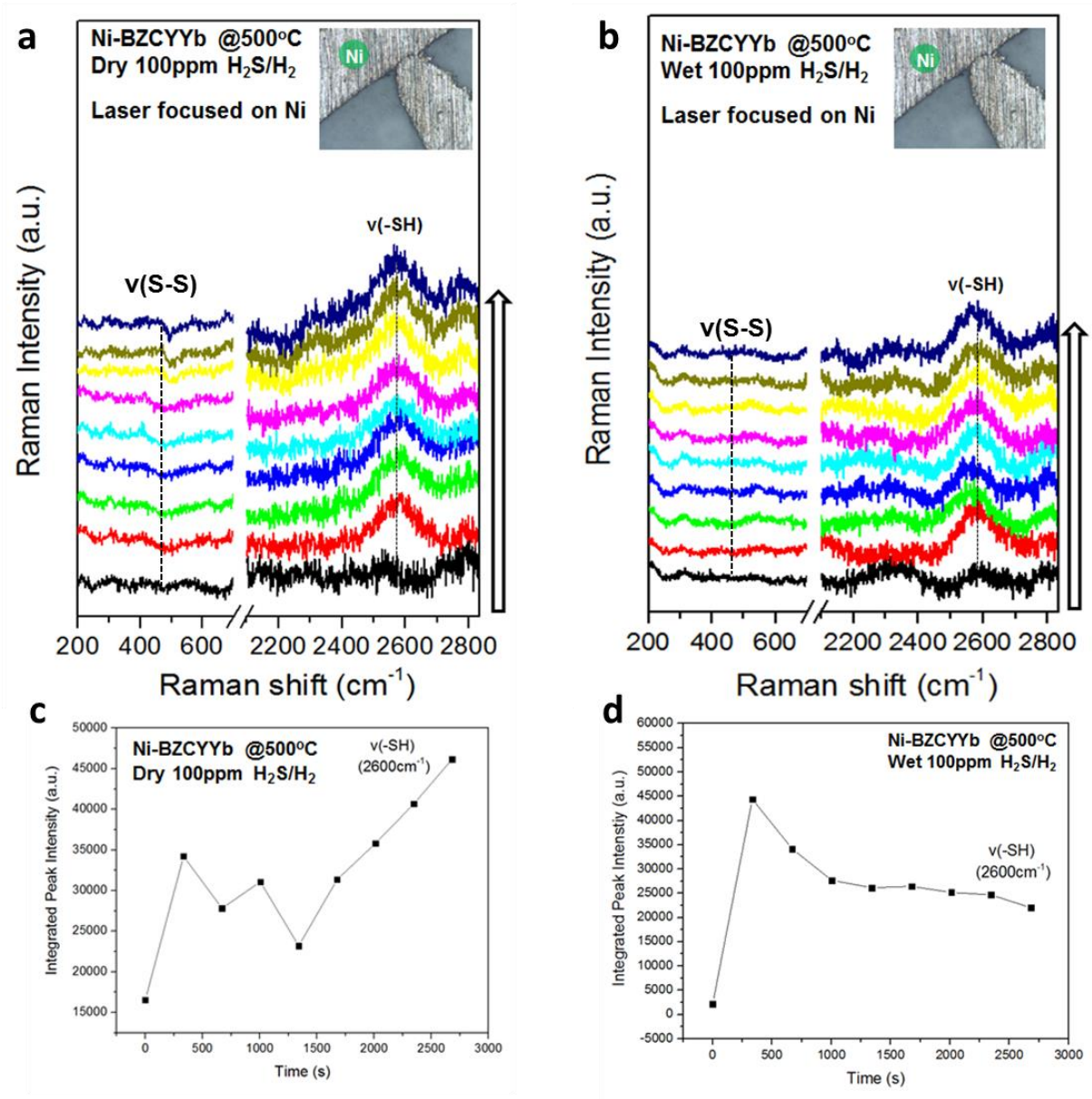

Figure 46. *In situ* SERS analysis of Ni-BZCYYb model electrode upon exposure to **(a)** dry and **(b)** wet 100ppm H_2S/H_2 at 500°C. Laser was focused on Ni surface. **(c), (d)** Integrated peak intensities of key spectral features as function of time for dry and wet respectively.

To investigate the reaction on the Ni surface, the Raman laser was focused on Ni of model electrode. Figure 46**(a)** shows *in situ* Raman spectroscopic evolution when Dry 100ppm H_2S/H_2 was introduced at 500^oC. Slight hump on ~460cm^{-1} may attribute to v(S-S) formation, which is sign of sulfur accumulation on Ni. In higher vibrational region, v(-SH) was found at ~2600cm^{-1}[64-66]. It has been hypothesized by previous work[1] that Ni can be an active metal to dissociate H_2S into S*. The elemental step of H_2S dissociation reaction on Ni may be proposed as follows:

$H_2S \rightarrow H_2S^*$ (1)

$H_2S^* \rightarrow SH^* + H^*$ (2)

$SH^* \rightarrow S^* + H^*$ (3)

Therefore, Raman evolution of v(-SH) could be corresponds to H_2S^* or –SH* on Ni metal surface. Integrated Peak intensity shown in Figure 46**(c)** shows v(-SH) intensity increases over time, indicating –SH is aggregating on Ni surface.

Same experiment was repeated with 3v% water introduced. *In situ* Raman spectroscopic evolution of wet 100ppm H_2S/H_2 at 500^oC is shown in Figure 46**(b)**. There was no specific sign of v(S-S) formation. However, v(-SH) was also found ~2600cm^{-1}. It is very likely H_2S dissociation on Ni does not have great effect upon water presence in the system. The elemental reaction of H_2S dissociation is proposed as above. Unlike dry atmosphere, v(-SH) does not increase over time. Rather, it decreases over time (Figure

46**(d)**). It seems water facilitates the sulfate dissociation reaction so that there are no accumulation of v(-SH) is found on Ni.

To gain reaction information happening on Ni-BZCYYb interface, Raman laser was focused on interface of model electrode. Figure 47**(a)** shows *in situ* Raman spectroscopic evolution. As dry 100 ppm H_2S/H_2 is introduced to the system, surface $-SO_4$ functional group developed in ~480s and it was replaced to S_n^{2-} (n=4~8) [101-104]. As predicted, sulfur deposition on TPB area is proven by *in situ* Raman spectroscopy.

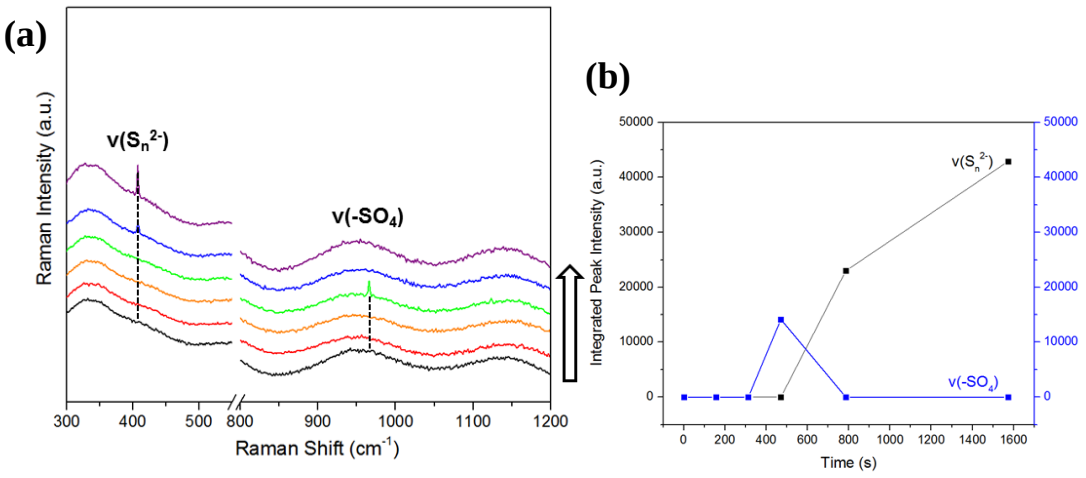

Figure 47. **(a)** *In situ* SERS analysis of Ni-BZCYYb model electrode upon exposure to dry 100ppm H_2S/H_2 at 500°C. Laser was focused on Ni-BZCYYb interface. **(b)** Integrated peak intensities of key spectral features as function of time.

Similarly, to gain information on the reaction on Ni-BZCYYb interface when wet atmosphere is introduced with sulfur, Raman laser was focused on interface of model

electrode. Figure 48**(a)** shows *in situ* Raman spectroscopic evolution of HSO_4^-, –OH, and H_2O^*.

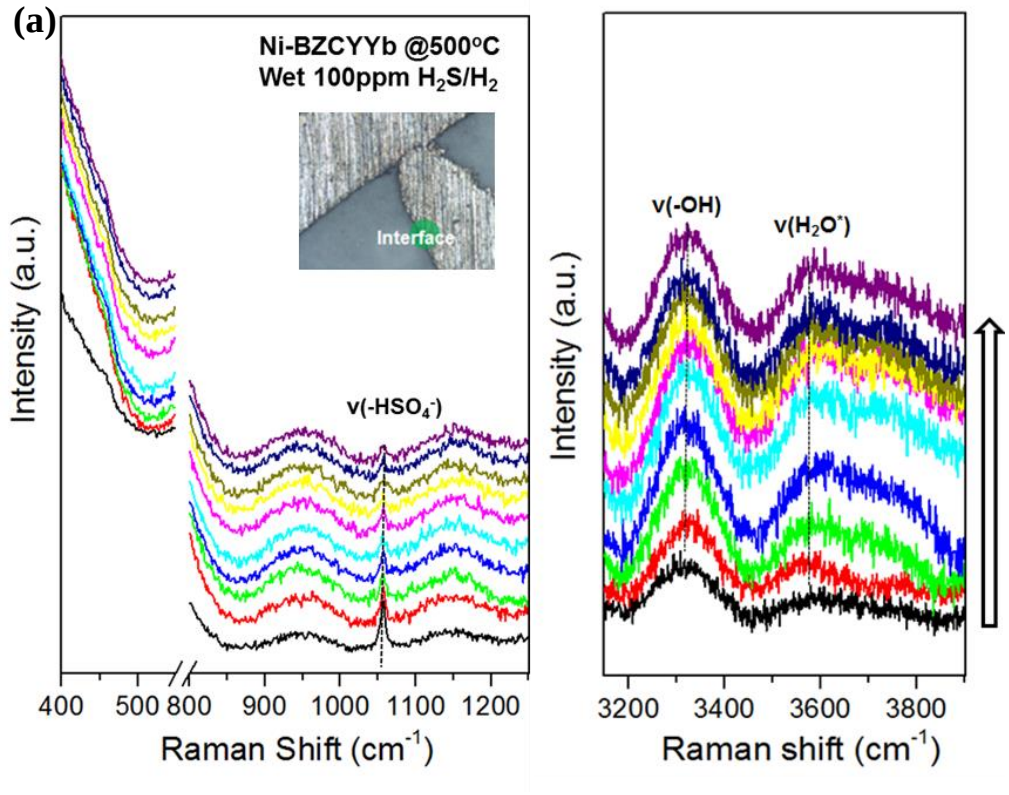

(b)

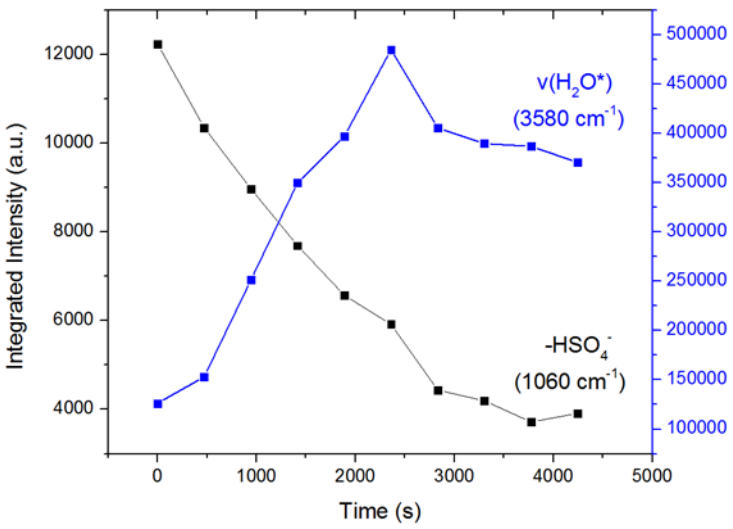

Figure 48. **(a)** *In situ* SERS analysis of Ni-BZCYYb model electrode upon exposure to wet 100ppm H_2S/H_2 at 500°C. Laser was focused on Ni-BZCYYb interface. **(b)** Integrated peak intensities of key spectral features as function of time.

(a)

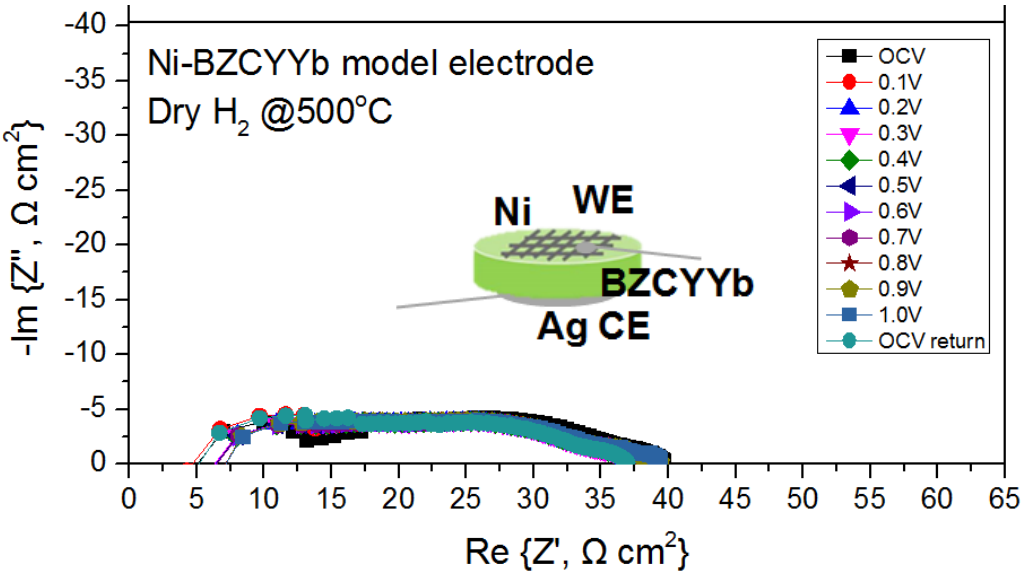

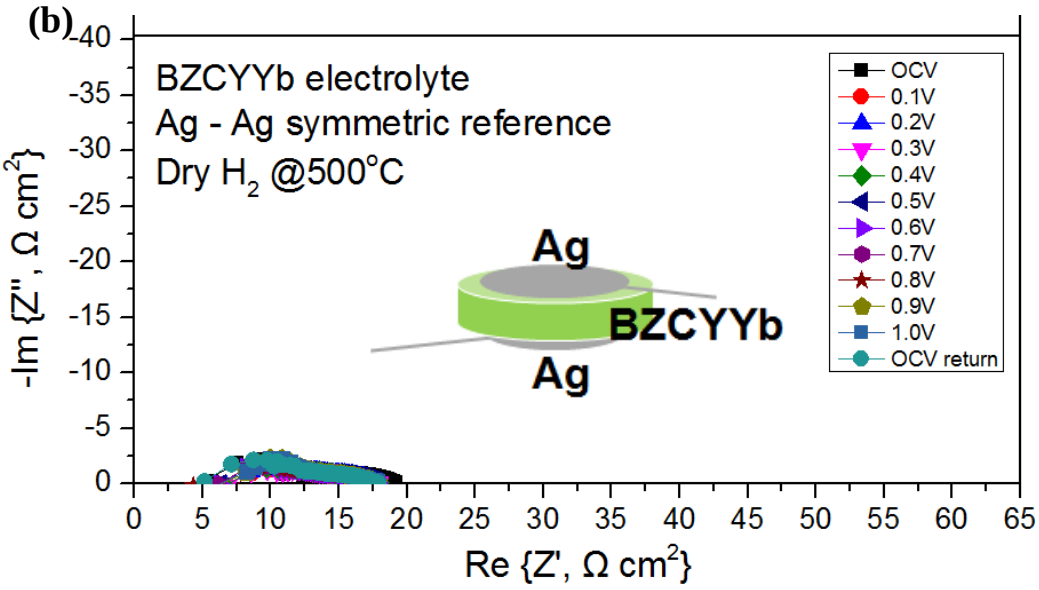

Figure 49. **(a)** Electrochemical impedance spectra of a Ni-BZCYYb model electrode measured in Dry H_2 with different anodic bias at 500°C. Counter electrode of Ag is used. **(b)** Comparison of Electrochemical impedance spectra when both electrodes are Ag.

EIS profile from OCV to 1.0V is measured in Dry H_2 at 500°C. While Ni-BZCYYb side is connected as working electrode (WE), the other side is brush-painted with Ag paste to perform as counter electrode (CE). For the reference, Ag-Ag symmetric cell with BZCYYb electrolyte with same thickness is tested in same condition. Note that Ag electrode R_p should be half of the arc (~7.36Ω) shown in Figure 49**(b)**, since it is in symmetric configuration. By EIS testing, it can be hypothesized that high frequency arc is from Ag electrode (CE), and Low frequency arc is due to Ni-BZCYYb electrode. Since Ag electrode resistance is relatively smaller than Ni-BZCYYb side (~35.2Ω), it can safely be assumed that major resistance change should come from Ni-BZCYYb (WE) side. Despite of applying anodic bias, polarization resistance (R_p) in H_2 does not change

much. There can be two reasons to explain this phenomenon. Firstly, there is no oxygen partial pressure between WE and CE, therefore applying different voltage does not give significant change of oxygen profile in BZCYYb electrolyte. Secondly, due to small TPB area, the variation of resistance can be trivial.

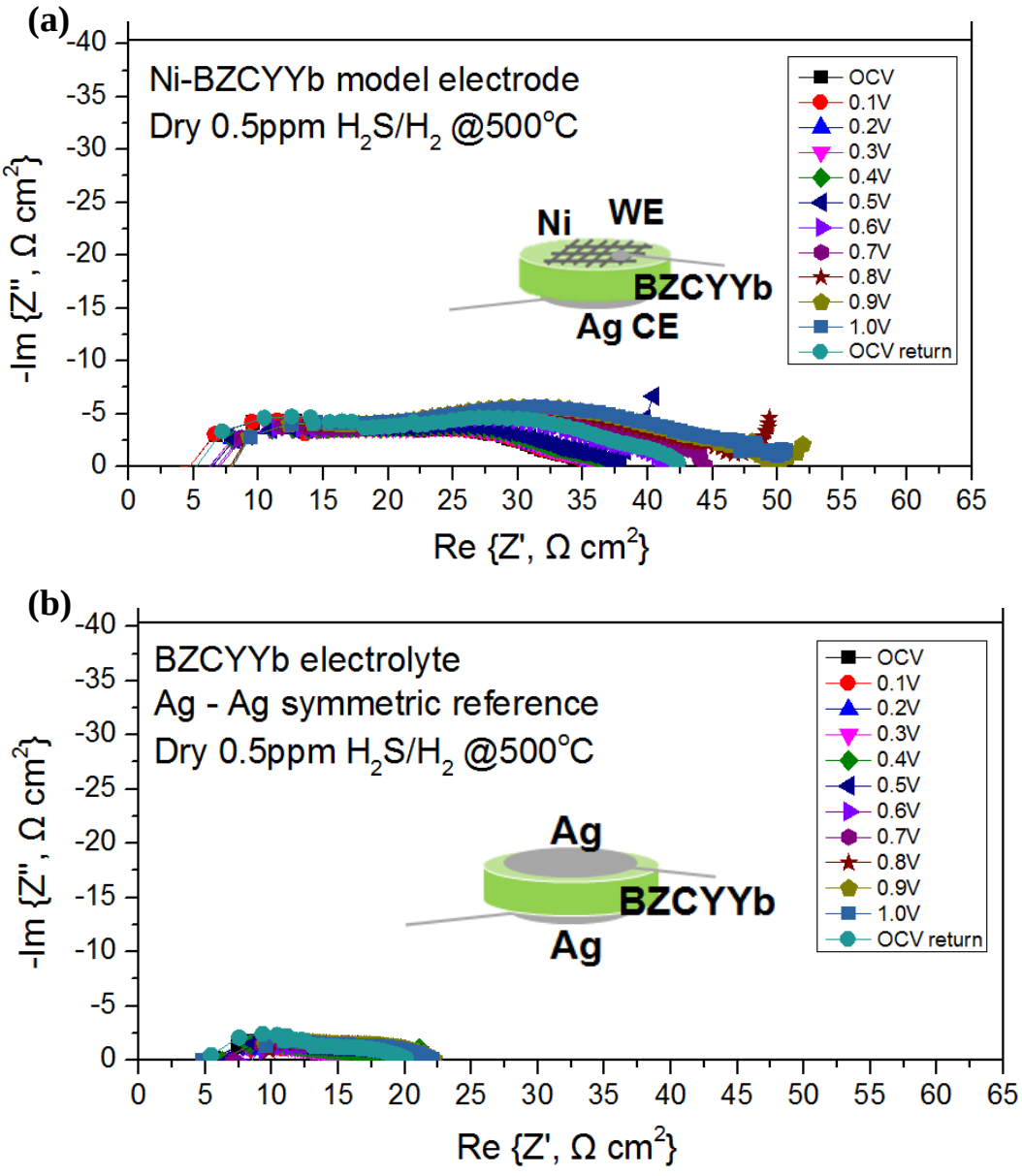

Figure 50. **(a)** Electrochemical impedance spectra of a Ni-BZCYYb model electrode measured in Dry 0.5ppm H_2S/H_2 with different anodic bias at 500°C. Counter electrode

of Ag is used. **(b)** Comparison of Electrochemical impedance spectra when both electrodes are Ag.

Then gas is switched with Dry 0.5ppm H_2S/H_2 to track the R_p change of model electrode. Similarly, EIS profile from OCV to 1.0V is measured at 500^oC (Figure 50).

Unlike in pure H_2, Ni-BZCYYb model electrode R_p increases as Anodic Bias applies in dry H_2S condition. When 1.0V of DC bias is applied, R_{total} increases to 51.2Ω (OCV: ~35.2 Ω). On the other hand, Ag reference cell R_p does not change a lot, suggesting main resistance increase is responsible of Ni-BZCYYb WE. Note that Ag electrode R_p should be half of the arc shown in Figure 50**(b)**, since it is in symmetric configuration.

By EIS testing, it can be concluded that sulfur poisoning is deeply related with the voltage applied to the cell.

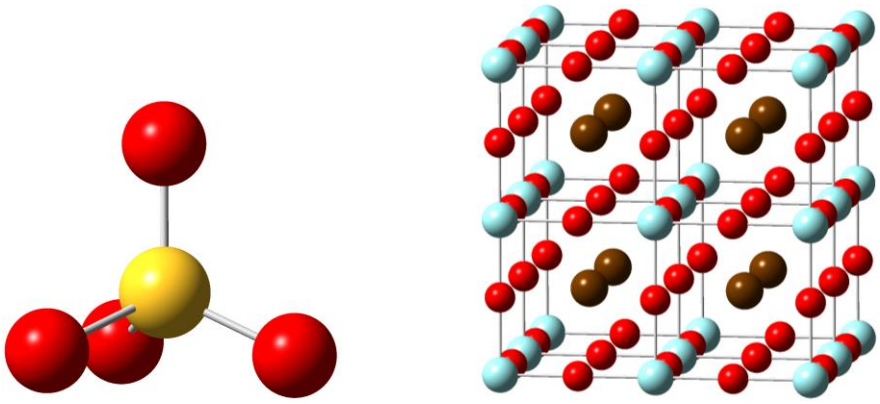

Figure 51. Molecular representation of SO_4^{2-} and $BaZrO_3$ used in computational modeling.

Table 6. Geometrical illustration of SO_4 on $BaZrO_3$ to find most stable adsorption site. The cyan, green, red, yellow and white spheres are represented as Zr, Ba, O, S and H atoms, respectively.

SO_4			
	1o-binding on b-site	**1o-binding on active-o-site** **(most stable adsorption)**	1o-binding on crystal-o-site

side-view	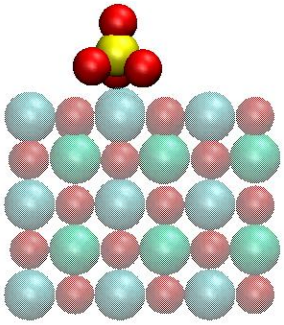	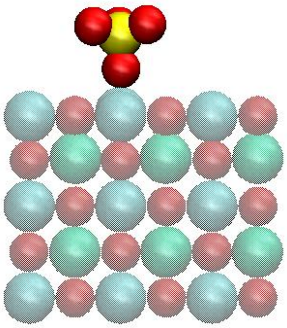	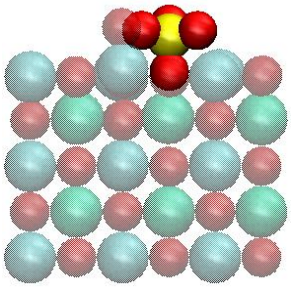
top-view	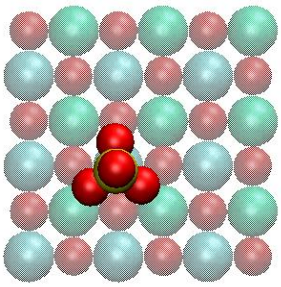	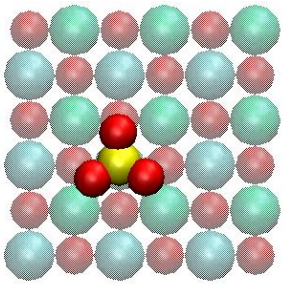	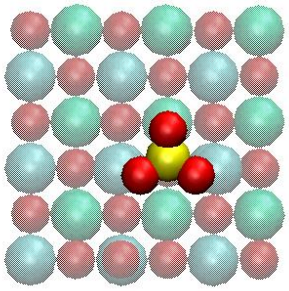
E_{total}	-1012.12	-1012.60	-1012.58
	2o-binding in Td form	3o-binding	4o-binding(so3-like)
side-view	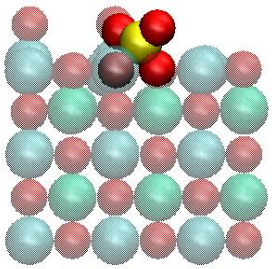	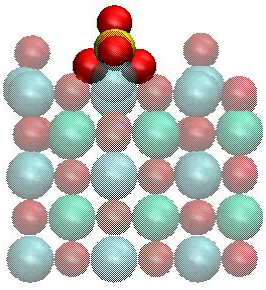	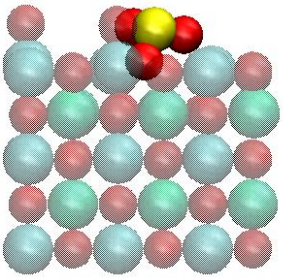

top-view	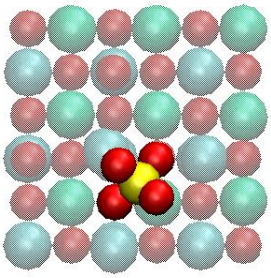	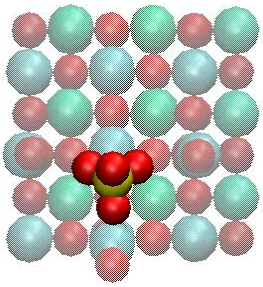	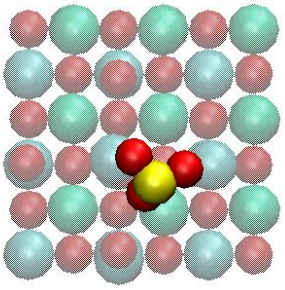
E_{total}	-1006.88	-1005.40	-1007.55

Table 7. Geometrical illustration of H_2S on $BaZrO_3$ to find most stable adsorption site. The cyan, green, red, yellow and white spheres are represented as Zr, Ba, O, S and H atoms, respectively.

H_2S			
	on b-site	**on active-o-site** **(most stable adsorption)**	on crystal-o-site
side-view	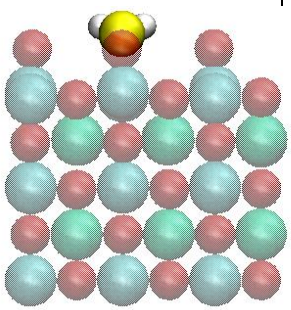	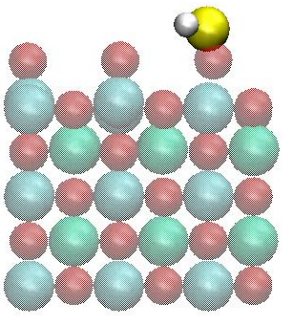	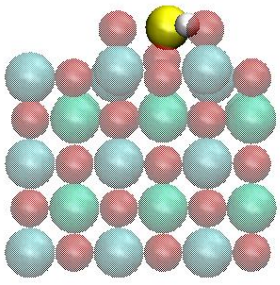

top-view	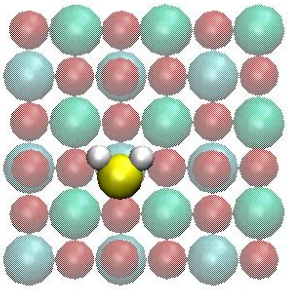	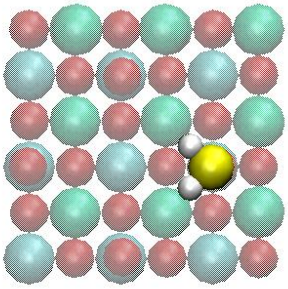	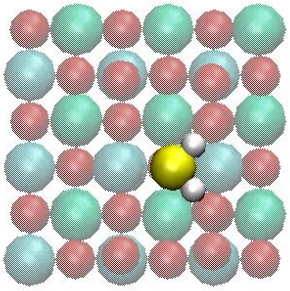
Etotal	-1009.05	-1011.43	-1009.29
	on active-o-site in dissociative form		
side-view	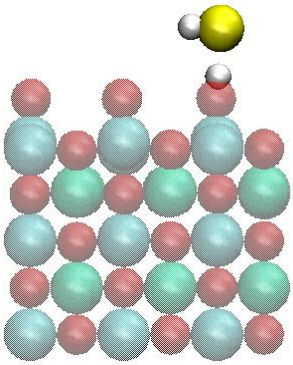		
top-view	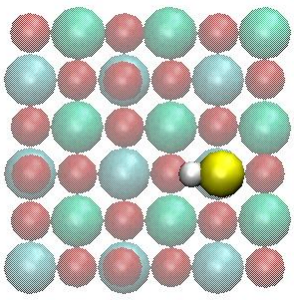		

Etotal	-1009.71		

Oxidation reaction forming SO_4:

Steps	BZO ΔE (eV)	doping Y ΔE (eV)	doping Yb ΔE (eV)
R1: $H_2S_{(g)} + O_O \rightarrow H_2SO_O$	-3.57	-3.94	-3.83
R2: $H_2SO_O + O_O \rightarrow HSO_O + HO_O$	-2.31	-2.26	-1.87
R3: $HSO_O + HO_O \rightarrow SO_O + H_2O_O$	-1.18	-1.54	-2.04
R3': $SO_O + H_2O_o \rightarrow SO_o + V_O + H_2O_{(g)}$	0.77	1.33	1.15
R4: $SO_O + O_O \rightarrow OSO_O + V_O$	-4.96	-4.59	-3.91
R4': $OSO_O \rightarrow SO_{2(g)} + V_O$	0.59	0.58	-0.09
R5: $OSO_O + O_O \rightarrow O_2SO_O + V_O$	-2.22	-2.22	-2.83
R6: $O_2SO_O + O_O \rightarrow O_3SO_O + V_O$	-1.86	-2.01	-1.72
R6': $O_3SO_O + H_2O_O \rightarrow O_3SO_O + H_2O_{(g)}$	1.03	1.26	1.58
ΔE for total oxidation reaction	-15.06	-15.31	-14.62

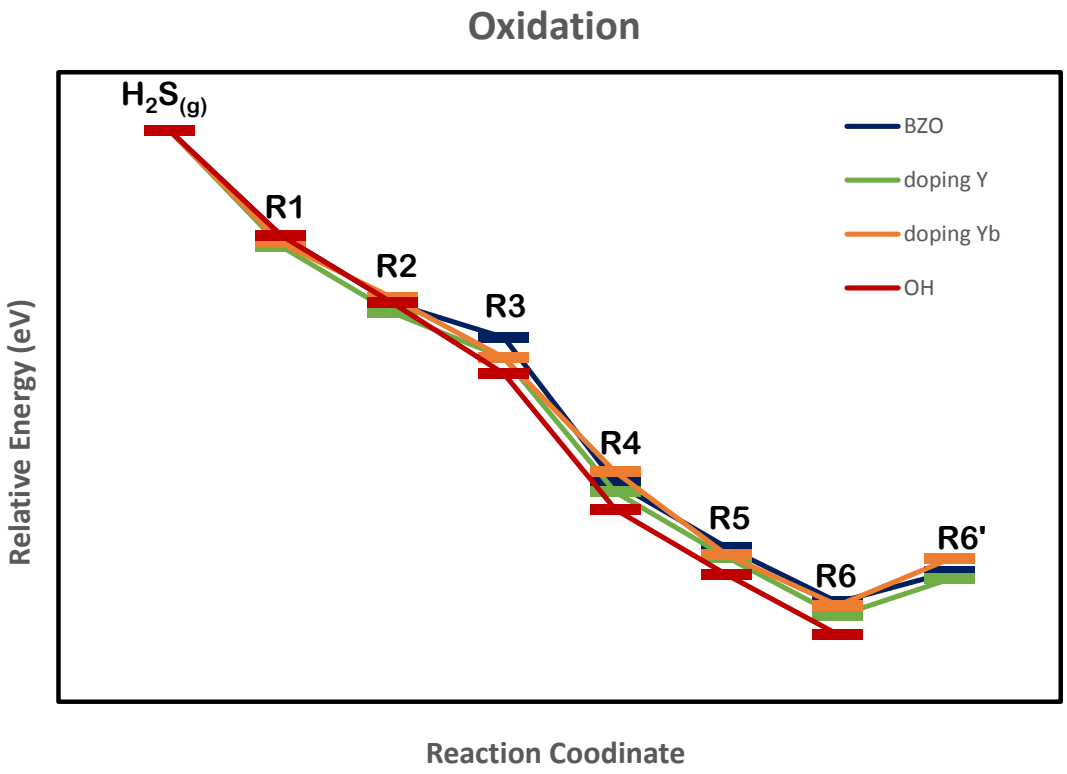

Figure 52. PES and the related structures of intermediate states in each step for the oxidation (poisoning) process of $H_2S_{(g)} + 6O^{2-}{}_{(b)} \rightarrow SO_4{}^{2-}{}_{(b)} + 2OH^-{}_{(b)} + 8e^-$ on Y or Yb doped $BaZrO_3$.

Reduction reaction for SO_4 removing

Steps	BZO ΔE (eV)	doping Y ΔE (eV)	doping Yb ΔE (eV)
R7: $O_3SO_O + V_O + H_2O_{(g)} \rightarrow O_3SO_O + H_2O_O$	-1.02	-0.94	-0.99
R8: $O_3SO_O + H_2O_O \rightarrow HO_3SO_O + HO_O$	-0.09	-0.07	0.13
R9: $HO_3SO_O + V_O \rightarrow O_2SO_O + HO_O$	1.32	1.30	1.16
R9': $O_2SO_O \rightarrow O_O + SO_{2(g)}$	2.38	3.09	2.76
R10: $O_2SO_O + V_O + H_2O_{(g)} \rightarrow O_2SO_O + H_2O_O$	-0.79	-0.74	-0.71
R11: $O_2SO_O + H_2O_O \rightarrow HO_2SO_O + HO_O$	0.72	0.81	0.88
R12: $HO_2SO_O + V_O \rightarrow OSO_O + HO_O$	0.20	0.19	0.11
R13: $OSO_O \rightarrow SO_{2(g)} + V_O$	0.44	0.40	0.32
R9": $O_2SO_O + HO_O \rightarrow HO_2SO_O + O_O$	1.84	1.92	1.99
R10": $HO_2SO_O \rightarrow OSO_O + HO_O$	0.27	0.25	0.18
ΔE for total reduction reaction	**0.79**	**0.95**	**0.64**

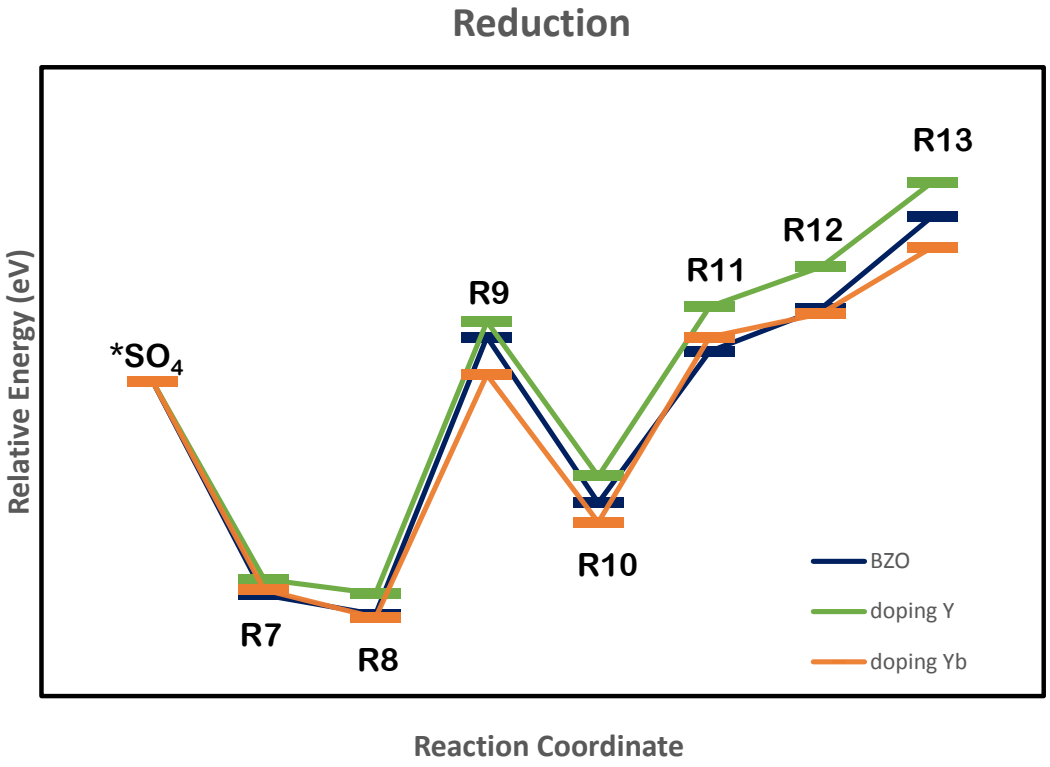

Figure 53. PES and the related structures of intermediate states in each step for the reduction ($SO_4^{2-}{}_{(b)}$ removal) process of $SO_4^{2-}{}_{(b)} + 2H_2O_{(g)} + 2e^- \rightarrow SO_{2(g)} + 4OH^-{}_{(b)}$ on Y or Yb doped $BaZrO_3$.

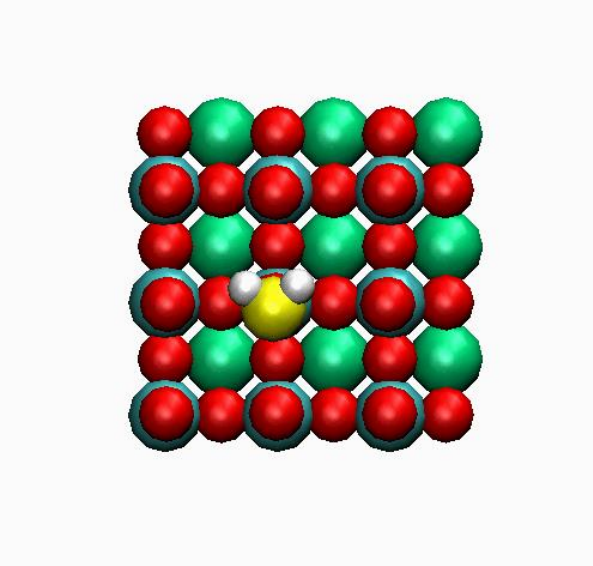

Figure 54. Animation for oxidation ($SO_4^{2-}{}_{(b)}$ formation) process of $H_2S_{(g)} + 6O^{2-}{}_{(b)} \rightarrow SO_4^{2-}{}_{(b)} + 2OH^-{}_{(b)} + 8e^-$

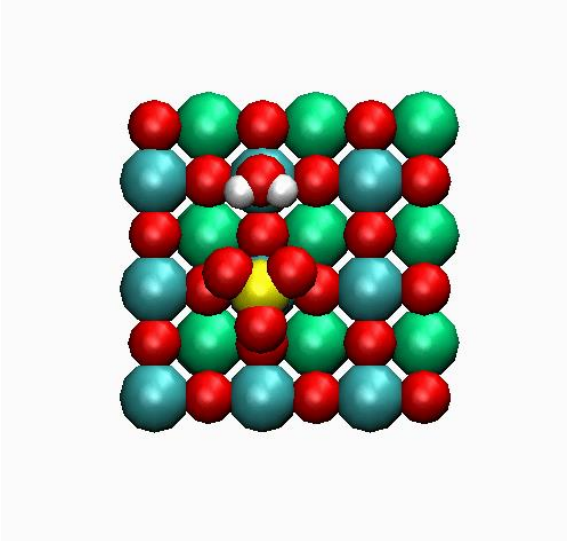

Figure 55. Animation for reduction (water-mediated $SO_4^{2-}{}_{(b)}$ removal) process of $SO_4^{2-}{}_{(b)} + 2H_2O_{(g)} + 2e^- \rightarrow SO_{2(g)} + 4OH^-{}_{(b)}$

CHAPTER 5. UNRAVELING ENHANCED OXYGEN REDUCTION REACTION MECHANISM ON DOUBLE PEROVSKITE INDUCED BY WATER-ASSISTED SURFACE MODIFICATIONS

5.1 Introduction

The demand for clean energy technologies is growing rapidly owing to the depletion of fossil fuels and global warming. The oxygen reduction reaction (ORR) is one of key reactions in developing novel high-efficiency renewable energy conversion approaches,[105-107] while its sluggish kinetics in solid oxide fuel cells (SOFCs) has been a grand challenge. Accordingly, cost-effective and high-efficient ORR cathode materials in SOFCs have been widely studied, aiming for commercialization.[19,108] It is imperative to clearly understand related mechanisms for rational design of novel energy materials. To date, perovskite-structured materials have received significant attention because of the high catalytic activity toward the ORR and the easy tuning of materials chemical properties by varying dopants.[109] However, one of the major problems of these transition-metal oxides is their low stability under SOFC operating conditions.[5,110-112] For example, lanthanum strontium cobalt ferrite (LSCF) is known to be one of the best SOFC cathode materials since its e_g filling is close to 1,[107] while its ORR activity is easily affected by water in air.[113-115] In addition to the ORR activity, the high stability in humid air is crucial for the commercial viability of SOFCs. Double perovskites ($AA'B_2O_{5+d}$) have

been known as a promising substitute for pseudocubic perovskites[108,116] in terms of the excellent ORR activity and stability. Moreover, it is known that double perovskites have a superior diffusivity and a surface exchange coefficient compared to ABO_3 perovskites[117-119]. It is also reported that $PrBaCo_2O_{5+d}$ exhibits the enhanced ORR activity by increasing the water vapor pressure,[120] proposing the bulk diffusion of proton into the structure.[79] However, its detail is unavailable in the literature, and the ORR mechanism augmented by the water promotion is veiled. Also, it is reported that Ca-doped double perovskite $NdBa_{1-x}Ca_xCo_2O_{5+d}$ could have the astoundingly extended stability due to Ca's perfect size match with the host cations, as well as the excellent ORR performance owing to the increased electron affinity of mobile oxygen species with Ca.[118] Therefore, we rationally design $PrBa_{0.8}Ca_{0.2}Co_2O_{5+d}$ (PBCC) that has the enhanced ORR activity by the water promotion along with an exceptional stability. Furthermore, the ORR mechanism has been carefully elucidated by using *in situ* Raman spectroscopy in conjunction with the independent electrochemical impedance spectroscopy (EIS). The comprehensive study demonstrated in this work can support the fundamental understanding of the water-assisted ORR at high temperature, leading to an advanced design of SOFC cathode materials.

5.2 Water-promoted Oxygen Reduction Reaction Activity of PBCC electrodes

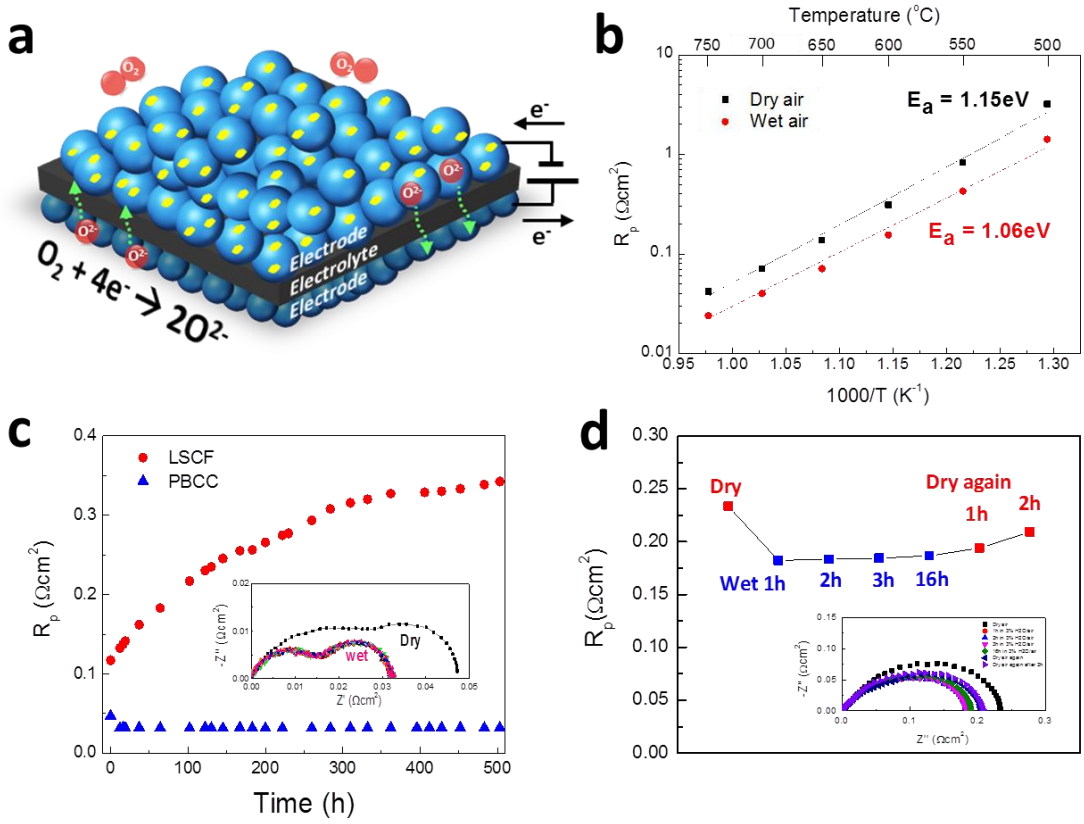

Figure 56. **Electrochemical performance of PBCC** (a) Schematics of a PBCC/SDC/PBCC symmetric cell (b) Temperature dependence of polarization resistance of PBCC electrode in Dry/Wet (3v% H_2O) air (c) Long-term stability of PBCC electrode in wet air compared with LSCF electrode at 750°C. (inset) Electrochemical impedance spectroscopy of PBCC electrode. Polarization of cell has dramatically decreased upon water exposure (d) Polarization resistance of PBCC electrode by switching atmosphere between Dry/ Wet air at 600°C.

The impedance spectra for symmetric cells are measured in order to elucidate the electrocatalytic activity for the ORR by using AC impedance spectroscopy at various

temperatures in air as shown in Figure 56. The behavior of impedance at the high and intermediate frequencies are related to ion and electron transfer at the electrode, electrolyte, and collector/electrode interfaces, while that at the low frequency is associated with non-charge transfer, such as oxygen surface exchange and gas-phase diffusion inside and outside of the porous PBCC electrode.[108] Moreover, the large population of mobile oxygen vacancies may contribute to enhanced oxygen kinetics associated with the oxygen bulk diffusion and the surface exchange. The area specific resistance (ASR) of PBCC is only 0.030-0.040 $\Omega\,cm^2$ at 750 ^oC in air and 3 vol% H_2O/air. The polarization resistance (R_p) of the PBCC symmetric cell is quickly reduced as wet air is introduced to the system. At 750 ^oC, R_p of the PBCC cathode under humid air (0.032 $\Omega\,cm^2$) is almost 4-fold lower than that of the LSCF cathode which shows a constant degradation over time (0.12 $\Omega\,cm^2$ to 0.34 $\Omega\,cm^2$) (Figure 56(c)). The activation energy of PBCC electrodes in wet air is lower than in dry air (1.06 eV versus 1.15 eV), indicating a faster ORR surface kinetics by adding water. Similar to the considerably low proton conductivity of the samarium-doped-ceria (SDC) electrolyte,[121] the reduction of R_p by water addition may be related to the intrinsic property of PBCC electrodes. Further, unlike ABO_3-structured perovskite oxides (e.g., LSCF), PBCC exhibits the excellent stability for 500 hours when exposed to a water-containing atmosphere. To identify if the electrochemical performance of PBCC is purely driven by water, the gas environment is switched to dry air, resulting in the increase in R_p (Figure 56(d)). Then the PBCC symmetric cell is measured under the various water vapor pressures (i.e., dry and 3 vol%, 10 vol%, and 20 vol% H_2O). The R_p in 3 vol% and 10 vol% H_2O shows a far better

performance than that in 20 vol% and dry air (Figure 64). We found that PBCC's ORR activities are highly augmented by the water addition.

5.3 Microstructure of Multi-phase Catalyst Coating on Wet Annealed PBCC

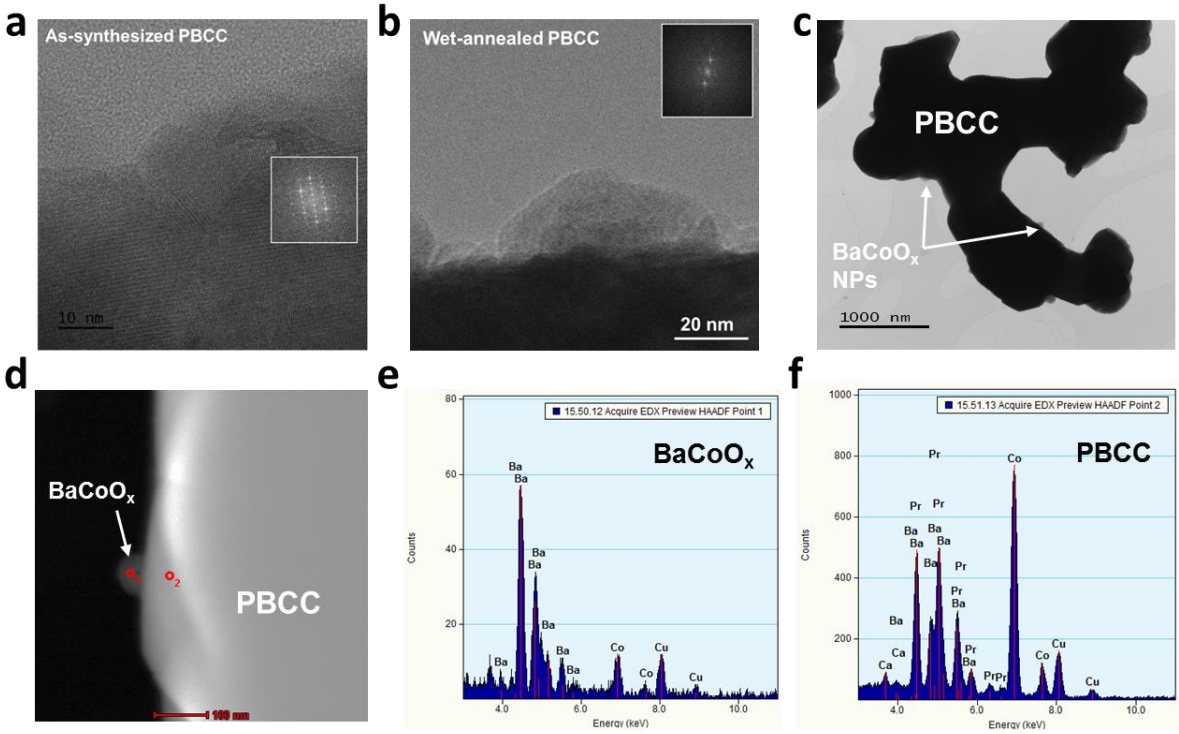

Figure 57. **Morphology of wet annealed PBCC** (a) HRTEM image of As-synthesized PBCC (inset) FFT pattern shows super lattice confirms double perovskite structure (b) HRTEM image of PBCC, annealed in 3v% H_2O at 600^{o}C for 3 hours (c) TEM image of wet annealed PBCC power (d) HADDF image of PBCC with $BaCoO_x$ NPs exsolution on surface (e) EDX data of HADDF point 1 confirms $BaCoO_x$, (f) EDX data of HADDF point 2 confirms PBCC.

To understand the water-promoted ORR kinetics, it is necessary to look into morphology of wet annealed PBCC surfaces. Shown in Figure 57(a) is a high-resolution transmission electron microscopy (HRTEM) image of as-synthesized PBCC. The fast Fourier transform (FFT) pattern shows a super-lattice that confirms the double perovskite structure of PBCC. While there is no observable surface decoration in the as-synthesized sample, high-angle annular dark-field scanning transmission electron microscopy (HAADF-STEM) image of wet-annealed PBCC demonstrates multi-phase surfaces composed of nanoparticles (NPs) (Figure 57(d)). The energy-dispersive X-ray spectroscopy (EDX) analysis confirms that $BaCoO_x$ (BCO) NPs are formed on bulk PBCC and produces heterogeneous surfaces (Figure 57(e), (f)). It is known that perovskites' catalytic activities can be improved by controlling the cation segregation level.[114] The co-exsolution on $PrBaCo_2O_{6-\delta}$ can readily happen by changing oxygen partial pressure[122], and the formation of multi-phase catalyst coating with BCO NP is reported by using PBCC thin films.[108] The BCO NPs can dramatically enhance the ORR catalytic activity with a preferentially high O_2 uptake capability.[108] The surface morphology analyses performed by TEM suggest that H_2O vapor introduction on PBCC electrodes can induce the *in situ* formation of multi-phase catalyst coating of BCO NPs which lead to enhanced ORR kinetics. H_2O decorated NPs on PBCC can further be confirmed by scanning electron microscopy (SEM) images (Figure 68), and more NPs can be formed by introducing of a higher vapor pressure of H_2O, turning the PBCC surface into more heterogeneous surfaces and resulting in higher ORR activities.

5.4 *In Situ/Operando* Raman Spectroscopy

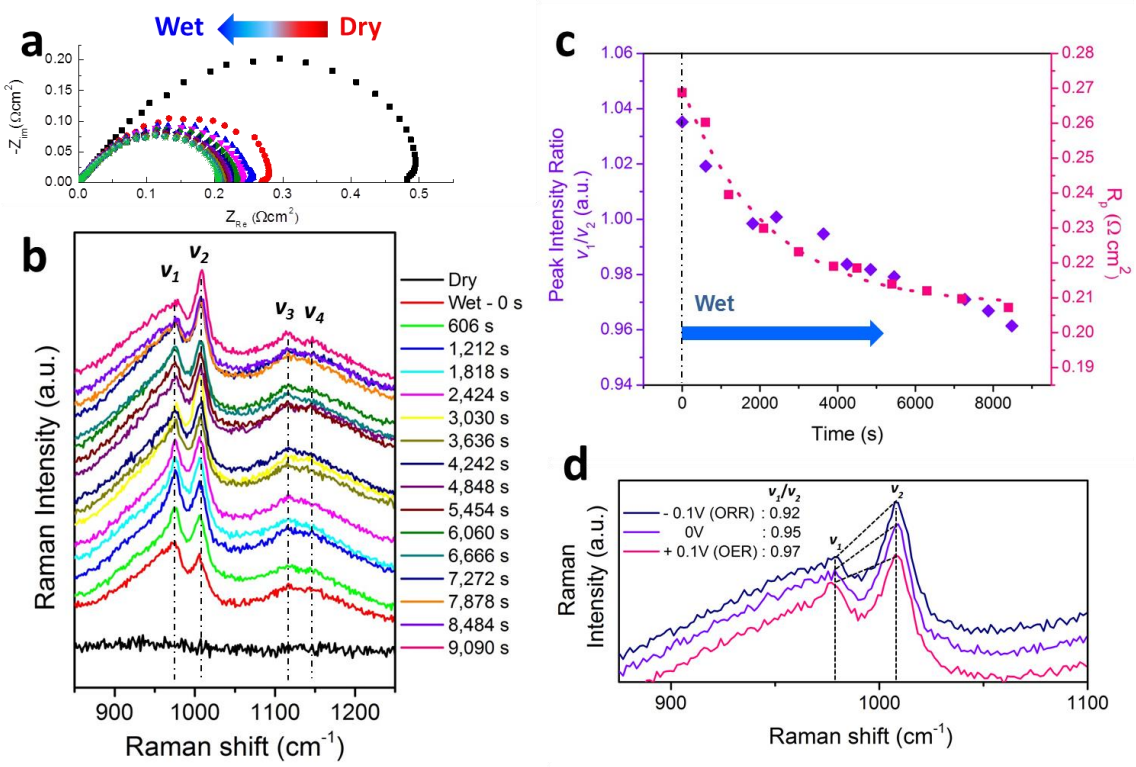

Figure 58. **Unraveling surface chemistry of PBCC in wet air** (a) Electrochemical impedance spectroscopy (EIS) of PBCC symmetric cell in wet air condition (3v% H_2O/air) at 600°C (b) *In situ* Raman spectroscopic evolution of PBCC surface in wet air condition (3v% H_2O/air) at 600°C. Upon water exposure various oxygen species are found on surface which supports enhanced ORR activity (c) A quantitative correlation between key features (v_1/v_2) of *in situ* Raman spectrum and polarization resistance of PBCC symmetric cell. (d) *Operando* Raman spectroscopic evolution under electric bias.

Table 8. Summary of Raman peaks under wet and dry conditions and their characteristics.

c	condition		characteristics
	under wet air	under dry air[1]	
v_1	977 cm^{-1}	958 cm^{-1}	surface hydroxyl species
v_2	1,006 cm^{-1}	–	Superoxo
v_3	1,114 cm^{-1}	1,129 cm^{-1}	Superoxo
v_4	1,148 cm^{-1}	–	Superoxo

1. The gas environment was changed from wet air to dry air.

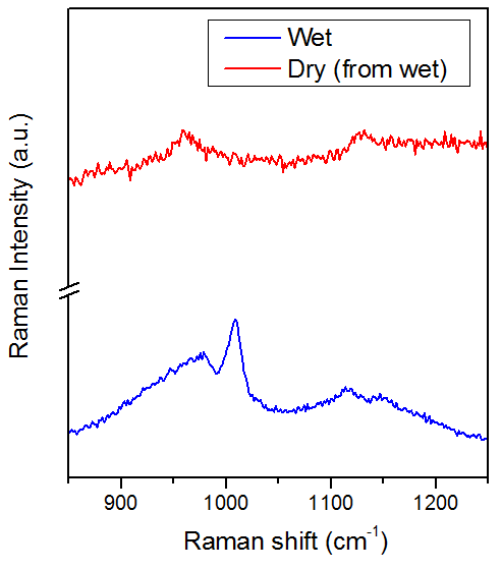

Figure 59. Comparison of Raman spectroscopy of PBCC surface from wet to dry air condition.

As discussed, more effective BCO NP formations on PBCC by water can enhance the ORR kinetics. However, the water-promotion mechanism may not be fully explored only with the electrochemical approach as we observed that water addition itself can alter the R_p. As well known, to understand the dynamics of enhanced ORR processes by unraveling crucial adsorbed surface species under operating conditions and correlating with the electrochemical data, a comprehensive study on electrode surfaces is an essential step.[19] Thus in this study, the water-promoted ORR mechanism was further elucidated by means of *in situ* time-resolved Raman spectroscopy which accurately detects surface oxygen species (*i.e.*, superoxo (O_2^-) and peroxo (O_2^{2-}) species).[123,124] Then, the information about surface chemistry obtained using Raman spectroscopy will be carefully correlated with the electrochemical performance measured by EIS. In this regard, a porous PBCC symmetric cell with a SDC electrolyte is prepared to examine the water-promoting effect at 600^{o}C. As shown in Figure 58(a), the R_p of the cell is quickly reduced as wet air is introduced to the system. To synchronize with EIS, Raman spectra were measured every 10 minutes, and the *in situ* spectroscopic evolution of the PBCC electrode surface is displayed in Figure 58(b). Since the space group of PBCC belongs to P4/mmm, it has little Raman activity,[125] so that no specific bands appear under dry conditions. On the other hand, switching to wet air reveals various surface species (*i.e.*, hydroxyl and oxygen species). In this study, we, thus, investigate the combined effect of hydroxyl and oxygen species to explain the water-promoted enhancement of the ORR. As mentioned, although computational studies are available on ABO_3-structured perovskites[126,127], *in situ* Raman spectroscopic measurements for the ORR on double perovskite PBCC at high temperature have not been reported in the literature. For

example, predicted vibrational frequencies of molecularly adsorbed peroxo species are ranged from 875 cm^{-1} to 1002 cm^{-1}, while those of superoxo species are ranged from 1,013 to 1,292 cm^{-1}.[2,126-131] It is worth noting that surface superoxo species can be elongated by nearby proton to form hydrogen bonding which eventually causes redshift in vibrational frequency.[124] Also, chemisorbed oxygen species on an oxygen vacancy site can produce superoxo and peroxo species[132,133] with lower frequencies than those molecularly adsorbed ones (1,556 cm^{-1}). However, as mentioned, those Raman peaks appeared after the water addition may be mixed with hydroxyl and oxygen species since the PBCC cathode surface efficiently dissociates water ($H_2O \rightarrow H + OH$). As demonstrated, the water addition can lower the activation energy from 1.15 eV to 1.06 eV, suggesting for a catalytic effect. _ENREF_134_ENREF_135_ENREF_130 The reason of various electronically charged oxygen anion formation on PBCC can be explained that double perovskites are MIEC, and the hotspot for ORR is not confined on the electrolyte-electrode interface[134]. Since the Raman peaks may be mixed with hydroxyl and oxygen species, periodic density functional theory (DFT) calculations will be applied to assign the peaks in the following section. The peak heights of the v_1 and v_2 modes at ~977 cm^{-1} and ~1,006 cm^{-1}, respectively become reversed after 1,800 sec, while the v_3 and v_4 modes at ~1,114 cm^{-1} and ~1,148 cm^{-1}, respectively turn more distinct after 4,050 sec.

Since rate determining species will accumulate as reaction reaches equilibrium, it can be assumed that these two reactants are the major species related to the rate-determining-step (RDS) of water-promoting ORR. Therefore, a relative intensity ratio of the v_1 mode and the v_2 mode is calculated and quantitatively correlated with R_p of the cell

as a function of time. Coupling two different techniques can validate mechanism in most effective way, since values of vibrational properties can be considered as quantitative indication of electrode performance. As shown in Figure 58(c), the peak intensity ratio (v_1/v_2) and R_p shows an excellent correlation. In particular, as the peak intensity ratio reduces, R_p decreases, suggesting the surface species of v_2 may be contribute to a rate-determining step in wet air[107]. Our *in situ* surface characterization strongly supports PBCC's water-promoting effects on the ORR catalytic activity at high temperature similar to that for Pt/CeO_2 .[135,136] To verify if the water addition truly promotes the ORR kinetics of PBCC cathode materials, the gas environment was changed from wet to dry conditions by disconnecting the H_2O vapor (Figure 59). Interestingly, when H_2O is discontinued, great depression of v_2 is found in Raman spectroscopy. Abasement of v_2 implies no further dissociative adsorption of water to form surface hydroxyl is proceed on PBCC surface, and therefore elongated superoxo species induced by hydrogen bonding is no longer persisted on surface.

ORR is multi-step charge transfer reactions accompanied with electrons, therefore, amount of surface oxygen species can be altered by applied cathodic bias[128]. To validate hypothesis, cathodic bias was applied to break equilibrium and the resulting Raman Spectroscopy is shown in Figure 58(d). Cathodic bias surely has impact on surface chemistry, and the peak intensity ratio between v_1/v_2 has varied from 0.97 (OER, 0.1 V anodic bias) to 0.92 (ORR, -0.1 V cathodic bias). Particularly, when cathodic bias of -0.1V is applied, surface has ORR-driven effect and v_2 band intensity gets stronger. When cathodic bias of +0.1V is applied, surface has OER-driven effect and band intensity of v_1 gets stronger.

To ensure that water-promoted oxygen species which we observed with *operando* Raman can only be found on PBCC surface, *operando* Raman of LSCF porous electrode with water is conducted as well at 600 ^{o}C (Figure 69). In this case, LSCF demonstrated a sharp peak at 1,123 cm^{-1} which we believe a super-oxide species[127] in dry condition. However, as water introduced, superoxide decreases over time indicating LSCF does not have capability to process water as fuel. Rather, the presence of water makes oxygen intermediates to disappear on the surface. This is consistent with in situ ^{18}O isotope exchange experiments that they concluded that water and oxygen compete each other for same surface exchange site on LSCF.[113]

5.5 H_2O uptake characteristics of PBCC

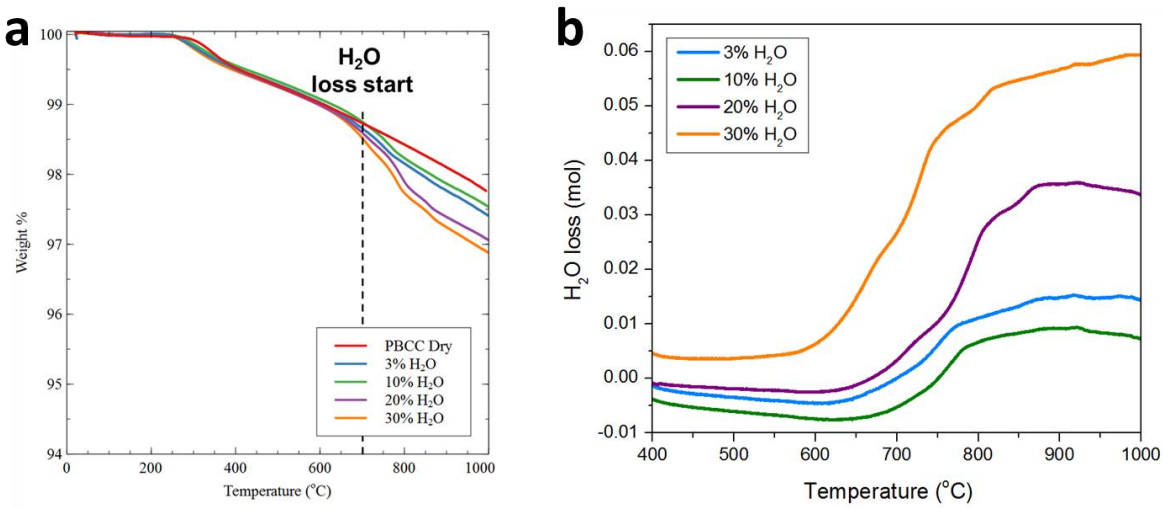

Figure 60. **H_2O uptake behavior of PBCC** (a) Thermogravimetric profiles of PBCC powders exposed to different concentration of water vapor. (b) Calculated amount of inserted H_2O loss in PBCC oxide

To understand water uptake characteristics in PBCC, thermogravimetric analysis (TGA) is conducted (Figure 60). PBCC powder is first calcined at 1100^{o}C to form a single phase, and powder is exposed to various water vapor pressures (pH_2O = 3v%, 10v%, 20v% 30v%) at 600^{o}C for 3 hours. Chemical compatibility of PBCC with H_2O is checked with XRD which is shown in Figure 63(f), and there is no observable bulk phase change. While Dry annealed PBCC does not have a significant oxygen non-stoichiometry change in 400~1000^{o}C, H_2O exposed PBCC shows structural water departure decrease observed around 700^{o}C.[120] From TGA data, the extent of water in PBCC is calculated in Figure 4(b). As increasing water vapor pressure, PBCC can uptake higher amount of water, up to 5.9mol% in 30v% H_2O. The TGA results enable evaluation of thermodynamics of proton insertion in PBCC. The proton insertion mechanism could be hypothesized as followed:

$$\mathbf{H_2O(g) + V_o^{\cdot\cdot} \rightarrow (OH_2)_o^{\cdot\cdot}} \quad \mathbf{(1)}$$

$$\mathbf{(OH_2)_o^{\cdot\cdot} + O_o^{x} \rightarrow 2(OH)_o^{\cdot}} \quad \mathbf{(2)}$$

Reaction 1 refers to water insertion into oxygen vacancy of the PBCC, and reaction 2 shows formation of proton inside of perovskite structure. By combining two equations,

$$\mathbf{H_2O + V_o^{\cdot\cdot} + O_o^{x} \leftrightarrow 2OH_o^{\cdot}}$$

$$K_w = \frac{\left[OH_o^{\cdot}\right]^2}{pH_2O\left[V_o^{\cdot\cdot}\right]\left[O_o^x\right]} = exp[-\frac{\Delta H}{R}\left(\frac{1}{T}\right) + \frac{\Delta S}{R}]$$

By using oxygen stoichiometry (5+δ) of 5.75 at 400^{o}C as a reference[125], $[O_o^x]_{dry}$ at 600^{o}C can be calculated as 5.716, with $[V_o``]_{dry} = 6 - [O_o^x] = 0.284$. Since, structural water departure gets its plateau at 1000^{o}C (Figure 4(b)), it can safely assumed that H_2O loss at 1000^{o}C is the total amount of proton (hydroxyl group) that had been inserted in bulk PBCC crystal structure.

$$[OH_o^{\cdot}]_{wet} = 2[H_2O]_{total\ loss}$$

The defect concentrations under wet conditions then can be obtained by following equations;

$$[O_o^x]_{wet} = [O_o^x]_{dry} - \frac{1}{2}[OH_o^{\cdot}]_{wet}$$

$$[V_o^{\cdot\cdot}]_{wet} = [V_o^{\cdot\cdot}]_{dry} - \frac{1}{2}[OH_o^{\cdot}]_{wet}$$

By above equations, K_w value at 600^{o}C can be extracted as ~0.018 (pH_2O = 0.03, $[O_o^x]_{wet}$ = 5.701, $[V_o``]_{wet}$ = 0.270, $[OH_o^{\cdot}]_{wet}$ = 0.029), which is comparable with another double perovskite material, PBSCF's value(Kw = ~0.01 at 600^{o}C)[79]. By using van't Hoff equation, hydration enthalpy (ΔH) and entropy (ΔS) can be determined as -120.28kJ/mol and -171.24J/mol•K respectively (by comparison between 800^{o}C, 3% water hydration parameters; K_w = 0.0008, $[O_o^x]_{wet}$ = 5.676, $[V_o``]_{wet}$ = 0.317, $[OH_o^{\cdot}]_{wet}$ = = $\frac{1}{2}$ ($[H_2O]_{total\ loss}$ - $[H_2O]_{loss}$) = 0.007). Compared to PBSCF which has ΔH = ~-70kJ/mol, ΔS = ~-113J/mol•K at 600^{o}C[79], PBCC seems to have demerit in lower hydration entropy,

however compensating water hydration with lower enthalpy. Therefore, proton concentration of PBCC at 600^{o}C shares very similar value with PBSCF ($[OH_o`]_{wet\text{-}PBCC}$ = 1.43mol%, $[OH_o`]_{wet\text{-}PBSCF}$ ~1.5mol%)[79], which is about 6 times higher value rather than simple perovskite, $BaCo_{0.4}Fe_{0.4}Zr_{0.2}O_{3-\delta}$ (~0.25mol% at 600^{o}C, which is equivalent as 0.5mol% value as a double perovskite) which is designed as triple conducing oxide[137]. Sihyuk Choi et al., mentioned that different configuration of crystal structure of double perovskites may originates higher dissolved hydroxyl groups rather than simple perovskites[79]. As a conclusion, PBCC shows capability of water uptake in perovskite, which is also suggested by Binghong Han et al., who observed nano-scale crystal structural oscillation by *in situ* TEM while introducing water vapor to perovskites.[138]

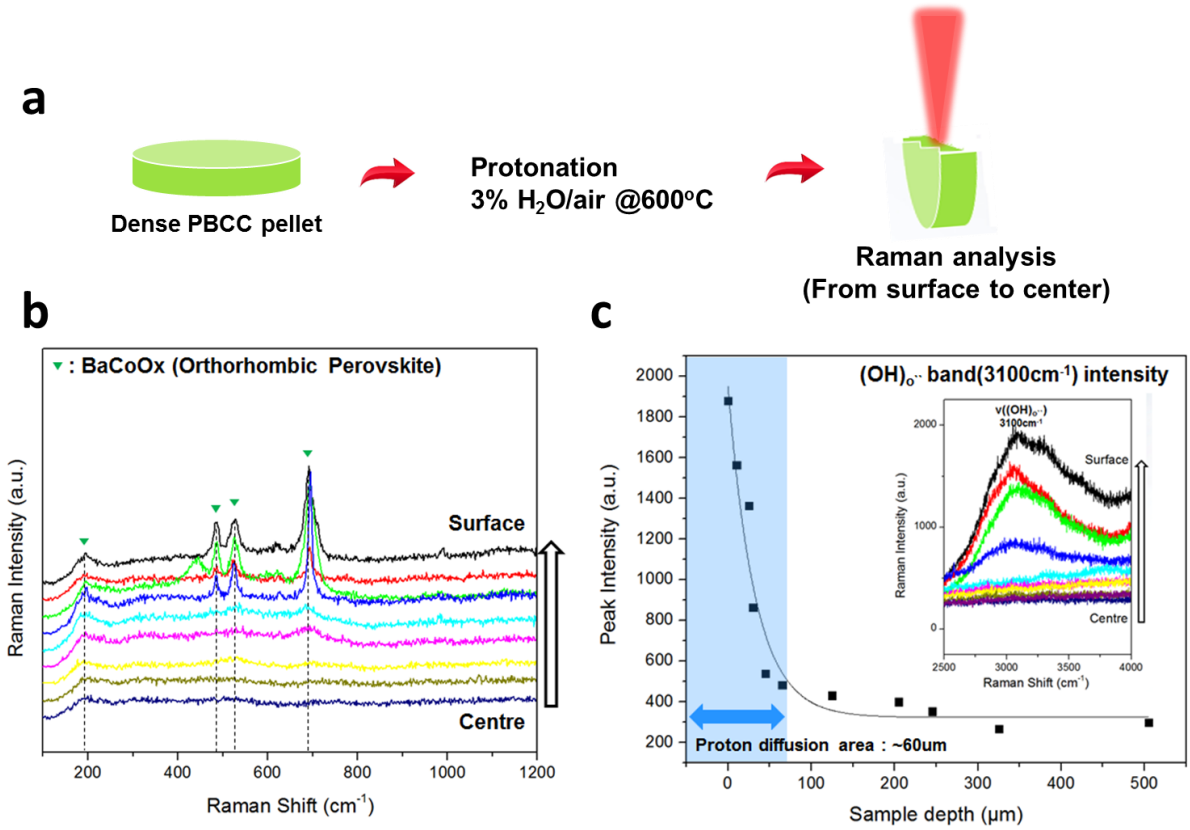

Figure 61. **Study of bulk chemistry of protonated PBCC** (a) Schematic procedure of Raman Profilometry with dense PBCC pellet (b) Raman spectroscopy in lower vibrational region, the exsolution of BaCoOx is observed due to the proton insertion (c) Raman profilometry of (v(-OH)) band intensity as function of sample depth. The data trend agrees with Fick's law which supports bulk proton diffusion inside PBCC double perovskite structure. (inset) Raman spectroscopy in higher vibrational region with band centered at (v(-OH)) band. ($3100cm^{-1}$)

To study bulk chemistry of PBCC, technique of Raman profilometry is utilized and schematic is shown in Figure 61(a). Raman profilometry is a useful method to

analyze proton distribution in dense ceramic pellet[139,140]. First, dense PBCC pellet of 1mm is protonated in wet air (3% water / air) @600^{o}C for 200 hours. After protonation, cross section of pellet is analyzed with Raman spectroscopy from surface to center. In this study, broad band centered at 3100cm^{-1} is assigned as v((-OH)$_{o}$`) to associate proton insertion in PBCC double perovskite. It has been considered broad band features in higher vibrational bands are assigned as strong hydrogen bonds, which is an evidence of proton conductivity in material[139,141].

As Figure 61(b) inset demonstrates, Raman spectra collected from PBCC cross-section (from centre to surface) shows development of v((-OH)$_{o}$`) band in higher vibrational region(2500 ~ 4000cm$^{-1}$) . Additionally, distribution of spectroscopic v((-OH)$_{o}$`) band intensity along sample depth (Figure 61(b)) shows good agreement with Fick's 2nd law, which supports bulk proton diffusion inside of PBCC double perovskite structure. Fick's 2nd law is presented as followed;

$$\frac{\partial[\boldsymbol{OH_o^{\cdot}}]}{\partial \mathrm{t}} = D\frac{\partial[\boldsymbol{OH_o^{\cdot}}]^2}{\partial x^2}$$

Where D is the diffusivity of hydroxyl groups. By assuming Raman intensity of v((-OH)$_{o}$`) is proportional with concentration of **[OH$_{o}$`]**, evaluation of diffusivity can be performed. Concentration of $[\boldsymbol{OH_o^{\cdot}}](\mathrm{x,t})$ can be represented as followed;

$$[\boldsymbol{OH_o^{\cdot}}](\mathrm{x,t}) = [\boldsymbol{OH_o^{\cdot}}]_{\boldsymbol{surface}}\boldsymbol{erfc}\left(\frac{\boldsymbol{x}}{\boldsymbol{2\sqrt{Dt}}}\right)$$

In this case, we only considered **[OH$_{o}$`]** propagates in on direction with time. By using this equation, we extract diffusivity values of $9.66 \times 10^{-12}\ cm^2/s$ at 600^{o}C. This

assumption seems reasonable, since diffusion length of $2\sqrt{Dt}$ = 52.7μm is comparable with v((-OH)$_o$`) propagation with sample depth in Raman profilometry. Also, calculated **[OH$_o$`]** profile based on extracted diffusivity value ($9.66 \times 10^{-12}\ cm^2/s$) reasonably matches with v((-OH)$_o$`) intensity found in Raman spectroscopy (Figure 70).

To confirm the structure purity, XRD is performed before and after protonation, however, there is no sign of structure failure or formation of secondary phase (Figure 63**(d)**). Water introduction in perovskite can facilitate dopant segregation in perovskite structure[114], and it can drive exsolution of nanoparticles on surface, which is already shown in SEM image (Figure 63**(c)**). Due to water introduction, BCO NP exsolution of PBCC is facilitated and supporting lower vibrational region Raman spectra (100cm^{-1} ~ 1200cm^{-1}) are displayed in Figure 61(b). BCO demonstrates a Raman band that belongs to Co_3O_4 phase, which illustrates its band at 190cm^{-1} ($F_{2g}^{(3)}$) , 490cm^{-1}(E_g) , 520cm^{-1}($F_{2g}^{(2)}$) and 690cm^{-1}(A_{1g}) [142] . As we mentioned earlier, Co_3O_4 can act as a water-oxidizing catalyst[124]. The distribution BCO NPs, exactly matches with band intensity of v((-OH)$_o$`) which supports NP exsolution is originated from water introduction.

5.6 DFT calculation for H_2O effect

Periodic density functional theory (DFT) calculations were carried out using the Vienna ab initio simulation package (VASP)[143,144] with the projector-augmented-wave (PAW) method.[145] For the bulk structure optimization, $PrBa_{0.75}Ca_{0.25}CoO_6$ (PBCC; $Pr_4Ba_3Ca_1Co_8O_{24}$; *P4/mmm*) was used similar to the previous studies.[19,146] We performed

the spin-polarization method with the generalized gradient approximation (GGA) with using the Perdew-Burke-Ernzerhof (PBE)[147] exchange-correlation functional for PBCC.[148] A kinetic energy cutoff for a plane wave basis set of 415 eV was used. Monkhorst-Pack meshes[149] with the (3 × 3 × 3) and (3 × 3 × 1) were applied for bulk and 2-D surface calculations. For the 2D-surface calculations, slabs were separated by a vacuum space of 15 Å to avoid any interactions between slabs. PBCC(010) was chosen for the surface calculation. The adsorption energy (E_{ad}) of O_2 and H_2O on a surface was calculated by E_{ad} = E[adsorbate-surface] – (E[surface] + E[adsorbate]), where E[adsorbate-surface] and E[surface] are the predicted electronic energies for an adsorbed surface species on a surface and its bare surface, respectively. E[adsorbate] is that for gas-phase triplet O_2 or H_2O. In order to determine the coadsorption effect between surface oxygen and hydroxyl species on PBCC, coadsorption energies were also calculated using E_{coad} = [E(adsorbate-surface) – (E[surface] + n·E[O_2] + m·E[H_2]/2)]/(n + m), where n and m are the number of oxygen and hydroxyl species. Vibrational frequencies were calculated using the VASP using the optimized structures. The reaction barriers were determined by the climbing image-nudged elastic band (CI-NEB)[150] method.

Interestingly, with DFT calculation we found out that concentration of proton can affect the stretching mode of oxygen species. In particular, as we can see in the Figure 62(b), as the number of surface hydroxyl species increases, O-O bond gets more elongated by nearby hydrogen bonding, and therefore redshift of v(O-O) frequency occurred. Therefore, elongated superoxo can be in the vibrational frequency regime of 1012 ~ 1257 cm^{-1}, while elongated peroxo species are presented in 857~918 cm^{-1}. This DFT based

peak calculation is also comparable with the rapid-scan FTIR results which the authors noted that surface proton can stretch the nearby superoxo species during water oxidation process.[124] As such, the spectral observation of v_2, v_3 and v_4 are perfectly fits into the frequency regime of proton elongated superoxo species. However, observed frequency of v_1 (967 cm^{-1}) is rather higher than those calculated for peroxo species (857~918 cm^{-1}). Therefore it is more reasonable to assign v_1 as bending mode of surface hydroxyl group which usually found at ~960 cm^{-1}.[151-153]

Based on this, we performed a further systematic rate constant prediction by varying the hydroxyl species on the surface. Accordingly, the reaction scheme supports that the water-addition to the PBCC cathode materials efficiently augments the ORR kinetics by reducing the barrier height of the oxygen dissociation and diffusion into the sub-lattice. Overall, the excellent correlation between time-dependent Raman measurements and EIS's R_p could be generalized for rational design of novel SOFC cathode materials by applying the molecular-level based design factors (*i.e.*, a reaction barrier prediction for a rate-determining step) and by defining the optimal surface coverage of hydroxyl species, achieving the lowest barrier height under SOFC conditions. Water dissociatively adsorbs on PBCC, forming surface hydroxyl species, while gas-phase oxygen adsorbs either preferentially on BCO NPs or on CoO-terminated PBCC surfaces, followed by the formation of superoxo and peroxo species without a barrier. After the concurrent dissociation and diffusion to the sub-lattice owing to the effective attraction with surface hydroxyl species, oxygen vacancies are migrated down to the electrolyte.

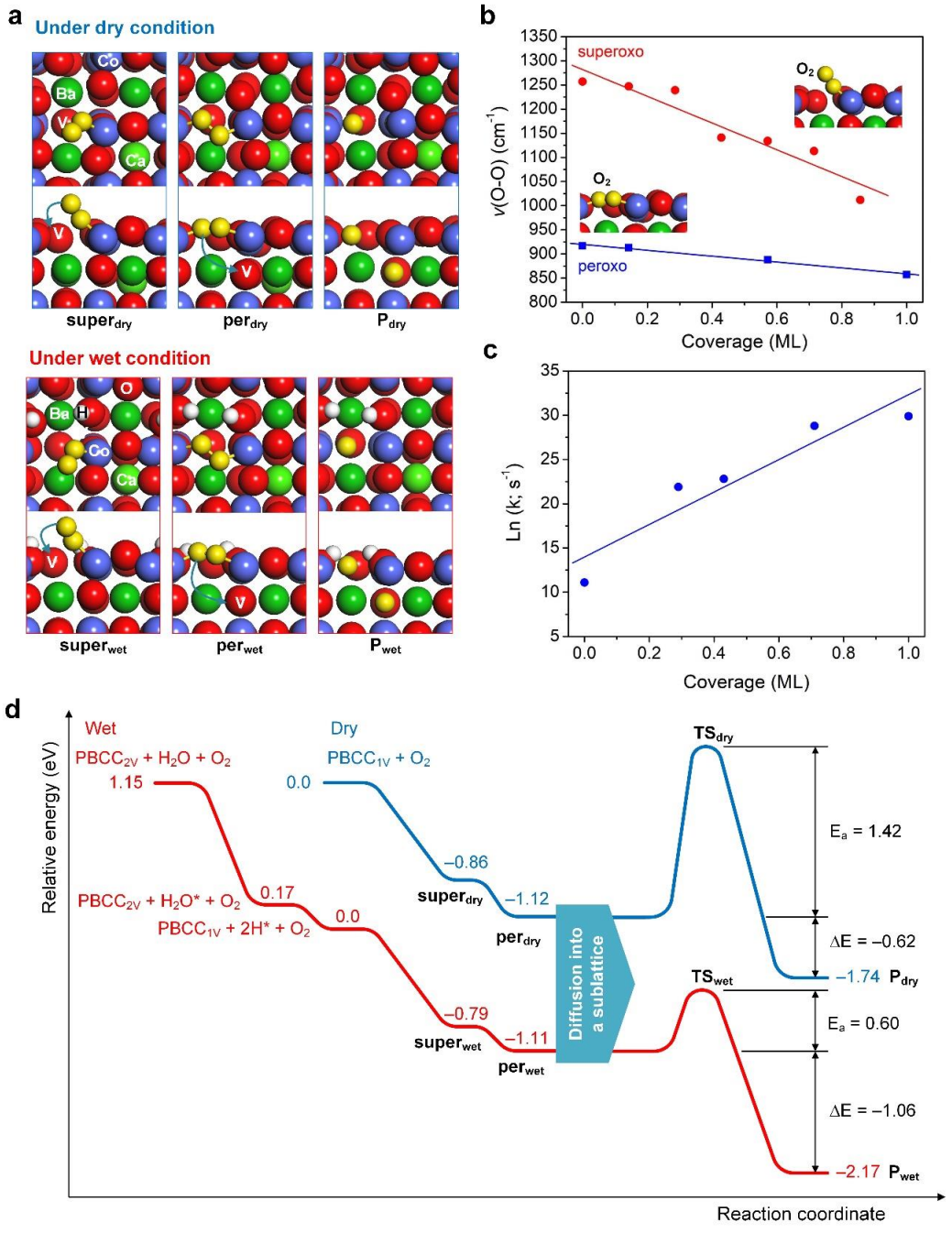

Figure 62. (a) Geometrical illustration of typical surface species adsorbed on PBCC(010) used for the mechanistic and vibrational frequency calculations. (b) Correlation of calculated vibrational frequencies of the O-O stretching mode for superoxo and peroxo species with and without water as a function of surface hydroxyl species. “0” refers to a

dry condition. (c) Rate constants for the concurrent dissociation and diffusion to the sub-lattice at 600^{o}C. (d) Schematic of energy profiles for oxygen reduction on PBCC(010) under dry and wet conditions. E_a and ΔE are the reaction barrier height of the concurrent dissociation and diffusion to the sub-lattice and the reaction energy at 0K.

5.7 Conclusion

In conclusion, PBCC can go through a dramatic surface modification composed of NPs coatings on surface by simply introducing small amount of water vapor with air. The water-modified surface of PBCC markedly speeds up electrocatalytic activity for ORR and polarization of the cathode reduces more than half (from 0.5 Ω cm^2 (Dry air) to 0.2 Ω cm^2 (3v% H_2O + air)) at 600^{o}C. *Operando* Raman characterization of PBCC electrode in wet air could reveal oxygen molecules preferentially chemisorbed on the surface of water-modified PBCC with charged oxygen species which is key clues for water-assisted ORR mechanism in high temperature. The symbiotic combination of unique water-modified surface morphology and its capability of dissociative adsorption of H_2O could turbo-change the ORR catalytic activity of PBCC, while it maintained stable performance and bulk structure over 500 hours in 750^{o}C. Demonstrated PBCC cathode is attractive not only for SOFCs, but also for PCFC cathode which essentially includes H_2O as main product, which can be beneficial for long-term stability. Also outstanding water-stability of this material can be utilized as water-splitting electrode for production of H_2 as well.

5.8 Supplementary Information

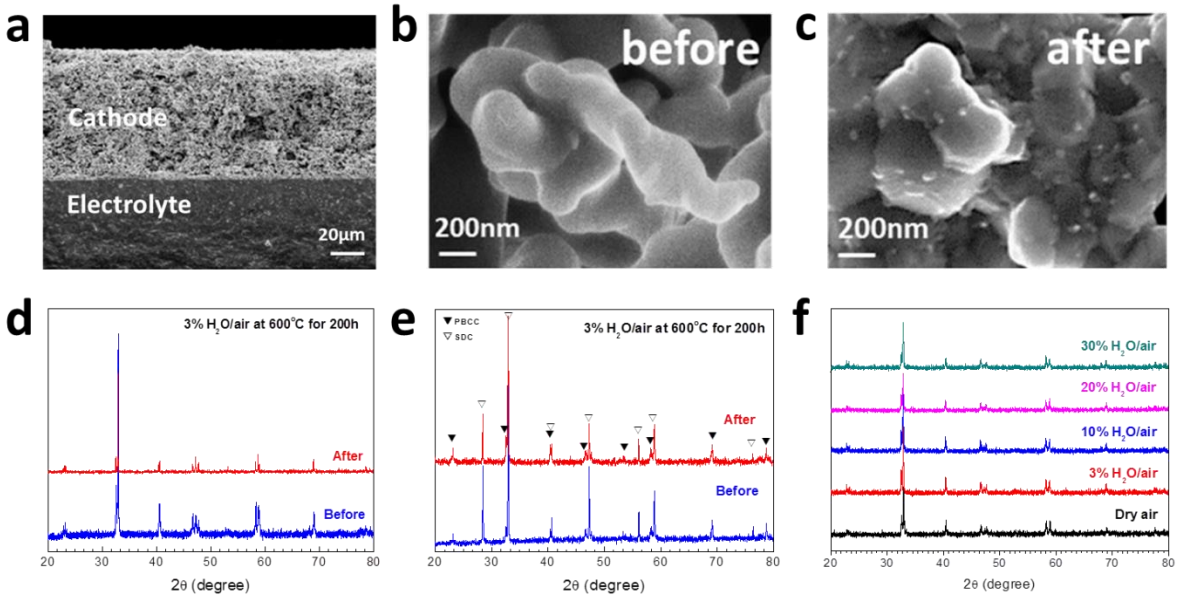

Figure 63. **Structural characterization** (a) SEM image of Cross-sectional view of PBCC/SDC cell (b) SEM image of surface view of PBCC electrode before introducing water (c) SEM image of surface view of PBCC electrode after introducing water (d) XRD of PBCC dense pellet used for Raman profilometry measurement. (e) XRD of PBCC/SDC/PBCC cell tested with 3v% H_2O for 200 hours. (f) XRD of PBCC powder exposed to different water vapor pressure

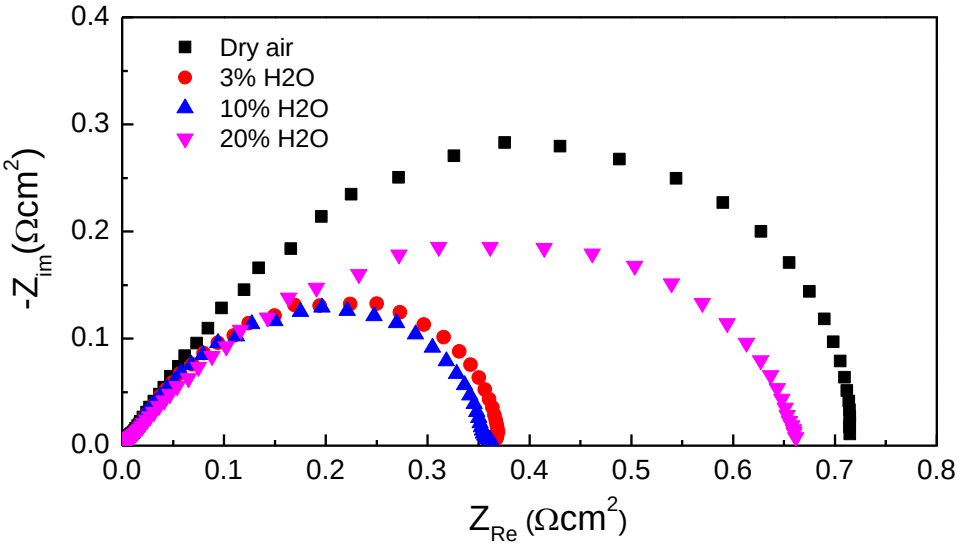

Figure 64. **PBCC/SDC/PBCC symmetric cell testing in different water content air(Dry, 3v%, 10v% 20v% H_2O) at 600°C**

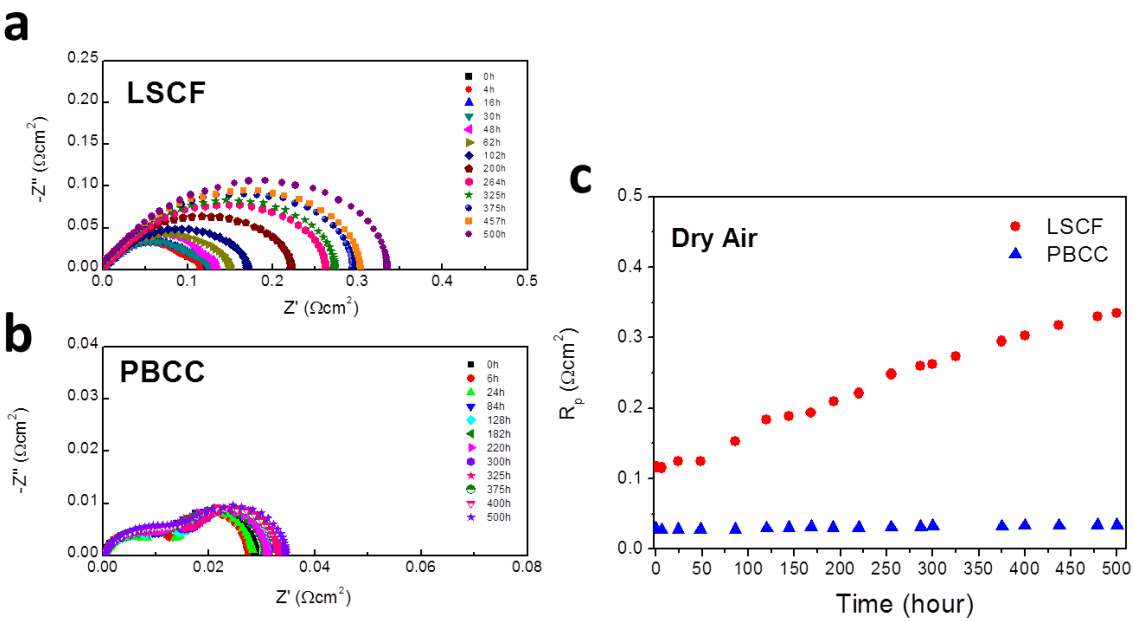

Figure 65. **(a)** Electrochemical impedance spectroscopy of LSCF/SDC/LSCF in dry air at 750°C **(b)** Electrochemical impedance spectroscopy of PBCC/SDC/PBCC in dry air at

750°C **(c)** Long-term stability of PBCC electrode in dry air compared with LSCF electrode at 750°C.

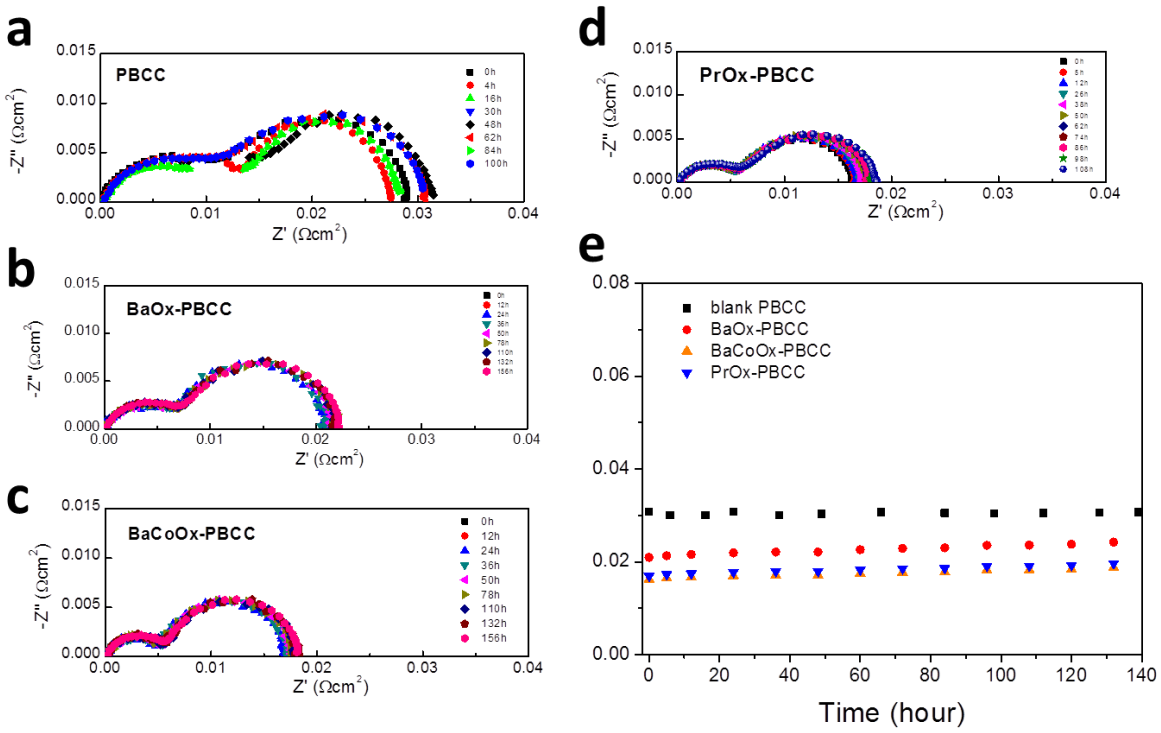

Figure 66. **(a)** Electrochemical impedance spectroscopy of PBCC/SDC/PBCC in dry air at 750°C **(b)** Electrochemical impedance spectroscopy of BaOx-PBCC/SDC/ BaOx-PBCC in dry air at 750°C **(c)** Electrochemical impedance spectroscopy of BaCoOx-PBCC/SDC/ BaCoOx-PBCC in dry air at 750°C **(d)** Long-term stability of catalyst-infiltrated PBCC electrodes (BaOx, BaCoOx, PrOx) in dry air compared with blank PBCC electrode at 750°C.

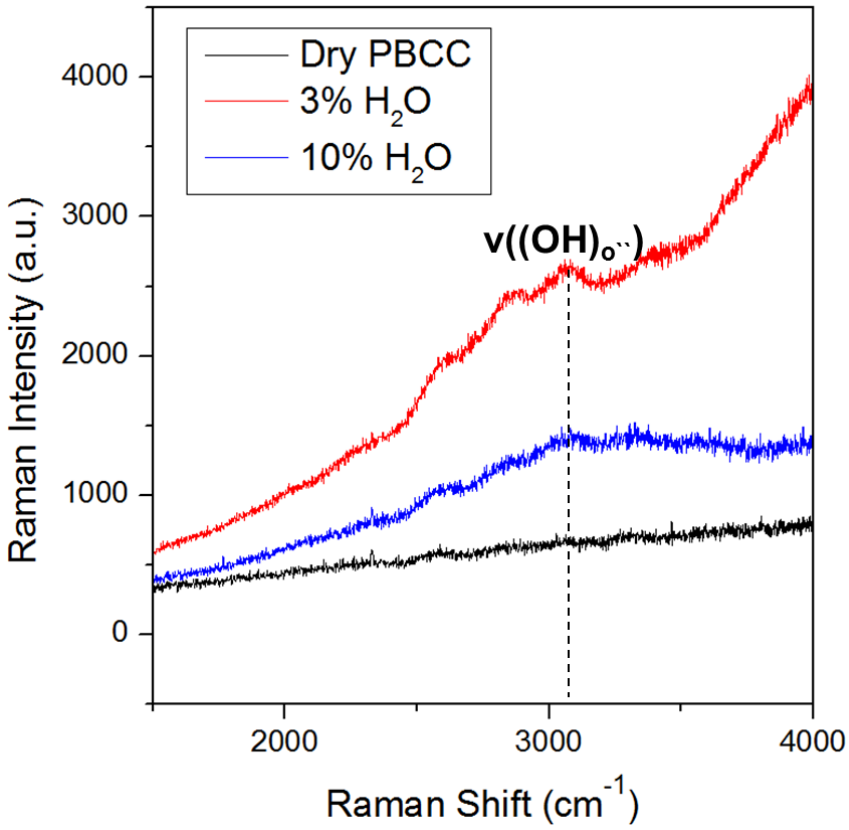

Figure 67. Raman spectroscopy of PBCC powder annealed in different water vapor pressure (Dry, 3v% H_2O, 10v% H_2O) at 600^{o}C for 3 hours

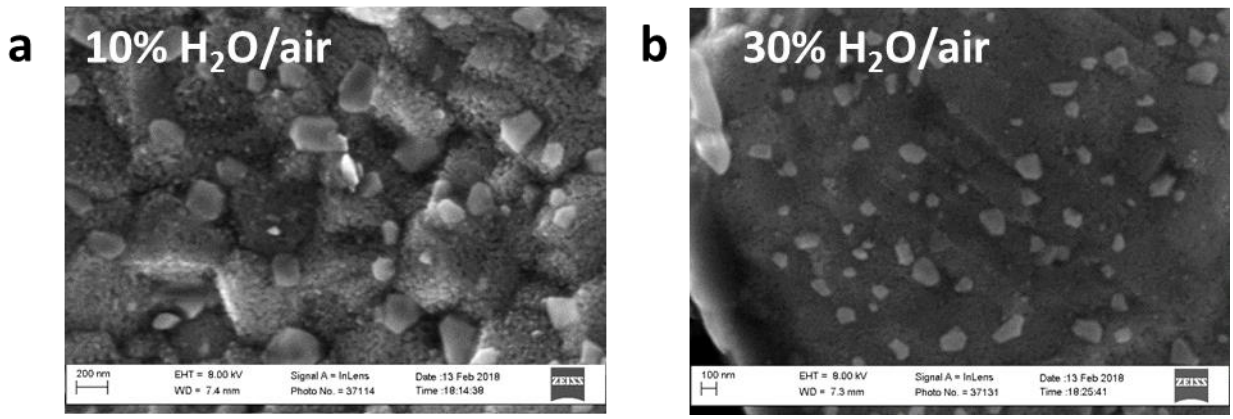

Figure 68. SEM image of surface view of PBCC powder after introducing **(a)** 10v% water at 600^{o}C for 3 hours, **(b)** 30v% water at 600^{o}C for 3 hours

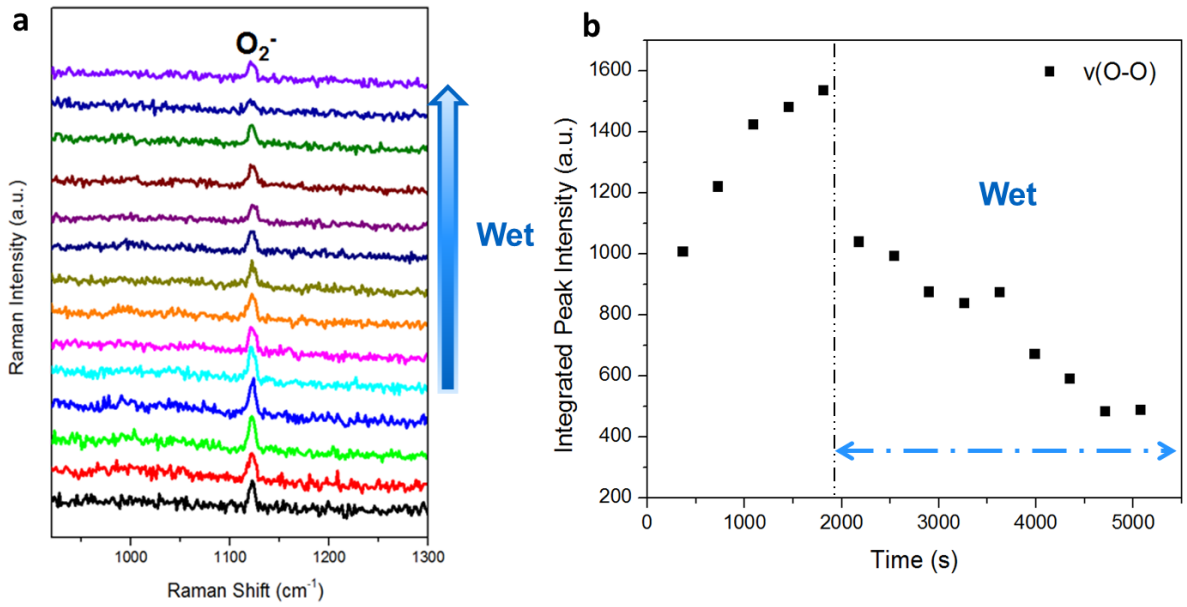

Figure 69. (a) *In situ* Raman spectroscopic evolution of O_2^- as introducing 3v% H_2O vapor on LSCF surface (b) Integrated peak intensity of O_2^- over time

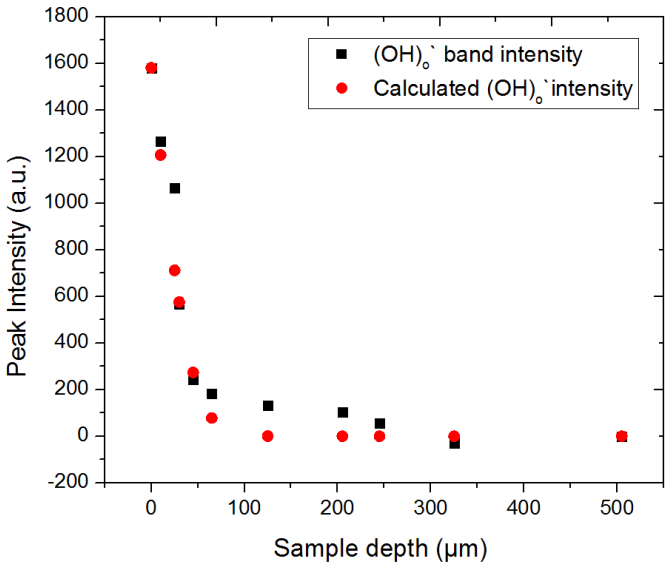

Figure 70. Raman profilometry of (v(-OH)) band intensity as function of sample depth. Black dot shows experimental data while Red dot represents calculated (v(-OH)) band intensity based on diffusivity value of $9.66 \times 10^{-12}\ cm^2/s$.

5.9 Experimental

5.9.1 Material synthesis

PBCC powders were synthesized using a citric-combustion method. Stoichiometric amounts of $Pr(NO_3)_3 \cdot 6H_2O$, $Ba(NO_3)_2$, $Ca(NO_3)_2 \cdot 4H_2O$, and $Co(NO_3)_2 \cdot 6H_2O$ were dissolved in distilled water with proper amount of citric acid. An adequate amount of ethylene glycol was added into the solution after the mixture was dissolved. After a viscous resin was formed, the mixture was heated to roughly 250 ^oC in air and followed by combustion to form fine powders, which were calcined at 900 ^oC for 2 h. The resulting powders were then ball-milled for 24 h. The calcined PBCC powders were ball milled again, then sintered at 1125^oC for 5 h to achieve single phase as confirmed by X-ray diffraction (XRD, PANalytical X-Ray Diffractometer, Alpha-1). The microstructure and morphology of the PBCC electrode before/after exposure to water were examined using a scanning electron microscope (SEM, LEO-1530).

For Raman analysis, the PBCC powders were dry pressed and sintered at 1200 ^oC for 5 h, with a heating/cooling rate of 1.5 $^oC\ min^{-1}$ to obtain > 95% relative density in air atmosphere. To determine the area specific resistance (PBCC) of PBCC for oxygen reduction, PBCC electrodes were prepared by tape casting method, which was then applied onto both sides of a $Sm_{0.2}Ce_{0.8}O_{1.9}$ (SDC) electrolyte pellet using a SDC bonding slurry. SDC electrolytes were prepared by uniaxially pressing commercially available SDC powder and sintering at 1450^oC for 5 h to achieve relative density of ~98%. PBCC tapes were adhered to both side of the SDC electrolyte using a SDC slurry as a bonding

layer (3-5 μm). Lastly, the PBCC/SDC/PBCC symmetric cells were fired at 1080^{o}C in air for 2 h.

5.9.2 Electrochemical impedance spectra measurements

Impedance spectra were acquired using a Solartron 1255 HF frequency response analyzer interfaced with an EG&G PAR potentiostat model 273A with an AC amplitude of 10 mV in the frequency range from 100 kHz to 0.01 Hz.

5.9.3 Proton uptake measurement

Thermogravimetric analysis of the PBCC powder was performed on a TA Instruments SDT Q600. The samples were heated from room temperature to 1000^{o}C at 10^{o}C per minute under argon flowing at 100 SCCM. Starting at approximately 200^{o}C, the PBCC which was not exposed to water has a gradual weight loss, likely due to loss of surface adsorbed water and the formation of oxygen vacancies in the material. The hydrated PBCC shows a similar trend but at ~ 700^{o}C there is an additional weight loss event. This corresponds to the loss of bulk absorbed water which we showed in our earlier Raman analysis. Moreover, PBCC which was exposed to higher humidity levels shows a higher weight loss which indicates equilibrium between the humidity level and the concentration was water absorbed into the material.

5.9.4 In stiu / operando Raman Spectroscopy

Raman spectra were obtained using a Renishaw RM 1000 spectromicroscopy system (~2 μm spot size). An air-cooled Ar laser (CVI Melles Griot) emitted at 514 nm was used for excitation of Raman signal in this study with a total power of 14 mW. A Harrick environmental chamber was used for *operando* Raman tests. [76] An *in situ / operando* time-resolved study was conducted by placing the laser spot on the same location. To perform *operando* Raman spectroscopy study, PBCC/SDC/PBCC symmetric cell is attached with Ag wires. To ensure good electrical connection, Ag paste is used. Synthetic Air (N_2 79%, O_2 21%, Airgas) is metered with mass flow controllers and introduced into the chamber. To introduce 3v% water into the gas, a room temperature bubbler was used.

CHAPTER 6. DIRECT OBSERVATION OF IN SITU SPIN STATE REARRANGEMENT OF PEROVSKITE OXIDE AND IDENTIFYING INTERMEDIATES DURING OXYGEN REDUCTION REACTION

6.1 Introduction

Compared to hydrogen oxidation reaction, oxygen reduction reaction (ORR) is known to be naturally sluggish[154,155], and pushing performance of cathode forward would be the main breakthrough for fuel cell to compete with conventional combustion engine. Although oxygen involving electrochemical reactions including reduction and evolution are globally occurring in electrode of metal-air batteries, fuel cells and electrolysers, specific reactions in detail can vary with phase of electrolyte, temperature, and gas pressures. Among them, ORR happens on air-electrode of SOFC can be represented by Kroger-Vink notation as:

$$O_2 + 4e^- + 2V_o^{\cdot\cdot} = 2O_o^x$$

The solid-state reaction described above has little energy barrier as temperature is elevated as oxygen hopping in bulk can be facilitated[156]. While Oxygen involving reaction happen on interface between liquid electrolyte and metal - metal oxide can be easily monitored through surface-sensitive techniques[128,157], tracking bulk incorporation of oxygen and annihilation of vacancy impose a different degree of difficulties on understanding of ORR kinetics in SOFC cathodes[158,159]. Also, the high temperature itself act as a barrier to analyze the mechanism with conventional characterization techniques[23].

For these reasons, high temperature ORR is less understood than room temperature liquid electrolyte-based ORR ($O_2 + 2H_2O + 4e^- = 4OH^-$). For example, shao-horn's group created an effective descriptor of e_g occupancy in aqueous OER perovskite catalysts, which arise from the hybridization between transition metal *d* band and O*2*p band[107,160]. Guided by this insight, the rational design of superior OER catalyst such as $Ba_{0.5}Sr_{0.5}Co_{0.8}Fe_{0.2}O_{3-\delta}$ or $SrNb_{0.1}Co_{0.7}Fe_{0.2}O_3$ is enabled[161,162]. Although bulk-O*2*p centre successfully explained electro-catalytic activity of perovskites in SOFC as well[163], William et., al pointed out surface redox electrochemistry has insufficient information yet and observation of oxygen adsorbate can produce valuable information as well[156]. Significance should be addressed that surface of perovskite($LaCoO_3$) can have different spin state rather than bulk, therefore, can exhibit different electrocatalytic activity toward OER even in same material[164]. One of vibrational spectroscopy, Raman spectroscopy is expected to serve as powerful surface-sensitive tool to observe reaction intermediates and structure of materials at the same time[23,76,165]. Since, suggested rate limiting steps for ORR are surface charge transfer reactions[156,166-168], monitoring surface will be even more meaningful, because overall reaction speed will be determined on the surface. Therefore, to truly understand and to control ORR, deeper understanding of surface intermediates is inevitable.

Although there has been extensive contribution on studying ORR intermediates[107,108,116,120,154,169], little information of oxygen intermediate is reported on surface of perovskite (ABO_3) materials. This is due to the intrinsic Raman inactivity of rhombohedral symmetry perovskites such as LSCF and LSM cathodes makes difficult to understand oxygen surface species on surface[23]. Nevertheless, scientific enthusiasm on

perovskite leads to numerous first-principle studies to envision ORR pathways on SOFCs[2,126,127]. The computational efforts successfully synthesized possible oxygen intermediates and its v(O-O) vibrational frequencies, so that it can be later confirmed by vibrational spectroscopies in future.

To enable examination of oxygen intermediates through Raman spectroscopy, we designed a unique model electrode with asymmetric cell configuration that has dense LSCF cathode on one side to manipulate ORR to explicitly happen on the surface of LSCF. By this strategy, we could successfully identify various oxygen molecules including gaseous oxygen (O_2), peroxide (O_2^{2-}) and superoxide anion (O_2^-) as intermediates of ORR pathway on LSCF electrode at elevated temperature (600^{o}C) using *operando* Raman spectroscopy. Also, by examining the structural evolution, we are surprised to report that LSCF can go through Jahn-Teller distortion indicating bias-induced spin-state rearrangement is possible even in high temperature as well. Fundamental understanding of high temperature ORR kinetics would decipher the bottlenecks in chain-reaction to assist advanced design of cathode material for future fuel cell industry. Additionally, the unique set-up used in this study can be readily transferred as a baseline platform for other catalyst study with various atmospheric environments with possible contaminants to examine how these changes makes impact on ORR.

6.2 Oxygen Reduction Reaction on LSCF (2PB)

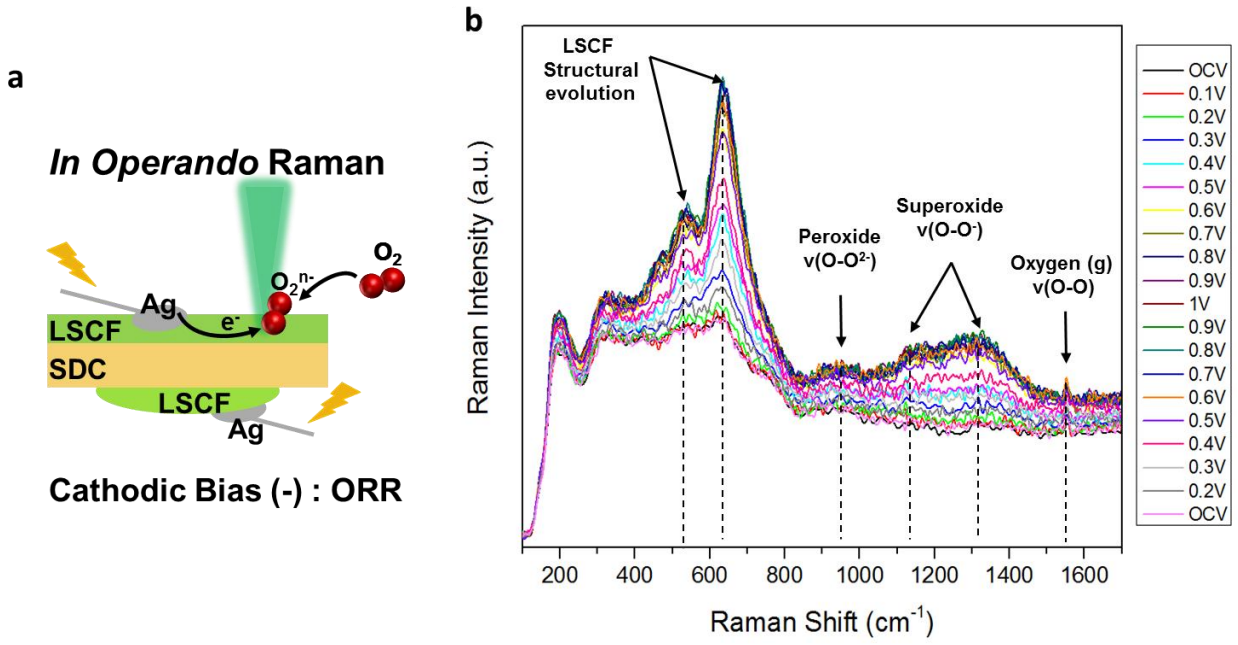

Figure 71. (a) Schematic diagram of *operando* Raman spectroscopy explaining ORR schematic in cathodic (-) bias applied to the cell. Raman laser is focused on LSCF alone (2PB) (b) Superimposed *operando* Raman spectroscopic evolution under cathodic bias from OCV to 1V.

Identifying intermediate species with adequate vibrational spectroscopic technique can give profound understanding in reaction pathway. Moreover, if spectroscopic property is coupled with electrochemical properties, it can generate a powerful predictive model for mechanism. Therefore, *operando* Raman spectroscopy coupled with Electrochemical Impedance Spectroscopy (EIS) is performed. To perform *operando* Raman spectroscopy, asymmetric cell with dense LSCF cathode on one side with SDC electrolyte is used. Although, conventional cell configuration with porous electrode has merit in facile mass transport, most of oxygen will diffuse into pores, and ORR will preferentially happen on triple phase boundary (3PB), where LSCF and SDC

meet (Figure 78(a), Red line). Since, Raman laser cannot penetrate though conductive LSCF phase, detection of oxygen intermediates on surface can be challenging. Therefore, we devised a model electrode with dense LSCF layer so that every ORR reaction step can happen exclusively on surface of LSCF (2PB reaction, Figure 78(b), Red line). With this configuration, detection of oxygen intermediates related to ORR will be possible when Raman laser is focused on surface of LSCF.

At 600^{o}C, O_2 is metered into Raman chamber to identify the surface species formation on LSCF electrode. Although, a great contribution is made with *in situ* XRD that allows one to understand the oxygen non-stoichiometry in the bulk electrode[159,170,171], monitoring surface redox activity as function of cathodic bias can lead to intriguing results as well[156,172]. As changing cathodic bias, operando Raman analysis revealed 3 major band group evolutions (Figure 71(b)); 1. LSCF structural evolution (576cm^{-1}, 633cm^{-1}), 2. Oxygen intermediates (Peroxide (O_2^{2-}) : 943cm^{-1}, Superoxide (O_2^{-}) : 1132, 1327cm^{-1}), and gaseous Oxygen (1551cm^{-1}).

Since LSCF belong to the $R\bar{3}c$ space group, which represents near-cubic rhombohedral perovskite structure, its symmetry shows little Raman activity.[23,173] However, when cathodic bias is applied to provide electrons, structural evolution of LSCF can be observed as shown in Figure 71(b). The band evolutions at 576cm^{-1} (A_g), 633cm^{-1}(B_{2g}) are assigned as Jahn-teller distortion to orthogonal perovskite (*Pbnm*) structure[2,174,175]. It is reported that Jahn-teller effect does not influence lattice deformation under high temperature, since various spin-state for transition metal become possible[2,176,177]. This is also agreed with our *in situ* Raman spectra taken in different temperatures shown in Figure 79, that Jahn-teller distortion gets insignificant as LSCF

ramping up to higher temperature. However, *operando* Raman result shown here suggest that even in high temperature, spin-state arrangement of perovskite is operative with cathodic bias. Although, the spin state of Co^{3+} ion was controversial, that it can have low, intermediate, and high spin, recently it has been proven that it can has multiple spin at a time[164,178]. For Co^{3+} ion, with intermediate spin ($t_{2g}^5e_g^1$) with ABO_5 configuration, it can demonstrate a unique Jahn-Teller distortion with e_g filling as 1[160,164]. As suggested with previous in situ XRD studies, vacancy in LSCF will accumulate when cathodic bias is applied, and it seems applied cathodic bias lead Co^{3+} ion to be in intermediate spin with vacancy facing surface[158,160]. The fact that vacancy and oxygen intermediates can co-exist in same time-line, is undoubtedly an indication that surface charge transfer-reaction is the rate-limiting step in ORR In other words, if rate of vacancy annihilation is fast enough, bias induced Jahn-teller effect, which is an consequence of accumulation of vacancy, would not operative on LSCF surface.

Surface structural alteration from rhombohedral to orthogonal structure can be interpreted as Sr cation migration due to bias as well. It is reported that at high cation-vacancy concentration, LSCF crystallizes in rhombohedral($R\bar{3}c$) structure, while for less cation-defective compositions to an orthogonal (*Pbnm*) structure.[173,179] By in situ XPS, it is proved that Sr cation can migrate electrode interior as cathodic/anodic bias applied to the electrode[180], and it is reported that cathodic bias will prevent Sr segregation on surface[114]. Due to applied cathodic bias, Sr on surface will migrate toward electrolyte, and surface of LSCF will have less cation-defective compositions with orthogonal perovskite structure, which shows good agreement with our *operando* Raman observation.

Although assignments of observed surface oxygen intermediates on metal and metal oxides are controversial, predicted O-O vibrational frequencies of molecularly adsorbed intermediates of peroxo- or superoxo-like species range from 875cm^{-1} to 1292cm^{-1}. [2,128] DFT calculation of Raman band of adsorbed peroxide and superoxide intermediates on $La_{1-x}Sr_xCo_{1-y}Fe_yO_{3-\delta}$ have been carried out to be 933cm^{-1}(Co-per), 1156cm^{-1}(Sr-per) or 1321cm^{-1}(La-super).[127] Also, vibrational mode of superoxide (O_2^-) has been reported at 1015-1377 cm^{-1}.[2,127-130] Therefore, assignments of Raman bands seems reasonable. Furthermore, Raman bands of gaseous Oxygen have been reported at ~1556cm^{-1} with sharp peak which agrees with our observation[126,181].

ORR steps on LSCF are suggested as followed[2]:

$O_{2(g)} + e^- = O_2^-$ (superoxide formation)

$O_2^- + e^- = O_2^{2-}$ (peroxide formation)

$O_2^{2-} + 2e^- = 2O^{2-}$ (oxygen-dissociation)

$2O^{2-} + 2V_o`` = 2O_o^x$ (Oxygen fill in the vacancy)

Overall, $\frac{1}{2}O_{2(g)} + V_o`` + 2e^- = O_o^x$

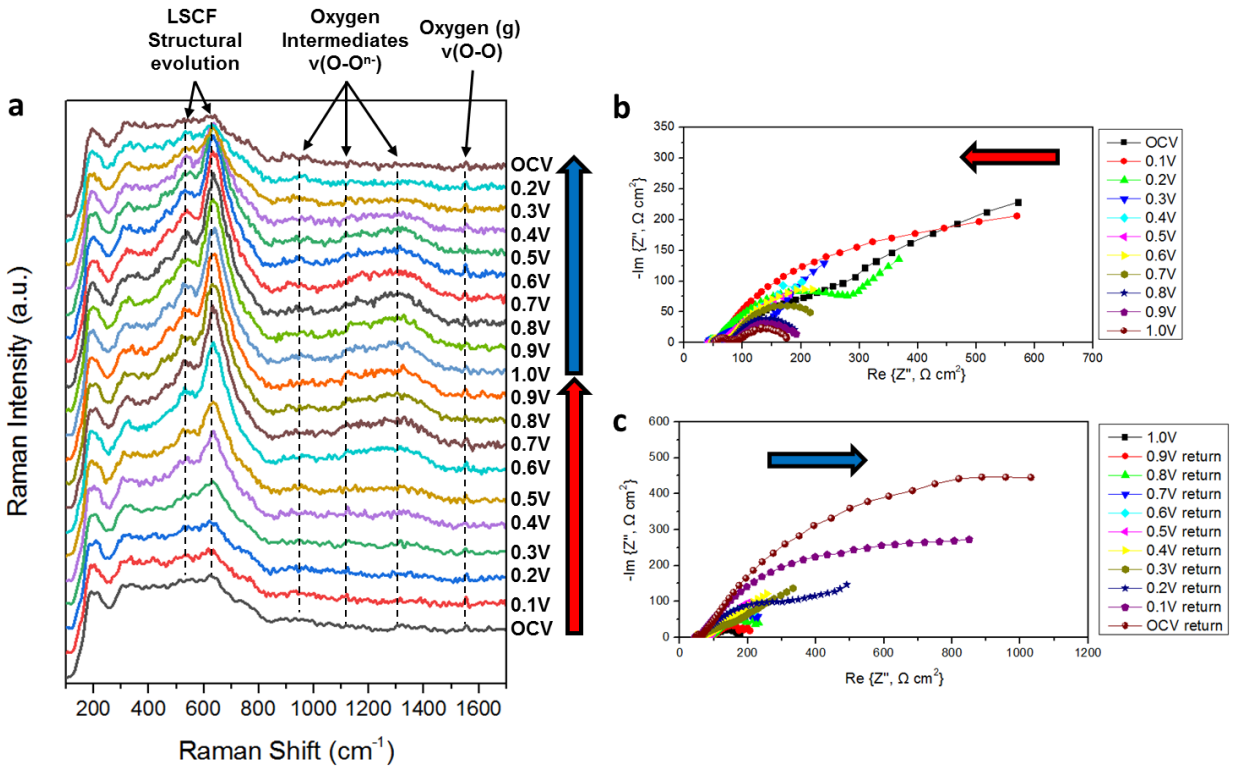

Figure 72. O*perando* Raman spectroscopic evolution under cathodic bias. (b) Electrochemical Impedance Spectroscopy (EIS) of LSCF asymmetric cell in O_2 at 600^{o}C from OCV to 1V (c) Electrochemical Impedance Spectroscopy (EIS) of LSCF asymmetric cell in O_2 at 600^{o}C from 1V to OCV

Since ORR is composed of charge-transfer reactions with electrons as described above, applied voltage can affect the amount of intermediates found on surface[128]. Through Ag current collector, cathodic (-) voltage is applied to the cell to provide electrons to LSCF from external circuit (Figure 71(a)) As applying higher cathodic bias, the band intensity of oxygen intermediates shows increasing trend, indicating gaseous oxygen($O_{2(g)}$) reacts to form peroxide(O_2^{2-}) and superoxide(O_2^-) on surface of LSCF

electrode as (Figure 71**(b),** Figure 72**(a)**). Synchronously, EIS is performed and result is shown in Figure 72**(b)**. The value of Spectroscopic properties as a function of Electrochemical operation can be considered as quantitative indication of oxygen intermediate adsorption and desorption on LSCF electrode. To perform quantitative correlation, bands of gaseous oxygen and chemisorbed-oxygen species are integrated with bandwidth of $20cm^{-1}$, and integrated intensity is plotted with polarization resistance (R_p) as function of cell potential. Figure 73 shows a good agreement between polarization resistance and integrated intensity of oxygen intermediates. In particular, as cathodic bias is applied, polarization resistance decreases, as oxygen adsorbs on surface to form oxygen intermediates. Jahn-Teller band evolution of LSCF (A_g, B_{2g}) is integrated as well (Figure 73**(a)**) and it also shows good agreement with amount of oxygen intermediates and polarization of the cell.

On the contrary, when lower cathodic bias (from 1.0V to OCV) is applied to LSCF electrode, the band intensity of oxygen intermediates decrease (Figure 73**(b)**) and Jahn-Teller effect is relieved on LSCF. Repeatedly, quantitative correlation between vibrational properties and electrochemical properties is done and the result is shown in Figure 3 with good agreement.

To prove applied cathodic bias (-) lead to structural evolution of LSCF and increased oxygen intermediates on surface, anodic bias (+) is applied to model cell so that ORR is preferentially happening on counter electrode where Raman laser is not scanning (Figure 80). In this case, neither of structural evolution nor oxygen intermediates appearance can be found on LSCF model electrode which confirms that Raman evolution on working electrode is truly driven by the cathodic bias applied on model electrode

(Figure 81). Also, synchronized EIS does not match any Raman evolution happening on model electrode surface.

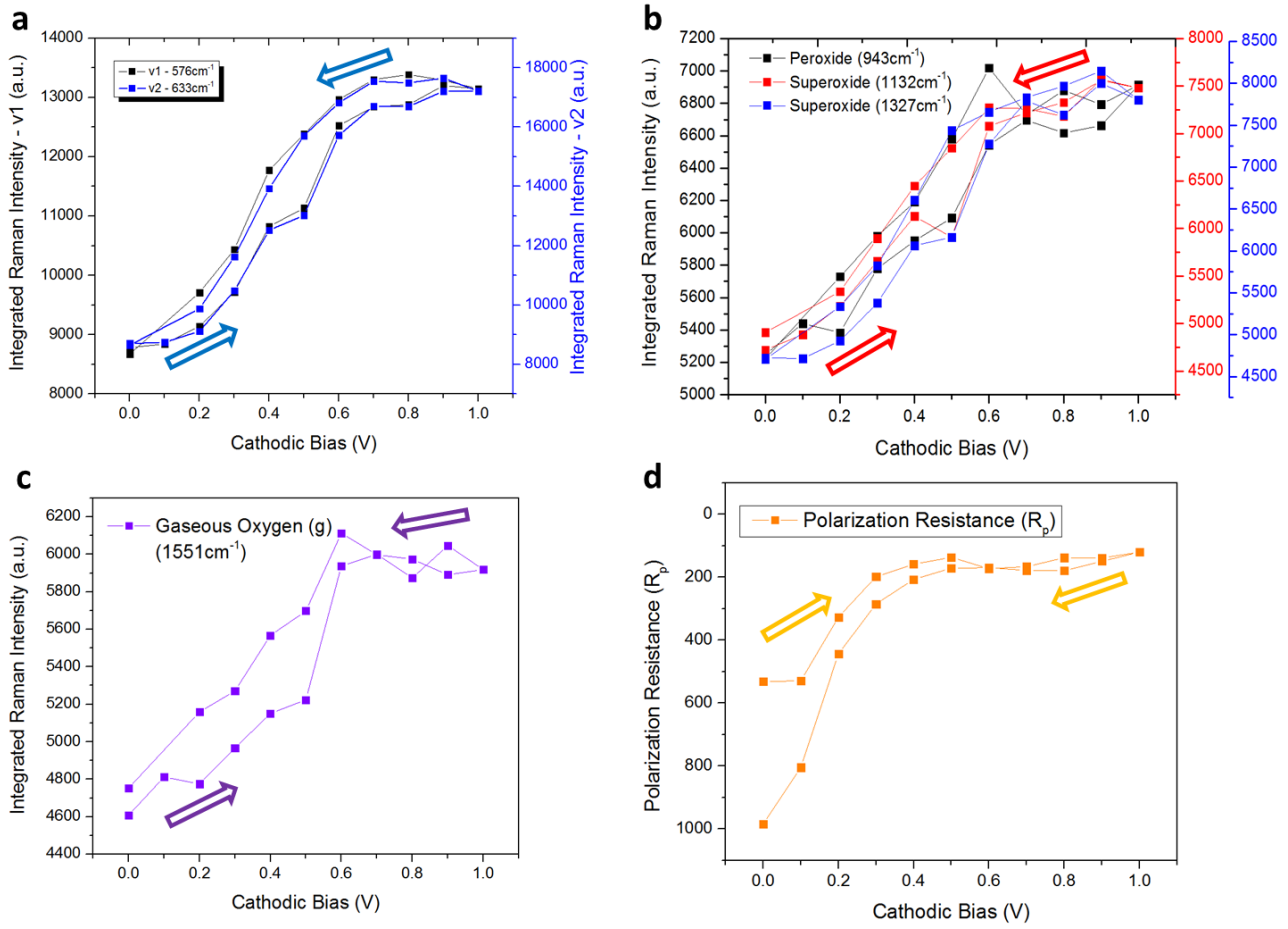

Figure 73. Quantitative correlation between *Operando* spectroscopic evolution of (a) LSCF structure, (b) Oxygen intermediates, (c) Adsorbed gaseous Oxygen and (d) polarization resistance (R_p) of LSCF asymmetric cell versus applied cathodic (-) bias

6.3 Oxygen Reduction Reaction on LSCF-SDC interface (3PB)

By varying geometry of model cell, and by adjusting Raman laser focus to different region, different ORR pathways on cathode can be studied rather than LSCF 2PB. To perform, dense LSCF electrode is sputtered on SDC electrolyte with mask to create a line of 3PB (SDC-LSCF interface) (Figure 82). The model cell is then loaded on Operando Raman chamber, and Raman laser is focused on interface between SDC and LSCF to monitor surface Raman evolution on 3PB at 600°C with O_2 flow. As described in Figure 74**(b)**, structural evolution of SDC, LSCF and accumulation of oxygen intermediates could be observed operando Raman spectroscopy by varying cathodic bias applied on cell.

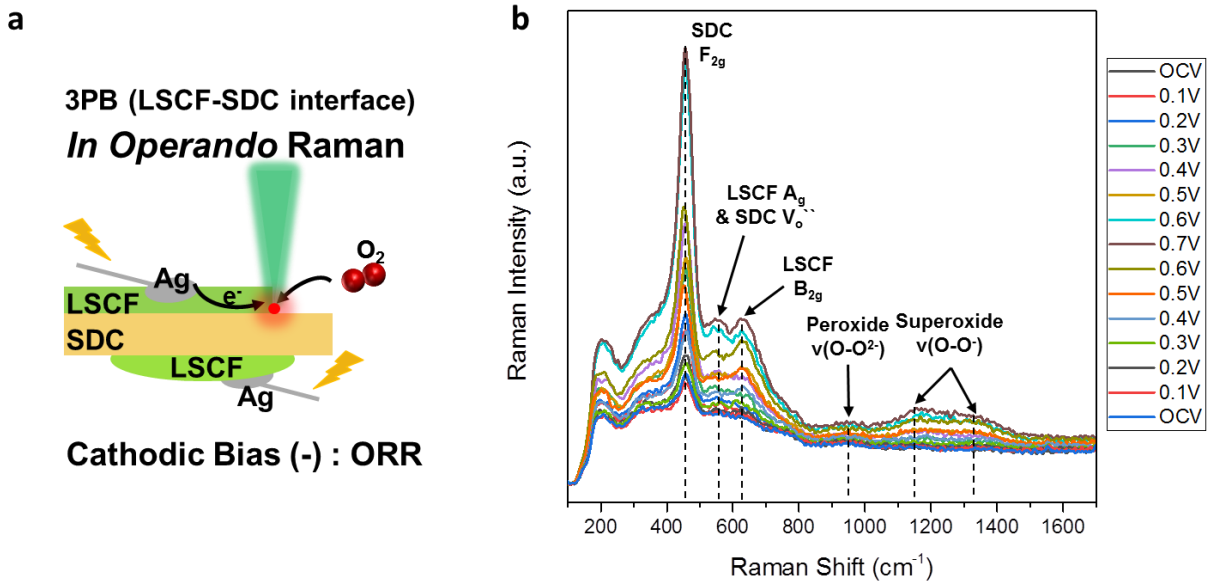

Figure 74. (a) Schematic diagram of *operando* Raman spectroscopy, where laser is focused on 3PB (LSCF-SDC interface) (b) Superimposed *operando* Raman spectroscopic evolution under cathodic bias from OCV to 0.7V.

As we already observe from *operando* Raman using 2PB LSCF model cell that was explicitly described in previous section, orthorhombic structure evolution of LSCF ($576cm^{-1}$, $633cm^{-1}$) and accumulation of Oxygen intermediates (Peroxide (O_2^{2-}) : $943cm^{-1}$, Superoxide (O_2^-) : 1156, $1341cm^{-1}$) can be again confirmed on 3PB as well. Significant difference in 3PB (SDC-LSCF) ORR pathway is the band evolution of SDC's F_{2g} band (Ce-O_8 Crystal unit, Fluorite) appears at ~$460cm^{-1}$.[182] Band intensity of F_{2g} mode gets stronger as increasing the cathodic bias (-) from OCV to 0.7 V (Figure 75**(a),(d)**). Intensity increase of F_{2g} can be interpreted as surface of SDC leads to relatively ordered situation with an oxygen polyhedron around metal cations, which means an perfect fluorite structure with less oxygen vacancy[183,184]. Therefore, it can be assumed that dissociated oxygen atoms on LSCF will spill over on SDC, and vacancy of SDC is taken by diffused oxygen to 3PB ($O^{2-}_{/LSCF} + V_{o``/SDC} = O_o^{x}{}_{/SDC}$)[2]. Although, Ce^{3+} related oxygen vacancy peak is usually found in $560cm^{-1}$, it is hard to make a fair comparison in band intensity, since A_g mode of LSCF ($576cm^{-1}$) overlaps in this region[185]. Rather than Ce^{3+} related oxygen vacancy peak and A_g mode of LSCF, quantitative correlation between vibrational properties with electrochemical properties has been made. Key spectral features in Raman Spectroscopy are integrated with bandwidth of $20cm^{-1}$, and synchronously measured EIS is presented in Figure 75**(b), (c), (f)**. Unlike, 3PB focused Raman evolution does not show a good agreement with polarization resistance measured with EIS, indicating that 3PB ORR pathway is not dominant in model cell. In particular, while evolution of Raman bands shows exponential increase with cathodic bias, polarization resistance shows large decrease at lower cathodic bias then reaches plateau in higher cathodic bias. This phenomenon is expected, since we designed the ORR

performance of model cell to be majorly controlled by dense 2PB LSCF, and it is reasonable that a single line of 3PB LSCF-SDC cannot overwhelm to be a rate limiting pathway.

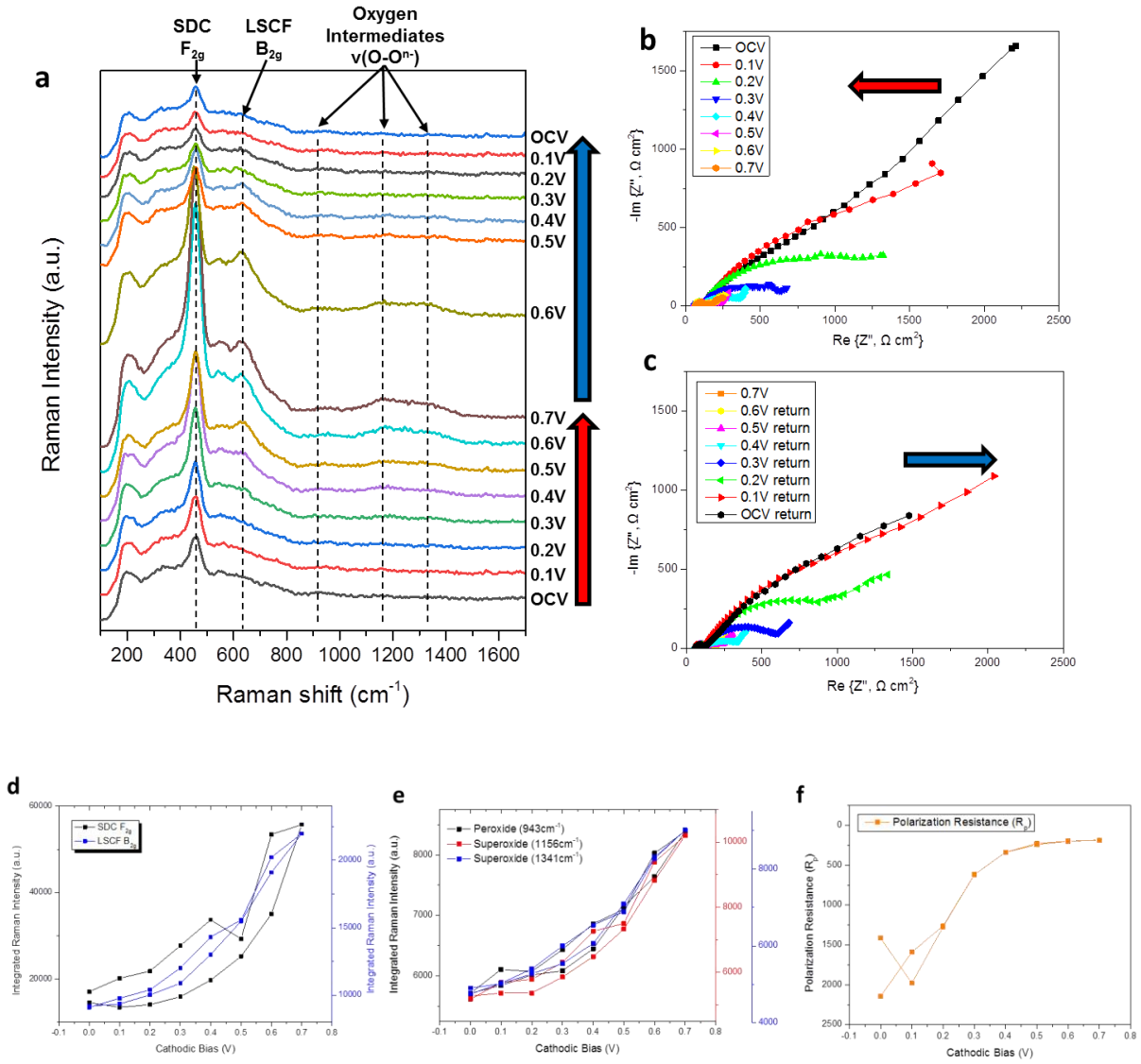

Figure 75. *Operando* Raman spectroscopic evolution under cathodic bias from OCV to 0.7V focused on 3PB. (b) Electrochemical Impedance Spectroscopy (EIS) of LSCF asymmetric cell in O_2 at 600^{o}C from OCV to 0.7V (c) Electrochemical Impedance

Spectroscopy (EIS) of LSCF asymmetric cell in O_2 at 600^oC from 0.7V to OCV. Quantitative correlation between *Operando* spectroscopic evolution of (d) SDC F_{2g} mode, LSCF B_{2g} mode, (e) Oxygen intermediates and (f) (d) polarization resistance (R_p) of LSCF asymmetric cell versus applied cathodic (-) bias

While using the same model electrode, focus of Raman laser is moved to SDC alone region (2PB) to check evolution of SDC F_{2g} mode can be observed as in 3PB (Figure 83). Unlike 3PB region, SDC did not go through F_{2g} band evolution in varying cathodic bias from OCV to 0.7V. Since doped Ceria demonstrates a little electrical conductivity compared to LSCF, it seems facilitated ORR driven by cathodic bias is not operative on SDC alone region[186].

6.4 Conclusion

In this work, by using *operando* Raman spectroscopy on thin-film LSCF electrodes, we confirmed existence of oxygen anions under realistic operating condition for SOFCs. Additionally, we found that surface of LSCF can go through Jahn-teller distortion in cathodic bias. The structural evolution of LSCF and oxygen intermediates, combined with EIS results demonstrated a good coincidence suggesting all features are closely related and addressing the fact that covalency between transition metal and oxygen plays an important role in ORR. These experimental evidence resolves the

complexity in reaction pathway in high temperature ORR, which can lead to considerably easier formulation of ORR mechanism.

By adjusting geometry of model cell and focus of Raman beam, ORR pathways on LSCF-SDC interface (3PB) and SDC (2PB) is studied as well. Similar to LSCF 2PB, LSCF-SDC interface illustrates a Raman evolution triggered by cathodic bias. However, SDC alone 2PB did not show any Raman evolution driven by cathodic bias, indicating electrically facilitated ORR is not operative on SDC due likely to SDC's low electric conductivity.

6.5 Investigation into Surface Chemistry of the Heterogeneous Catalyst

6.5.1 BCO infiltration

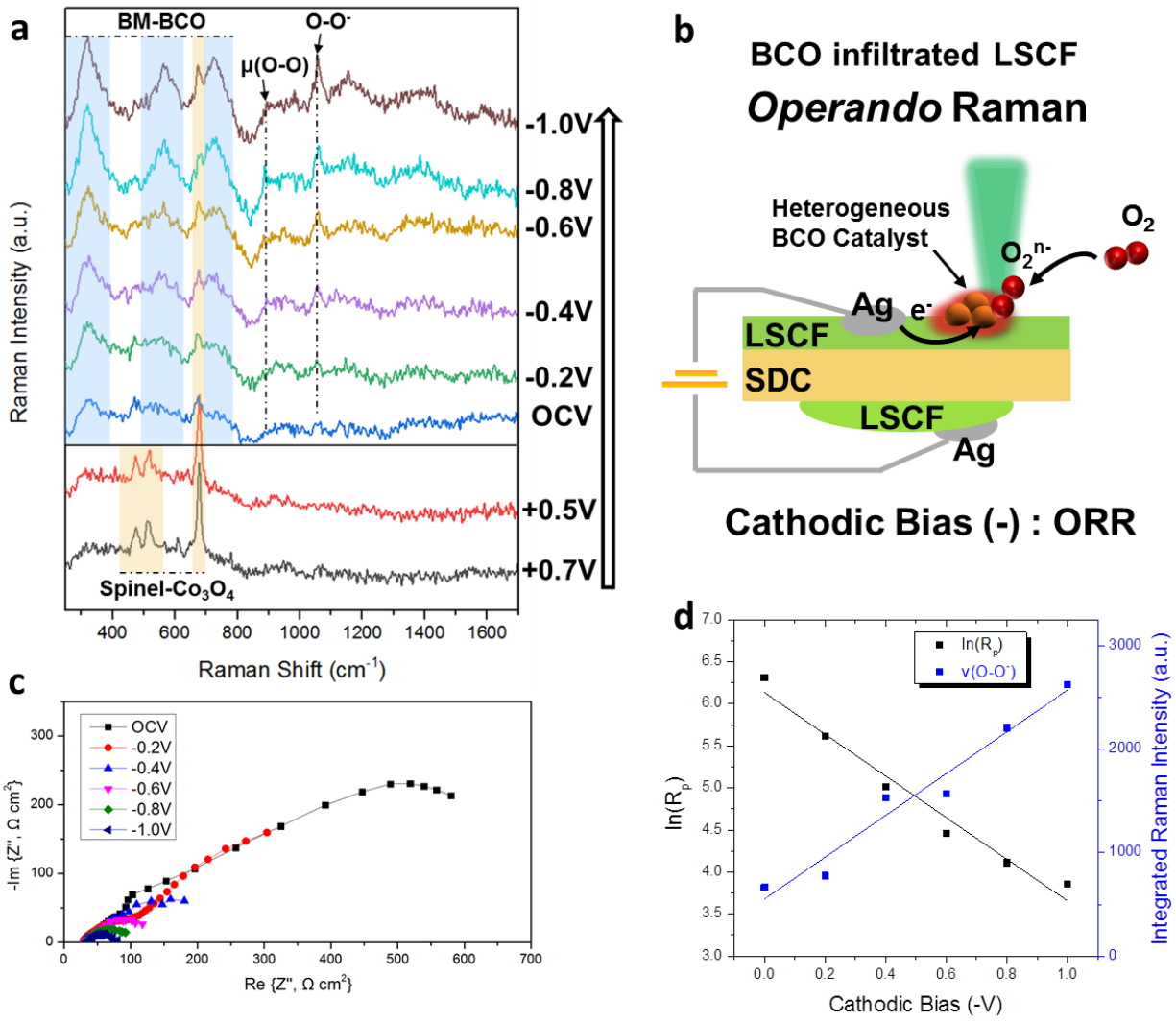

Figure 76. (a) *Operando* Raman spectroscopic evolution of BCO catalyst surface at 600°C with 1 atm O_2 atmosphere (b) Schematics for *operando* Raman spectroscopy set-up with BCO infiltrated LSCF model cell coupled with impedance spectroscopy. (c) Resulting impedance spectroscopy (d) Quantitative correlation between Raman intensity of superoxo-like species and polarization resistance.

Great prospects for BCO catalyst have been explored with symmetric cell configurations and ECR measurement. Infiltration of BCO on LSCF produced a significant improvement in catalytic activity toward ORR alongside noteworthy durability against noxious contaminants. With such good chemical compatibility with state-of-the-art LSCF cathode, BCO offers one of the best options to serve as heterogeneous catalysts while its surface modification can be effortlessly accomplished with solution-infiltration technique. Hence, it is now essential to gain fundamental information why BCO infiltration brings dramatic enhancement on ORR catalytic activity.

To gain fundamental understanding, one important step forward is to carefully examine the heterogeneous surface of BCO catalyst. Thereby, surface-sensitive *operando* Raman spectroscopy analysis is conducted to assess surface chemistry of BCO catalyst under conditions relevant to cathode of SOFC. Uniquely designed model cell with dense LSCF electrode is solution-infiltrated with BCO catalyst to elaborate surface. The model cell was placed operando Raman spectroscopic chamber with electrical connection to impedance spectroscopy, and chamber temperature was elevated to 600^{o}C with 1atm O_2 (Figure 76).

As shown in Figure 76(a), BCO shows a flexible oxygen stoichiometry between anodic to cathodic sweeping. In anodic sweeping, three Raman active phonon modes attribute to spinel structure (Co_3O_4) can be found, E_g (487 cm^{-1}), F_{2g} (529 cm^{-1}), and A_{1g} (692 cm^{-1})[142]. On the other hand, transition into brownmillerite (BM)-like phase $BaCoO_{2.5}$ (320 cm^{-1}, 564 cm^{-1}, 727 cm^{-1}) can be detected in cathodic sweeping[187]. This result manifests that BCO will turn into a phase with more oxygen vacancies to occupy favorable ORR kinetics. Along with phase transition, new band at 1057cm^{-1} is gradually

emerged with cathodic bias. Active oxygen intermediates are reported with vibrational spectroscopy in a regime of 800-1150 cm^{-1} [124,128], and Hsin-Yi et al., recently reported superoxide moieties at 1068cm^{-1} with Co_3O_4 electro-catalyst[188]. Therefore, we assigned newly evolved band as active superoxo-like species which should be a key participants in ORR pathways of BCO catalyst. With further increase of bias, additional band at 889cm^{-1} can be identified. In ORR pathways, superoxo-like species will be further reduced into peroxo-like species (μ(O-O)) with more negative charges thus O-O distance is further stretched accompanied by red shift of vibrational frequency [126,127]. Because peroxo-like species have been identified in the wavenumber region of 886-936cm^{-1} [127,188], it is reasonable to assign newly developed 889cm^{-1} band as a peroxo-like species resulting from reduction of superoxo-like species (1057cm^{-1}). The characteristic active oxygen intermediate bands with strong intensity imply the active role of BCO catalyst with reference to ORR. The extraordinary oxygen uptake capability of BCO nanoparticles was also addressed by Density Functional Theory calculation due to the presence of large amount of surface oxygen vacancies[108].

However, if surface intermediates analysis is not well-correlated with electrochemical polarization of the cell, the interpretation of spectroscopic evolution can be elusive. To avoid certain issue, the model electrode performance was recorded with impedance spectroscopy with synchronized spectroscopic evolution (Figure 76 (c), (d)). By generating quantitative correlation between vibrational features with polarization of electrode, we deliver substantial information that BCO modified LSCF surface polarization decreases in a logarithmic scale with linear increment of superoxo-like species. Thereby, it is now unambiguous that heterogeneous BCO catalyst decoration

facilitates active oxygen adsorptions which results in advanced electrochemical performance. Overall, careful examination of surface science is conducted with *operando* Raman spectroscopy.

6.5.2 SCO infiltration

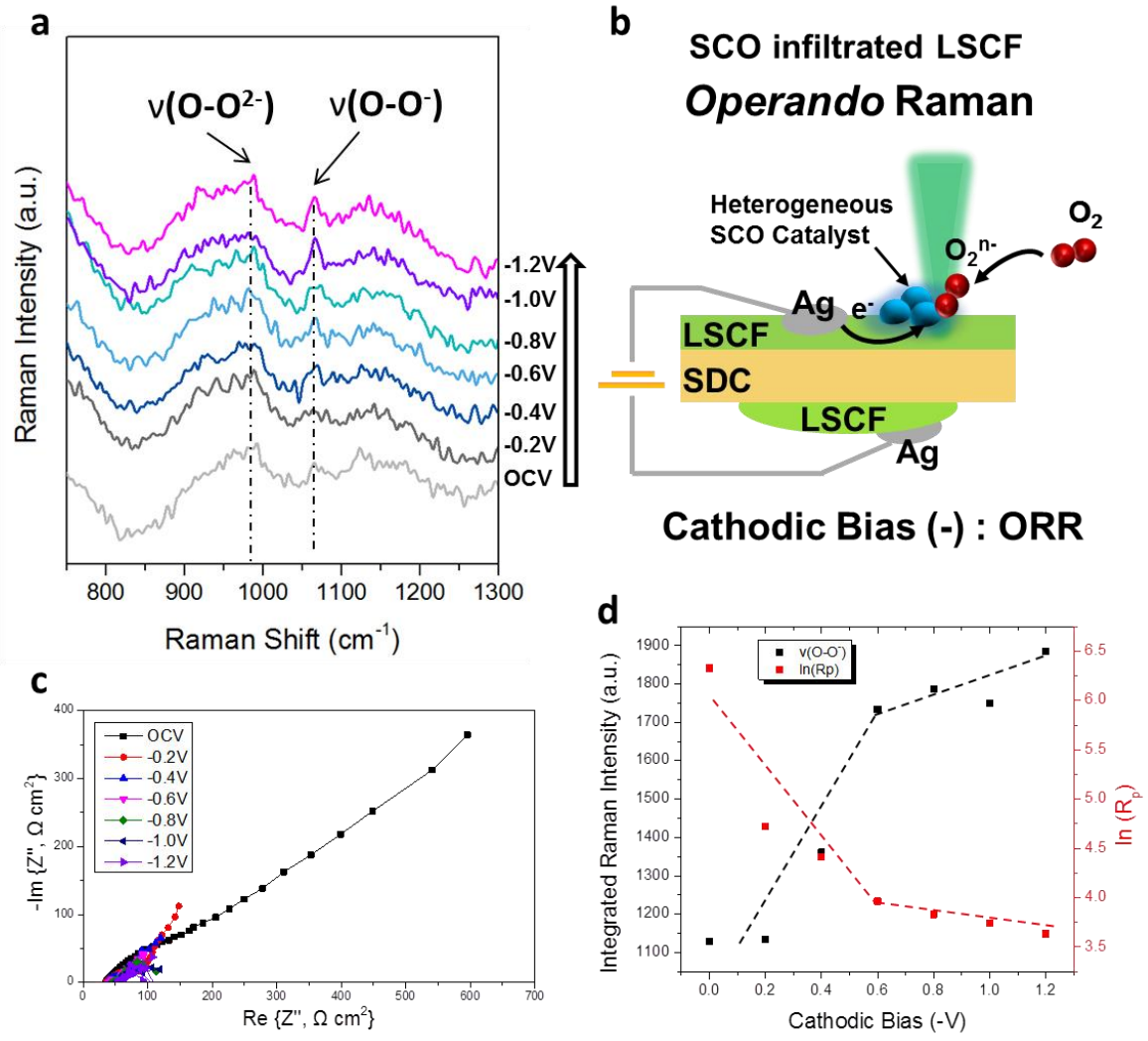

Figure 77. (a) *Operando* Raman spectroscopic evolution of SCO catalyst surface at 600°C with 1 atm O_2 atmosphere (b) Schematics for *operando* Raman spectroscopy set-

up with SCO infiltrated LSCF model cell coupled with impedance spectroscopy. (c) Resulting impedance spectroscopy (d) Quantitative correlation between Raman intensity of superoxo-like species and polarization resistance. Dotted trend line is added to guide the eye of audience.

While SrO segregation is a well-known degradation mechanism that threats long-term stability of fuel cell based on state-of-the-art LSCF cathodes, solution-infiltration of SCO catalyst effectively suppresses Sr segregation and mitigated performance degradation at its best. Both stability and catalytic activity of LSCF can be fully promoted when active SCO catalyst elaborates the backbone of LSCF. The high OER catalytic activity of $SrCoO_{2.7}$ catalyst was proposed as well, although experimental condition was in room temperature[189]. According to Mefford et al., Sr^{2+} substitution in $La_{1-x}Sr_xCoO_{3-d}$ creates ligand holes which results in more oxygen vacancy with high activities. It is also attractive that solution-infiltration needs only a trace amount of catalyst thereby offers cost-effective post modification option for commercial LSCF cathode. Since application of SCO catalyst brings such manifold positive perspectives, it is now imperative to inspect surface science of SCO infiltrated LSCF electrode to understand performance enhancement.

To have deeper understanding on enhanced ORR catalytic pathway formulates on SCO infiltrated LSCF, surface-sensitive *operando* Raman spectroscopy was performed to track surface chemistry. Designed model cell with dense LSCF electrode is decorated with heterogeneous SCO catalyst by infiltration method, and cell is connected to

impedance spectroscopy while synchronized Raman beam illuminates the catalyst surface (Figure 77(b)). Resulting high temperature Raman evolution is shown in Figure 77. The counter electrode is composed with porous LSCF electrode so that working electrode can play as rate-limiting-step. This design enables polarization of electrode to be majorly controlled by model electrode which allows easy detection of reaction intermediates.

When cathodic bias is applied on the cell to facilitate ORR, new band at 1065cm^{-1} is progressively developed. The wavenumber is much red-shifted rather than gaseous oxygen peaks (1557cm^{-1}), indicating that observed O-O bond length is stretched. The wavenumber regime of 800-1150 cm^{-1} is where active oxygen intermediates are reported, and superoxide moieties ($O\text{-}O^{-}$, 1068cm^{-1}) is reported by Hsin-Yi et al., recently with Co_3O_4 electro-catalyst[188]. Hence, we assigned newly evolved 1068cm^{-1} band as superoxo-like species on SCO catalyst. Superoxo-like species accumulating behavior under increasing cathodic bias is correlated with concurrent polarization measurement authorized by impedance spectroscopy (Figure 77(d)). Interestingly, electrode polarization demonstrates a trend similar to Tafel kinetics, indicating our model electrode functioned as rate-limiting-step as we intended. Superoxo-like species intensity shows a good agreement with trend of polarization resistance, particularly high intensity of superoxo-like species results in low polarization resistance.

It is interesting to mention that SCO modified surface inherently exhibits 989 cm^{-1} peak even with no current drawing, contrast to plain LSCF which has little Raman sensitivity due to its centrosymmetric structure (*R3c*). In first-principles study by Zhenbin et al., they envisioned peroxide ($O\text{-}O^{2-}$) vibrational frequency is in a wavenumber region between 886 ~ 936 cm^{-1} and indicated an energy barrier to overcome for peroxide to

dissociate in LSCF[127]. While SCO infiltration leads to an environment with favorable oxygen adsorptions, charge-transfer reaction is notorious for its sluggishness in ORR kinetics[156]. The reaction bottleneck may responsible for accumulation of peroxo-like adsorbed species and therefore they are detectable with spectroscopic evidence found in 989cm^{-1}.

Overall, spectroscopic evolution on SCO infiltrated LSCF is examined. The characteristic band corresponds to active oxygen intermediates that originally not detectable on plain LSCF are undoubtedly an indication that SCO modified surface has superior ORR kinetics. Specifically, infiltration of SCO conveys expanded amount of oxygen vacancy, which expedites oxygen adsorption along with higher electrochemical performance.

6.6 Experimental

6.6.1 Fabrication of LSCF model Cell

Electrolyte supported model cells were fabricated to allow for *operando* Raman investigation. Commercial $Sm_{0.2}Ce_{0.8}O_{2-\delta}$ (SDC; Fuel Cell Materials, US) and 2 wt% Polyvinyl Butyral (Sigma-Aldrich) were balled milled in ethanol for 24 hours, dried, uniaxial pressed to 3 tons in a 10 mm die, and sintered at 1450 ℃ for 5 hours to form dense electrolyte pellets. One side of the pellets were polished to a 0.1 µm finish using an Allied MetPrep 3TM. To form the porous counter electrode, slurry of $La_{0.6}Sr_{0.4}Co_{0.2}Fe_{0.8}O_{3-\delta}$ (LSCF; Fuel Cell Materials, US), V006 (Heraeus, US), and

acetone (Sigma-Aldrich) in a 1:1:0.6 mass ratio was ball milled for 24 hours. Four coats of the slurry was brushed onto the unpolished SDC side, allowing ten minutes to dry between coats, and fired at 1080 ℃ for 2 hours. The dense electrode was fabricated via a sputtering process. The chamber was pumped down to below $5*10^{-5}$ mbar and back filled to $2.5*10^{-2}$ mbar by flowing 90 sccm of Argon. The 1 inch LSCF target was RF sputtered at 15W for 8 hours onto the room temperature polished SDC. Post deposition annealing was performed at 800 ℃ for 2 hours.

6.6.2 Operando Raman Spectroscopy

Raman spectra were obtained using a Renishaw RM 1000 spectromicroscopy system (~2 μm spot size). An air-cooled Ar laser (CVI Melles Griot) emitted at 514 nm was used for excitation of Raman signal in this study with a total power of 15 mW. A Harrick environmental chamber was used for *in situ* Raman tests. [76] An *in situ* time-resolved study was conducted by placing the laser spot on the same location. To perform *operando* Raman spectroscopy study, the dense LSCF electrode is connected as working electrode (WE), and the porous LSCF electrode is connected as counter electrode (CE). Gas (UHP300 O_2, Airgas) is metered with mass flow controllers and introduced into the chamber. An *in situ* Raman evolution of LSCF model electrode at different temperature is shown in **Figure S2**.

6.6.3 XRD diffraction

Compositional analysis was performed using a Panalytical X'Pert Pro Alpha-1 X-ray Diffractometer. Sputtered samples were annealed prior to XRD analysis to crystallize the film as amorphous phases are not identifiable using XRD. XRD shows diffraction profiles for the bare SDC electrolyte pellet, LSCF target, and LSCF film on SDC pellet. The analysis shows all phases are crystalline with no unknown or unexpected phases. The peaks labeled LSCF show the composition of the target and film are LSCF 6428, while the peaks labeled SDC show the phase of the electrolyte is pure SDC. As expected, the thin film sample shows both SDC and LSCF, as the X-ray penetration depth is larger than the LSCF film thickness. These results verify that LSCF was successfully deposited on SDC.

6.7 Supplementary Information

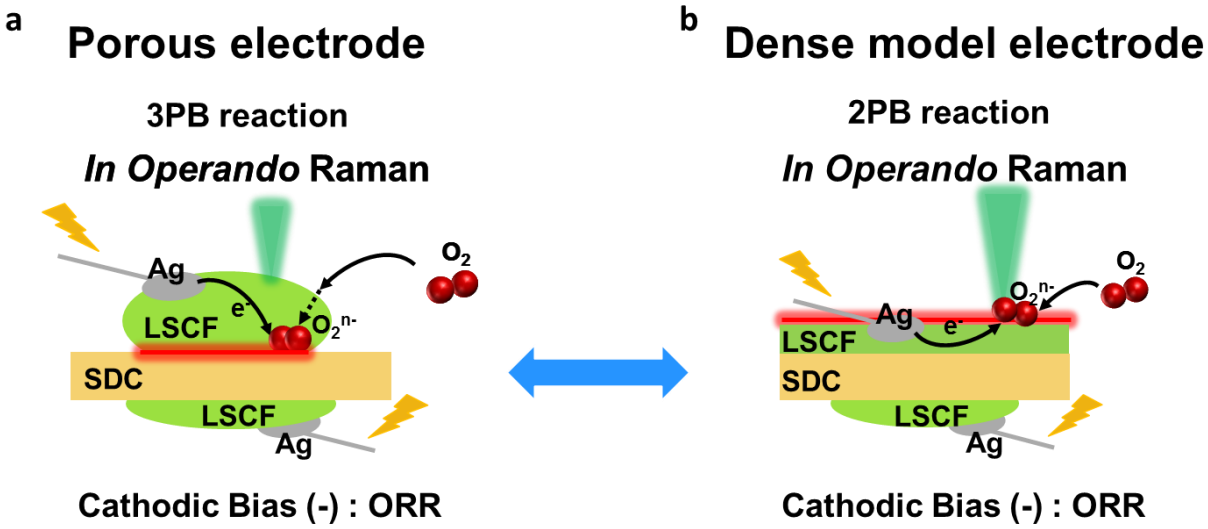

Figure 78. Schematic diagram of *operando* Raman spectroscopy explaining ORR schematic in cathodic (-) bias applied to the cell. Red line represents hotspot where ORR

will preferentially take place. (a) Conventional porous electrode with symmetric geometry, (b) Designed model electrode with dense LSCF layer

Figure S1. Schematic diagram of *operando* Raman spectroscopy explaining ORR schematic in cathodic (-) bias applied to the cell. Red line represents hotspot where ORR will preferentially take place. (a) Conventional porous electrode with symmetric geometry, (b) Designed model electrode with dense LSCF layer

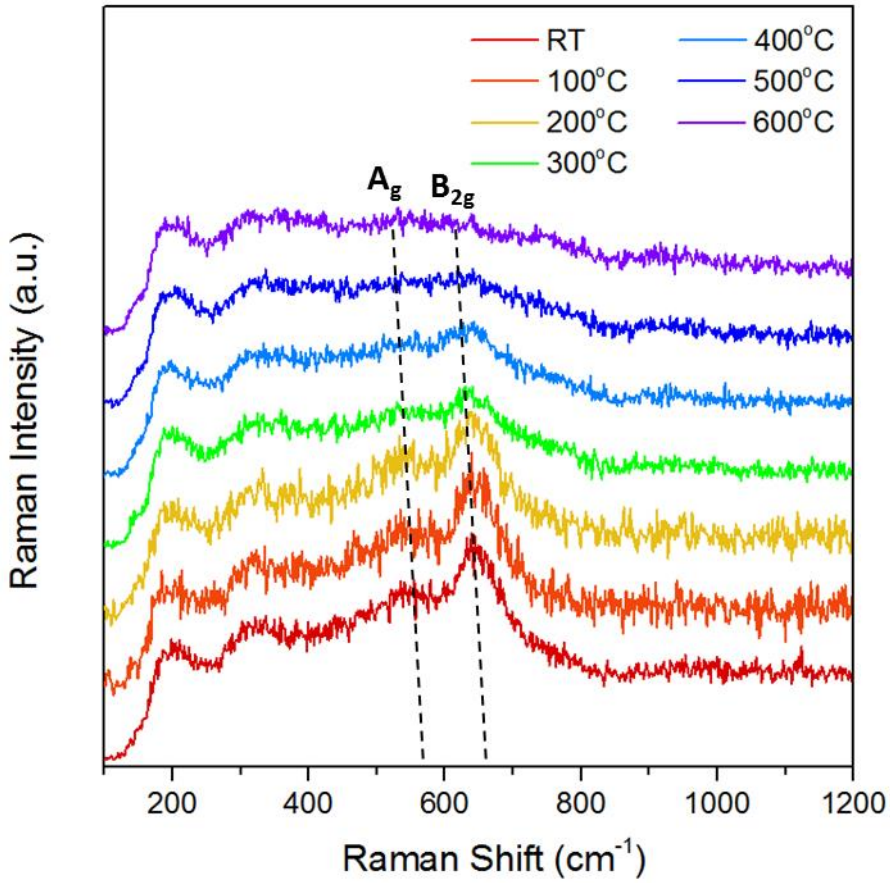

Figure 79. *In situ* Raman measurement of LSCF model electrode at different temperatures. Band intensity of A_g mode and B_{2g} mode of orthogonal perovskite

decreases as temperature increases indicating that LSCF loses surface oxygen to have more vacancy, which lead to a rhombohedral perovskite with little Raman activity.

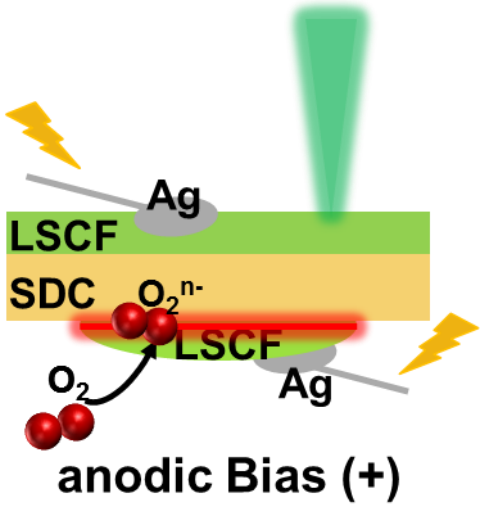

Figure 80. Schematic diagram of *operando* Raman spectroscopy explaining anodic (+) bias applied to the cell. Red line represents hotspot where ORR will preferentially take place.

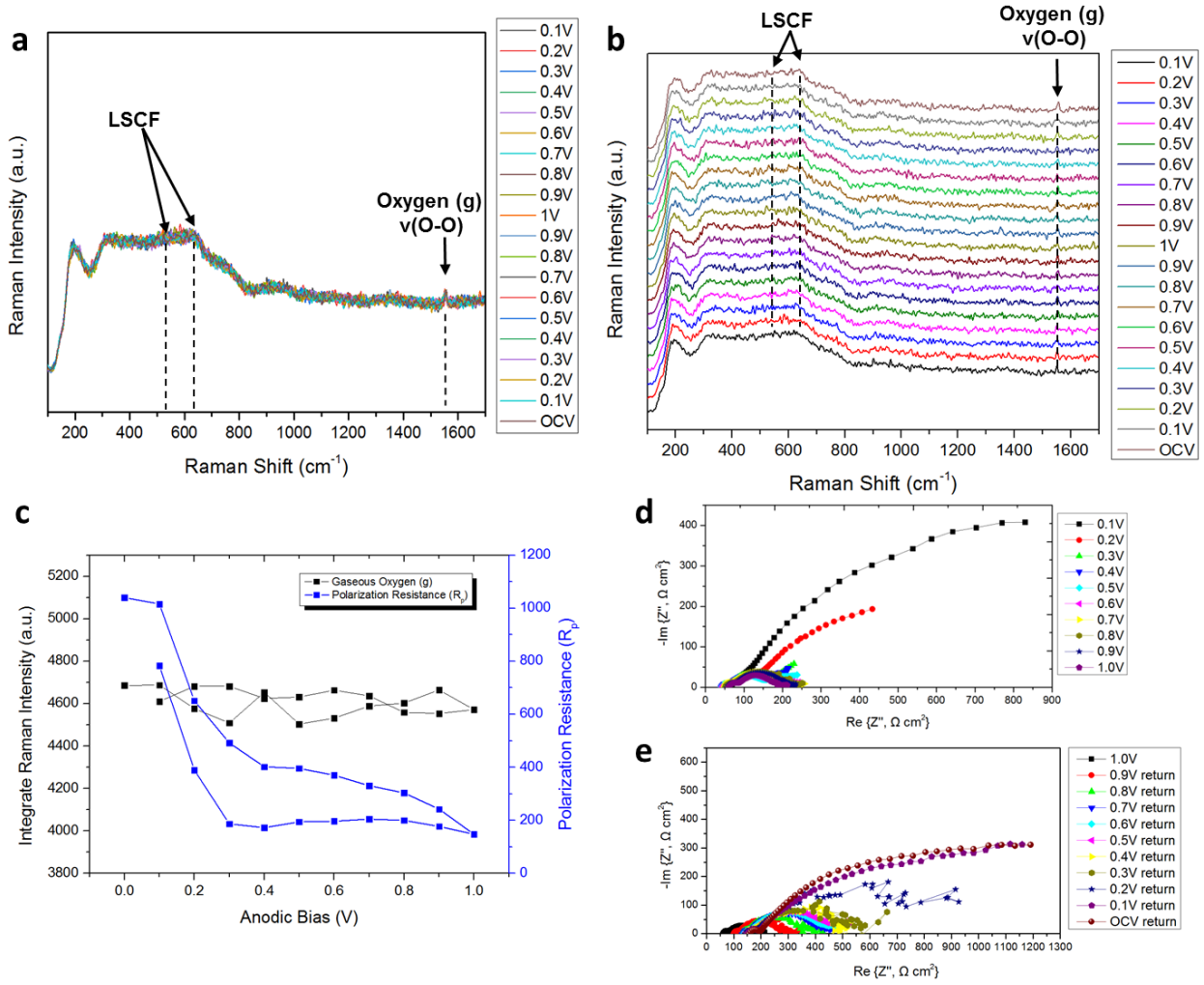

Figure 81. (a) Superimposed *Operando* Raman spectroscopic evolution under anodic bias (b) *Operando* Raman spectroscopic evolution under anodic bias (c) Quantitative correlation between EIS and Spectral feature. Unlike cathodic bias where ORR is happened on model electrode (where Raman laser is focused on), there are no visible correlation between Raman and R_p since ORR is mainly happening on counter electrode. (d) Electrochemical Impedance Spectroscopy (EIS) of LSCF asymmetric cell in O_2 at 600^{o}C from OCV to 1V (anodic) (c) Electrochemical Impedance Spectroscopy (EIS) of LSCF asymmetric cell in O_2 at 600^{o}C from 1V (anodic) to OCV

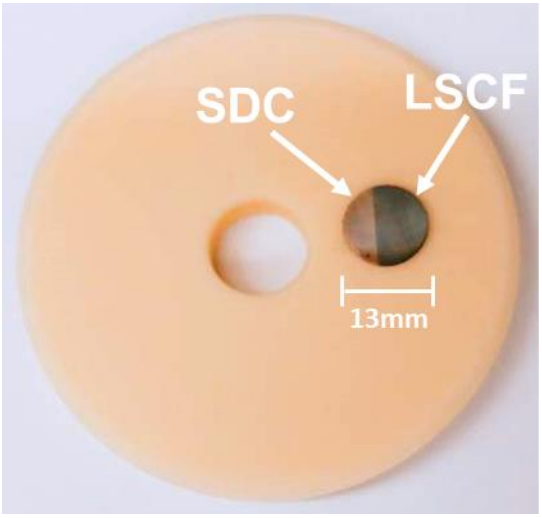

Figure 82. Camera image of LSCF-SDC 3PB model cell. Dense layer of LSCF is sputtered on SDC with mask to produce a line of 3PB.

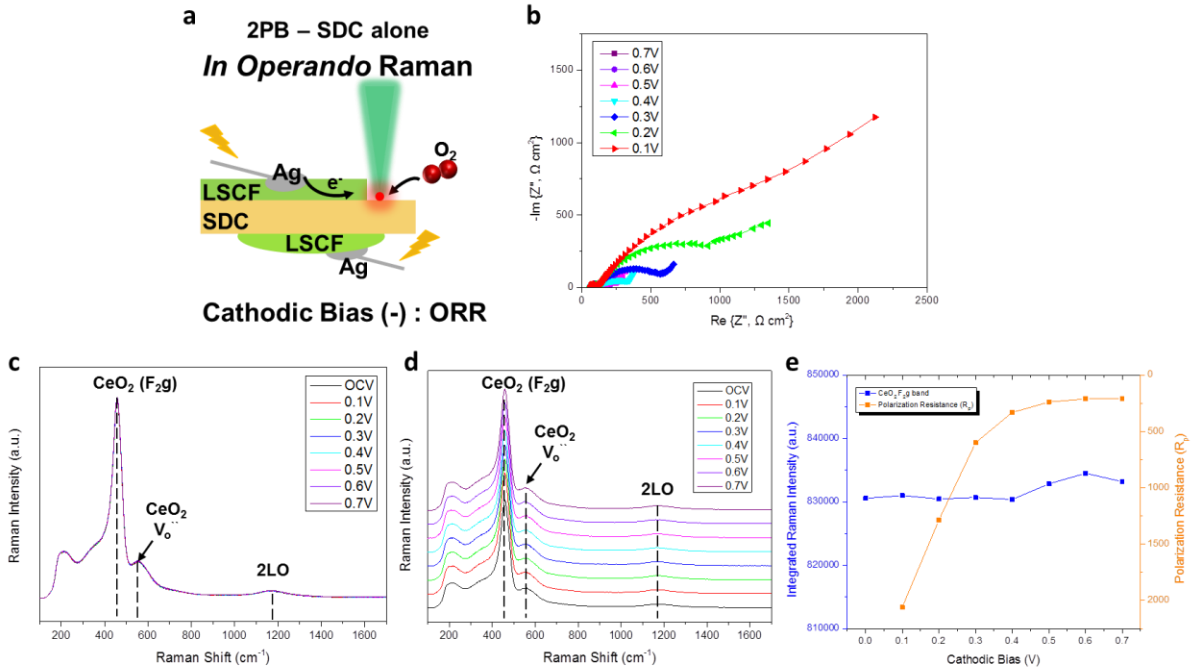

Figure 83. (a) Schematic diagram of *operando* Raman spectroscopy explaining ORR schematic in cathodic (-) bias applied to the cell while Raman laser is focused on SDC alone region. (b) Electrochemical Impedance Spectroscopy (EIS) of LSCF model cell in O_2 at 600^{o}C from 0.1V to 0.7V (cathodic) (c) Superimposed *Operando* Raman spectroscopic evolution under cathodic bias (d) *Operando* Raman spectroscopic evolution under cathodic bias (e) Quantitative correlation between EIS and Spectral feature.

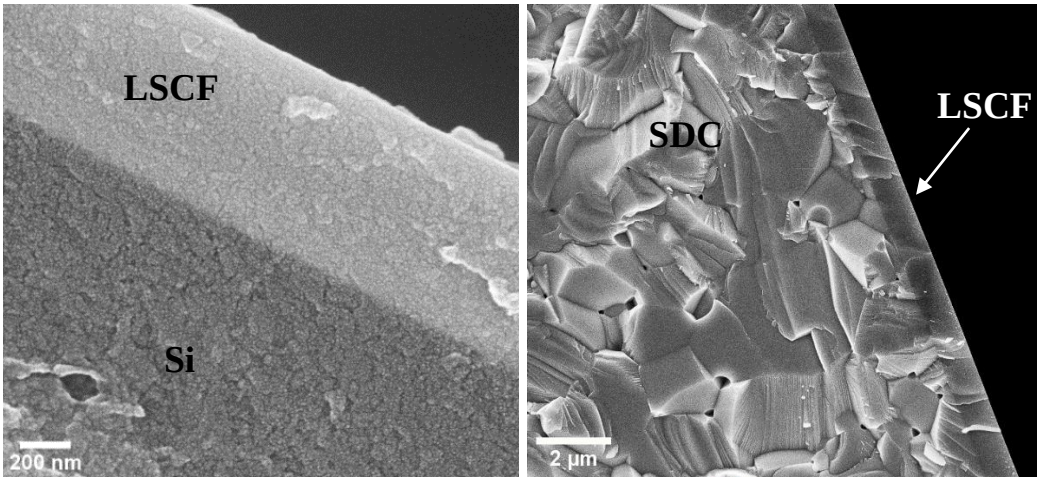

Figure 84. Figure SEM LSCF thin films on Si and SDC. SEM shows the cross section of the sputtered LSCF films on silicon and polished SDC. The images show the film is dense and free of cracks.

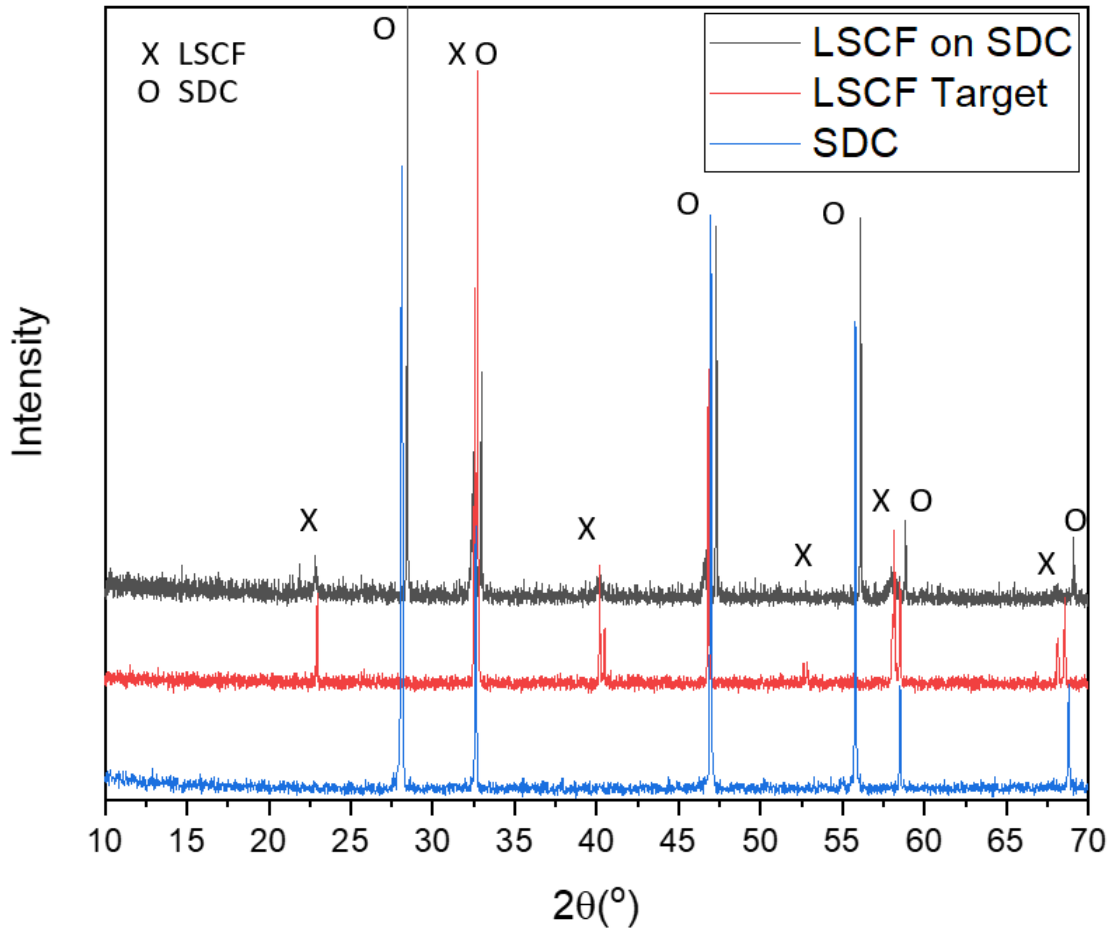

Figure 85. X-ray Diffraction profiles of the LSCF film on SDC electrolyte, LSFC target, and bare SDC electrolyte showing the pure and crystalline phases achieved.

CHAPTER 7. CONCLUDING REMARKS AND BROADER IMPACTS

7.1 Concluding Remarks and Broader impacts

The goal of the thesis is to develop and apply novel technologies to build a quantitative correlation between surface intermediates with electrochemical performance of electrodes, and expand its understanding to molecular dynamics. Concurrent measurement of surface intermediates and polarization resistance measurement under applied bias can give us critical understanding how reaction pathways formulate. By controlling atmospheres, we can understand the dynamics of performance degradation of cell experiences under various contaminants, which is critical in developing novel and robust electrode materials. Therefore, this thesis focuses on *in situ / operando* probing of SOFC electrode surface in realistic operating condition to gain fundamental understanding of solid-gas interactions. The effort to understand surface science of electrode is further extended to develop operando platform with synchronized impedance measurement and some studies were successfully transferred to DFT calculations as well.

Beyond the development of *operando* platforms, I have applied my skills to improve understanding of many other solid-gas interactions for SOFC electrode. Unique characterization method used in this study can be readily transferred to the other SOFC anode material studies as well. For instance, cermet model electrode can be replaced by different metal (e.g., Pt, Cu) or different oxygen ion conductors (e.g., YSZ, GDC) readily. By controlling the inlet fuel gas, not only sulfur-poisoning but also carbon coking or steam reforming on model anode could be easily studied. Moreover, the unique

experimental set-up and methodologies are not limited to anode study, and can also be applied for cathode contamination to unravel the degradation mechanism by the CO_2[19].

In Chapter 3, we discussed about Ni-YSZ anodes steam reforming catalytic activity, and studied how sulfur can affect its steam reforming catalytic activity. Natural gas is an attractive fuel of choice for solid oxide fuel cells (SOFCs) because it is primarily composed of methane. It is known that fuel cell operation of methane (CH_4) with high steam (H_2O) level can lead to internal reforming for production of Hydrogen (H_2) which can alleviate the coking on Ni-based anodes. However, natural gas often contains ppm level of sulfur which can lead to failure of Ni-based fuel cell anodes. While steam-reforming and sulfur-poisoning have been extensively studied in isolation, little information has been reported on the combined effects. In chapter 3, we report a long-term SOFC operation of simulated natural gas (H_2S laden CH_4) with steam reforming. In electrochemical data, it can be concluded that amount of sulfur in CH_4 can hamper steam reforming catalytic activity of Ni-YSZ. To gain insight for sulfur-poisoning mechanism, designed model electrode is used to conduct *in situ/operando* Raman Analysis. While *in situ* Raman evolution with pure steam-CH_4 revealed CO bands on surface of Ni-YSZ which is an evidence for steam-reforming, sulfur contaminated Ni-YSZ instead shows v(S-S) with no further evolution of CO band. The two distinct spectral results lead to a conclusion that sulfur adsorption on TPB hamper the steam reforming catalytic activity of Ni-YSZ.

In Chapter 4, we discussed about anti-sulfur nature of proton conducting oxide. While protonic ceramic anodes such as Ni-$BaZr_{0.1}Ce_{0.7}Y_{0.1}Yb_{0.1}O_{3-d}$ (BZCYYb) showed its promise for sulfur tolerant anodes, extreme low concentration (ppm level) of sulfur

molecules renders it difficult to investigate corrosion and/or tolerance dynamics by conventional surface characterization techniques. In chapter 4, we present the detailed information of water-mediated sulfur tolerance mechanism of Ni-BZCYYb in realistic operating condition empowered by surface-sensitive, *operando* surface enhanced Raman spectroscopy (SERS) analysis coupled with impedance spectroscopy. In contrast to the conventional view that introduced sulfur(S^*) will be mainly removed through oxygen anion delivery from ionic conductor phase, we find that -SO_4 surface functional group is a primary intermediate species on proton conducting oxide. As reflected in SERS spectral features and followed DFT calculation, we propose that presence of water and distinctive water uptake characteristics of proton conducting oxides facilitate SO_2 reforming from adsorbed –SO_4. The unique approach of *operando* SERS with model electrodes offers an effective tool for investigating complex mechanisms.

In chapter 5, we demonstrated a water-stable cathode based on double perovskite, and explained how water enhances ORR rate on double perovskite. Developing water-stable material for oxygen reduction reaction (ORR) is a main hurdle for clean energy technology, especially for Solid Oxide Fuel Cell (SOFCs) cathode, since many state-of-the-art cathodes (e.g., LSCF, LSM) are reported to have compromised ORR catalytic activity under humid air. While there were many contributions made, ORR in high temperature still needs deeper understanding to develop water-stable cathodes. In chapter 5, we rationally design a mixed ionic & electronic conductor (MIEC) double perovskite material PBCC ($PrBa_{0.8}Ca_{0.2}Co_2O_{5+d}$), which is not only water-stable, but also has water-promoting ORR. Furthermore, for the first time, *operando* Raman characterization of chemisorbed oxygen species on double perovskite electrode at elevated temperature is

successfully conducted and therefore, water-promoting ORR mechanism on high temperature could be hypothesized. This work highlights the molecular insights of water-promoting ORR mechanism and comprehensive analysis combined in this work will help rational design of water-stable ORR catalysts for future.

In chapter 6, we examined structural alteration of LSCF cathode during cathodic polarization. Monitoring surface of perovskites during oxygen reduction reaction (ORR) may give profound understanding on molecular insight of electro-catalysts. Although many first-principle studies illustrated oxygen intermediates on perovskites, intrinsic Raman inactivity of near-cubic perovskites and conventional porous electrode morphology limits the detection of surface redox centres. In chapter 6, we report a direct observation of ORR pathways on thin-film $La_{0.6}Sr_{0.4}Co_{0.2}Fe_{0.8}O_{3-d}$ (LSCF) electrode at elevated temperature enabled by surface-sensitive, *operando* Raman spectroscopy coupled with impedance spectroscopy. Counter to conventional perspectives that Jahn-teller degeneracy imposes trivial impact at high temperature, we find LSCF go through significant Jahn-teller distortion together with contemporaneous superoxo, peroxo-like species accumulation. We propose LSCF structural distortion attributes to spin-state rearrangement, populates its electronic structure near fermi level to exchange electrons with oxygen adsorbates. This result highlights the deeper understanding of ORR intermediates and concurrent Jahn-Teller distortion in oxygen-deficient perovskite as redox partner.

As I already explained, there are multiple gaseous species which has not been explored in detail mechanisms, and only a few materials were studied in this thesis. If we think about the combination of materials, morphology, interface, heterogeneous catalysts,

temperature, atmospheres, etc., it still needs tons of effort, and numerous studies can be engendered accompanied by valuable insights (Figure 86). The developed methodology is applicable to study of electrode/catalyst materials in other chemical and electrochemical systems as well. I believe my dedication in this thesis offers profound understanding on surface science of SOFC electrode, thus leads to a development of novel electrode that is commercially viable.

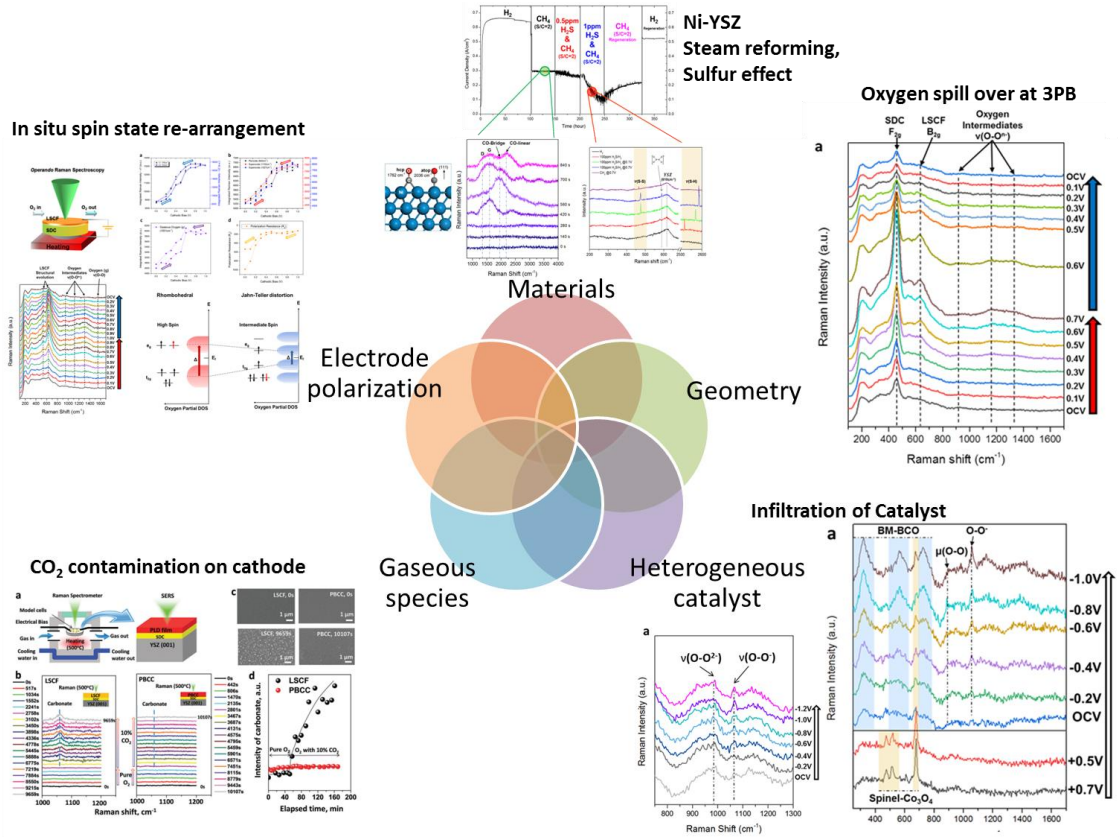

Figure 86. Broader impacts of developed *operando* Raman spectroscopic platform.

In my thesis, I provided scientific basis for knowledge-based design of durable anodes against sulfur poisoning for SOFCs powered by sulfur-contained fuels. For instance, the distinct surface information between oxygen ionic conductor and mixed

ionic conductor (proton conducting oxide) demonstrated in my thesis can give a valuable insight for realistic operation of solid oxide fuel cell. As we found out on Ni-YSZ, at high operation temperature sulfur exists in elemental sulfur, while cooling down of the sample will eventually forms a bulk-sulfide which will urge a permanent damage on overall microstructure and thus cause an irreversible damage. For fuel cell, good thermal cycling performance must be achieved for its commercialization. This is particularly important when power is not required or in the event of emergency shutdown.[190] Due to its high operating temperature, SOFC stands a long period of time for thermal cycling. In this sense, formation of bulk-sulfide should be avoided to accomplish a good thermal cycling stability. Therefore before cooling down of the fuel cell, the adsorbed sulfur should be cleaned with proper purging gas to retain its original structures and performance. However, because Ni-YSZ anode does not have good water adsorption capability, even with high water supply (steam to carbon ratio = 2) it could not clean the sulfur-poisoned surface itself. As I mentioned, sole expectation of oxygen anion flux to remove sulfur contaminant may be insufficient to achieve robust operation of fuel cells. Rather, use of proton conducting oxide can be an effective strategy. The toxicity of sulfur compounds is determined by how much electron pair are available for sulfur species to interact with metals. In this sense, proton conducting oxides are prone to form $–SO_4$ to protect Ni metal, and at the same time, introduction of water can clean the $–SO_4$ to reform as SO_2. If we develop a nano-structured anode so that Ni particles are well dispersed with proton conducting oxide, Ni itself can be preserved during sulfur-contained fuel, and introduction of steam purge before thermal cooling would perfectly clean the anode surface so that it would not prompts bulk-sulfide formation on SOFC anodes. Further, as

we found in DFT calculation, formation of vacancy on proton conducting oxide can actually affects their hydration capability. Therefore, introduction of proper dopants in proton conducting oxide to create vacancies can be an effective strategy to optimize the water adsorption capability of anodes therefore can help a situation where there is not enough inlet water vapor supply, while anode can itself oxidize H_2 fuel to generate H_2O to perform self-sufficient reforming of $–SO_4$ to SO_2. For the ionic conductor with no proton conductivity such as YSZ and GDC, use of desulfurizer can be a solution or the reforming layer of proton conducting oxide should be considered to gain water-mediated sulfur-tolerance. Realistically, in the clean natural gas or practical gases available in the market (i.e., Diesel, Gasoline), the level of sulfur content usually do not exceeds 30 ppm, and therefore after proper reforming of the carbonaceous fuels, 3vol% of water may be enough for proton conducting oxide based anodes to have good tolerance (based on chapter 4, 3vol% H_2O can clean 100ppm H_2S/H_2 developed $–SO_4$).[1] However if higher concentration of sulfur such as jet-fuel is used, higher concentration of water supply should be considered. Recently, high water vapor operation (steam to H_2 = 2) based on proton conducting oxide such as Ni-BZY anode is reported to have good sulfur-tolerance as well as good thermal cycling capability.[77] Actually, the detailed quantitative information of water-mediated sulfur-tolerance regarding water-sulfur partial pressure should be further analyzed for series of proton conducting oxides to create a phase map which can guide a rational operating conditions for future SOFCs. It should be noted that even though the anode materials can tolerate high concentration of sulfur contaminant, the fuel cell exhaust should be cleaned before emitted to the air.

In my thesis, I also identified surface intermediates of ORR by *in situ/operando* Raman measurement, thus providing information vital to the design of high-performance cathode for ORR. Double perovskite structured cathode should be considered when fuel cell is operated under humid ambient air. According to Grimaud et al., the potential of these mixed ionic conductors can be fully promoted when proton conducting electrolyte is used.[120] By using BZCYYb electrolyte, it is found out that R_p of the cathode can be controlled by following equation.

$$R_p \propto pO_2^{-n} \cdot pH_2O^{-m}$$

Where n and m being the reaction orders with respect to pO_2 and pH_2O, respectively. Therefore in their article, when water vapor pressure is increases, polarization resistance decreases even with >20v% water, while PBCC based on SDC electrolyte only demonstrated decrease in polarization resistance until 10v% water. We explained water concentration threshold behavior by calculating coadsorption energies of a superoxo species with hydroxyl species. As we can see in the Figure 87, if surface exchange site is completely saturated with hydroxyl group, there will be no active sites for O_2 to adsorb and O_2 need to compete with water for active sites. Therefore the adsorption energy increases after surface proton coverage exceeds 0.4 ML.

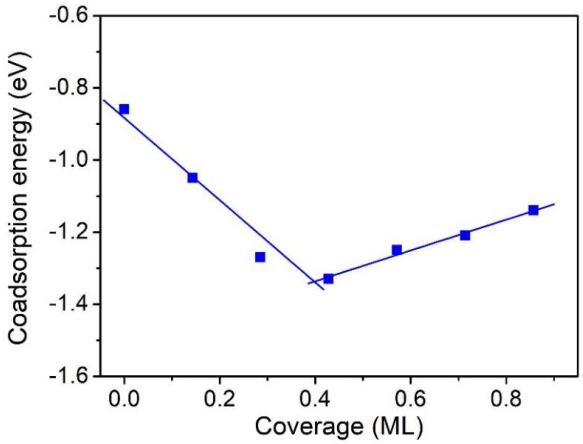

Figure 87. Coadsorption energies of a superoxo species with hydroxyl species on defective PBCC(010).

If proton transport is blocked by electrolyte such as SDC, proton will only confined in the cathode and therefore after water saturation, proper water-release should happen to expect proper O_2 adsorption on double perovskite to perform ORR. In this sense, use of proton conducting electrolyte will guarantee a facile transport of proton which prevents the water saturation on these cathode materials. Also, the active site of water-release reaction can be extended to proton conducting electrolyte, electrolyte-electrode interface as well. Therefore, to fully promote the ORR promotion of double perovskites, utilization of proton conducting electrolyte can be a promising approach.

7.2 Limitation of the characterization method and potential breakthroughs

Although my study signifies its impact on realistic kinetic control that is relevant to SOFCs, it is worth noting the limitations of these characterization methods so that further improvement can be made in future.

7.2.1 Limitations of spectral interpretation

One challenge is the spectral assignment of Raman bands to unknown species. The databases of Raman spectroscopy are not well-established compared to those of XRD, and spectral assignment of Raman analysis still heavily depends on comparisons against reported values from literature. Even with similar geometry of functional groups, its vibrational frequency can largely deviate by its composition of elements, and environmental surrounding that can potentially affect bonding energy. Therefore, interpretation of Raman bands can be especially challenging when observed vibrational feature has never been reported.

Potential breakthrough can be satisfied by DFT calculation to precisely predict vibrational modes of unknown species/phases. Many DFT calculations successfully generate vibrational frequency of certain phases, and/or adsorbate bond lengths. By correlating empirical observation with computation method, trustworthy assignment for unknown species can be accomplished.

7.2.2 Limitation of analysis based on one laser spot

Raman spectroscopy relies on beam scattering, and laser illuminates a confined spot (2μm ~ 5μm). Therefore, it is risky to claim a small illuminated spot represents whole electrode area and caution is warranted to analyse *in situ* spectroscopic result. To avoid certain issue, our group developed model electrodes with well-defined geometry

which guarantees uniform surface for Raman measurement. Also, correlation with electrochemical performance is followed to indicate spectral evolution observed in certain area coincide the circumstance of general electrode surfaces. However, crystal facet of polycrystalline electrode can be very diverse, while different facet imposes different catalytic activity. Furthermore, it can be even more challenging when tries to study heterogeneous catalyst surface.

Possible solution can be made with Raman mapping. By area scanning of Raman spectroscopy, authentic study can be completed with designating active and/or poisoned area. However, Raman mapping is not a perfect solution, since area scanning will be performed in time order, and simultaneous measurement of all spot cannot be conducted. Thus, Raman mapping can be inappropriate to study incipient change that does not reach equilibrium. Another advance can be carried out by designing a single crystalline or spin-regulated electrode. Utilization of those electrodes with defined crystal facet should be beneficial for rigorous kinetic studies.

7.2.3 Limitation of SERS

Although SERS have been successfully exploited for high temperature SOFC electrode measurements, there is still room for improvements. For example, temperature hurdle for developed $Ag@SiO_2$ are restrained to 500^oC and it is still low temperature compared to actual operating condition of SOFC (500^oC ~ 1000^oC). Many key electrochemical reactions will be facilitated in higher temperature, thus it is important to develop SERS NPs with enhanced thermal stability. To achieve this goal, SERS NPs with

ZrO_2 or TiO_2 shell seems promising as alternatives for those with SiO_2 shell. Also, core of different metal such as Gold, and different thickness and geometry of SERS NPs should be considered to have beneficial SERS enhancement in higher temperature.

While SiO_2 is known to be inert to most catalytic reaction, deposition of nanoparticles on surface can bias surface measurement since it can physically block electrode surfaces. Therefore, development of new electrode with unique geometry can be advantageous. If model electrode with impregnated SERS NPs can be achieved, it will be expected to serve as a new paradigm for future surface chemistry measurements [24].

CHAPTER 8. RECOMMENDATIONS

In this study, *operando* Raman spectroscopy coupled with electrochemical performance shows great prospect for future catalytic studies on SOFC electrodes. However, as mentioned in earlier sections there are intrinsic limitations stem from Raman spectroscopy. Therefore I propose to employ various techniques as "add-on" with *operando* platform so that it can perform as near-perfect tool for electrode studies.

For example, only adsorbed intermediates will be detected with Raman spectroscopy thus resulting gaseous product from inlet fuel can be elusive. Furthermore, important reaction product such as reformed H_2 from carbonaceous fuel does not have certain Raman bands. Monitoring reactant-product partial pressure is undoubtedly important to conclude kinetic activity of catalysts. Therefore by attaching mass spectroscopy to exhaust line, gaseous product can be readily analyzed to provide deeper understanding.

Moreover, add-on of Diffuse Reflectance Infrared Fourier Transform Spectroscopy (DRIFTS) is desirable to gain superior understanding on reaction mechanisms regarding hydrocarbon reforming. Although, many adsorbed species are known to have active Raman modes, some reaction intermediates such as formyl (–COH) group has insufficient Raman intensity while its existence can be easily picked up with DRIFTS technique. By using complementary spectroscopy based on IR, important reaction intermediates which cannot be examined with Raman spectroscopy can be discovered to further elaborate our molecular understanding to formulate complete mechanisms.

Also, environmental chamber with stainless steel jacket used in this study is under one atmosphere condition, while actual fuel cell operates in full cell condition that electrolytes offers separating membrane between oxidizing and reducing atmosphere. To truly replicate the reaction condition of fuel cells, development of freshly devised environmental chamber that allows both atmospheres is anticipated.

REFERENCESREFERENCES

1 Cheng, Z. *et al.* From Ni-YSZ to sulfur-tolerant anode materials for SOFCs: electrochemical behavior, in situ characterization, modeling, and future perspectives. *Energy & Environmental Science* **4**, 4380-4409 (2011).

2 Choi, Y., Mebane, D. S., Wang, J.-H. & Liu, M. Continuum and quantum-chemical modeling of oxygen reduction on the cathode in a solid oxide fuel cell. *Topics in Catalysis* **46**, 386-401 (2007).

3 Liu, M. *et al.* Direct octane fuel cells: A promising power for transportation. *Nano Energy* **1**, 448-455 (2012).

4 Mogensen, D., Grunwaldt, J. D., Hendriksen, P. V., Dam-Johansen, K. & Nielsen, J. U. Internal steam reforming in solid oxide fuel cells: Status and opportunities of kinetic studies and their impact on modelling. *Journal of Power Sources* **196**, 25-38 (2011).

5 Ding, D., Li, X., Lai, S. Y., Gerdes, K. & Liu, M. Enhancing SOFC cathode performance by surface modification through infiltration. *Energy & Environmental Science* **7**, 552-575, doi:10.1039/C3EE42926A (2014).

6 Neagu, D. *et al.* Nano-socketed nickel particles with enhanced coking resistance grown in situ by redox exsolution. *Nature communications* **6**, 8120 (2015).

7 Jensen, S. H., Larsen, P. H. & Mogensen, M. Hydrogen and synthetic fuel production from renewable energy sources. *International Journal of Hydrogen Energy* **32**, 3253-3257 (2007).

8 Jiang, Y. & Virkar, A. V. Fuel composition and diluent effect on gas transport and performance of anode-supported SOFCs. *Journal of the Electrochemical Society* **150**, A942-A951 (2003).

9 Yang, L. *et al.* Enhanced sulfur and coking tolerance of a mixed ion conductor for SOFCs: BaZr0. 1Ce0. 7Y0. 2–xYbxO3–δ. *Science* **326**, 126-129 (2009).

10 Gorte, R. J. Cooling down ceramic fuel cells. *Science* **349**, 1290 (2015).

11 Wachsman, E. D. & Lee, K. T. Lowering the temperature of solid oxide fuel cells. *Science* **334**, 935-939 (2011).

12 Kaur, G. *Solid Oxide Fuel Cell Components*. (Springer, 2016).

13 Hilpert, K., Das, D., Miller, M., Peck, D. & Weiss, R. Chromium vapor species over solid oxide fuel cell interconnect materials and their potential for degradation processes. *Journal of the Electrochemical Society* **143**, 3642-3647 (1996).

14 Chen, Y. *et al.* An effective strategy to enhancing tolerance to contaminants poisoning of solid oxide fuel cell cathodes. *Nano Energy* **47**, 474-480 (2018).

15 Matsuzaki, Y. & Yasuda, I. The poisoning effect of sulfur-containing impurity gas on a SOFC anode: Part I. Dependence on temperature, time, and impurity concentration. *Solid State Ionics* **132**, 261-269 (2000).

16 Yang, L., Cheng, Z., Liu, M. & Wilson, L. New insights into sulfur poisoning behavior of Ni-YSZ anode from long-term operation of anode-supported SOFCs. *Energy & Environmental Science* **3**, 1804, doi:10.1039/c0ee00386g (2010).

17 Cheng, Z. & Liu, M. Characterization of sulfur poisoning of Ni–YSZ anodes for solid oxide fuel cells using in situ Raman microspectroscopy. *Solid State Ionics* **178**, 925-935 (2007).

18 Lee, K., Song, C. & Janik, M. J. Ab initio thermodynamics examination of sulfur species present on Rh, Ni, and binary Rh–Ni surfaces under steam reforming reaction conditions. *Langmuir* **28**, 5660-5668 (2012).

19 Chen, Y. *et al.* A highly active, CO2-tolerant electrode for the oxygen reduction reaction. *Energy & Environmental Science* **11**, 2458-2466, doi:10.1039/C8EE01140K (2018).

20 Paul L. Stiles, J. A. D., Nilam C. Shah, and Richard P. Van Duyne. Surface-Enhanced Raman Spectroscopy. *Annual Review of Analytical Chemistry* **1**, 601-626 (2008).

21 Whitney, A. V., Elam, J. W., Stair, P. C. & Van Duyne, R. P. Toward a thermally robust operando surface-enhanced Raman spectroscopy substrate. *The Journal of Physical Chemistry C* **111**, 16827-16832 (2007).

22 Li, J. F. *et al.* Shell-isolated nanoparticle-enhanced Raman spectroscopy. *nature* **464**, 392-395 (2010).

23 Li, X. *et al.* High-temperature surface enhanced Raman spectroscopy for in situ study of solid oxide fuel cell materials. *Energy & Environmental Science* **7**, 306-310 (2014).

24 Li, X., Blinn, K., Chen, D. & Liu, M. In Situ and Surface-Enhanced Raman Spectroscopy Study of Electrode Materials in Solid Oxide Fuel Cells. *Electrochemical Energy Reviews* **1**, 433-459, doi:10.1007/s41918-018-0017-9 (2018).

25 Willets, K. A. & Van Duyne, R. P. Localized surface plasmon resonance spectroscopy and sensing. *Annu. Rev. Phys. Chem.* **58**, 267-297 (2007).

26 Reece, C. An introduction to electrochemical impedance spectroscopy. *Jefferson Lab* (2005).

27 Chen, Y. *et al.* A robust fuel cell operated on nearly dry methane at 500 ℃ enabled by synergistic thermal catalysis and electrocatalysis. *Nature Energy*, doi:10.1038/s41560-018-0262-5 (2018).

28 BloomEnergy. *ES-5700 Energy Server*, <www.bloomenergy.com> (2012).

29 *Affordable fuel cell power systems for every need*, <http://www.redoxpowersystems.com/> (2015).

30 *A change of power*, <http://www.cerespower.com/> (2014).

31 Rostrup-Nielsen, J. R. Coking on nickel catalysts for steam reforming of hydrocarbons. *Journal of Catalysis* **33**, 184-201, doi:10.1016/0021-9517(74)90263-2 (1974).

32 Park, S., Vohs, J. M. & Gorte, R. J. Direct oxidation of hydrocarbons in a solid-oxide fuel cell. *Nature* **404**, 265-267 (2000).

33 Yang, L. *et al.* Promotion of water-mediated carbon removal by nanostructured barium oxide/nickel interfaces in solid oxide fuel cells. *Nature Communications* **2** (2011).

34 Kan, H. & Lee, H. Sn-doped Ni/YSZ anode catalysts with enhanced carbon deposition resistance for an intermediate temperature SOFC. *Applied Catalysis B: Environmental* **97**, 108-114, doi:10.1016/j.apcatb.2010.03.029 (2010).

35 Atkinson, A. *et al.* Advanced anodes for high-temperature fuel cells. *Nature Materials* **3**, 17-27 (2004).

36 Sasaki, K. & Teraoka, Y. Equilibria in Fuel Cell Gases: I. Equilibrium Compositions and Reforming Conditions. *Journal of The Electrochemical Society* **150**, A878-A884, doi:10.1149/1.1577337 (2003).

37 Lee, W. Y., Hanna, J. & Ghoniem, A. F. On the Predictions of Carbon Deposition on the Nickel Anode of a SOFC and Its Impact on Open-Circuit Conditions. *Journal of The Electrochemical Society* **160**, F94-F105, doi:10.1149/2.051302jes (2013).

38 Da Silva, A. L. & Heck, N. C. Thermodynamics of sulfur poisoning in solid oxide fuel cells revisited: The effect of H<inf>2</inf>S concentration, temperature, current density and fuel utilization. *Journal of Power Sources* **296**, 92-101, doi:10.1016/j.jpowsour.2015.07.046 (2015).

39 Rostrup-Nielsen, J. R. Some principles relating to the regeneration of sulfur-poisoned nickel catalyst. *Journal of Catalysis* **21**, 171-178, doi:10.1016/0021-9517(71)90135-7 (1971).

40 Riesz, C., Dirksen, H. & Kirkpatrick, W. Sulfur poisoning of nickel catalysts. *Institute of Gas Technology Research Bulletin* **10** (1951).

41 Kuhn, J. N., Lakshminarayanan, N. & Ozkan, U. S. Effect of hydrogen sulfide on the catalytic activity of Ni-YSZ cermets. *Journal of Molecular Catalysis A: Chemical* **282**, 9-21, doi:10.1016/j.molcata.2007.11.032 (2008).

42 Timmermann, H. *et al.* Internal Reforming of Methane at Ni/YSZ and Ni/CGO SOFC Cermet Anodes. *Fuel Cells* **6**, 307-313, doi:10.1002/fuce.200600002 (2006).

43 Rostrup-Nielsen, J. R. Sulfur-passivated nickel catalysts for carbon-free steam reforming of methane. *Journal of Catalysis* **85**, 31-43, doi:10.1016/0021-9517(84)90107-6 (1984).

44 Rostrup-Nielsen, J. R. CATALYTIC STEAM REFORMING. *Catalysis: Science and Technology* **5**, 1-117 (1984).

45 Rostrup-Nielsen, J. R. Chemisorption of hydrogen sulfide on a supported nickel catalyst. *Journal of Catalysis* **11**, 220-227 (1968).

46 Sehested, J. Four challenges for nickel steam-reforming catalysts. *Catalysis Today* **111**, 103-110, doi:10.1016/j.cattod.2005.10.002 (2006).

47 Boldrin, P. *et al.* Strategies for carbon and sulfur tolerant solid oxide fuel cell materials, incorporating lessons from heterogeneous catalysis. *Chemical Reviews* **116**, 13633-13684 (2016).

48 Dong, J., Cheng, Z., Zha, S. & Liu, M. Identification of nickel sulfides on Ni–YSZ cermet exposed to H 2 fuel containing H 2 S using Raman spectroscopy. *Journal of Power Sources* **156**, 461-465 (2006).

49 Li, T. S., Wang, W. G., Chen, T., Miao, H. & Xu, C. Hydrogen sulfide poisoning in solid oxide fuel cells under accelerated testing conditions. *Journal of Power Sources* **195**, 7025-7032 (2010).

50 Wang, J.-H. & Liu, M. Computational study of sulfur–nickel interactions: A new S–Ni phase diagram. *Electrochemistry Communications* **9**, 2212-2217, doi:https://doi.org/10.1016/j.elecom.2007.06.022 (2007).

51 Li, X. *et al.* An operando surface enhanced Raman spectroscopy (SERS) study of carbon deposition on SOFC anodes. *Physical Chemistry Chemical Physics* **17**, 21112-21119 (2015).

52 Li, X. *et al. In Situ Probing of the Mechanisms of Coking Resistance on Catalyst-Modified Anodes for Solid Oxide Fuel Cells*. Vol. 27 (2015).

53 Hua, B., Li, M., Chi, B. & Jian, L. Enhanced electrochemical performance and carbon deposition resistance of Ni–YSZ anode of solid oxide fuel cells by in situ formed Ni–MnO layer for CH 4 on-cell reforming. *Journal of Materials Chemistry A* **2**, 1150-1158 (2014).

54 Riegraf, M., Hoerlein, M. P., Costa, R., Schiller, G. & Friedrich, K. A. Sulfur Poisoning of Electrochemical Reformate Conversion on Nickel/Gadolinium-Doped Ceria Electrodes. *ACS Catalysis* **7**, 7760-7771, doi:10.1021/acscatal.7b02177 (2017).

55 Riegraf, M. *et al.* The Influence of Sulfur Formation on Performance and Reforming Chemistry of SOFC Anodes Operating on Methane Containing Fuel. *Journal of The Electrochemical Society* **162**, F1324-F1332 (2015).

56 Rasmussen, J. F. B. & Hagen, A. The effect of H2S on the performance of SOFCs using methane containing fuel. *Fuel Cells* **10**, 1135-1142 (2010).

57 Blinn, K. S., Li, X., Liu, M., Bottomley, L. A. & Liu, M. Probing and mapping electrode surfaces in solid oxide fuel cells. *Journal of visualized experiments: JoVE* (2012).

58 Krasser, W., Fadini, A. & Renouprez, A. The Raman spectrum of carbon monoxide chemisorbed on silica-supported nickel. *Journal of Catalysis* **62**, 94-98 (1980).

59 Hao, X., Wang, B., Wang, Q., Zhang, R. & Li, D. Insight into both coverage and surface structure dependent CO adsorption and activation on different Ni surfaces from DFT and atomistic thermodynamics. *Physical Chemistry Chemical Physics* **18**, 17606-17618, doi:10.1039/C6CP01689H (2016).

60 Cheng, Z. *et al.* A Solid Oxide Fuel Cell Running on H2S/CH4 Fuel Mixtures. *Electrochemical and solid-state letters* **9**, A31-A33 (2006).

61 Krasser, W. & Renouprez, A. Enhanced Raman spectra of coadsorbed carbon monoxide and hydrogen on small nickel particles. *Journal of Raman Spectroscopy* **11**, 425-429 (1981).

62 Stencel, J. & Bradley, E. Raman spectra of carbon monoxide adsorbed on oriented crystalline nickel surfaces. *Journal of Raman Spectroscopy* **8**, 203-205 (1979).

63 Choi, Y. M., Compson, C., Lin, M. C. & Liu, M. A mechanistic study of H2S decomposition on Ni- and Cu-based anode surfaces in a solid oxide fuel cell. *Chemical Physics Letters* **421**, 179-183, doi:https://doi.org/10.1016/j.cplett.2006.01.059 (2006).

64 Bazylewski, P., Divigalpitiya, R. & Fanchini, G. In situ Raman spectroscopy distinguishes between reversible and irreversible thiol modifications in l-cysteine. *RSC Advances* **7**, 2964-2970 (2017).

65 Uehara, J. & Aramaki, K. A Surface-Enhanced Raman Spectroscopy Study on Adsorption of Some Sulfur-Containing Corrosion Inhibitors on Iron in Hydrochloric Acid Solutions. *Journal of the Electrochemical Society* **138**, 3245-3251 (1991).

66 Schmidt, C. & Seward, T. M. Raman spectroscopic quantification of sulfur species in aqueous fluids: Ratios of relative molar scattering factors of Raman bands of H2S, HS−, SO2, HSO4−, SO42−, S2O32−, S3− and H2O at ambient

conditions and information on changes with pressure and temperature. *Chemical Geology* **467**, 64-75 (2017).

67 Yan, N. *et al.* The surface evolution of La0.4Sr0.6TiO3+δ anode in solid oxide fuel cells: Understanding the sulfur-promotion effect. *Journal of Power Sources* **343**, 127-134, doi:https://doi.org/10.1016/j.jpowsour.2017.01.048 (2017).

68 Ward, A. T. Raman spectroscopy of sulfur, sulfur-selenium, and sulfur-arsenic mixtures. *The Journal of Physical Chemistry* **72**, 4133-4139 (1968).

69 Sato, S., Higuchi, S. & Tanaka, S. Identification and determination of oxygen-containing inorganosulfur compounds by laser Raman spectrometry. *Applied spectroscopy* **39**, 822-827 (1985).

70 Ozaki, Y., Storer, A. & Carey, P. The Raman and resonance Raman spectra of some substituted dialkyl dithioesters and their rotational isomers. *Canadian Journal of Chemistry* **60**, 190-198 (1982).

71 Nakamoto, K. *Infrared and Raman Spectra of Inorganic and Coordination Compounds, Part B: Applications in Coordination, Organometallic, and Bioinorganic Chemistry*. (Wiley, 2009).

72 Li, J., Croiset, E. & Ricardez-Sandoval, L. Methane dissociation on Ni (100), Ni (111), and Ni (553): A comparative density functional theory study. *Journal of Molecular Catalysis A: Chemical* **365**, 103-114 (2012).

73 Carrasco, J., Barrio, L., Liu, P., Rodriguez, J. A. & Ganduglia-Pirovano, M. V. Theoretical studies of the adsorption of CO and C on Ni (111) and Ni/CeO2 (111): evidence of a strong metal–support interaction. *The Journal of Physical Chemistry C* **117**, 8241-8250 (2013).

74 da Silva, A. L. & Heck, N. C. Thermodynamics of sulfur poisoning in solid oxide fuel cells revisited: the effect of H 2 S concentration, temperature, current density and fuel utilization. *Journal of Power Sources* **296**, 92-101 (2015).

75 Cheng, Z., Abernathy, H. & Liu, M. Raman spectroscopy of nickel sulfide Ni3S2. *The Journal of Physical Chemistry C* **111**, 17997-18000 (2007).

76 Blinn, K. S. *et al.* Raman spectroscopic monitoring of carbon deposition on hydrocarbon-fed solid oxide fuel cell anodes. *Energy & Environmental Science* **5**, 7913-7917 (2012).

77 Duan, C. *et al.* Highly durable, coking and sulfur tolerant, fuel-flexible protonic ceramic fuel cells. *Nature* **557**, 217-222, doi:10.1038/s41586-018-0082-6 (2018).

78 Sengodan, S. *et al.* Enhancing sulfur tolerance of a Ni-YSZ anode through BaZr0. 1Ce0. 7Y0. 1Yb0. 1O3− δ infiltration. *Journal of The Electrochemical Society* **161**, F668-F673 (2014).

79 Choi, S. *et al.* Exceptional power density and stability at intermediate temperatures in protonic ceramic fuel cells. *Nature Energy*, 1 (2018).

80 Chen, Y. *et al.* An In Situ Formed, Dual-Phase Cathode with a Highly Active Catalyst Coating for Protonic Ceramic Fuel Cells. *Advanced Functional Materials* **28** (2018).

81 Duan, C. *et al.* Readily processed protonic ceramic fuel cells with high performance at low temperatures. *Science* **349**, 1321 (2015).

82 Catalysis as it goes. *Nature Catalysis* **1**, 165-166, doi:10.1038/s41929-018-0050-4 (2018).

83 Liu, M. *et al.* High-performance Ni–BaZr0. 1Ce0. 7Y0. 1Yb0. 1O3− δ (BZCYYb) membranes for hydrogen separation. *international journal of hydrogen energy* **38**, 14743-14749 (2013).

84 Ben Mabrouk, K., Kauffmann, T. H., Aroui, H. & Fontana, M. D. Raman study of cation effect on sulfate vibration modes in solid state and in aqueous solutions. *Journal of Raman Spectroscopy* **44**, 1603-1608 (2013).

85 Harroun, S. G., Bergman, J., Jablonski, E. & Brosseau, C. L. Surface-enhanced Raman spectroscopy analysis of house paint and wallpaper samples from an 18 th century historic property. *Analyst* **136**, 3453-3460 (2011).

86 Chen, Y., Xie, C., Li, Y., Song, C. & Bolin, T. B. Sulfur poisoning mechanism of steam reforming catalysts: an X-ray absorption near edge structure (XANES) spectroscopic study. *Physical Chemistry Chemical Physics* **12**, 5707-5711, doi:10.1039/B925910B (2010).

87 Argyle, M. & Bartholomew, C. Heterogeneous Catalyst Deactivation and Regeneration: A Review. *Catalysts* **5**, 145 (2015).

88 Herzberg, G. & Crawford Jr, B. L. Infrared and Raman spectra of polyatomic molecules. *The Journal of Physical Chemistry* **50**, 288-288 (1946).

89 Lutz, H. D., Eckers, W., Schneider, G. & Haeuseler, H. Raman and infrared spectra of barium and strontium hydroxides and hydroxide hydrates. *Spectrochimica Acta Part A: Molecular Spectroscopy* **37**, 561-567, doi:https://doi.org/10.1016/0584-8539(81)80048-7 (1981).

90 Bandura, A., Evarestov, R. & Kuruch, D. Hybrid HF–DFT modeling of monolayer water adsorption on (001) surface of cubic BaHfO3 and BaZrO3 crystals. *Surface science* **604**, 1591-1597 (2010).

91 Li, J., Luo, J.-L., Chuang, K. T. & Sanger, A. R. Chemical stability of Y-doped Ba (Ce, Zr) O3 perovskites in H2S-containing H2. *Electrochimica Acta* **53**, 3701-3707 (2008).

92 Chueh, W. C., Hao, Y., Jung, W. & Haile, S. M. High electrochemical activity of the oxide phase in model ceria–Pt and ceria–Ni composite anodes. *Nature materials* **11**, 155 (2012).

93 Kresse, G. & Furthmüller, J. Efficient iterative schemes for ab initio total-energy calculations using a plane-wave basis set. *Physical Review B* **54**, 11169-11186 (1996).

94 Kresse, G. & Hafner, J. Ab initio molecular dynamics for liquid metals. *Physical Review B* **47**, 558-561 (1993).

95 Kresse, G. & Hafner, J. Ab initio molecular-dynamics simulation of the liquid-metal-amorphous-semiconductor transition in germanium. *Physical Review B* **49**, 14251-14269 (1994).

96 Ceperley, D. M. & Alder, B. J. Ground State of the Electron Gas by a Stochastic Method. *Physical Review Letters* **45**, 566-569 (1980).

97 Perdew, J. P. & Wang, Y. Accurate and simple analytic representation of the electron-gas correlation energy. *Physical Review B* **45**, 13244-13249 (1992).

98 Blöchl, P. E. Projector augmented-wave method. *Physical Review B* **50**, 17953-17979 (1994).

99 Kresse, G. & Joubert, D. From ultrasoft pseudopotentials to the projector augmented-wave method. *Physical Review B* **59**, 1758-1775 (1999).

100 Monkhorst, H. J. & Pack, J. D. Special points for Brillouin-zone integrations. *Physical Review B* **13**, 5188-5192 (1976).
101 Hagen, M. *et al.* In-situ Raman investigation of polysulfide formation in Li-S cells. *Journal of The Electrochemical Society* **160**, A1205-A1214 (2013).
102 Hannauer, J. *et al.* The Quest for Polysulfides in Lithium–Sulfur Battery Electrolytes: An Operando Confocal Raman Spectroscopy Study. *ChemPhysChem* **16**, 2755-2759 (2015).
103 Yeon, J.-T. *et al.* Raman spectroscopic and X-ray diffraction studies of sulfur composite electrodes during discharge and charge. *Journal of The Electrochemical Society* **159**, A1308-A1314 (2012).
104 Zhu, W. *et al.* Investigation of the reaction mechanism of lithium sulfur batteries in different electrolyte systems by in situ Raman spectroscopy and in situ X-ray diffraction. *Sustainable Energy & Fuels* **1**, 737-747 (2017).
105 Gasteiger, H. A. & Marković, N. M. Just a dream—or future reality? *science* **324**, 48-49 (2009).
106 Whitesides, G. M. & Crabtree, G. W. Don't forget long-term fundamental research in energy. *science* **315**, 796-798 (2007).
107 Suntivich, J. *et al.* Design principles for oxygen-reduction activity on perovskite oxide catalysts for fuel cells and metal–air batteries. *Nature chemistry* **3**, 546-550 (2011).
108 Chen, Y. *et al.* A Highly Efficient Multi-phase Catalyst Dramatically Enhances the Rate of Oxygen Reduction. *Joule* (2018).
109 Suntivich, J. *et al.* Design principles for oxygen-reduction activity on perovskite oxide catalysts for fuel cells and metal–air batteries. *Nature chemistry* **3**, 546 (2011).
110 Lynch, M. E. *et al.* Enhancement of La0.6Sr0.4Co0.2Fe0.8O3-δ durability and surface electrocatalytic activity by La0.85Sr0.15MnO3±δ investigated using a new test electrode platform. *Energy & Environmental Science* **4**, 2249-2258, doi:10.1039/C1EE01188J (2011).
111 Simner, S. P., Anderson, M. D., Engelhard, M. H. & Stevenson, J. W. Degradation Mechanisms of La–Sr–Co–Fe–O3 SOFC Cathodes. *Electrochemical and Solid-State Letters* **9**, A478-A481 (2006).
112 Wang, H. *et al.* Mechanisms of performance degradation of (La, Sr)(Co, Fe) O3-δ solid oxide fuel cell cathodes. *Journal of The Electrochemical Society* **163**, F581-F585 (2016).
113 Huang, Y., Pellegrinelli, C. & Wachsman, E. Fundamental Impact of Humidity on SOFC Cathode ORR. *Journal of The Electrochemical Society* **163**, F171-F182 (2016).
114 Li, Y. *et al.* Controlling cation segregation in perovskite-based electrodes for high electro-catalytic activity and durability. *Chemical Society Reviews* **46**, 6345-6378, doi:10.1039/C7CS00120G (2017).
115 Benson, S., Waller, D. & Kilner, J. Degradation of La0. 6Sr0. 4Fe0. 8Co0. 2 O 3− δ in Carbon Dioxide and Water Atmospheres. *Journal of The Electrochemical Society* **146**, 1305-1309 (1999).
116 Grimaud, A. *et al.* Double perovskites as a family of highly active catalysts for oxygen evolution in alkaline solution. *Nature communications* **4**, 2439 (2013).

117 Choi, S. *et al.* Highly efficient and robust cathode materials for low-temperature solid oxide fuel cells: PrBa 0.5 Sr 0.5 Co 2− x Fe x O 5+ δ. *Scientific reports* **3**, 2426 (2013).

118 Yoo, S. *et al.* Development of Double-Perovskite Compounds as Cathode Materials for Low-Temperature Solid Oxide Fuel Cells. *Angewandte Chemie International Edition* **53**, 13064-13067 (2014).

119 Sengodan, S. *et al.* Layered oxygen-deficient double perovskite as an efficient and stable anode for direct hydrocarbon solid oxide fuel cells. *Nature Materials* **14**, 205 (2015).

120 Grimaud, A. *et al.* Hydration properties and rate determining steps of the oxygen reduction reaction of perovskite-related oxides as H+-SOFC cathodes. *Journal of The Electrochemical Society* **159**, B683-B694 (2012).

121 Jiang, S. P., Yan, Y. & Lu, M. *Materials for High-Temperature Fuel Cells*. (Wiley, 2013).

122 Tsvetkov, D., Ivanov, I., Malyshkin, D. & Zuev, A. Y. Oxygen content, cobalt oxide exsolution and defect structure of the double perovskite PrBaCo 2 O 6− δ. *Journal of Materials Chemistry A* **4**, 1962-1969 (2016).

123 Radjenovic, P. M. & Hardwick, L. J. Time-resolved SERS study of the oxygen reduction reaction in ionic liquid electrolytes for non-aqueous lithium–oxygen cells. *Faraday Discussions* **206**, 379-392, doi:10.1039/C7FD00170C (2018).

124 Zhang, M., de Respinis, M. & Frei, H. Time-resolved observations of water oxidation intermediates on a cobalt oxide nanoparticle catalyst. *Nature Chemistry* **6**, 362, doi:10.1038/nchem.1874

https://www.nature.com/articles/nchem.1874#supplementary-information (2014).

125 Lim, C. *et al.* Influence of Ca-doping in layered perovskite PrBaCo 2 O 5+ δ on the phase transition and cathodic performance of a solid oxide fuel cell. *Journal of Materials Chemistry A* **4**, 6479-6486 (2016).

126 Choi, Y., Lin, M. e. C. & Liu, M. Computational study on the catalytic mechanism of oxygen reduction on La0. 5Sr0. 5MnO3 in solid oxide fuel cells. *Angewandte Chemie International Edition* **46**, 7214-7219 (2007).

127 Wang, Z. *et al.* Oxygen reduction and transport on the La1-xSrxCo1-yFeyO3-[small delta] cathode in solid oxide fuel cells: a first-principles study. *Journal of Materials Chemistry A* **1**, 12932-12940, doi:10.1039/C3TA11554B (2013).

128 Shao, M.-h., Liu, P. & Adzic, R. R. Superoxide anion is the intermediate in the oxygen reduction reaction on platinum electrodes. *Journal of the American Chemical Society* **128**, 7408-7409 (2006).

129 Yu, H. *et al.* Ultra-Low Pt Loading Catalyst Layers for PEMFC Using Reactive Spray Deposition Technology. *ECS Transactions* **69**, 487-496 (2015).

130 Tsubaki, M. & Yu, N.-T. Resonance Raman investigation of dioxygen bonding in oxycobaltmyoglobin and oxycobalthemoglobin: structural implication of splittings of the bound O--O stretching vibration. *Proceedings of the National Academy of Sciences* **78**, 3581-3585 (1981).

131 Cho, J. *et al.* Geometric and electronic structure and reactivity of a mononuclear 'side-on' nickel(iii)–peroxo complex. *Nature Chemistry* **1**, 568, doi:10.1038/nchem.366

https://www.nature.com/articles/nchem.366#supplementary-information (2009).
132 Guzman, J., Carrettin, S. & Corma, A. Spectroscopic evidence for the supply of reactive oxygen during CO oxidation catalyzed by gold supported on nanocrystalline CeO2. *Journal of the American Chemical Society* **127**, 3286-3287 (2005).
133 Guzman, J. *et al.* CO Oxidation Catalyzed by Supported Gold: Cooperation between Gold and Nanocrystalline Rare-Earth Supports Forms Reactive Surface Superoxide and Peroxide Species. *Angewandte Chemie International Edition* **44**, 4778-4781 (2005).
134 Kim, J., Seo, W.-y., Shin, J., Liu, M. & Kim, G. Composite cathodes composed of NdBa0.5Sr0.5Co2O5+[small delta] and Ce0.9Gd0.1O1.95 for intermediate-temperature solid oxide fuel cells. *Journal of Materials Chemistry A* **1**, 515-519, doi:10.1039/C2TA00025C (2013).
135 Sakai, N. *et al.* Significant effect of water on surface reaction and related electrochemical properties of mixed conducting oxides. *Solid State Ionics* **175**, 387-391 (2004).
136 Kozhukharov, V. Ceramic materials for SOFCs: Current status. (2016).
137 Zohourian, R., Merkle, R. & Maier, J. Proton uptake into the protonic cathode material BaCo0.4Fe0.4Zr0.2O3-δ and comparison to protonic electrolyte materials. *Solid State Ionics* **299**, 64-69, doi:https://doi.org/10.1016/j.ssi.2016.09.012 (2017).
138 Han, B. *et al.* Nanoscale structural oscillations in perovskite oxides induced by oxygen evolution. *Nature materials* **16**, 121 (2017).
139 Slodczyk, A., Colomban, P., Willemin, S., Lacroix, O. & Sala, B. Indirect Raman identification of the proton insertion in the high-temperature [Ba/Sr][Zr/Ti] O3-modified perovskite protonic conductors. *Journal of Raman Spectroscopy* **40**, 513-521 (2009).
140 Colomban, P., Zaafrani, O. & Slodczyk, A. Proton Content and Nature in Perovskite Ceramic Membranes for Medium Temperature Fuel Cells and Electrolysers. *Membranes* **2**, 493-509, doi:10.3390/membranes2030493 (2012).
141 Grimaud, A. *et al.* Transport properties and in-situ Raman spectroscopy study of BaCe 0.9 Y 0.1 O 3− δ as a function of water partial pressures. *Solid State Ionics* **191**, 24-31 (2011).
142 Rivas-Murias, B. & Salgueiriño, V. Thermodynamic CoO–Co3O4 crossover using Raman spectroscopy in magnetic octahedron-shaped nanocrystals. *Journal of Raman Spectroscopy* **48**, 837-841 (2017).
143 Kresse, G. & Furthmuller, J. Efficient iterative schemes for ab initio total-energy calculations using a plane-wave basis set. *Phys. Rev. B* **54**, 11169-11186 (1996).
144 Kresse, G. & Hafner, J. Ab initio molecular dynamics for liquid metals. *Phys. Rev. B* **47**, 558-561 (1993).
145 Blöchl, P. E. Projector augmented-wave method. *Phys. Rev. B* **50**, 17953-17979 (1994).
146 Chen, Y. *et al.* A Highly Efficient Multi-phase Catalyst Dramatically Enhances the Rate of Oxygen Reduction. *Joule* **2**, 938-949, doi:https://doi.org/10.1016/j.joule.2018.02.008 (2018).

147 Perdew, J. P., Burke, K. & Ernzerhof, M. Generalized Gradient Approximation Made Simple. *Phys. Rev. Lett.* **77**, 3865-3868 (1996).

148 Mastrikov, Y. A., Kuklja, M. M., Kotomin, E. A. & Maier, J. First-principles modelling of complex perovskite $(Ba_{1-x}Sr_x)(Co_{1-y}Fe_y)O_{3-\delta}$ for solid oxide fuel cell and gas separation membrane applications. *Energy & Environ. Sci.* **3**, 1544-1550 (2010).

149 Monkhorst, H. J. & Pack, J. D. Special points for Brillouin-zone integrations. *Phys. Rev. B* **13**, 5188-5192 (1976).

150 Henkelman, G., Uberuaga, B. P. & Jónsson, H. A climbing image nudged elastic band method for finding saddle points and minimum energy paths. *J. Chem. Phys.* **113**, 9901-9904 (2000).

151 Zhang, F. *et al.* Facile growth of mesoporous Co3O4 nanowire arrays on Ni foam for high performance electrochemical capacitors. *Journal of Power Sources* **203**, 250-256 (2012).

152 Xie, X. *et al.* Synthesis of nanorod-shaped cobalt hydroxycarbonate and oxide with the mediation of ethylene glycol. *The Journal of Physical Chemistry C* **114**, 2116-2123 (2010).

153 Alrehaily, L., Joseph, J. & Wren, J. Radiation-induced formation of Co 3 O 4 nanoparticles from Co 2+(aq): probing the kinetics using radical scavengers. *Physical Chemistry Chemical Physics* **17**, 24138-24150 (2015).

154 Gasteiger, H. A., Kocha, S. S., Sompalli, B. & Wagner, F. T. Activity benchmarks and requirements for Pt, Pt-alloy, and non-Pt oxygen reduction catalysts for PEMFCs. *Applied Catalysis B: Environmental* **56**, 9-35 (2005).

155 Piana, M., Catanorchi, S. & Gasteiger, H. Kinetics of non-platinum group metal catalysts for the oxygen reduction reaction in alkaline medium. *ECS Transactions* **16**, 2045-2055 (2008).

156 Mueller, D. N., Machala, M. L., Bluhm, H. & Chueh, W. C. Redox activity of surface oxygen anions in oxygen-deficient perovskite oxides during electrochemical reactions. *Nature Communications* **6**, 6097, doi:10.1038/ncomms7097

https://www.nature.com/articles/ncomms7097#supplementary-information (2015).

157 Yan, Z. *et al.* Anion insertion enhanced electrodeposition of robust metal hydroxide/oxide electrodes for oxygen evolution. *Nature Communications* **9**, 2373, doi:10.1038/s41467-018-04788-3 (2018).

158 Kivi, I. *et al.* Changes in LSC and LSCF cathode crystallographic parameters measured by electrochemical in situ high-temperature XRD. *ECS Transactions* **57**, 1841-1849 (2013).

159 Lu, Q. & Yildiz, B. Voltage-Controlled Topotactic Phase Transition in Thin-Film SrCoOx Monitored by In Situ X-ray Diffraction. *Nano Letters* **16**, 1186-1193, doi:10.1021/acs.nanolett.5b04492 (2016).

160 Hwang, J. *et al.* Perovskites in catalysis and electrocatalysis. *Science* **358**, 751 (2017).

161 Zhu, Y. *et al.* SrNb0. 1Co0. 7Fe0. 2O3− δ perovskite as a next-generation electrocatalyst for oxygen evolution in alkaline solution. *Angewandte Chemie* **127**, 3969-3973 (2015).

162 Suntivich, J., May, K. J., Gasteiger, H. A., Goodenough, J. B. & Shao-Horn, Y. A Perovskite Oxide Optimized for Oxygen Evolution Catalysis from Molecular Orbital Principles. *Science* **334**, 1383 (2011).

163 Lee, Y.-L., Kleis, J., Rossmeisl, J., Shao-Horn, Y. & Morgan, D. Prediction of solid oxide fuel cell cathode activity with first-principles descriptors. *Energy & Environmental Science* **4**, 3966-3970 (2011).

164 Tong, Y. *et al.* Spin-State Regulation of Perovskite Cobaltite to Realize Enhanced Oxygen Evolution Activity. *Chem* **3**, 812-821, doi:https://doi.org/10.1016/j.chempr.2017.09.003 (2017).

165 Chen, D. *et al.* Unraveling the nature of anomalously fast energy storage in T-Nb2O5. *Journal of the American Chemical Society* **139**, 7071-7081 (2017).

166 De Souza, R. A universal empirical expression for the isotope surface exchange coefficients (k*) of acceptor-doped perovskite and fluorite oxides. *Physical Chemistry Chemical Physics* **8**, 890-897 (2006).

167 Merkle, R. & Maier, J. How is oxygen incorporated into oxides? A comprehensive kinetic study of a simple solid-state reaction with SrTiO3 as a model material. *Angewandte Chemie International Edition* **47**, 3874-3894 (2008).

168 Jung, W. & Tuller, H. L. A New Model Describing Solid Oxide Fuel Cell Cathode Kinetics: Model Thin Film SrTi1-xFexO3-δ Mixed Conducting Oxides–a Case Study. *Advanced Energy Materials* **1**, 1184-1191 (2011).

169 Cao, X. *et al.* Insights into the Catalytic Activity of Barium Carbonate for Oxygen Reduction Reaction. *The Journal of Physical Chemistry C* **120**, 22895-22902 (2016).

170 Biegalski, M. D. *et al.* In situ examination of oxygen non-stoichiometry in La0. 80Sr0. 20CoO3− δ thin films at intermediate and low temperatures by x-ray diffraction. *Applied Physics Letters* **104**, 161910 (2014).

171 Ingram, B. *et al.* In situ X-ray studies of oxygen surface exchange behavior in thin film La0. 6Sr0. 4Co0. 2Fe0. 8O3− δ. *Applied Physics Letters* **101**, 051603 (2012).

172 Herlihy, D. M. *et al.* Detecting the oxyl radical of photocatalytic water oxidation at an n-SrTiO 3/aqueous interface through its subsurface vibration. *Nature chemistry* **8**, 549 (2016).

173 Tai, L.-W., Nasrallah, M., Anderson, H., Sparlin, D. & Sehlin, S. Structure and electrical properties of La1− xSrxCo1− yFeyO3. Part 2. The system La1− xSrxCo0. 2Fe0. 8O3. *Solid State Ionics* **76**, 273-283 (1995).

174 Iliev, M. *et al. Raman Spectroscopy of Orthorhombic Perovskitelike YMnO3 and LaMnO3*. Vol. 57 (1998).

175 Iliev, M. N. & Abrashev, M. V. Raman phonons and Raman Jahn–Teller bands in perovskite-like manganites. *Journal of Raman Spectroscopy* **32**, 805-811 (2001).

176 Ganopadhyay, S. *et al.* First Step in Multiscale Simulations of the Ionic Conductors: DFT Study of Oxygen Vacancy Migration Combined with Experimental Characterization of BSFC.

177 Evarestov, R., Kotomin, E., Heifets, E., Maier, J. & Borstel, G. Ab initio Hartree-Fock calculations of LaMnO3 (110) surfaces. *Solid state communications* **127**, 367-371 (2003).

178 Hong, W. T. *et al.* Tuning the Spin State in LaCoO3 Thin Films for Enhanced High-Temperature Oxygen Electrocatalysis. *The Journal of Physical Chemistry Letters* **4**, 2493-2499, doi:10.1021/jz401271m (2013).

179 Zhang, S., Han, N. & Tan, X. Density functional theory calculations of atomic, electronic and thermodynamic properties of cubic LaCoO3 and La1-xSrxCoO3 surfaces. *RSC Advances* **5**, 760-769, doi:10.1039/C4RA12563K (2015).

180 Huber, A.-K. *et al.* In situ study of electrochemical activation and surface segregation of the SOFC electrode material La0.75Sr0.25Cr0.5Mn0.5O3±δ. *Physical Chemistry Chemical Physics* **14**, 751-758, doi:10.1039/C1CP21743G (2012).

181 Weber, A. & McGinnis, E. A. The Raman spectrum of gaseous oxygen. *Journal of Molecular Spectroscopy* **4**, 195-200 (1960).

182 Piumetti, M. *et al.* Nanostructured Ceria-Based Materials: Effect of the Hydrothermal Synthesis Conditions on the Structural Properties and Catalytic Activity. *Catalysts* **7**, 174 (2017).

183 Trovarelli, A. & Fornasiero, P. *Catalysis by Ceria and Related Materials*. (Imperial College Press, 2013).

184 Sullivan, J. A., Dulgheru, P., Atribak, I., Bueno-López, A. & García-García, A. Attempts at an in situ Raman study of ceria/zirconia catalysts in PM combustion. *Applied Catalysis B: Environmental* **108-109**, 134-139, doi:https://doi.org/10.1016/j.apcatb.2011.08.018 (2011).

185 Matsui, T. *et al.* In Operando Raman Spectroscopy Study on Oxygen Chemical Potential Change in Ni− SDC Cermet Anode for Solid Oxide Fuel Cells. *Journal of The Electrochemical Society* **163**, F1146-F1150 (2016).

186 Muller, G., Ringuede, A. & Laberty-Robert, C. Synthesis, characterization and electrical properties of La0.7Sr0.3Co0.2Fe0.8O3/Gd–CeO2 thin films (≤500 nm). *Journal of Materials Chemistry A* **2**, 6448-6455, doi:10.1039/C3TA14505K (2014).

187 Glamazda, A. *et al.* Structural instability of the CoO4 tetrahedral chain in SrCoO3− δ thin films. *Journal of Applied Physics* **118**, 085313 (2015).

188 Wang, H.-Y. *et al.* In Situ Spectroscopic Identification of μ-OO Bridging on Spinel Co3O4 Water Oxidation Electrocatalyst. *The Journal of Physical Chemistry Letters* **7**, 4847-4853, doi:10.1021/acs.jpclett.6b02147 (2016).

189 Mefford, J. T. *et al.* Water electrolysis on La1−xSrxCoO3−δ perovskite electrocatalysts. *Nature Communications* **7**, 11053, doi:10.1038/ncomms11053 https://www.nature.com/articles/ncomms11053#supplementary-information (2016).

190 Kim, Y. J., Hwang, S. C., Lee, J. G. & Lim, H.-T. Thermal cycling of anode supported solid oxide fuel cells under various conditions: Electrical anode protection. *International Journal of Hydrogen Energy* **41**, 23173-23182 (2016).